Structure and Properties of Materials Under Extreme Conditions

Moody, Gregory

Award date:
2019

Structure and Properties of Materials Under Extreme Conditions

submitted by

Gregory Stephen Moody

for the degree of Doctor of Philosophy

of the

University of Bath

Department of Physics

April 12, 2019

COPYRIGHT

Signature of Author.....

Gregory Stephen Moody

Declaration of any previous submission of the work

The material presented here for examination for the award of a higher degree by research has not been incorporated into a submission for another degree.

Signature of Author.....

Declaration of authorship

I am the author of this thesis, and the work described therein was carried out by myself personally, with the following exceptions:

- Chapter 4: The $MgSiO_3$ samples were prepared by L. Skinner (Stanford University). The ambient X-ray diffraction experiment was performed by C. Benmore (Argonne National Laboratory), and the recovered from 17.5 GPa X-ray diffraction experiment was performed by A. Hannon (Rutherford Appleton Laboratory). The accompanying molecular dynamics simulations were provided by M. Salanne (Pierre and Marie-Curie University) and Y. Ishii (Osaka University).
- Chapter 5: The $CaSiO_3$ samples were prepared by K. Pizzey (University of Bath), and the PEARL experiment was performed by K. Pizzey. The accompanying molecular dynamics simulations were provided by M. Salanne and Y. Ishii.
- Chapter 6: The AsSe samples were prepared by K. Pizzey, and the PEARL experiment was performed by K. Pizzey.

Signature of Author.....

to Christine Moody

1963 - 2002

Abstract

The method of *in situ* neutron diffraction was used to investigate the pressure-induced structural transformations at ambient temperature, in the modified silicate network glasses $MgSiO_3$ and $CaSiO_3$, and the chalcogenide glass AsSe. Additionally, a series of calibration experiments were conducted to investigate the power-temperature relationships of a high pressure high temperature (HPHT) setup for neutron diffraction.

The structure of magnesium silicate glass ($MgSiO_3$) was investigated at pressures up to 17.5(5) GPa using *in situ* neutron diffraction. The densification process was found to be dominated by an increase in the Mg-O coordination number $\bar{n}^{\mathrm{O}}_{\mathrm{Mg}}$ from 4.50(5) at ambient to 6.1(1) at 17.5(5) GPa. Additionally, the distribution of Mg-O bond lengths r_{MgO} was found to be highly asymmetric at ambient conditions. This asymmetry is manifested by a high r shoulder originating from the Mg-O pair-distribution function $g_{\mathrm{MgO}}(r)$, which disappears at higher pressures. In contrast, no change was observed in the Si-O coordination number or bond length. The experimental work was complemented by molecular dynamics simulations. It is proposed that the pressure induced change to the Mg coordination environment is driven by an increase in the fraction of magnesium to bridging oxygen atom bonds in the network.

The structure of calcium silicate glass ($CaSiO_3$) was investigated at pressures up to 17.5(5) GPa using *in situ* neutron diffraction. A small increase in the Si-O coordination number $\bar{n}^{\mathrm{O}}_{\mathrm{Si}}$ was observed, from 4.0 at ambient, to 4.12(10) at 17.5(5) GPa. This coordination change is intermediate between that measured for $MgSiO_3$ and SiO_2 glasses. It is proposed that the inclusion of a network modifying cation to silica glass delays the pressure-driven distortion of the SiO_4 tetrahedra, and that Mg^{2+} delays this process to a greater extent than Ca^{2+}. The experimental work was complemented by molecular dynamics simulations. The Ca-O correlations are not directly accessible using neutron diffraction, but the accompanying molecular dynamics simulations have predicted an increase in the Ca-O coordination number $\bar{n}^{\mathrm{O}}_{\mathrm{Ca}}$ from 6.0 at ambient, to 7.4 at 17.5 GPa. It is proposed that, as in the case of $MgSiO_3$, the increased Ca coordination number is driven by an increase in fraction of calcium to bridging oxygen atom bonds present in the network.

The structure of arsenic selenide glass (AsSe) was investigated at pressures up to 14.4(5) GPa using *in situ* neutron diffraction. It was found that the effective coordination number $\bar{n}'$ decreases from a value of 2.35(10) at ambient, to 2.1(1) at 14.4(5) GPa. This result contrasts with previous work on the lower As concentration glass $As_{0.4}Se_{0.6}$, where a lower ambient effective coordination number of 2.2(1) was measured, and this value remained constant across the pressure range. It is proposed that the higher ambient effective coordination of AsSe results from the higher concentration of As in the glass, and that As is more susceptible to a pressure driven coordination change. Across the measured pressure range, the pair-distribution functions show that the position of the peak associated with nearest neighbour distances remains constant, whilst the peaks associated with intra-molecular distances shift to lower values of r. It is therefore proposed that the densification process of AsSe glass is dominated by a shortening of intra-molecular distances, rather than nearest neighbour bonds.

A series of calibration experiments were conducted to investigate the power-temperature relationship of a HPHT setup for neutron diffraction. Generally a linear relationship was observed, which was verified from fits, between power and/or gasket temperature, and sample temperature. Furthermore, an increase of sample pressure lowered the sample temperature for a given power. The results show that it is possible to operate the HPHT setup in an automated manner i.e without the need for a calibrant material, and that HPHT setups with altered components and/or dimensions could be calibrated in a similar way.

Acknowledgements

First and foremost I extend my thanks to Philip Salmon for his supervision of this project, and the helpful discussions over the past three years. I extend special thanks to Lawrence Gammond, for his assistance with the Paris-Edinburgh press calibration experiments. I thank the rest of the Liquids and Amorphous Materials Group members at the University of Bath: Anita Zeidler, Michela Buscemi, Annalisa Polidori and Rita Silva. I thank Craig Bull for his supervision and assistance with the PEARL experiment, and helping to get our setup in Bath operational. I thank Simon MacLeod for his supervison, and the AWE for financial support. I thank Yoshiki Ishii and Mathieu Salanne for providing the molecular dynamics simulations accompanying this work. I thank Henry Fischer for his assistance with the D4c experiments. Last but not least, I would like to extend my gratitude to the technicians and support staff who have made this research possible, especially to Paul Reddish who machined the original components for the HPHT setup.

List of Publications

- P. S. Salmon, G. S. Moody, Y. Ishii, K. J. Pizzey, A. Polidori, M. Salanne, A. Zeidler, M. Buscemi, H. E. Fischer, C. L. Bull, S. Klotz, R. Weber, C. J. Benmore and S. G. MacLeod. Pressure Induced Structural Transformations in Amorphous $MgSiO_3$ and $CaSiO_3$. Accepted for *J. Non-Cryst. Solids: X*, in press.

Contents

1 Introduction

Glass is a ubiquitous material that plays an important role in our everyday lives. It holds significant importance in science and technology, example applications include: photonics and opto-electronics [1–4], geophysics [5, 6], and biological systems [7]. In recent years, commercial high strength display glasses have been incorporated into a range of technologies, for example smartphones and automobiles [8]. Structurally, glass is a disordered material i.e it does not exhibit the long range order found in crystalline structures. However it does exhibit short and intermediate range order characterised for example, by structural motifs such as the SiO_4 tetrahedron found in silicate glasses [9]. In this example, the short range order originates from the inter-atomic bonds within SiO_4 tetrahedra, whilst the intermediate range order originates from the linking between these units.

In order to understand the physical and chemical properties of glasses, it is necessary to first have knowledge of their atomic level structures. A detailed understanding of the relationship between atomic level structure and macroscopic properties can provide valuable information that can for example, inform the design choices of glasses with specific properties. The work presented in this thesis primarily makes use of neutron diffraction, which is a powerful technique for investigating the atomic level structure of glasses [10]. Neutrons scatter directly from atomic nuclei, and may therefore be used as a direct probe of the atomic positions in a sample. Due to the physical nature of the scattering process it offers complementary information to other techniques such as X-ray diffraction. For example, neutrons are much more sensitive to light atomic nuclei than X-rays, which scatter instead from the electron clouds.

This thesis primarily concerns the structure of glasses under pressures of up to 17.5 GPa. Investigating the structure of glasses under high pressures allows changes in their atomic level structure to be followed gradually. It is possible for structural changes and the associated material properties to be maintained upon recovery to ambient conditions, an effect known as permanent densification [11, 12]. Abrupt structural changes may occur in so-called polyamorphic transitions [13, 14], and material properties such as the electrical conductivity and elastic moduli can be changed with the application of extreme conditions [15–18]. It is of interest therefore to use such knowledge to tune the material properties of glasses using pressure and heat treatment. The

structure of glasses is often an excellent analogue for the corresponding melt structures at high pressures, hence the study of glasses under extreme conditions can improve the understanding of the behaviour of geological fluids under mantle-like conditions [19].

In this thesis, the atomic level structure of three glass compositions is studied using *in situ* neutron diffraction, at pressures up to 17.5(5) GPa. The first two systems studied are the silicate network glasses magnesium silicate ($MgSiO_3$), and calcium silicate ($CaSiO_3$). The two glasses possess a broadly similar structure based on the tetrahedral network found in SiO_2 glass, but which is modified by the Mg^{2+} or Ca^{2+} cation [20, 21]. The third system studied is the chalcogenide glass arsenic selenide (AsSe). The structural motifs found in As_xSe_{1-x} glasses are very different from silicate networks, with pyramidial $AsSe_3$ units and larger cage-like As_4Se_4 units present [22–24]. The final work presented in this thesis is a series of experiments to calibrate a high pressure-high temperature (HPHT) sample cell, originally developed by Le Godec and adapted by Klotz [25, 26]. The aim of these experiments is to facilitate automated use of the setup, i.e the relationship between power and sample temperature is well known. This thesis is organised as follows:

- Chapter 2: The theory for high pressure neutron diffraction experiments is discussed including: the properties of the neutron, the theory of neutron diffraction in reciprocal space and real space, and pressure-volume equations of state.

- Chapter 3: The experimental techniques and instrumentation used in the high pressure neutron diffraction work presented in this thesis are discussed. Included is the design and operation of the D4c and PEARL diffractometers located at the Institut Laue-Langevin (ILL) and ISIS neutron sources, respectively, and the design and operation of the Paris-Edinburgh press which enables *in situ* high pressure neutron diffraction measurements to be made. The data analysis procedures used are also discussed.

- Chapter 4: The atomic level structure of magnesium silicate ($MgSiO_3$) glass is investigated using the D4c and PEARL diffractometers at pressures up to 8.2(5) GPa or 17.5(5) GPa, respectively. The results are used to examine the pressure-dependence of the coordination environments of silicon and magnesium in the structure. The results are complemented by molecular dynamics simulations using a newly developed aspherical ion model (AIM).

- Chapter 5: The atomic level structure of calcium silicate ($CaSiO_3$) glass is investigated using the D4c and PEARL diffractometers at pressures up to 8.2(5) GPa or 17.5(5) GPa, respectively. The results are used to examine the effect of the replacement of magnesium with calcium, on the densification mechanisms of the glass. The results are complemented by molecular dynamics simulations using a newly developed aspherical ion model (AIM).

- Chapter 6: The atomic level structure of the chalcogenide glass AsSe is investigated using the D4c and PEARL diffractometers at pressures up to 8.2(5) GPa or 14.4(5) GPa, respectively. The results are used to interpret the densification mechanisms of the glass, via the examination of the pressure dependence of the nearest neighbour coordination environment.

- Chapter 7: The results of a set of temperature calibration experiments of a high pressure high temperature (HPHT) setup for neutron diffraction are presented. The relationship between power and sample temperature is investigated with the aim of enabling automated use of the setup.

- Chapter 8: Final conclusions are drawn, and some examples of potential future work are presented.

2 Theory

This chapter provides the essential theory for neutron diffraction experiments studying disordered materials at high pressure. The topics addressed include: the properties of the neutron, how structural information can be obtained from neutron diffraction data, and pressure-volume equations of state. A comprehensive review of the theory of neutron diffraction for glasses is provided by Fischer *et al* [10], which is the basis of the formalism provided in this chapter.

2.1 Neutron Scattering and the Static Approximation

The neutron is a versatile probe of matter, commonly applied to investigate the structure of disordered materials. Neutrons possess no charge, and are therefore able to interact directly with atomic nuclei via the strong force. Neutrons possess a non-zero magnetic moment, and hence their interaction with unpaired spins in a sample can reveal information on the magnetic structure of the material. The de Broglie wavelength of thermal neutrons is comparable to inter-atomic spacings, and therefore their interaction with matter may be studied to determine structural information. The kinetic energy E of a neutron is related to its momentum $\mathbf{p}$ and de Broglie wavelength λ by

$$E = \frac{m_n \left|\mathbf{v}\right|^2}{2} = \frac{\left|\mathbf{p}\right|^2}{2m_n} = \frac{h^2}{2m_n\lambda^2}, \tag{2.1}$$

where $\mathrm{m}_n = 1.67 \cdot 10^{-27}$ kg is the mass of a neutron, $\mathbf{v}$ is its velocity and $\mathrm{h} = 6.63 \cdot 10^{-34}$ J s is Planck's constant. Hence the de Broglie wavelength of a neutron may be expressed as

$$\lambda = \frac{h}{\left|\mathbf{p}\right|} = \frac{h}{m_n \left|\mathbf{v}\right|}. \tag{2.2}$$

The magnitude of the wavevector of a neutron in the direction defined by its velocity $\mathbf{v}$ is

$$\left|\mathbf{k}\right| = \frac{2\pi}{\lambda}. \tag{2.3}$$

Consider the scattering event shown in Figure 2.1, where a neutron with an incident wavevector $\mathbf{k_i}$ and energy E_i is scattered to give a final wavevector $\mathbf{k_f}$ and energy E_f. The change in the momentum of the neutron can be written as

$$\triangle\mathbf{p} = \hbar\mathbf{k_i} - \hbar\mathbf{k_f} = \hbar\mathbf{Q}. \tag{2.4}$$

The scattering vector associated with the event is defined as

$$\mathbf{Q} = \mathbf{k_i} - \mathbf{k_f}. \tag{2.5}$$

From application of the cosine rule to the scattering triangle shown in Figure 2.1, the

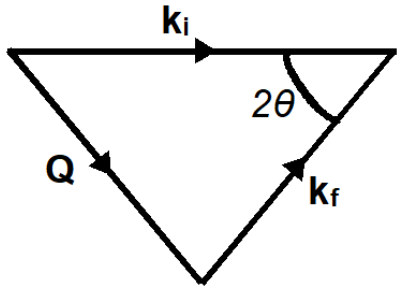

Figure 2.1: The scattering triangle showing the relationship between the incident and final neutron wavevectors $\mathbf{k_i}$ and $\mathbf{k_f}$, the scattering vector $\mathbf{Q}$ and the scattering angle 2θ.

magnitude of the scattering vector Q can be written in terms of the scattering angle 2θ as

$$Q^2 = k_i^2 + k_f^2 - 2k_i k_f \cos 2\theta. \tag{2.6}$$

The corresponding energy a neutron loses due to a scattering event is defined as

$$\Delta E = E_i - E_f = \frac{\hbar^2 \left|k_i^2\right|}{2m_n} - \frac{\hbar^2 \left|k_f^2\right|}{2m_n} = \hbar\omega, \tag{2.7}$$

where E_i and E_f denote the energies of the neutron before and after the scattering event, respectively. If the energy exchange between the neutron and the sample is very small relative to the neutron's initial energy i.e $\Delta E \ll E_i$, then the magnitude of the incident and final wavevectors of the neutron will be approximately equal, i.e $|\mathbf{k_i}| \approx |\mathbf{k_f}|$. This assumption is known as the static approximation. Applying this to equation 2.6, it can be shown that

$$Q = \frac{4\pi}{\lambda} \sin\theta. \tag{2.8}$$

2.2 Neutron Diffraction

Consider the schematic of a neutron diffraction experiment shown in Figure 2.2. A sample is placed at the origin of coordinates, which scatters a collimated beam of

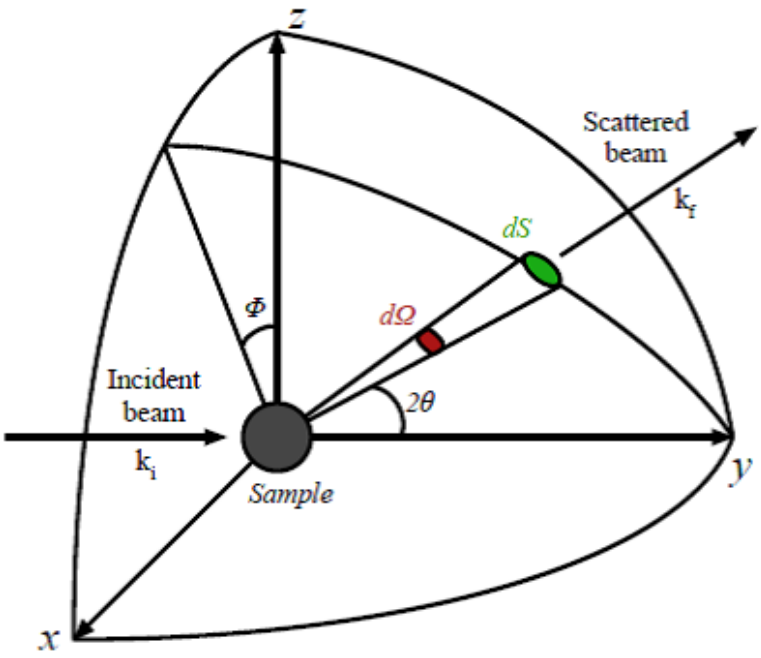

Figure 2.2: A diagram of a basic neutron diffraction setup. Incident neutrons with a wavevector $\mathbf{k_i}$ are scattered by a sample at a fixed position, through an angle of 2θ. They reach a detector of surface area dS at a distance R from the centre of the sample, which subtends a small solid angle $d\Omega$. Image reproduced from [27].

incident neutrons with flux Φ. The scattered neutrons are counted by a detector of area $\mathrm{d}S$ at a distance R from the origin. In a diffraction experiment, the differential scattering cross section is measured and is defined as

$$\frac{\mathrm{d}\sigma}{\mathrm{d}\Omega} = \frac{\text{Number of neutrons scattered into d}\Omega \text{ per second}}{\Phi \mathrm{d}\Omega}, \tag{2.9}$$

where $\mathrm{d}\Omega = \mathrm{d}S \ / \ R^2$ and is the solid angle subtended by the detector. Neutrons interact with a nucleus via the strong force which has a typical length of $\sim 10^{-14}$ m. This length is much shorter than the typical de Broglie wavelength of a thermal neutron of $\sim 10^{-10}$ m, therefore neutrons scatter isotropically from the nucleus. The scattering cross-section for a single spin-less bound nucleus is given by

$$\sigma = 4\pi b^2 \tag{2.10}$$

where b is the bound scattering length, and describes how strongly a neutron scatters from the nucleus. The scattering lengths vary significantly between different elements

and indeed, different isotopes of the same element. Figure 2.3 shows the coherent neutron scattering lengths as a function of atomic weight. Consider a diffraction exper-

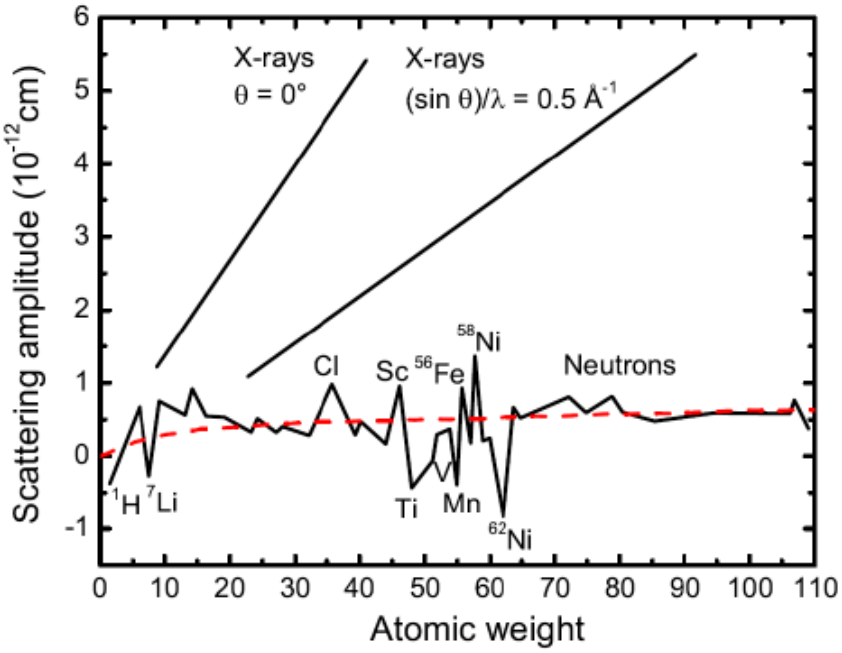

Figure 2.3: The coherent scattering lengths for neutrons and X-rays as a function of atomic weight. The X-ray scattering amplitude depends on the momentum transfer Q and is proportional to $\sin\theta/\lambda$. Furthermore, it increases with atomic number and does not vary between isotopes of the same element. Conversely, the neutron scattering amplitude is independent of Q and varies randomly with atomic number, and between isotopes of the same element. The dashed red curve indicates the potential scattering for neutrons. Image reproduced from [28, 29].

iment studying a sample containing n different chemical species. Here the differential scattering cross section can be written as

$$\begin{aligned}\frac{1}{N}\frac{d\sigma}{d\Omega}(Q) &= F(Q) + \sum_{\alpha=1}^{n} c_\alpha (b_\alpha^2 + b_{\alpha,\mathrm{inc}}^2) + P(Q) \\ &= F(Q) + \sum_{\alpha=1}^{n} c_\alpha (b_\alpha^2 + b_{\alpha,\mathrm{inc}}^2)[1 + P_\alpha(Q)] + P_{\mathrm{distinct}}(Q),\end{aligned} \tag{2.11}$$

where N is the number of scattering centres illuminated by the beam, c_a is the atomic fraction of chemical species α, b_α is the coherent neutron scattering length of chemical

species α and $b_{\alpha,\text{inc}}$ is the incoherent scattering length of chemical species α. The coherent scattering length is the mean value of the distribution of scattering lengths, and the incoherent scattering length originates from the variation of the scattering lengths about their mean value [10]. A comprehensive list of the known neutron scattering lengths and cross sections is provided by Sears [30]. $F(Q)$ is known as the total structure factor and contains structural information on the sample. The objective of a neutron diffraction experiment is to extract this term from the measured diffraction pattern for a sample. The term $P(Q)$ is an inelasticity correction term, and arises from the recoil of a nucleus during a scattering event. It is therefore a correction for events in which the static approximation does not hold, and becomes more significant for lighter atomic nuclei. $P(Q)$ may be expressed in terms of contributions from the self scattering $P_\alpha(Q)$, and distinct scattering $P_{\text{distinct}}(Q)$ parts of $\frac{d\sigma}{d\Omega}(Q)$. The Placzek correction [31] is normally used to calculate $P(Q)$. However for very light nuclei such as hydrogen, there currently exists no method to calculate the correction exactly.

2.3 The Faber-Ziman Formalism

Faber-Ziman [32] developed a formalism for writing the total structure factor *F(Q)* in terms of Faber-Ziman partial structure factors, which describe the correlations between pairs of atomic nuclei in a sample

$$F(Q) = \sum_{\alpha=1}^{n}\sum_{\beta=1}^{n} c_\alpha c_\beta b_\alpha b_\beta [S_{\alpha\beta}(Q) - 1]. \tag{2.12}$$

$S_{\alpha\beta}(Q)$ is the Faber-Ziman partial structure factor which describes the pair-correlations between chemical species α and β, and takes a limiting value of $S_{\alpha\beta}(Q \to \infty) = 1$. The total structure factor can be Fourier transformed to give the total pair-distribution function

$$\begin{aligned} G(r) &= \frac{1}{2\pi^2 r\rho}\int_0^\infty QF(Q)\sin(Qr)dQ \\ &= \sum_{\alpha=1}^{n}\sum_{\beta=1}^{n} c_\alpha c_\beta b_\alpha b_\beta [g_{\alpha\beta}(r) - 1], \end{aligned} \tag{2.13}$$

where r is a distance in real space, ρ is the atomic number density and $g_{\alpha\beta}(r)$ is the partial pair-distribution function for chemical species α and β. The latter is a measure of the probability of finding an atom of type β at a distance r from an atom of type α [33].

At distances shorter than the smallest separation between two atoms, $g_{\alpha\beta}(r \to 0) = 0$ such that the total pair distribution function gives the limit

$$\begin{aligned} G(r \to 0) &= -\sum_{\alpha=1}^{n}\sum_{\beta=1}^{n} c_\alpha c_\beta b_\alpha b_\beta \\ &= - < b >^2, \end{aligned} \tag{2.14}$$

where $< b >$ is the average coherent scattering length of the sample. The partial structure factors and partial pair-distribution functions are related via the Fourier transform pair:

$$S_{\alpha\beta}(Q) - 1 = \frac{4\pi\rho}{Q}\int_0^\infty r[g_{\alpha\beta}(r) - 1]\sin(Qr)dr, \tag{2.15}$$

$$g_{\alpha\beta}(r) - 1 = \frac{1}{2\pi^2 r\rho}\int_0^\infty Q[S_{\alpha\beta}(Q) - 1]\sin(Qr)dQ. \tag{2.16}$$

The total structure factor and total pair-distribution function may be rewritten to account for the mean scattering length as

$$S(Q) = \frac{F(Q)}{< b >^2} + 1 \tag{2.17}$$

$$G'(r) = \frac{G(r)}{< b >^2} + 1. \tag{2.18}$$

The coordination number $\bar{n}_\alpha^\beta$ gives the mean number of atoms of chemical species β contained in a spherical shell surrounding an atom of species α. The coordination number $\bar{n}_\alpha^\beta$ is calculated from the following expression

$$\bar{n}_\alpha^\beta = 4\pi\rho c_\beta \int_{r_1}^{r_2} g_{\alpha\beta}(r) r^2 dr, \tag{2.19}$$

where r_1 and r_2 denote the inner and outer radii of the shell respectively. If a peak in the total pair-distribution function $G(r)$ can be attributed to a single partial pair-distribution function $g_{\alpha\beta}(r)$, it is usually possible to integrate over the peak to calculate the coordination number directly. Similarly, the position of the peak reflects the mean bond distance corresponding to $g_{\alpha\beta}(r)$, assuming that the peak is symmetric. In some materials a peak in $g_{\alpha\beta}(r)$ may be asymmetric and in this situation it is often useful to calculate the weighted peak position, defined as

$$\bar{r}_{\alpha\beta} = \frac{\int_{r_1}^{r_2} r g_{\alpha\beta}(r) dr}{\int_{r_1}^{r_2} g_{\alpha\beta}(r) dr}. \tag{2.20}$$

In experiments a diffractometer is limited to a finite Q-range. It is therefore necessary to introduce a step modification function $M(Q)$, defined as

$$M(Q) = \begin{cases} 1 & Q \leq \mathrm{Q_{max}} \\ 0 & Q > \mathrm{Q_{max}}, \end{cases} \tag{2.21}$$

where Q_{max} is the maximum value of Q that is used to truncate the dataset, and is usually chosen according the measurement range of the diffractometer. It is therefore possible to redefine the total pair-distribution function as

$$G(r) = \frac{1}{2\pi^2 r\rho}\int_0^\infty QF(Q)M(Q)\sin(Qr)dQ. \tag{2.22}$$

An alternative method of calculating the coordination number is to fit the partial pair-distribution functions that make up the total pair-distribution function. This method is required when there are overlapping partial pair-distribution functions and the coordination number cannot be calculated by integrating directly. It can also be used to take into account the finite Q-range accessible to a diffractometer. The density correlation function is defined as

$$D_{\mathrm{exp}}(r) = \frac{2}{\pi}\int_0^\infty Q\frac{F(Q)}{< b >^2}\sin(Qr)M(Q)dQ, \tag{2.23}$$

in which the normalisation by $|G(r \to 0)|$ ensures that the weighting factors of the partial pair-distribution functions $g_{\alpha\beta}(r)$ sum to unity. It is possible to rewrite the expression for the density correlation functions as [34]:

$$\begin{aligned} D_{\mathrm{exp}}(r) &= 4\pi\rho r\frac{G(r)}{< b >^2} \otimes P(r) \\ &= 4\pi\rho r\sum_{\alpha=1}^{n}\sum_{\beta=1}^{n}\frac{c_\alpha c_\beta b_\alpha b_\beta}{|G(r \to 0)|} r g_{\alpha\beta}(r) \otimes P(r) - 4\pi\rho r, \end{aligned} \tag{2.24}$$

where the symbol $\otimes$ denotes the 1-D convolution operator. $P(r)$ is the Fourier transform of the modification function $M(Q)$, which in the case of the step function given in Equation 2.21, is defined as

$$\begin{aligned} P(r) &= \frac{1}{\pi}\int_0^{Q_{\mathrm{max}}}\cos(Qr)dr \\ &= \frac{Q_{\mathrm{max}}}{\pi}\mathrm{sinc}(Q_{\mathrm{max}}r), \end{aligned} \tag{2.25}$$

where the cardinal sine function is defined as

$$\mathrm{sinc}(x) = \frac{\sin(x)}{x}. \tag{2.26}$$

The measured density correlation function can be fitted using a sum of weighted Gaussian functions as follows:

$$\begin{aligned} D_{\mathrm{fit}}(r, r_{\alpha\beta}(i), \bar{n}^{\beta}_{\alpha}(i), \sigma_{\alpha\beta}(i)) = \sum_i \Bigg[w_{\alpha\beta}(i) \frac{\bar{n}^{\beta}_{\alpha}(i)}{c_\beta(i) r_{\alpha\beta}(i)} \frac{1}{\sqrt{2\pi}\sigma_{\alpha\beta}(i)} \times \\ \exp\left(\frac{-(r - r_{\alpha\beta}(i))^2}{2\sigma_{\alpha\beta}(i)^2} \right) \otimes P(r) \Bigg] - 4\pi\rho r, \end{aligned} \tag{2.27}$$

where $r_{\alpha\beta}(i)$ is the peak position and $\sigma_{\alpha\beta}(i)$ is the standard deviation of the Gaussian function i. The weighting factor $w_{\alpha\beta}(i)$ is given by

$$w_{\alpha\beta} = \begin{cases} \frac{2c_\alpha c_\beta b_\alpha b_\beta}{|G(0)|} & \alpha \neq \beta \\ \frac{c_\alpha^2 b_\alpha^2}{|G(0)|} & \alpha = \beta. \end{cases} \tag{2.28}$$

As the coordination number and peak position are refinable parameters of the fit, it is possible to optimise the fitted Gaussian functions to calculate these quantities. The $D_{\mathrm{fit}}(r)$ function can be optimised by minimising the goodness of fit parameter R^2_χ, defined as [35]

$$R^2_\chi\Big(r_{\alpha\beta}(i), \bar{n}^{\beta}_{\alpha}(i), \sigma_{\alpha\beta}(i)\Big) = \frac{\sum_i [D_{\mathrm{exp}}(r) - D_{\mathrm{fit}}(r)]^2}{\sum_i D^2_{\mathrm{exp}}(r)}. \tag{2.29}$$

To fit the $D(r)$ functions obtained in this work, the RDFGenie program was used. The program was written by P. S. Salmon, and implements the procedures described by Martin *et al.* [34].

2.4 Equations of State

In high pressure experiments it is necessary to understand how the atomic number density changes as a function of the sample pressure. An equation of state describes the thermodynamic state of a system as a function of the state variables: pressure (P), temperature (T) and volume (V). A review of the equations of state typically applied in diffraction work is provided by R. J. Angel [36], and is the basis of the formalism provided here. The compression of a system is defined as

$$\eta = \frac{V(P)}{V_0} \tag{2.30}$$

where *V(P)* is the volume at a given pressure P, and V_0 is the equivalent volume at ambient conditions. Typically, the molar volume is used as a standard. The compression can be related to the atomic number density using the expression

$$\rho(P) = \frac{\rho_0}{\eta} = \frac{\rho_0 V_0}{V(P)}, \tag{2.31}$$

where $\rho(P)$ and ρ_0 denote the atomic number densities at a given pressure P and ambient conditions, respectively. The work presented in this thesis was performed under cold-compression i.e high pressure and ambient temperature. Hence, the isothermal equations of state can be applied. The isothermal bulk modulus of a material measures its resistance to compression resulting from a uniform pressure, at constant temperature. It is defined as

$$B = -V\frac{\partial P}{\partial V} = -\frac{\partial P}{\partial \ln(V)}. \tag{2.32}$$

The isothermal bulk modulus at ambient conditions is denoted as B_0, and is often used as a parameter in equations of state. The Murnaghan equation of state [37] assumes that the isothermal bulk modulus varies linearly with pressure, and is defined as

$$P(V, V_0, B_0, B_0') = \frac{B_0}{B_0'}\left[\left(\frac{V}{V_0}\right)^{-B_0'} - 1\right], \tag{2.33}$$

where B_0' is the first order derivative with respect to pressure, of the isothermal bulk modulus at ambient conditions. However, experimental work has shown the Murnaghan equation to accurately reproduce $P - V$ data only to compressions of ∼10 %, i.e η ∼0.9 [36]. The Birch-Murnaghan equation of state (BM-EOS) [38] is the most common isothermal equation of state, and is based on finite strain theory. The Eulerian strain is used as a parameter in the BM-EOS, and is defined as

$$f_E = \frac{1}{2}\left(\eta^{-\frac{2}{3}} - 1\right). \tag{2.34}$$

The BM-EOS is a Taylor expansion in terms of Eulerian strain, which expanded to the fourth order is

$$P(f_E, B_0, B_0', B_0'') = 3B_0 f_E(1 + 2f_E)^{\frac{5}{2}} \times \left\{1 + \frac{3}{2}(B_0' - 4)f_E + \frac{3}{2}\left[B_0 B_0'' + (B_0' - 4)(B_0' - 3) + \frac{35}{9}\right]f_E^2\right\}, \tag{2.35}$$

where B_0'' is the second order derivative of the isothermal bulk modulus with respect to pressure, at ambient conditions. In the third order BM-EOS, the coefficient of f_E^2 is set to zero so that

$$P(f_E, B_0, B_0') = 3B_0 f_E(1+2f_E)^{\frac{5}{2}}\left[1+\frac{3}{2}(B_0'-4)f_E\right]. \tag{2.36}$$

By combining equations 2.34 and 2.36, the third-order BM-EOS can be expressed as

$$P(\eta, B_0, B_0') = \frac{3}{2}B_0\left(\eta^{-\frac{7}{3}}-\eta^{-\frac{5}{3}}\right)\left[1+\frac{3}{4}\Big(B_0'-4\Big)\Big(\eta^{-\frac{2}{3}}-1\Big)\right]. \tag{2.37}$$

By setting the derivative B_0' to equal 4, the second order BM-EOS can be expressed as

$$P(\eta, B_0) = \frac{3}{2}B_0\left(\eta^{-\frac{7}{3}}-\eta^{-\frac{5}{3}}\right). \tag{2.38}$$

It is often difficult to visually judge the quality of a fit of this equation of state to measured data. A powerful technique for analysing the goodness of fit is to convert the data into a plot of normalised stress versus Eulerian strain, known as an $f_E - F_E$ plot where the normalised stress is defined by

$$F_E = \frac{P}{3f_E(1+2f_E)^{\frac{5}{2}}}. \tag{2.39}$$

It is possible to combine equations 2.35 and 2.39 to derive an expression for the normalised stress as a function of the Eulerian strain as

$$F_E = B_0\left\{1+\frac{3}{2}(B_0'-4)f_E+\frac{3}{2}\Big[B_0B_0''+(B_0'-4)+(B_0'-3)+\frac{35}{9}\Big]f_E^2\right\}. \tag{2.40}$$

A direct indication of the compressional behaviour of the sample can be obtained by using this technique. If the data lies on a zero gradient line (i.e. F_E is constant), a second order BM-EOS is sufficient for fitting the data. If the data lies on a straight line with a gradient, a third order BM-EOS is necessary for fitting the data. If the data lies on a quadratic curve, a fourth order BM-EOS is necessary to fit the data correctly. In the case that a fourth order BM-EOS is used, it is necessary to fit a quadratic equation to the $F_E - f_E$ data to obtain values for B_0, B_0' and B_0''. In the case that a third order BM-EOS is used, by setting the coefficient of f_E^2 to equal zero as before, a linear relationship between F_E and f_E can be derived as

$$F_E = \frac{3}{2}(B_0'-4)B_0 f_E + B_0. \tag{2.41}$$

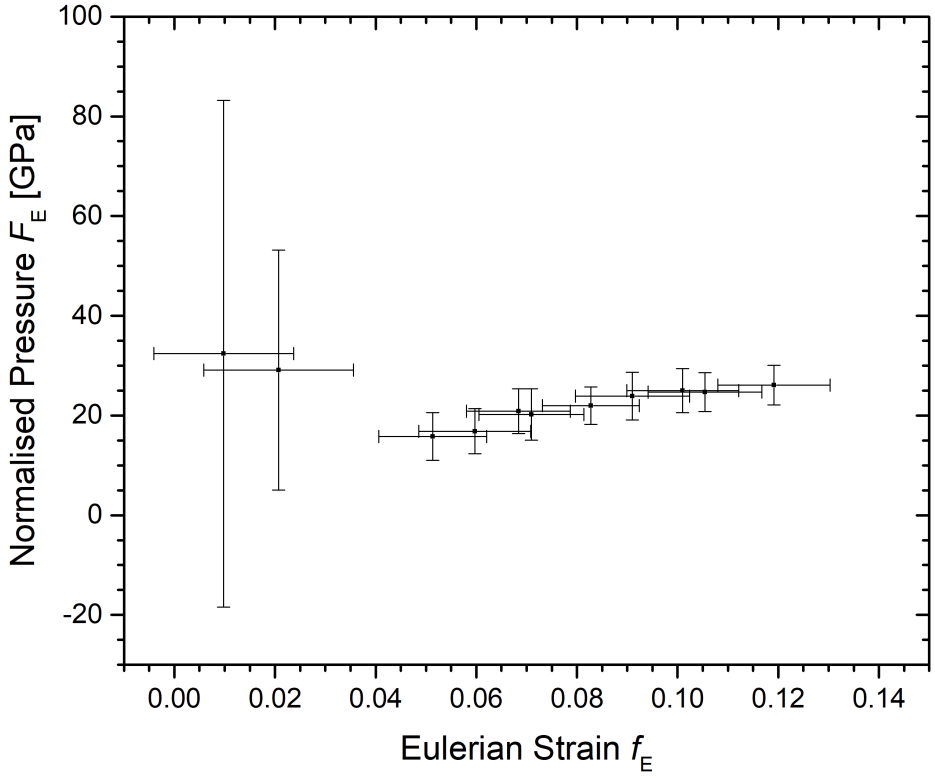

Figure 2.4: An example of an $f_E - F_E$ plot, obtained from the pressure-volume equation of state for $MgSiO_3$ glass measured by Petitgirard *et. al* [39]. The f_E and F_E values were calculated using equations 2.34 and 2.39, respectively. The data lies on a curve, which indicates that a fourth order BM-EOS is necessary to correctly fit the data.

Hence, precise values for the parameters B_0 and B_0' can be obtained from fitting a straight line to the $F_E - f_E$ data. Figure 2.4 shows the $f_E - F_E$ plot corresponding to the pressure-volume equation of state for $MgSiO_3$ glass, measured by Petitgirard *et. al* [39].

3 Experimental Procedure

This chapter describes the experimental procedures used to collect high pressure neutron diffraction data. Section 3.1 describes the ILL neutron source and the D4c diffractometer, and section 3.2 describes the ISIS neutron source and the PEARL diffractometer. Section 3.3 describes the Paris-Edinburgh press which was the apparatus used to collect high pressure neutron diffraction data in this work, and how it is used on both the D4c and PEARL diffractometers. Section 3.4 descibes the data analysis procedures used for neutron diffraction data from D4c and PEARL. Finally, a comparison of neutron diffraction data from D4c and PEARL is provided in section 3.5.

3.1 The ILL Reactor Neutron Source

The Institut Laue-Langevin (ILL) is a research nuclear reactor in Grenoble, France. The ILL is known as a steady-state neutron source, because it uses the nuclear fission process to sustain a continuous beam of neutrons. The reactor core has a single highly enriched uranium fuel element, which is cooled by a tank of heavy water D_2O [40]. Neutrons are produced via the following reactions in which emitted neutrons are used to self-sustain the reaction [41]:

$$^{235}_{92}\mathrm{U} + n \rightarrow {}^{91}_{36}\mathrm{Kr}* + {}^{145}_{56}\mathrm{Ba}* + \mathrm{Energy}, \tag{3.1}$$

$$^{91}_{36}\mathrm{Kr}* + {}^{145}_{56}\mathrm{Ba}* \rightarrow {}^{90}_{36}\mathrm{Kr} + {}^{144}_{56}\mathrm{Ba} + 2n + \gamma. \tag{3.2}$$

The neutrons produced are initially highly energetic and are slowed down via inelastic collisions with a moderator, which produces a Maxwell-Boltzmann distribution of kinetic energies. The specific material used depends on the desired energy (and therefore wavelength) of the moderated neutrons: the ILL employs a hot graphite source at 2400 K, a thermal D_2O source at 300 K, and two cold D_2 sources at 20 K. Figure 3.1 shows the basic setup of a diffraction experiment using a steady-state neutron source. A beam of moderated neutrons is first collimated using a neutron absorbing material, and then a monochromator is used to select a specific wavelength via Bragg scattering. The selected wavelength neutrons are directed towards the sample via the monochromator, and further collimated. The scattered neutrons are detected at an angle of 2θ, and because wavelength λ is fixed the magnitude of the scattering vector Q may be

calculated as

$$Q = \frac{4\pi}{\lambda}\sin\theta. \tag{3.3}$$

3.1.1 The D4c Diffractometer

The D4c diffractometer [42] is devoted to the study of disordered materials. A schematic of the instrument is provided in Figure 3.2. The instrument uses neutrons originating from the hot source graphite moderator employed at the ILL. Specific neutron wavelengths are selected via Bragg reflection from a copper monochromator. There are three neutron wavelengths used: $\lambda = 0.35$ Å via the Cu (331) reflection, $\lambda = 0.50$ Å via the Cu (220) reflection and $\lambda = 0.70$ Å via the Cu (200) reflection. The incident neutron flux is measured using a monitor placed between the monochromator and the slits used to define the beam at the sample position. The sample is placed inside an evacuated belljar with an outer diameter of 46 cm and a height of 55 cm. The dimensions of the incident beam at the sample position are defined via the use of vertical and horizontal slits: the maximum height and width are 5 cm and 2 cm, respectively. The detector bank has nine 1D ^{3}He pressurised microstrip detectors, each covering a 2θ angular range of 8°, with a 7° spacing between them. The entire detector array is able to rotate about the sample axis, and an entire angular range of $1.5° \leq 2\theta \leq 137°$ can be covered. Depending on the incident neutron wavelength used, the corresponding Q ranges are:

- 0.5 Å$^{-1} \leq Q \leq 33$ Å^{-1} ($\lambda = 0.35$ Å)
- 0.3 Å$^{-1} \leq Q \leq 24$ Å^{-1} ($\lambda = 0.50$ Å)
- 0.2 Å$^{-1} \leq Q \leq 17$ Å^{-1} ($\lambda = 0.70$ Å)

3.2 The ISIS Spallation Neutron Source

The ISIS neutron source is a spallation type source, located at the Rutherford Appleton Laboratory, U.K. In a spallation source, pulses of neutrons are produced from collisions of high energy particles with a target material. Initially an ion source produces H^- ions which are then grouped together by a Radio Frequency Quadropole (RFQ) at regular intervals [43]. Each group is fired into a LINAC, which further accelerates the ion beam. The beam then enters a synchrotron where its electrons are removed on entry by a tin

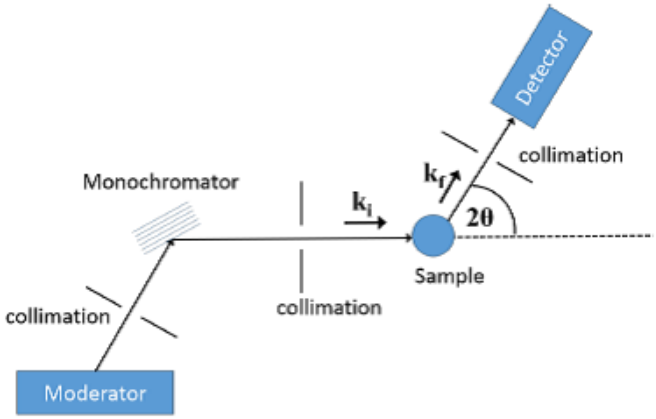

Figure 3.1: Schematic of an experiment at a steady state neutron source. Diagram reproduced from [44].

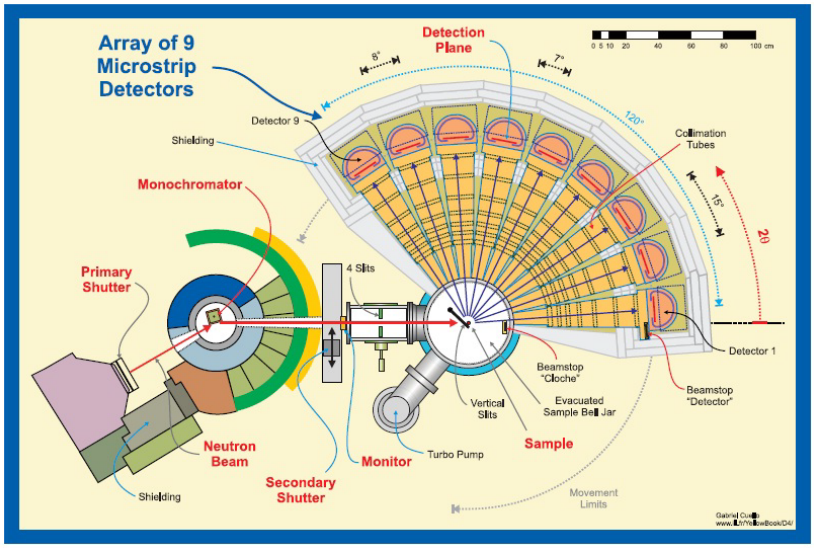

Figure 3.2: Schematic of the D4c Diffractometer. Image reproduced from [42].

foil. The resulting proton beam is further accelerated to a high energy of ∼800 MeV, and then collides with a tantalum target producing neutrons [43]. Protons are fired onto the target with a pulse repetition rate of 50 Hz. This frequency corresponds to the rate at which the resultant pulses of neutrons are produced.

Like the ILL, the neutrons produced are initially too energetic for diffraction purposes, and therefore need to be moderated. ISIS uses three different moderator materials depending on the distribution of neutron energies required: hydrogen, methane or water. Figure 3.3 shows the wavelength distribution of the three types of moderators in use at ISIS. All diffractometers at ISIS operate on the principle of time-of-flight diffraction. Figure 3.4 shows the basic setup of a neutron diffraction experiment using the total time-of-flight method, in which the intensity of neutrons is measured as a function of the time of flight between the moderator, sample and detector. The neutrons incident on the sample possess a distribution of wavelengths, where the neutron wavelength is given by

$$\lambda = \frac{ht}{m_n(L_1 + L_2)}, \tag{3.4}$$

where L_1 is the moderator to sample distance, L_2 is the sample to detector distance and t is the time for the neutron to travel the distance $L_1 + L_2$. Therefore, the momentum transfer Q may be expressed as

$$Q = \frac{4\pi m_n}{ht}(L_1 + L_2)\sin\theta. \tag{3.5}$$

3.2.1 The PEARL Diffractometer

The PEARL diffractometer shown in Figure 3.5, is located at the ISIS pulsed neutron source at the Rutherford Appleton Laboratory, Oxfordshire, U.K. PEARL uses neutrons from a liquid methane moderator, held at a constant temperature of 110 K. This results in a Maxwell-Boltzmann type distribution of neutron energies, but there are also a minority of so-called epithermal neutrons which posses a much higher kinetic energy and are not fully moderated by the moderator material. In operation with the Paris-Edinburgh press, PEARL uses nine detector banks, each arranged at a scattering angle 2θ of approximately 90° to the incident neutron flight path [45]. In operation with the Paris-Edinburgh press, PEARL offers a scattering vector Q

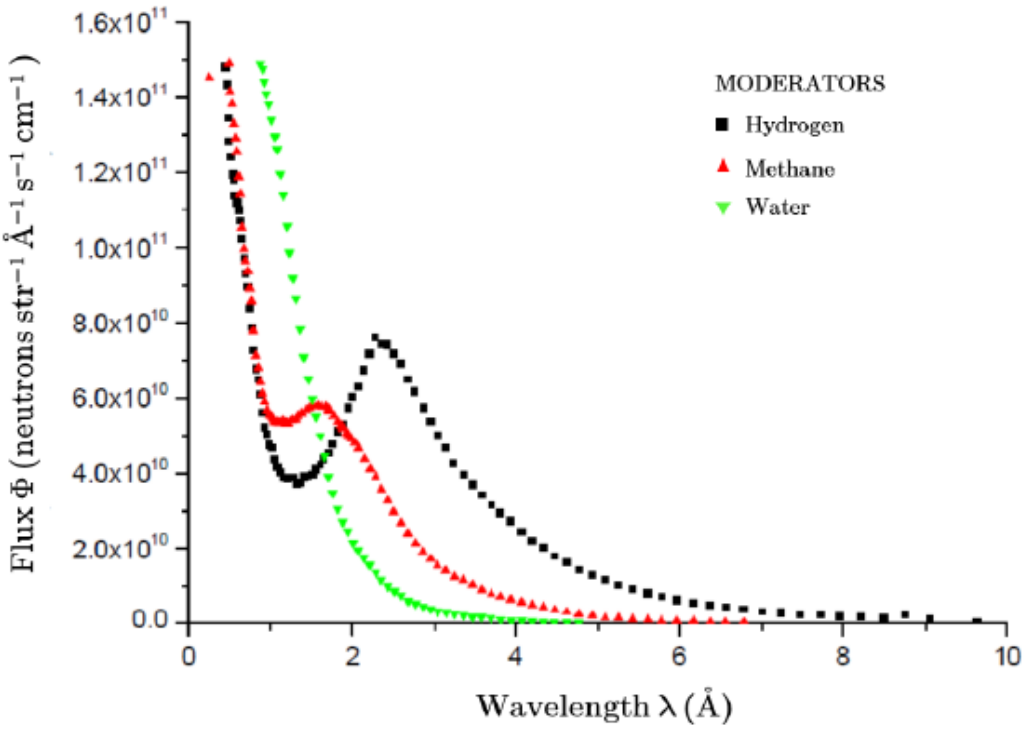

Figure 3.3: The wavelength distribution of the hydrogen, methane or water moderators used at ISIS. Image reproduced from [46].

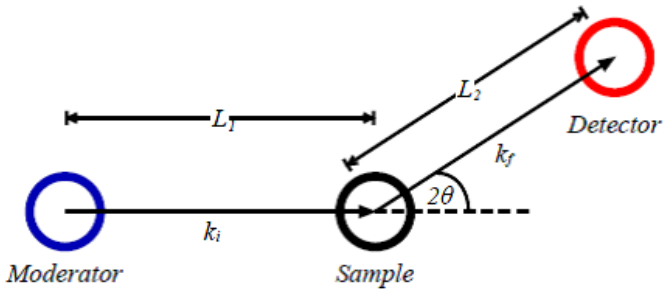

Figure 3.4: Schematic of a time of flight neutron diffraction experiment, where k_i and k_f are the incident and scattered neutron wavevectors, respectively. Image reproduced from [27].

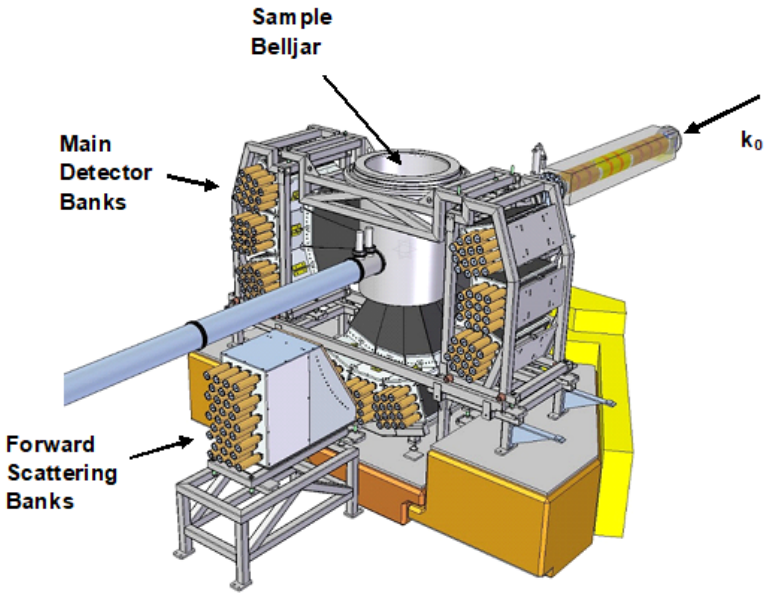

Figure 3.5: Schematic of the PEARL diffractometer showing the direction of the incident neutron beam k_0, and the main and forward scattering detector banks [109]. The sample belljar is also shown, which is evacuated during measurements.

range of 1.55 Å^{-1} $\leq Q \leq$ 20.3 Å^{-1}. There are five additional detector banks: three at 100° $\leq 2\theta \leq$ 160°, and two at 20° $\leq 2\theta \leq$ 50° [45]. However, in normal operation with the Paris-Edinburgh press these detector banks are obstructed by the press and are therefore not used.

3.3 The Paris-Edinburgh Press

The Paris-Edinburgh (PE) press is a large volume pressure cell that enables *in situ* neutron diffraction measurements up to maximum reliable sample pressures of 17.5 GPa. The PE press enables a larger sample volume than traditional diamond-anvil cells (DAC), making neutron diffraction experiments viable. Klotz [47] provides a detailed discussion of the Paris-Edinburgh press, and Salmon and Zeidler [48] discuss the use of the Paris-Edinburgh press in neutron diffraction experiments on glassy materials.

Compression is achieved by the use of two identical opposed anvils with a toroidal profile. Oil pressure drives a piston which pushes the piston anvil onto the breech anvil, that is fixed in place. The sample sits inside a central region of the anvil called the die. By necessity, the die is made of a very hard material in order to provide adequate

pressure. The die sits within a tungsten carbide seat, which is further supported by a steel binding ring. The particular choice of anvil profile and material depends on the pressure range required. For the D4c experiments presented in this thesis, cubic boron-nitride (BN) anvils with a so-called single toroidal (ST) profile were used which enable a maximum reliable sample pressure of ∼8.5 GPa to be obtained. This type of anvil has the additional benefit of helping to improve the signal to noise ratio, since ^{10}B has a large neutron absorption cross section [30]. The PEARL experiments employed sintered diamond anvils with a so-called double toroidal (DT) profile, allowing a maximum sample pressure of ∼17.5 GPa to be obtained. Figure 3.6 compares the ST and DT anvil profiles.

During an experiment, oil pressure can be applied manually via the use of a hand pump, or via the use of an automated system. When oil pressure is applied, the force on the piston anvil is given by

$$F = P_{\text{oil}} A = Lg, \tag{3.6}$$

where P_{oil} is the oil pressure, A is the surface area of the piston, L is the load applied, and $g = 9.81$ m s^{-2}. The load applied is then used to calculate the sample pressure from a calibration curve which is derived from known pressure markers, for example by diffraction measurements of a crystalline material with a known equation of state. The calibration curves corresponding to ST BN anvils and DT sintered diamond anvils, are shown in Figures 3.7 and 3.8, respectively.

3.3.1 Pressure Samples

The sample geometry for the anvils takes the shape of a pellet that comprises a cylinder of height h and radius r_{s}, that is encased at both ends by two spherical caps of height h_{cap}. The exact dimensions of the pellet vary between ST and DT anvil profiles, but the overall shape remains the same. A ST pellet has the dimensions $h = 1.6$ mm, $r_{\text{s}} = 3$ mm and $h_{\text{cap}} = 1.6$ mm. A DT pellet has the dimensions $h = 1.6$ mm, $r_{\text{s}} = 2$ mm and $h_{\text{cap}} = 1.6$ mm. Drawings showing the dimensions of the ST and DT pellets are shown in Figures 3.9 and 3.10, respectively. The following equation can be used to calculate the volume of the pellet

$$V_{\text{pellet}} = V_{\text{cylinder}} + 2V_{\text{cap}} = \pi r_{\text{s}}^2 h + 2\left[\frac{1}{6}\pi h_{\text{cap}}(h_{\text{cap}}^2 + 3r_{\text{s}}^2)\right], \tag{3.7}$$

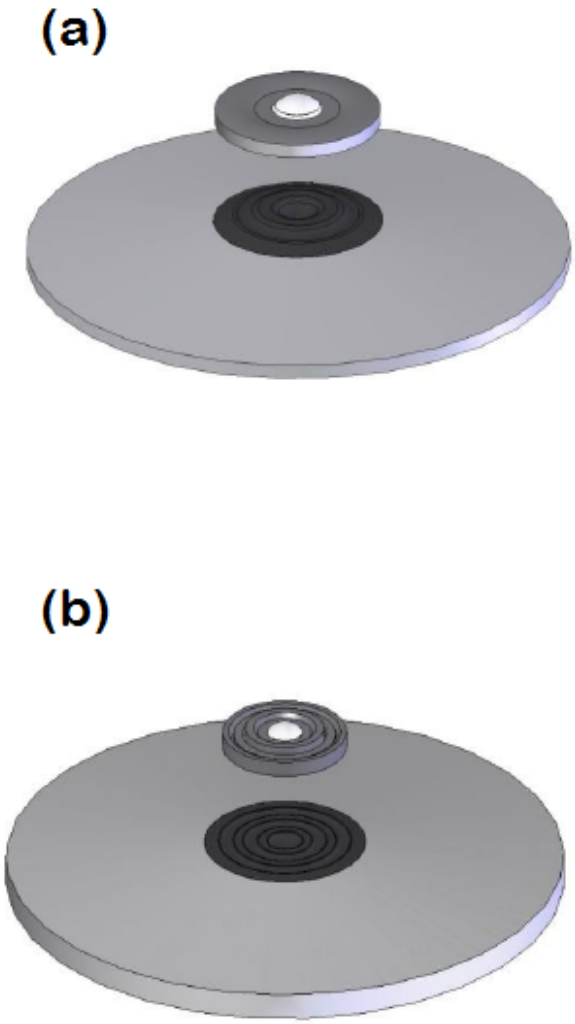

Figure 3.6: Drawings of the (a) ST and (b) DT type anvils, also showing their respective gaskets. The corresponding drawings of the ST and DT sample and gasket dimensions are shown in Figures 3.9 and 3.10, respectively. Image reproduced from [27], original information from [111].

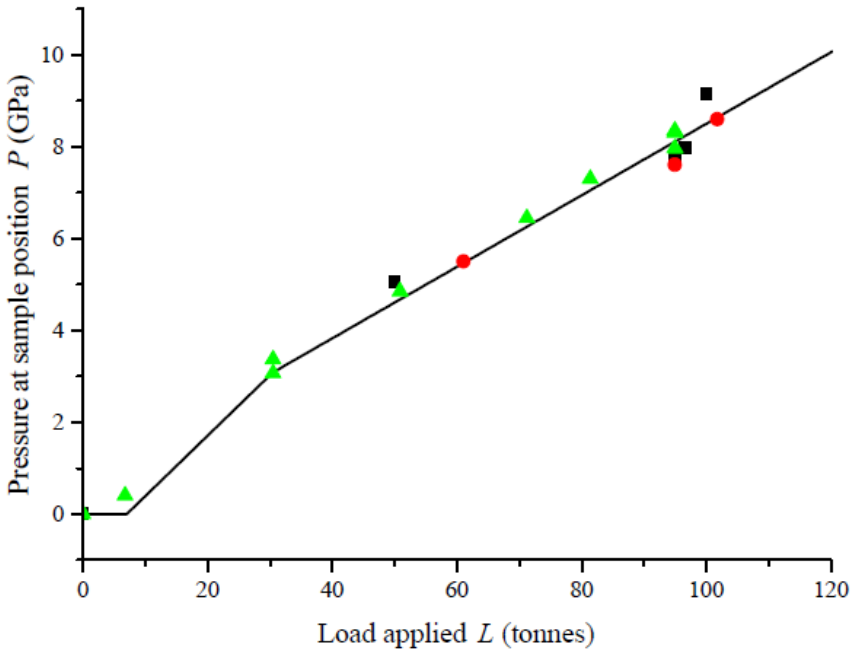

Figure 3.7: The calibration curve for the VX5 variant PE press [49] in operation with ST cubic BN anvils. The data points correspond to: (1) Calibration measurements made using a mixture of NaCl and amorphous $GeSe_2$ (green triangles), (2) Measurements of the dimensions of recovered gaskets (red circles) and (3) A Rietveld refinement of the diamond Bragg peaks measured during an experiment on amorphous GeO_2 compressed using sintered diamond ST anvils, with a unit cell volume to pressure conversion made on the basis of previous experiments on crystalline ice VII [50] (black squares).

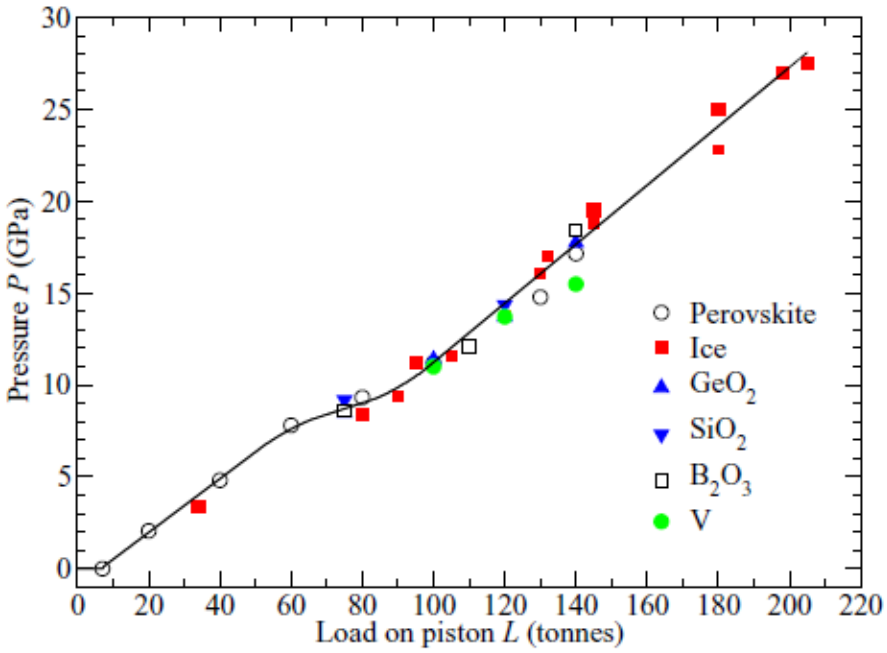

Figure 3.8: The calibration curve for the V3 variant PE press [49] in operation with DT sintered diamond anvils. The curve was constructed using data from (1) A diffraction experiment on a perovskite sample held in a methanol-ethanol pressure transmitting medium with the use of a MgO pressure marker [51], (2) A diffraction experiment on crystalline ice, (3) A Le Bail analysis of the diamond Bragg peaks from sintered diamond anvils measured for various samples: B_2O_3, SiO_2, GeO_2 and crystalline vanadium [52].

which gives a sample volume of 33.719 mm^3 for a ST pellet and 91.892 mm^3 for a DT pellet.

There are two possible methods of preparing a sample of the appropriate dimensions, where the technique used depends on how the sample material was prepared. If a sufficiently large and suitably sized piece of sample material is available, a pellet of the correct dimensions may be machined by using a Dremel multitool. The required mass of an ideal pellet can be calculated from the desired volume of the pellet, and the mass density of the sample material. The required shape is gradually sculpted, whilst periodically measuring its mass in order to achieve a pellet of dimensions and mass as close as possible to the ideal pellet. Once the mass and shape of the pellet is as close as possible to the 'ideal' pellet, it is placed in the sample position of the anvil.

Alternatively, if an appropriately sized piece of sample is not available, the material is finely ground into a powder using an agate mortar and pestle. The required mass of sample material is measured, and inserted into a specially designed hardened steel die which replicates the shape of a pellet. The die is placed into a press and compressed in stages. The height of the die is measured when empty, and then periodically as the powder is compressed to calculate the height of the powder inside. Once the procedure is complete, the die is decompressed and the resultant pellet is carefully placed in the sample position of the anvil.

3.3.2 $Ti_{0.676}Zr_{0.324}$ Gaskets

In neutron diffraction experiments, the sample is usually surrounded by a toroidal $Ti_{0.676}Zr_{0.324}$ gasket, which prevents it from ejecting radially outwards when pressure is applied. The coherent neutron scattering lengths of Ti and Zr are -3.438(2) fm and 7.16(3) fm, respectively [30]. This particular alloy composition is chosen because it gives an average coherent neutron scattering length $< b >$ of zero. The gaskets sit in grooves on the anvils that, upon compression, causes them to exert a force inwards on the sample. This force counters the outwards force exerted by the sample [53]. Figures 3.9 and 3.10 show diagrams of the ST and DT pellets and the corresponding $Ti_{0.676}Zr_{0.324}$ gaskets, respectively.

In a perfect random substitutional alloy that has an average coherent scattering length of zero, the measured total structure factor $F(Q)$ will be independent of Q. However $Ti_{0.676}Zr_{0.324}$ demonstrates a preference for like atom bonding, and crystallites

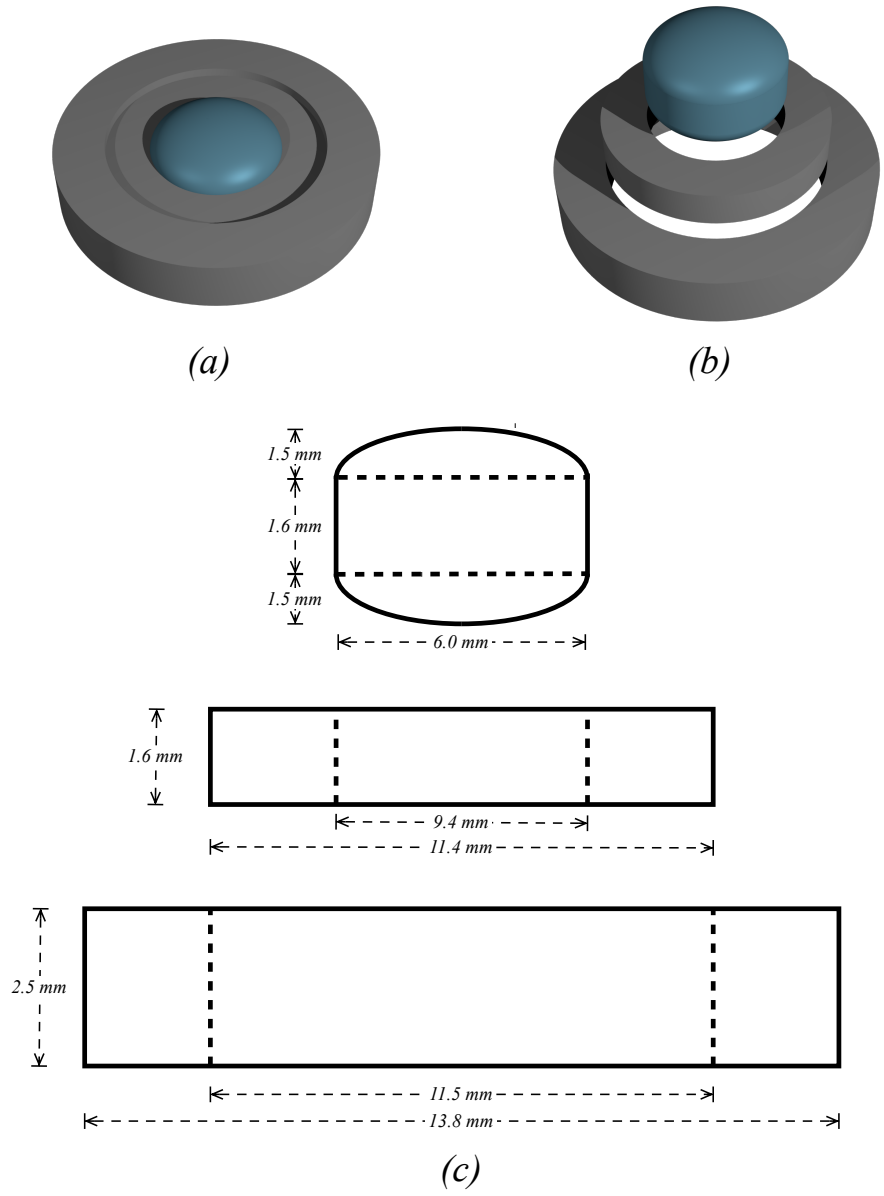

Figure 3.9: ST pellet and $Ti_{0.676}Zr_{0.324}$ gasket diagram showing: (a) a 3D model of the sample and uncompressed gaskets, (b) the 3D model with the individual components separated and (c) schematic drawings (not to scale) of the sample and gasket dimensions [27].

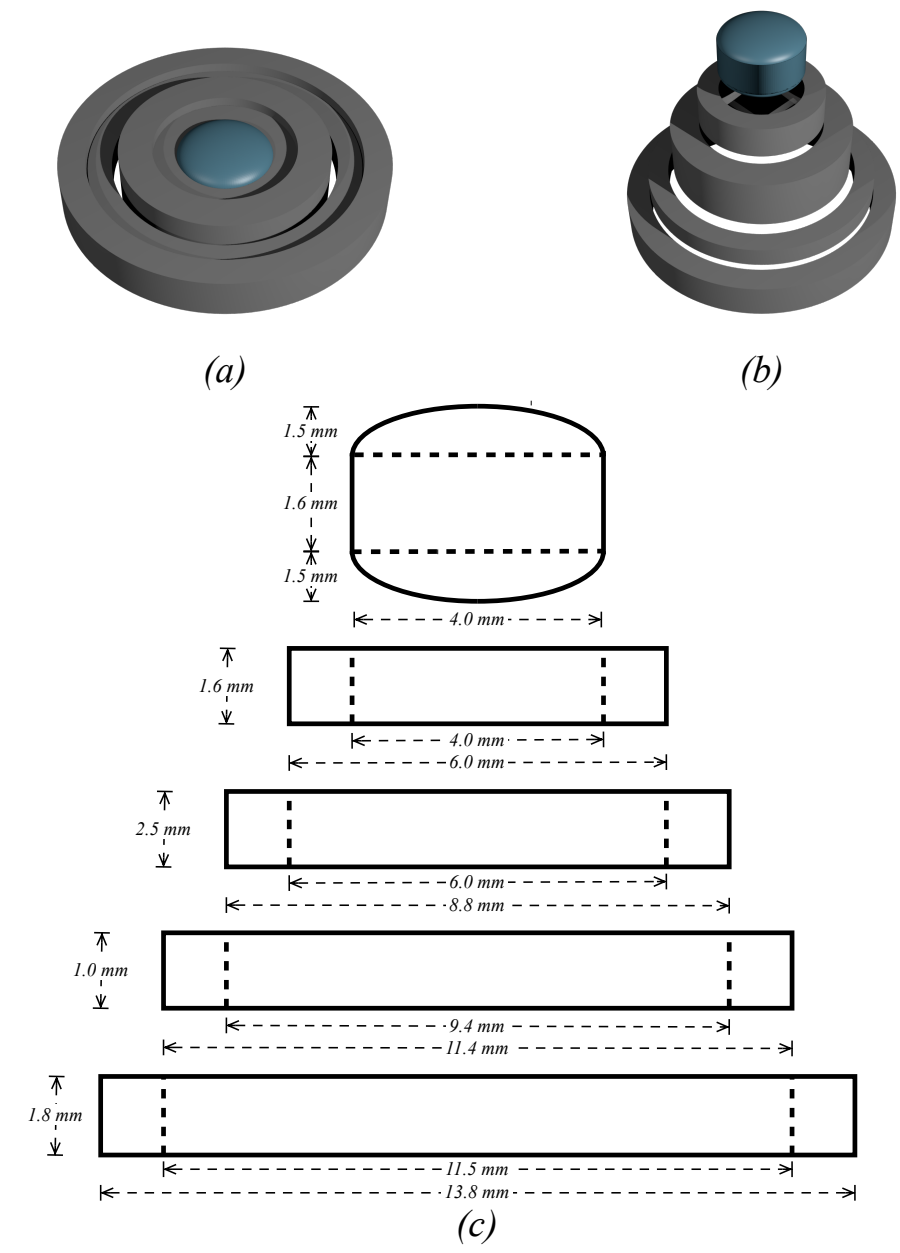

Figure 3.10: DT pellet and $Ti_{0.676}Zr_{0.324}$ gasket diagram showing: (a) a 3D model of the sample and uncompressed gaskets, (b) the 3D model with the individual components separated and (c) schematic drawings (not to scale) of the sample and gasket dimensions [27].

of like-atoms can form during the manufacturing process [47]. If the crystallites of like-atoms are sufficiently large, Bragg peaks are observed in the measured diffraction patterns. Furthermore because they are crystallites, the measured diffraction pattern is also orientation dependent. As pressure is applied, the intensity of these Bragg peaks diminishes as plastic deformation causes the crystallites to break apart. Figure 3.11 shows the raw diffraction patterns measured using the D4c diffractometer for an empty anvil with no gasket, and for $Ti_{0.676}$-$Zr_{0.324}$ gaskets at: ambient conditions, ambient conditions but previously compressed to 4.7 GPa, and 4.4 GPa but previously compressed to 8.2 GPa. The plot demonstrates that the largest Bragg peaks are observed in the ambient and previously uncompressed gasket, and that the Bragg peaks decrease in intensity as the pressure the gaskets are exposed to increases.

3.3.3 Using the Paris-Edinburgh press on the D4c diffractometer

D4c employs an in-plane scattering geometry which is shown in Figure 3.12, so-called because the scattered neutrons are in the same plane as the incident neutrons. Pressure experiments on D4c use the VX5 PE press variant which has two support columns that enable a large aperture, and the press can be oriented such that nearly all of the possible 2θ range can be measured. The maximum available Q value on experiments using this setup is $Q_{\max} = 21.5$ Å^{-1} at a neutron wavelength of $\lambda = 0.5$ Å. The D4c experiments presented in this thesis used cubic BN anvils, which enable a maximum reliable sample pressure of ∼8.5 GPa to be sustained. Additionally, the use of cubic BN anvils improves the signal to noise ratio as ^{10}B has a large neutron absorption cross section. To further enhance the signal to noise ratio, neutron absorbing $^{10}B_4C$ flags are placed just before the PE press, upstream of the sample position. The anvils are also encased in a neutron absorbing jacket made of cadmium. An incident beam profile of width 11 mm and height 4 mm is used which allows for full illumination of the sample, and partial illumination of the gaskets. In order to deduce the sample pressure when a particular oil pressure (and hence load) is applied, use is made of the calibration curve shown in Figure 3.7. In all experiments presented in this work, an automated system was used to regulate oil pressure.

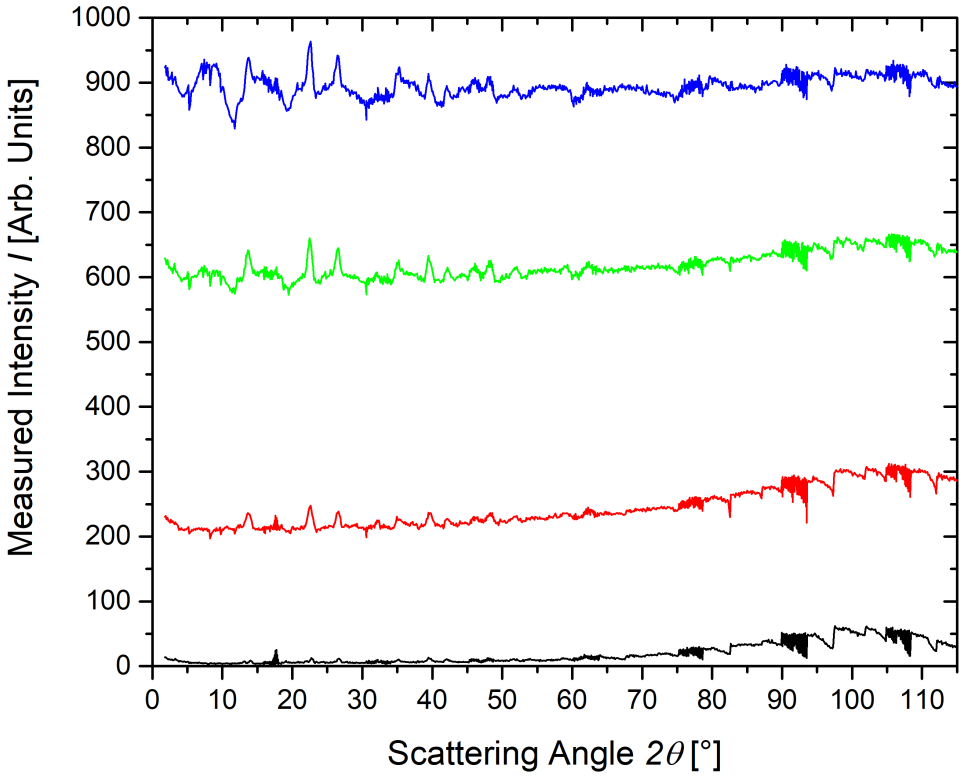

Figure 3.11: The diffraction patterns for different empty $Ti_{0.676}Zr_{0.324}$ gaskets (i.e containing no sample), measured using the D4c diffractometer with ST cubic-BN anvils. The lines correspond to: a previously uncompressed gasket measured at ambient conditions (blue), a gasket previously compressed to 4.7 GPa measured at ambient conditions (green), a gasket previously compressed to 8.2 GPa measured at 4.4 GPa (red), and the empty anvils devoid of any gasket (black).

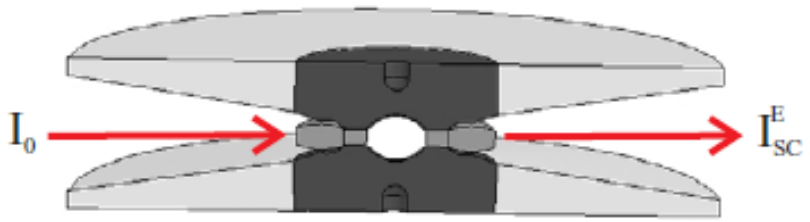

Figure 3.12: Representation of the in-plane scattering geometry as used on the D4c diffractometer, where I_0 denotes the incident beam intensity, and I_{SC}^{E} denotes the scattered beam intensity. Reproduced from [48].

3.3.4 Using the Paris-Edinburgh press on the PEARL diffractometer

In contrast to D4c, PEARL employs a transverse scattering geometry, in which neutrons are scattered in a plane perpendicular to that of the incident beam. The PEARL data presented in this report was collected using a V3 variant PE Press in conjunction with DT sintered diamond anvils which allow for a maximum reliable sample pressure of ∼17.5 GPa to be sustained. The available Q range for experiments using this setup is 1.55 Å^{-1} ≤ Q ≤ 20.3 Å^{-1}. Figure 3.13 shows the transverse scattering geometry as employed by PEARL, in which the incident beam impinges upon the breech anvil, and the detector banks measure the intensity of scattered neutrons perpendicular to the direction of this incident beam.

The incident beam is collimated by a gadolinium foil lining the hole in the backing plate of the breech anvil which the incident neutrons travel through. To improve the signal to noise ratio, the anvils are covered with neutron absorbing cadmium foil. The scattered neutrons are further collimated upstream of the detectors, so to ensure that only neutrons originating from the sample position are measured. In order to deduce the sample pressure when a particular oil pressure (and hence load) is applied, use is made of the calibration curve shown in Figure 3.8.

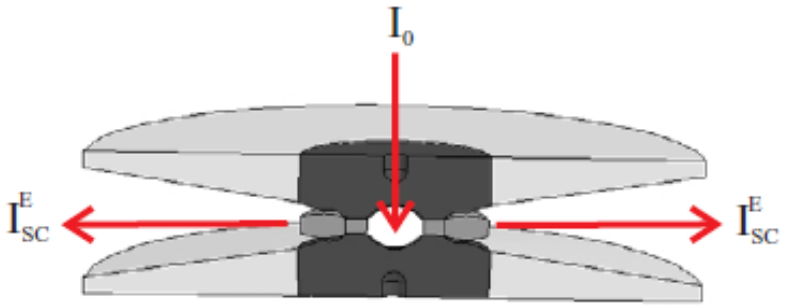

Figure 3.13: A representation of the transverse scattering geometry as used on the PEARL diffractometer. Reproduced from [48].

3.4 Neutron Diffraction Data Treatment

The theory described in Chapter 2 assumes the small sample limit, in which neutrons are not attenuated by the sample or its environment, and there are no multiple scattering events. If the small sample limit holds, the single scattered intensity measured for the sample is related to its differential scattering cross section by

$$I_{\mathrm{S}}(\theta) = a(\theta) N_{\mathrm{S}} \frac{d\sigma}{d\Omega}, \tag{3.8}$$

where a(θ) is a calibration coefficient used to convert cross sections to measured intensities, and N_{S} is the number of illuminated sample scattering centres. In practice however, this scenario is not met in high pressure neutron diffraction experiments. The incident and scattered beams of neutrons are attenuated by absorption and scattering events, and neutrons can undergo multiple scattering. Furthermore, a contribution to the measured diffraction pattern is introduced from the $Ti_{0.676}Zr_{0.324}$ gasket used to contain the sample, and the press assembly. The significance of these effects is also pressure dependent because, as pressure is increased, the geometry of the setup changes. For example, compression forces the sample and gasket to expand radially outwards, whilst simultaneously decreasing in height. It is therefore necessary to make suitable corrections to the measured datasets before any subsequent analysis can take place. The methods presented here follow the formalism previously described in [48, 49].

3.4.1 Data Corrections for D4c Experiments

For experiments using the D4c diffractometer, λ is fixed and the intensity of scattered neutrons is measured as a function of the scattering angle 2θ. The background corrected intensity for a sample inside its container $I^{\mathrm{E*}}_{\mathrm{SC}}(\theta)$ can be written as

$$I^{\mathrm{E*}}_{\mathrm{SC}}(\theta) = I^{\mathrm{E}}_{\mathrm{SC}}(\theta) - I^{\mathrm{E}}_{\mathrm{B}}(\theta) = A_{\mathrm{S,SC}}(\theta)I_{\mathrm{S}}(\theta) + A_{\mathrm{C,SC}}(\theta)I_{\mathrm{C}}(\theta) + a(\theta)M_{\mathrm{SC}}(\theta), \tag{3.9}$$

where $I^{\mathrm{E}}_{\mathrm{SC}}(\theta)$ is the measured intensity for a sample inside its container; $I^{\mathrm{E}}_{\mathrm{B}}(\theta)$ is the measured background intensity; $I_{\mathrm{S}}(\theta)$ and $I_{\mathrm{C}}(\theta)$ are the single scattered intensities for the bare sample and empty container respectively. $A_{i,j}(\theta)$ is an attenuation factor that accounts for neutrons scattered in medium i and attenuated in medium j, via absorption or scattering [54]; and $M_{\mathrm{SC}}(\theta)$ is the multiple scattering cross section for the sample in its container, which can be calculated within the quasi-isotropic approximation [55]. Using the same formalism, the background corrected measured intensity for an empty container can be written as

$$I^{\mathrm{E*}}_{\mathrm{C}}(\theta) = I^{\mathrm{E}}_{\mathrm{C}}(\theta) - I^{\mathrm{E}}_{\mathrm{B}}(\theta) = A_{\mathrm{C,C}}(\theta)I_{\mathrm{C}}(\theta) + a(\theta)M_{\mathrm{C}}(\theta), \tag{3.10}$$

where $M_{\mathrm{C}}(\theta)$ is the multiple scattering cross section of the container. By solving equations 3.8, 3.9 and 3.10 it is possible to derive the following expression for the differential scattering cross section

$$\frac{d\sigma}{d\Omega}\Big|_{\mathrm{S}} = \frac{1}{N_{\mathrm{S}}A_{\mathrm{S,SC}}(\theta)}\left[\left(\frac{I^{\mathrm{E*}}_{\mathrm{SC}}(\theta)}{a(\theta)} - M_{\mathrm{SC}}(\theta)\right) - \frac{A_{\mathrm{C,SC}}(\theta)}{A_{\mathrm{C,C}}(\theta)}\left(\frac{I^{\mathrm{E*}}_{\mathrm{C}}(\theta)}{a(\theta)} - M_{\mathrm{C}}(\theta)\right)\right]. \tag{3.11}$$

It is possible to find the calibration coefficient $a(\theta)$ by measuring the diffraction pattern for a piece of vanadium, inside the same type of container used to hold the sample. The differential scattering cross section of this piece of vanadium is given by

$$\frac{d\sigma}{d\Omega}\Big|_{\mathrm{V}} = \frac{1}{N_{\mathrm{V}}A_{\mathrm{V,VC}}(\theta)}\left[\left(\frac{I^{\mathrm{E*}}_{\mathrm{VC}}(\theta)}{a(\theta)} - M_{\mathrm{VC}}(\theta)\right) - \frac{A_{\mathrm{C,VC}}(\theta)}{A_{\mathrm{C,C}}(\theta)}\left(\frac{I^{\mathrm{E*}}_{\mathrm{C}}(\theta)}{a(\theta)} - M_{\mathrm{C}}(\theta)\right)\right]. \tag{3.12}$$

Vanadium has a very small coherent scattering length and a relatively large incoherent scattering length, with $b_{\mathrm{V}} = -0.3824(12)$ fm and $b_{\mathrm{V,inc}} = 6.35(4)$ fm, respectively [30]. For this reason, the differential scattering cross section of equation 2.11 can be simplified to give

$$\frac{d\sigma}{d\Omega}\Big|_{\mathrm{V}} \approx b^2_{\mathrm{V,inc}}[1 + P_{\mathrm{V}}(Q)] \tag{3.13}$$

where $P_{\mathrm{V}}(Q)$ is the inelasticity correction for vanadium originating from self scattering. Therefore, a vanadium measurement can be used to solve equation 3.12 for $a(\theta)$, by substitution of equation 3.13 into the left hand side [56, 57]. Typically in a high pressure neutron diffraction experiment using D4c, measurements are made of:

1) The sample inside its $Ti_{0.676}Zr_{0.324}$ gasket at the chosen pressure points. These measurements are made sequentially in order of increasing pressure, since the extent of hysteresis present in the PE press and/or sample material upon decompression is unknown.

2) An empty $Ti_{0.676}Zr_{0.324}$ gasket that has not previously been compressed, and empty previously compressed $Ti_{0.676}Zr_{0.324}$ gaskets recovered from different pressures. This is in order to be able to replicate the effect of increased pressure on the $Ti_{0.676}Zr_{0.324}$ gaskets when correcting the data.

3) The empty anvils (i.e when no sample or gaskets are present), at the normal separation of 4 mm, and at smaller separations to replicate the effect of compression (i.e the anvil separation becomes smaller).

4) A full sized vanadium pellet in an uncompressed gasket, and smaller vanadium pellets in a previously compressed gasket to replicate the effect of compression of the vanadium and gasket at higher pressures.

The uncompressed empty $Ti_{0.676}Zr_{0.324}$ gasket is used to correct the ambient dataset of the sample inside its gasket. As shown in Figure 3.11, when pressure is increased the intensity of Bragg peaks originating from crystallites in the $Ti_{0.676}Zr_{0.324}$ gaskets diminishes. For this reason, at higher pressures a weighted sum of empty $Ti_{0.676}Zr_{0.324}$ gaskets recovered from different pressures is used to correct the sample dataset. The background and container corrected sample intensity $I^{\mathrm{E}*}_{\mathrm{SC}}(\theta)$ is defined as

$$I^{\mathrm{E}*}_{\mathrm{SC}}(\theta) = I^{\mathrm{E}}_{\mathrm{SC}}(\theta) - I^{\mathrm{E}}_{\mathrm{B}}(\theta), \tag{3.14}$$

where $I^{\mathrm{E}}_{\mathrm{SC}}(\theta)$ and $I^{\mathrm{E}}_{\mathrm{B}}(\theta)$ are the measured intensity of the sample inside its container and the intensity of the background, respectively. $I^{\mathrm{E}}_{\mathrm{B}}(\theta)$ is calculated as a weighted sum of empty anvil and gasket measurements, such that

$$I^{\mathrm{E}}_{\mathrm{B}}(\theta) = x_{\mathrm{a}} I^{\mathrm{E}}_{\mathrm{a}}(\theta) + \sum_{\alpha=1}^{N} x_{\mathrm{g},\alpha} I^{\mathrm{E}}_{\mathrm{g},\alpha}(\theta), \tag{3.15}$$

where $I^{\mathrm{E}}_{\mathrm{a}}(\theta)$ and $I^{\mathrm{E}}_{\mathrm{g},\alpha}(\theta)$ are the measured intensities of the empty anvils, and an empty gasket α, respectively. The weighting coefficients x_{a} and $x_{\mathrm{g},\alpha}$ are optimised so that the

resultant diffraction pattern of $I_{\mathrm{SC}}^{\mathrm{E}*}(\theta)$ contains no contributions from the $Ti_{0.676}Zr_{0.324}$ gaskets or surrounding press assembly. Once a diffraction pattern for $I_{\mathrm{SC}}^{\mathrm{E}*}(\theta)$ has been obtained, equation 3.11 can be rewritten as

$$\frac{d\sigma}{d\Omega}\Big|_{\mathrm{S}} = \frac{1}{N_{\mathrm{S}} A_{\mathrm{S,SC}}(\theta)} \left[\frac{I_{\mathrm{SC}}^{\mathrm{E}*}(\theta)}{a(\theta)} - \left(M_{\mathrm{SC}}(\theta) - \frac{A_{\mathrm{C,SC}}(\theta)}{A_{\mathrm{C,C}}(\theta)} M_{\mathrm{C}}(\theta) \right) \right], \tag{3.16}$$

where the vanadium measurements are used to obtain the calibration coefficient $a(\theta)$. The vanadium datasets are corrected for background and container contributions in the same way as the sample datasets. In order to calculate the attenuation coefficients $A_{i,j}(\theta)$ and multiple scattering cross sections $M_i(\theta)$, the programs GUDRUN [58] and CYLMULTOF [59] are used, respectively.

Once the differential scattering cross section of the sample is obtained, the total structure factor $F(Q)$ can be calculated using equation 2.11. The $F(Q)$ function is Fourier transformed with the use of a modification function $M(Q)$, using equation 2.21. A Fourier transform using a finite Q limit introduces unphysical low r oscillations to the $G(r)$ function, in the region before the first real space peak. These oscillations are removed, and the dataset is then back Fourier transformed. If the resultant $F(Q)$ function does not agree with the original $F(Q)$ function within the experimental error, this indicates an issue with either the normalisation of the data or the background correction procedures used. A flowchart representing the data analysis procedures used for D4c experiments using the Paris-Edinburgh press is shown in Figure 3.14.

3.4.2 Data Corrections for PEARL Experiments

For experiments using the PEARL diffractometer, $2\theta \approx 90^{\circ}$ and the intensity is measured as a function of wavelength λ. Since 2θ is effectively constant, it is necessary to alter the formalism from the previous section to consider the Q dependence of the measured intensities. The formalism provided here was first discussed in [49]. Equation 3.9 can be rewritten as

$$I_{\mathrm{SC}}^{\mathrm{E}*}(Q) = I_{\mathrm{SC}}^{\mathrm{E}}(Q) - I_{\mathrm{B}}^{\mathrm{E}}(Q) = a(Q) N_{\mathrm{S}} A_{\mathrm{S,SC}}(Q) \frac{d\sigma}{d\Omega}\Big|_{\mathrm{S}} + a(Q) M_{\mathrm{SC}}(Q). \tag{3.17}$$

Likewise, the background corrected intensity for a vanadium measurement can be written as

$$I_{\mathrm{VC}}^{\mathrm{E}*}(Q) = I_{\mathrm{VC}}^{\mathrm{E}}(Q) - I_{\mathrm{B}}^{\mathrm{E}}(Q) = a(Q) N_{\mathrm{V}} A_{\mathrm{V,VC}}(Q) \frac{d\sigma}{d\Omega}\Big|_{\mathrm{V}} + a(Q) M_{\mathrm{VC}}(Q). \tag{3.18}$$

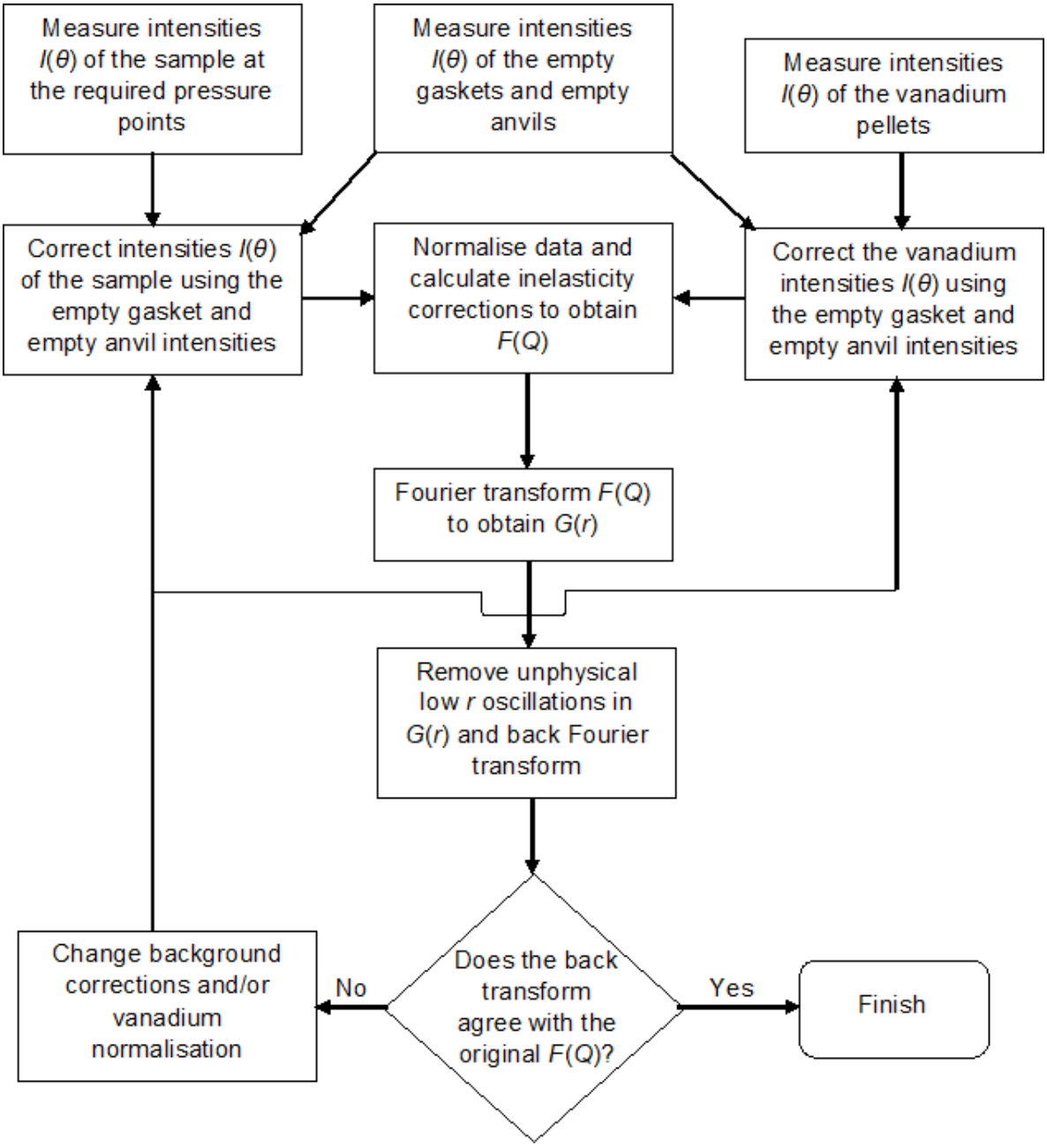

Figure 3.14: A flowchart showing the data analysis procedure used for high pressure neutron diffraction experiments using the D4c diffractometer.

By combining equation 3.13 with equations 3.17 and 3.18, it can be shown that the differential scattering cross section for the sample is given by

$$\begin{aligned}\frac{d\sigma}{d\Omega}\Big|_{\mathrm{S}} &= \frac{I^{\mathrm{E}*}_{\mathrm{SC}}(Q)}{I^{\mathrm{E}*}_{\mathrm{VC}}(Q)}\left\{\frac{N_{\mathrm{V}}A_{\mathrm{V,VC}}(Q)b^2_{\mathrm{V,inc}}[1+P_{\mathrm{V}}(Q)]+M_{\mathrm{VC}}(Q)}{N_{\mathrm{S}}A_{\mathrm{S,SC}}(Q)}\right\}+\frac{M_{\mathrm{SC}}(Q)}{N_{\mathrm{S}}A_{\mathrm{S,SC}}(Q)} \\ &= \frac{I^{\mathrm{E}*}_{\mathrm{SC}}(Q)}{I^{\mathrm{E}*}_{\mathrm{VC}}(Q)}W(Q)+X(Q).\end{aligned} \tag{3.19}$$

By using the expression for the differential scattering cross section provided in equation 2.11, an expression for the total structure factor $F(Q)$ of a sample containing n chemical species can be derived as

$$F(Q) = \frac{I^{\mathrm{E}*}_{\mathrm{SC}}(Q)}{I^{\mathrm{E}*}_{\mathrm{VC}}(Q)}W(Q)+X(Q)-\frac{\sigma_{\mathrm{self}}(Q)}{4\pi}, \tag{3.20}$$

where $\sigma_{\mathrm{self}}(Q)$ is the self scattering cross section for the sample and is given by

$$\frac{\sigma_{\mathrm{self}}(Q)}{4\pi} = \sum_{\alpha=1}^{n} c_\alpha(b^2_\alpha + b^2_{\alpha,\mathrm{inc}})[1+P_\alpha(Q)], \tag{3.21}$$

where c_α, b_α and $b_{\alpha,\mathrm{inc}}$ are the atomic concentration and the coherent and incoherent neutron scattering lengths of chemical species α, respectively. The PLATOM program [60] is used to calculate the inelasticity correction $P_\alpha(Q)$. In practice, it is found that $X(Q) << \frac{\sigma_{\mathrm{self}}}{4\pi}$ [49], therefore the total structure factor may be written as

$$F(Q) = \frac{I^{\mathrm{E}*}_{\mathrm{SC}}(Q)}{I^{\mathrm{E}*}_{\mathrm{VC}}(Q)}W(Q)-\frac{\sigma_{\mathrm{self}}(Q)}{4\pi}. \tag{3.22}$$

For a typical high pressure neutron diffraction experiment using PEARL, the following measurements are made:

1) The sample inside its $Ti_{0.676}Zr_{0.324}$ gasket at the chosen pressure points. These measurements are made sequentially in order of increasing pressure, since the extent of hysteresis present in the PE press and/or sample material upon decompression is unknown.

2) A vanadium pellet inside its $Ti_{0.676}Zr_{0.324}$ measured at similar (but not necessarily identical) pressure points to the sample. The pressure points are chosen so that the vanadium pellet's geometry matches the sample pellet's geometry, as closely as possible.

3) An empty uncompressed $Ti_{0.676}Zr_{0.324}$ gasket.

Using these measurements, the background corrected intensities for the sample and vanadium pellets $I^{\mathrm{E}*}_{\mathrm{SC}}(Q)$ and $I^{\mathrm{E}*}_{\mathrm{VC}}(Q)$ can be calculated as follows

$$I^{\mathrm{E}*}_{\mathrm{SC}}(Q) = I^{\mathrm{E}}_{\mathrm{SC}}(Q) - x_{\mathrm{S}} I^{\mathrm{E}}_{\mathrm{C}}(Q), \tag{3.23}$$

and

$$I^{\mathrm{E}*}_{\mathrm{VC}}(Q) = I^{\mathrm{E}}_{\mathrm{VC}}(Q) - x_{\mathrm{V}} I^{\mathrm{E}}_{\mathrm{C}}(Q), \tag{3.24}$$

where $I^{\mathrm{E}}_{\mathrm{SC}}(Q)$, $I^{\mathrm{E}}_{\mathrm{VC}}(Q)$ and $I^{\mathrm{E}}_{\mathrm{C}}(Q)$ are the measured intensities for the sample inside its gasket, the vanadium pellet inside its gasket and the empty gasket, respectively. The coefficients x_{S} and x_{V} are chosen to minimise the slope of the ratio $I^{\mathrm{E}*}_{\mathrm{SC}}(Q)$ / $I^{\mathrm{E}*}_{\mathrm{VC}}(Q)$. It is found that $W(Q)$ has very weak Q dependence, i.e it is essentially flat [49]. Hence, the expression for the total structure factor $F(Q)$ can be rewritten as [49]

$$\begin{aligned} F(Q) &= \frac{I^{\mathrm{E}*}_{\mathrm{SC}}(Q)}{I^{\mathrm{E}*}_{\mathrm{VC}}(Q)} W - \frac{\sigma_{\mathrm{self}}(Q)}{4\pi} \\ &= \frac{I^{\mathrm{E}}_{\mathrm{SC}}(Q) - x_{\mathrm{S}} I^{\mathrm{E}}_{\mathrm{C}}(Q)}{I^{\mathrm{E}}_{\mathrm{VC}}(Q) - x_{\mathrm{V}} I^{\mathrm{E}}_{\mathrm{C}}(Q)} W - \frac{\sigma_{\mathrm{self}}(Q)}{4\pi}, \end{aligned} \tag{3.25}$$

where W is a weighting factor chosen so that the ratio $\frac{I^{\mathrm{E}*}_{\mathrm{SC}}(Q)}{I^{\mathrm{E}*}_{\mathrm{VC}}(Q)}$ oscillates around the self scattering cross section $\frac{\sigma_{\mathrm{self}}(Q)}{4\pi}$. Once the total structure factor $F(Q)$ is calculated from equation 3.25, it is necessary to apply further correction procedures before the final $G(r)$ function can be obtained.

The accessible Q range using the PEARL diffractometer with the PE press is 1.55 Å^{-1} $\leq Q \leq$ 20.3 Å^{-1}. Hence, the low Q measurement range of the instrument is significantly lower than D4c. It is therefore necessary to correct the low-Q region of the data ($Q <$ 1.55 Å^{-1}) to obtain a correct $G(r)$ function. Firstly, the low Q region of the data is set to equal the expected $G(r \to 0)$ limit, and the entire dataset is scaled by a constant Z. Then, the $F(Q)$ function is Fourier transformed with the use of a modification function $M(Q)$, according to equation 2.21. Any large peaks in the low r region of the resulting $G(r)$ function are removed and set to equal the $G(r \to 0)$ limit calculated using equation 2.14, the $G(r)$ function is then back Fourier transformed. The purpose of this is to remove any residual slope present in the original $F(Q)$ dataset. The new $F(Q)$ function is labelled $F_1(Q)$.

To account for the absence of data for $Q <$ 1.55 Å^{-1}, a Lorentzian function is fitted in this region. It has been shown [49, 61, 62] that fitting a Lorentzian function to

the low Q region gives a good account of the so-called First Sharp Diffraction Peak (FSDP), and the function is fitted so as to pass through the expected limit $F(Q \rightarrow 0)$. The limit $F(Q \rightarrow 0)$ can either be measured on a diffractometer with a measurement range extending to lower Q, or can be calculated [63]. The $F(Q)$ function corrected with a fitted Lorentzian is labelled as $F_2(Q)$, and is again Fourier transformed. The low r oscillations in the resultant $G(r)$ are removed and the region is set to equal the calculated $G(r \rightarrow 0)$ limit. The dataset is then back Fourier transformed, and it is checked to see if the back transformed $F(Q)$ function is in agreement with the $F_2(Q)$ function, within the experimental error. If there is poor agreement between the two datasets, an iterative process in which Z, and the Lorentzian fit used, are varied. A flowchart representing the data analysis procedure for PEARL experiments using the PE press is shown in Figure 3.15.

3.5 Comparison of Neutron Diffraction Data from D4c and PEARL

It is helpful to provide a comparison of the general characteristics between neutron diffraction data obtained from D4c and PEARL. In a diffraction experiment, only a finite measurement range of momentum transfer Q is available. To account for this, the measured total structure factor $S(Q)$ is Fourier transformed using the relation

$$G'(r) = \frac{1}{2\pi^2 r\rho}\int_0^\infty Q[S(Q)-1]M(Q)\sin(Qr)dr, \tag{3.26}$$

where r is a real space distance and ρ is the atomic number density of the sample. $M(Q)$ is a modification function used to truncate the dataset according the chosen $Q_{\max}$ cutoff point, and is defined as

$$M(Q) = \begin{cases} 1 & Q \leq \mathrm{Q_{max}} \\ 0 & Q > \mathrm{Q_{max}}. \end{cases} \tag{3.27}$$

The larger the measurement range of Q and therefore the value of $Q_{\max}$ that is used, the greater the resolution of the resultant pair-distribution function. As D4c offers a higher Q limit ($Q_{\max} = 21.5$ Å^{-1} with the PE press), than PEARL ($Q_{\max} = 20.3$ Å^{-1}), the resolution of real space data obtained from PEARL is expected to be slightly poorer than the corresponding data obtained from D4c. It is found however that in all cases the

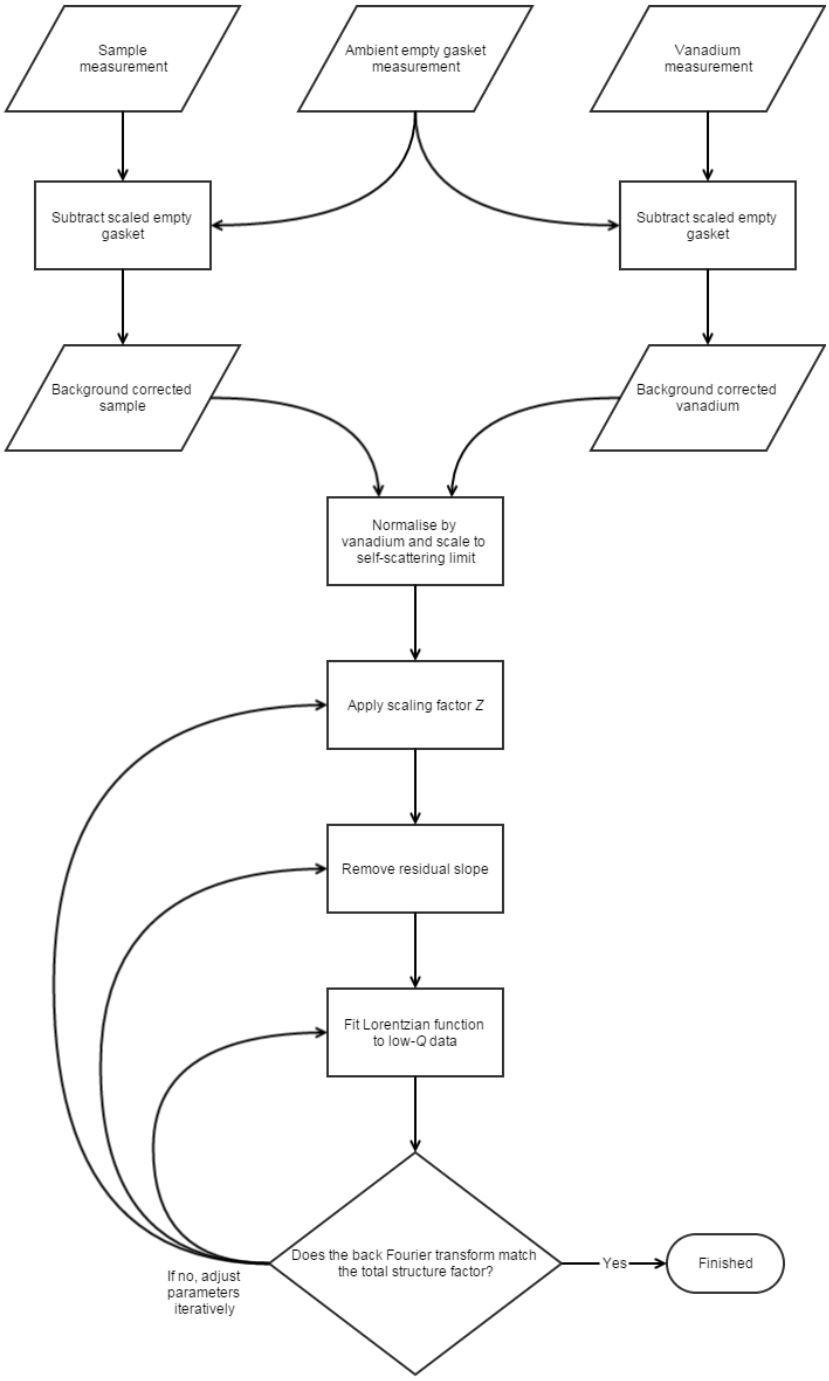

Figure 3.15: A flowchart showing the data analysis procedure used for high pressure neutron diffraction experiments using the PEARL diffractometer. Reproduced from [27].

real space resolution of diffraction obtained using PE press with PEARL is significantly poorer than would be expected as a result of the slightly lower $Q_{\max}$ cutoff.

The Lorch modification function [64] can be used as an alternative to the $M(Q)$ step function, and has the effect of broadening the peaks of the resultant pair-distribution function and removing unphysical Fourier transform artefacts. It is defined as

$$L(Q) = \begin{cases} \frac{\sin(\frac{Q\pi}{Q_{\max}})}{(\frac{Q\pi}{Q_{\max}})} & Q \leq \mathrm{Q}_{\max} \\ 0 & Q > \mathrm{Q}_{\max}. \end{cases} \tag{3.28}$$

It has been found for all the materials studied in this work, that the pair-distribution functions obtained from the PEARL diffractometer with a PE press contain broadened peaks that closely resemble the effect of a Lorch function having been applied. To demonstrate this, Figure 3.16 compares the pair-distribution functions $G'(r)$, obtained from the D4c and PEARL diffractometers for $MgSiO_3$ glass measured at ∼8.5 GPa, both Fourier transformed using the same maximum Q cutoff ($Q_{\max}$ = 20.3 Å^{-1}). It can be seen that peaks of the $G'(r)$ function originating from PEARL are more poorly resolved than the peaks of the $G'(r)$ function originating from D4c. However, if the $S(Q)$ function measured using D4c is Fourier transformed using a Lorch modification function with an identical Q cutoff value to that of PEARL, the two $G'(r)$ functions are in much closer agreement.

Figure 3.17 shows the total structure factors $S(Q)$ for $MgSiO_3$ glass at ∼8.5 GPa, measured by the D4c and PEARL diffractometers. It can be seen that the oscillations in the PEARL $S(Q)$ function are heavily dampened at higher Q compared to the D4c $S(Q)$ function. It is shown that if the $S(Q)$ function originating from PEARL is divided by a Lorch function calculated using the same Q cutoff value of 20.3 Å^{-1}, the new $S(Q)$ function is in much closer agreement to the D4c $S(Q)$ function. In this case, the large oscillations that occur for ∼15 Å$^{-1} \leq Q \leq$ 20.3 Å^{-1} in the PEARL dataset originate from the amplification of noise by division of the Lorch function as Q approaches $Q_{\max}$. However, the shapes of the two $S(Q)$ functions are in much closer agreement.

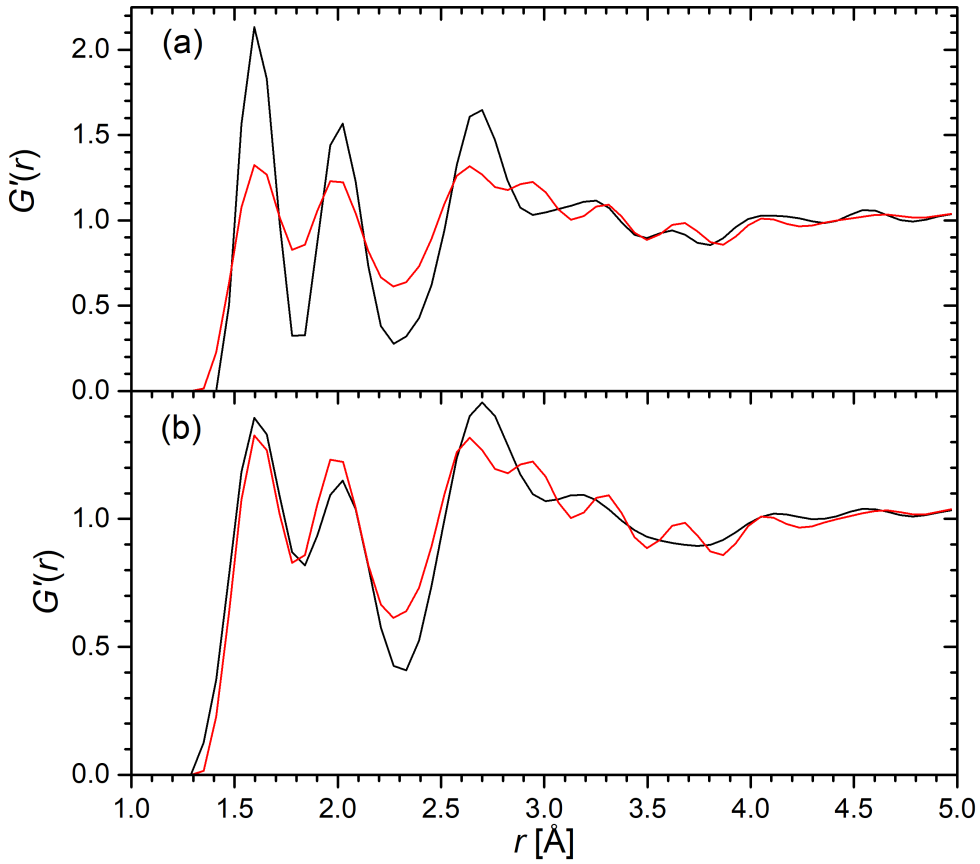

Figure 3.16: The total pair-distribution functions $G'(r)$ obtained using the D4c diffractometer (black lines), and the PEARL diffractometer (red lines). In (a), the plot compares the as-measured $G'(r)$ functions obtained from D4c and PEARL. In (b), the plot compares the as-measured $G'(r)$ function from PEARL, and the $G'(r)$ function obtained from D4c Fourier transformed with the application of a Lorch function. In both plots, the $G'(r)$ functions have been obtained by Fourier transforming using the same cutoff $Q_{\max} = 20.3$ Å^{-1}.

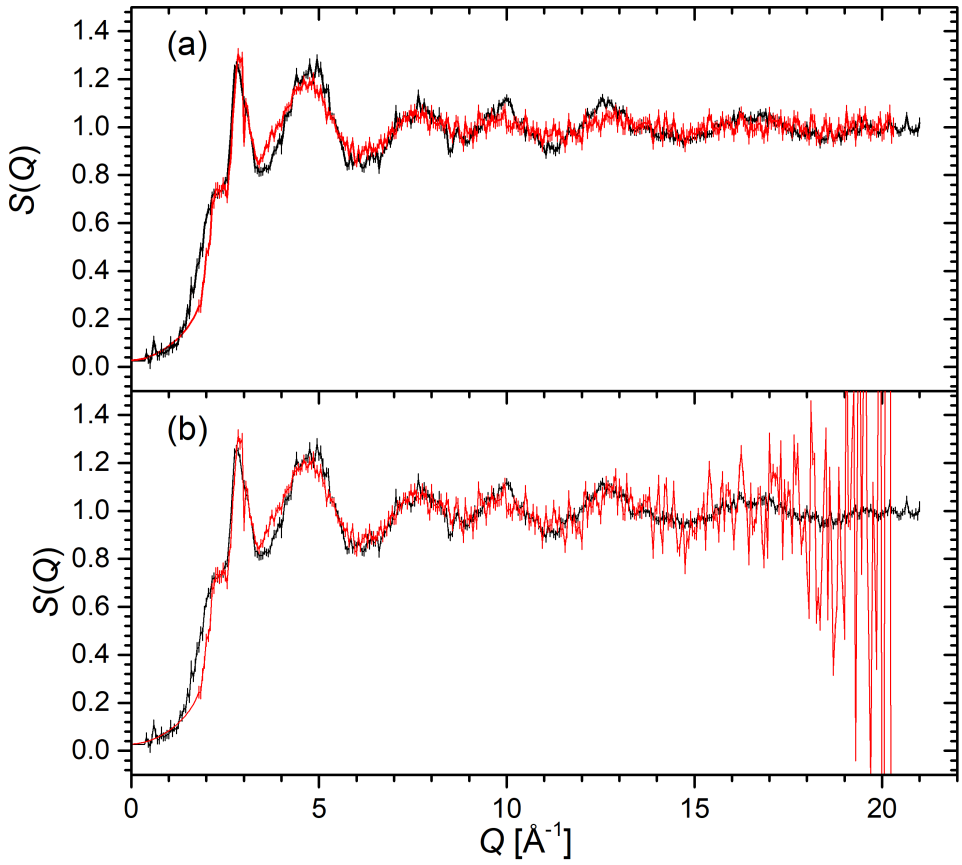

Figure 3.17: The measured total structure factors $S(Q)$ obtained using the D4c diffractometer (black lines), and the PEARL diffractometer (red lines). In (a), the plot compares the as-measured $S(Q)$ functions obtained from D4c and PEARL. In (b), the plot compares the as-measured $S(Q)$ function from D4c, and the $S(Q)$ function obtained from PEARL, divided by a Lorch function as calculated with $Q_{\max} = 20.3$ Å^{-1}.

4 Pressure Driven Structural Transformations In Magnesium Silicate Glass

4.1 Introduction

Magnesium silicate $(MgO)_x(SiO_2)_{1-x}$ glasses have been extensively studied on account of their scientific and technological importance. For example, Mg can be used to control the chemical durability and mechanical properties of bioactive glasses [65]. It is also possible to smoothly progress from a 'strong' to a 'fragile' glass forming material by increasing the Mg content [66].

The structure of magnesium silicates at high pressures is of particular importance to geophysics. For example, magnesium silicates form a high proportion of the Earth's mantle, and as such their liquid structure is relevant for understanding magma related processes [19]. The viscous flow of silicate liquids is of primary importance for understanding the evolution of the Earth, and knowledge of the structure of silicates at high pressures can help to elucidate the mechanisms of its formation.

Glassy $MgSiO_3$ is an example of a network glass. At ambient conditions, glassy $MgSiO_3$ forms a network of SiO_4 tetrahedra linked by Mg^{2+} cations [20]. The structure of such glasses can be described via the network forming vs network modifying ability of their constituent atoms or structural units. In magnesium silicate, SiO_2 acts as a network former by creating a network of SiO_4 corner sharing tetrahedra. Conversely, network modifiers act to alter the structure of such systems by forcing the network to modify itself around them. An illustration of the difference between a network former and network modifier is provided in Figure 4.1. In $MgSiO_3$ at ambient conditions, the small Mg-O coordination number of 4.5 [67] means that Mg can act either as a network former or as a network modifier, i.e. the role of Mg is ambiguous [68]. Altering a state variable such as pressure allows the collapse of the silicate network to be examined in incremental steps, and hence the transition in the role of Mg from a network former to a network modifier to be better understood.

The work presented in this chapter comprises two separate neutron diffraction experiments on glassy $MgSiO_3$, which is the magnesium-rich end member of the pyroxene silicate mineral series enstatite-ferrosilite ($MgSiO_3$ - $FeSiO_3$). The experiments were performed using a Paris-Edinburgh press and either the D4c diffractometer at pres-

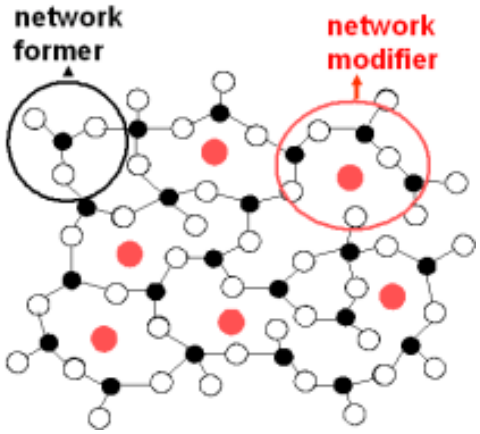

Figure 4.1: An illustration of the role of a network former vs. network modifier in a network glass. Network formers link the structure together, whilst network modifiers force the structure to modify itself around them. Reproduced from [69].

sures up to 8.2(5) GPa, or the PEARL diffractometer at pressures up to 17.5(5) GPa. The change in the silicon and magnesium coordination environments will be examined quantitatively, and comparisons will be offered with molecular dynamics simulations.

The chapter is organised as follows. The essential theory is discussed in section 4.2, and the experimental procedures used are discussed in section 4.3. The results from the diffraction experiments and accompanying molecular dynamics simulations are provided in section 4.4, and a discussion and comparison with the structure of orthoenstatite crystalline $MgSiO_3$ at high pressure is given in section 4.5. Finally, conclusions are drawn in section 4.6.

4.2 Theory

In neutron diffraction experiments, a modified version of Equation 2.13 is used which gives the Fourier transform relating the measured total structure factor $F(Q)$ to the total pair-distribution function $G(r)$,

$$G(r) = \frac{1}{2\pi^2 r\rho}\int_0^\infty QF(Q)\sin(Qr)M(Q)dr \tag{4.1}$$

where $M(Q)$ is a modification function, which is introduced for experimental work because a diffractometer can measure only over a finite Q range. $M(Q)$ is defined as

$$M(Q) = \begin{cases} 1 & Q \leq \mathrm{Q_{max}} \\ 0 & Q > \mathrm{Q_{max}} \end{cases} \tag{4.2}$$

where Q_{max} is the maximum value of Q that is used to truncate the dataset, and is usually chosen according the measurement range of the diffractometer. For a ternary glass such as $MgSiO_3$, the total pair-distribution function comprises six partial pair-distribution functions

$$\begin{aligned} G(r) = {} & \mathrm{c_{Mg}^2 b_{Mg}^2}[g_{\mathrm{MgMg}}(r) - 1] + \mathrm{c_{Si}^2 b_{Si}^2}[g_{\mathrm{SiSi}}(r) - 1] + \mathrm{c_O^2 b_O^2}[g_{\mathrm{OO}}(r) - 1] \\ & + 2\mathrm{c_{Mg} c_{Si} b_{Mg} b_{Si}}[g_{\mathrm{MgSi}}(r) - 1] + 2\mathrm{c_{Mg} c_O b_{Mg} b_O}[g_{\mathrm{MgO}}(r) - 1] + 2\mathrm{c_{Si} c_O b_{Si} b_O}[g_{\mathrm{SiO}}(r) - 1]. \end{aligned} \tag{4.3}$$

In the case that a peak is asymmetric, it is helpful to calculate a weighted peak position using

$$\bar{r}_{\alpha\beta} = \frac{\int_{r_1}^{r_2} r g_{\alpha\beta}(r) \mathrm{d}r}{\int_{r_1}^{r_2} g_{\alpha\beta}(r) \mathrm{d}r}. \tag{4.4}$$

If a given range in r is considered where all of the partial pair-distribution functions are equal to zero apart from the Si-O partial pair-distribution function $g_{\mathrm{SiO}}(r)$, it is possible to calculate the Si-O mean atomic coordination number as

$$\bar{n}_{\mathrm{Si}}^{\mathrm{O}} = \frac{2\pi\rho}{c_{\mathrm{Si}} b_{\mathrm{Si}} b_{\mathrm{O}}} \int_{r_1}^{r_2} [G(r) - \mathrm{G(r \to 0)}] r^2 \mathrm{d}r. \tag{4.5}$$

Similarly, the Mg-O mean atomic coordination number can be calculated using

$$\bar{n}_{\mathrm{Mg}}^{\mathrm{O}} = \frac{2\pi\rho}{c_{\mathrm{Mg}} b_{\mathrm{Mg}} b_{\mathrm{O}}} \int_{r_1}^{r_2} [G(r) - G(r \to 0)] r^2 \mathrm{d}r. \tag{4.6}$$

The limit $G(r \to 0)$ is given by

$$G(r \to 0) = -\sum_{\alpha} \sum_{\beta} c_\alpha c_\beta b_\alpha b_\beta = - < b >^2 = -0.29016(19) \text{ barn}. \tag{4.7}$$

As discussed in Chapter 2, it is sometimes necessary to convert the total pair-distribution function $G(r)$ to the density correlation function $D(r)$, using the relationship

$$D(r) = 4\pi\rho r \frac{G(r)}{< b >^2} = 4\pi\rho r \sum_{\alpha=1} \sum_{\beta=1} \frac{c_\alpha c_\beta b_\alpha b_\beta}{< b >^2} [g_{\alpha\beta}(r) - 1]. \tag{4.8}$$

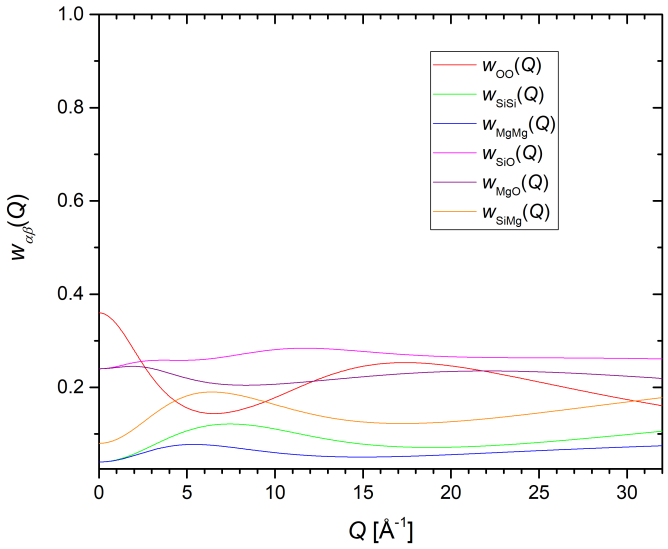

Figure 4.2: The six $D(r)$ weighting factors $w_{\alpha\beta}(Q)$ of $MgSiO_3$ calculated using the X-ray form factors for Mg^{2+}, Si^{4+} and O^{2-} as a function of momentum transfer Q [70].

The density correlation function $D(r)$ is comprised of a set of partial density correlation functions $d_{\alpha\beta}(r)$ where

$$d_{\alpha\beta}(r) = 4\pi\rho r[g_{\alpha\beta}(r) - 1]. \tag{4.9}$$

It is then possible to fit a Gaussian function convoluted with a sinc function to a peak associated with α-β correlations to obtain the mean coordination number $\bar{n}^{\beta}_{\alpha}$. This method is explained in more detail in Chapter 2. This technique has the advantage of accounting for the truncation of each $F(Q)$ function at a finite $Q_{\max}$ value, and any overlap between the partial pair-distribution functions $g_{\alpha\beta}$(r).

The total structure factors and pair-distribution functions may be rewritten to account for the mean neutron scattering length as

$$S(Q) = \frac{F(Q)}{< b >^2} + 1, \tag{4.10}$$

$$G'(r) = \frac{G(r)}{< b >^2} + 1. \tag{4.11}$$

The work presented in this chapter also made use of X-ray diffraction. The theory of an X-ray diffraction experiment is broadly the same as for neutron diffraction, however

the neutron scattering lengths b_α are replaced with the Q-dependent X-ray form factors $f_\alpha(Q)$. At a momentum transfer of zero, the form factor of a given atom or ion corresponds to the number of its electrons. The Q-dependent $D(r)$ weighting factors are plotted in Figure 4.2, which were calculated using the ionic X-ray form factors for Mg^{2+}, Si^{4+} and O^{2-}, using the following equations

$$w_{\alpha\beta}(Q) = \frac{c_\alpha^2 f_\alpha^2(Q)}{< f >^2} \quad \text{for} \quad \alpha = \beta, \tag{4.12}$$

$$w_{\alpha\beta}(Q) = \frac{2c_\alpha c_\beta f_\alpha(Q) f_\beta(Q)}{< f >^2} \quad \text{for} \quad \alpha \neq \beta, \tag{4.13}$$

where $< f >$ is the average X-ray form factor of the sample. The plot shows that the Si-O and Mg-O weighting factors $w_{\mathrm{SiO}}(Q)$ and $w_{\mathrm{MgO}}(Q)$ remain approximately constant over the measured range of momentum transfers (0-32 $\mathrm{\AA}^{-1}$). In order to calculate values of the mean Si-O and Mg-O coordination numbers from the X-ray diffraction results of this study, Gaussians convoluted with a sinc function were fitted to the first and second peaks of the $D(r)$ functions, respectively. Since the Q-dependent weighting factors remain approximately constant, the $Q = 0$ values of $w_{\mathrm{SiO}}(Q)$ and $w_{\mathrm{MgO}}(Q)$ were used to calculate the Si-O and Mg-O coordination numbers. The weighting factors for all pair-correlations present in $MgSiO_3$ are compared for both neutron and X-ray diffraction in Table 4.1. For neutron diffraction data, the X-ray form factors $f_\alpha(Q)$ in Equations 4.12 and 4.13 are replaced with the coherent scattering lengths b_α.

Pair-correlation $\alpha - \beta$	$w_{\alpha\beta}$ (Neutrons)	$w_{\alpha\beta}$ (X-rays, $Q = 0$)
Mg-Mg	0.03983	0.04
Si-Si	0.02373	0.04
O-O	0.417806	0.36
Mg-Si	0.06149	0.08
Mg-O	0.25799	0.24
Si-O	0.19915	0.24

Table 4.1: The six weighting factors of $MgSiO_3$ for neutron or X-ray diffraction, calculated using Equations 4.12 and 4.13.

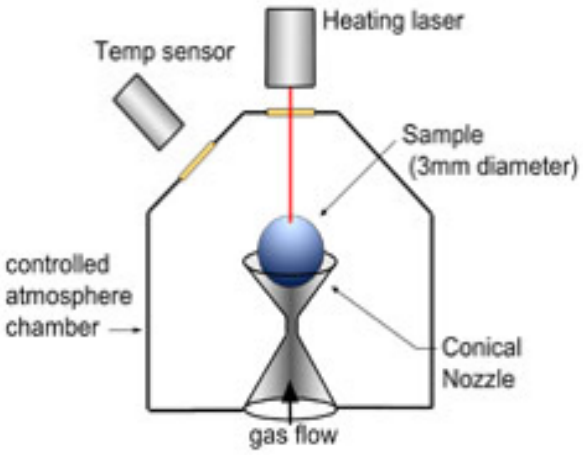

Figure 4.3: A schematic of an aerodynamic levitation setup. Reproduced from [71].

4.3 Experimental Method

4.3.1 Sample Preperation

The samples used for both experiments were prepared by L. Skinner (Stanford University), using the aerodynamic levitation technique [71]. A controlled flow of gas is used to aerodynamically levitate a sample, which is simultaneously heated by a laser. The key advantage of this method is that it is containerless and it is therefore less likely for contamination to be introduced into the sample, and for nucleation sites to develop. Furthermore, by switching off the laser, the sample can be quenched at a faster rate than more conventional techniques. The samples used for these experiments were levitated in argon gas, and were prepared in the form of small glass beads approximately 1.5 mm in diameter. A schematic of an aerodynamic levitator is shown in Figure 4.3.

X-ray diffraction patterns were measured for each glass bead at the 6-ID-D beamline at the Advanced Photon Source, Argonne, U.S.A [72]. The total structure factors $S(Q)$ are plotted in Figure 4.4, and show no significant deviation. The composition of the samples was verified to be almost perfectly stoichiometric, using Electron Probe Micro-analysis (EPMA) measurements at Corning Inc, USA [73]. The exact atomic composition was determined to be $(MgO)_{0.50438}(SiO_2)_{0.49560}$ which represents a deviance of less than 1% from the ideal $(MgO)_{0.5}(SiO_2)_{0.5}$ composition.

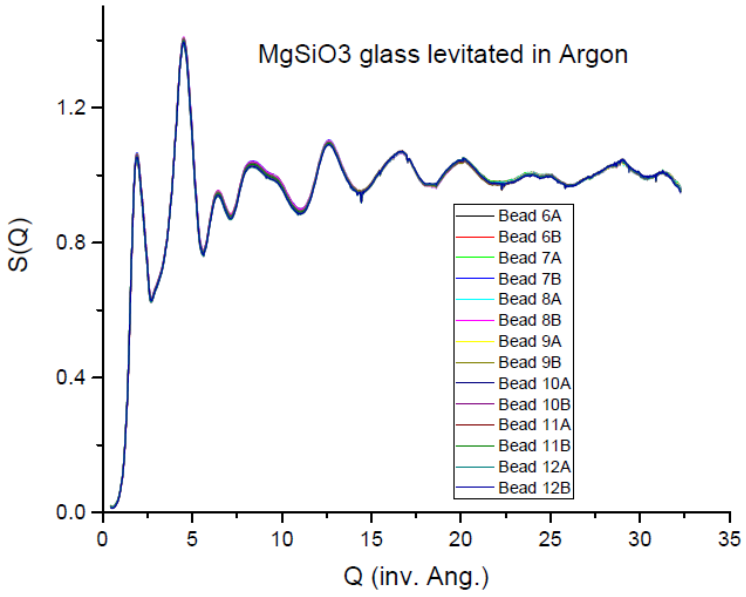

Figure 4.4: The total structure factors $S(Q)$ for the glassy $MgSiO_3$ beads, measured on the 6-ID-D diffractometer, Advanced Photon Source, U.S.A. [72]

4.3.2 D4c Experiment

The D4c neutron diffraction experiment studied magnesium silicate glass at ambient temperature ($T \approx 300$ K) and pressures up to 8.2(5) GPa. An incident neutron wavelength of 0.49841(1) Å was used to optimise the incident flux. Single toroid (ST) cubic BN anvils were used to compress the sample. Compression was controlled manually via the use of a hand pump throughout the entire experiment. No automated system to control the oil pressure was available, so the oil pressure typically relaxed by a small amount over the course of a pressure point measurement (20 - 30 bar). When changing oil pressure, periodic pauses were taken in order to allow the system to equilibrate. The pressure points measured for $MgSiO_3$ are shown in Table 4.2. During the course of a pressure point measurement, the ratio was taken of the measured intensities over different points in time. The purpose of this was to check that the ratio did not deviate from unity, i.e. if the measured intensities were consistent. No such deviation was observed over the course of the experiment. Vanadium measurements were made at ambient pressure of (a) an ST pellet of the usual dimensions inside a Ti-Zr gasket, (b) three deformed pellets with the same cap sizes but differing cylinder geometries and (c) two spherical caps machined to match the ST anvil profiles, in order to perform

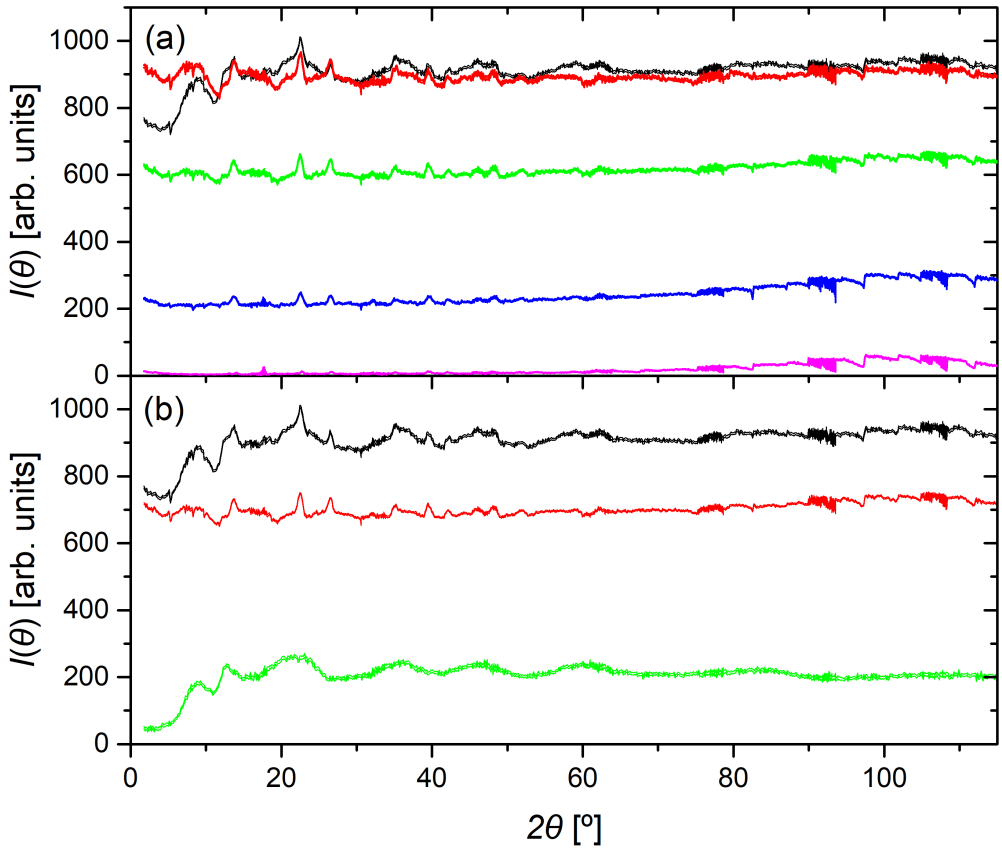

Figure 4.5: The data correction procedure used for the $MgSiO_3$ sample, measured at 3 GPa by the D4c diffractometer using the Paris-Edinburgh press in conjunction with ST BN anvils. Plot (a) shows the measured intensities for the sample inside its container $I^{\mathrm{E}}_{\mathrm{SC}}(\theta)$ (black), an empty uncompressed gasket $I^{\mathrm{E}}_{\mathrm{C1}}(\theta)$ (red), an empty uncompressed gasket that was previously compressed to 4.7 GPa $I^{\mathrm{E}}_{\mathrm{C2}}(\theta)$ (green), an empty gasket measured at 4.4 GPa that was previously compressed to 8.2 GPa $I^{\mathrm{E}}_{\mathrm{C3}}(\theta)$ (blue), and the empty anvils with no gasket or sample present $I^{\mathrm{E}}_{\mathrm{a}}(\theta)$ (magenta). Plot (b) shows the measured intensity for the sample inside its container $I^{\mathrm{E}}_{\mathrm{SC}}(\theta)$ (black); the background intensity $I^{\mathrm{E}}_{\mathrm{B}}(\theta)$ calculated using equation 3.15 with coefficients $x_{\mathrm{a}} = 0.1$, $x_{\mathrm{C1}} = 0.3$ and $x_{\mathrm{C2}} = 0.7$ (red); and the background and container corrected sample intensity $I^{\mathrm{E*}}_{\mathrm{SC}}(\theta)$ calculated using equation 3.14 (green).

the data correction procedure described in section 3.4. An additional measurement was made of the $MgSiO_3$ same beads used for the main experiment, inside a vanadium can. The D4c setup used in conjunction with a vanadium can offers a higher accessible Q range ($0.5\ \text{Å}^{-1} \leq Q \leq 23.5\ \text{Å}^{-1}$) and an improved signal to noise ratio.

The $MgSiO_3$ glass was prepared in the form of several small beads. The beads were weighed individually, and the appropriate mass was ground into a fine powder using an agate mortar and pestle. The ideal mass for a single toroid pellet of $MgSiO_3$ was calculated to be 0.24627(1) g. The required mass of powder was then transferred into a die specially designed to produce the shape of a ST pellet. The powder was compressed in stages, allowing a relaxation time of approximately 5 minutes between each stage. The resultant pellet was then immediately transferred into a Ti-Zr gasket placed onto the piston anvil, which was then placed into the Paris-Edinburgh press. The mass of the $MgSiO_3$ pellet was measured to be 0.24790(1) g and the mass of the Ti-Zr gasket was measured to be 1.4559(1) g.

Immediately after decompression, a measurement was taken of the $MgSiO_3$ pellet in order to investigate the extent of permanent densification in $MgSiO_3$ glass. A further diffraction measurement was taken of the same sample approximately one week after the initial experiment.

Oil Pressure [bar]	Applied Load [tns]	Sample Pressure [GPa]
100	6.8	Ambient
300	20.3	1.7(5)
450	30.5	3.0(5)
600	40.7	3.9(5)
900	61.0	5.7(5)
1200	81.3	7.1(5)
1400	94.9	8.2(5)

Table 4.2: The oil pressures and corresponding sample pressures for the D4c experiment on $MgSiO_3$ glass. The sample pressures were deduced from the calibration curve shown in Figure 3.7.

The data correction procedure followed the methodology described in section 3.4.1. Figure 4.5 shows an example of the correction procedure used for the experiment, and

illustrates graphically the steps used to obtain the background and container corrected sample intensity $I_{\mathrm{SC}}^{\mathrm{E}*}(\theta)$ for $MgSiO_3$ glass at 3 GPa.

4.3.3 PEARL Experiment

The PEARL neutron diffraction experiment studied magnesium silicate glass at ambient temperature ($T \approx 300$ K) and pressures up to 17.5(5) GPa. Sintered diamond double toroid (DT) anvils were used to compress the sample. Compression was controlled by an automated machine up to an oil pressure of $P_{\mathrm{oil}} = 980$ bar. After this, the oil pressure was increased manually via the use of a hand pump. The automated system ensured that the oil pressure was kept at a constant value, but use of the manual system meant that a small relaxation of the oil pressure was allowed to occur. The pressure points at which diffraction patterns were measured for $MgSiO_3$ glass are shown in Table 4.3. Equivalent measurements were made for a vanadium pellet of equal dimensions to the sample, and for an empty $Ti_{0.676}Zi_{0.324}$ gasket at ambient conditions, in order to perform the data correction procedures described in section 3.4. As for the D4c experiment, the ratio of scattered intensities at different times was taken over the course of a measurement to check for measurement consistency.

As discussed previously, the $MgSiO_3$ glass was provided in the form of several small glass beads. The ideal mass of a double toroid pellet of $MgSiO_3$ was calculated to be 0.089020(1) g. The pellets were weighed individually and the appropriate number were ground into a fine powder using an agate mortar and pestle. The powder was then transferred into a die specially designed to produce the shape of a double toroid pellet. The powder was then compressed in stages, and the sample was immediately transferred into a gasket placed on the piston anvil. The ideal mass of a vanadium double toroid pellet is 0.20232(1) g. To make a vanadium pellet, the appropriate mass of vanadium foil was carefully folded and placed into the die and then compressed using the same technique. The final pellet and gasket masses are shown in Table 4.4.

Immediately after the experiment, the recovered sample was thoroughly ground with an agate mortar and pestle. Approximately one month later, a measurement was taken using an Ag source laboratory X-ray diffractometer, at the Rutherford Appleton Laboratory, U.K.

The data correction procedure followed the methodology described in section 3.4.2. Figure 4.6 gives an example of the correction procedure used for the experiment, and

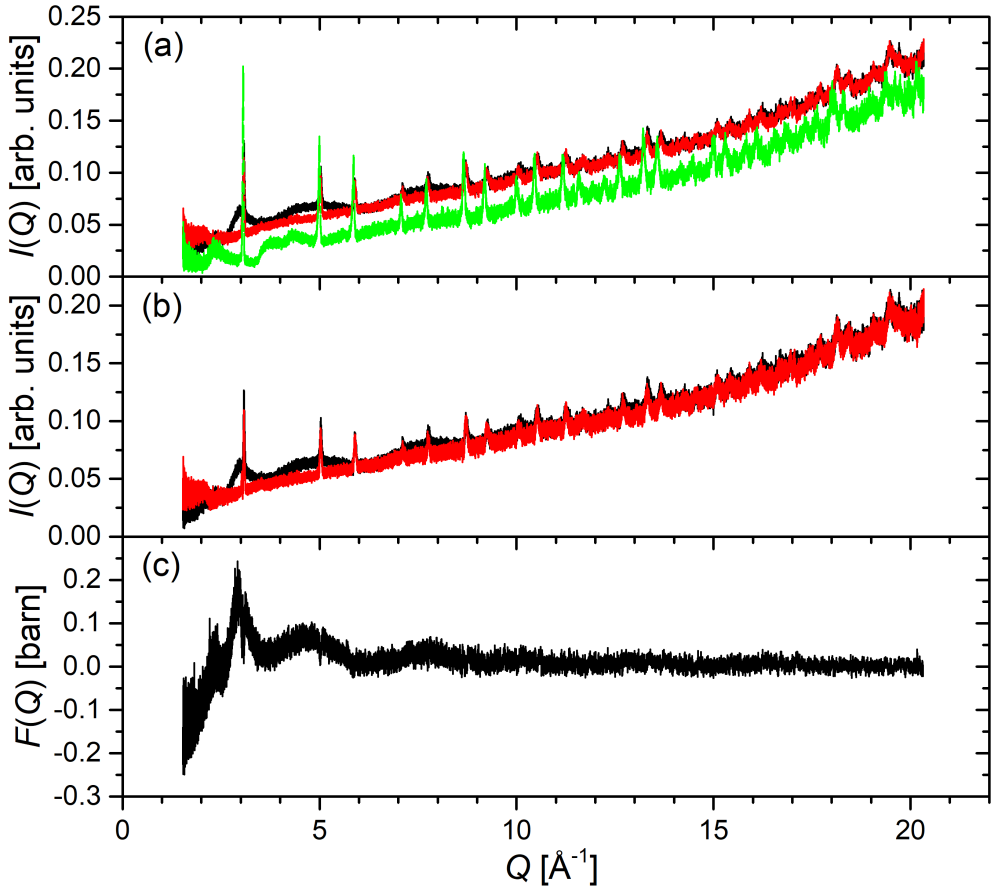

Figure 4.6: The data correction procedure used for the $MgSiO_3$ sample, measured at 17.5 GPa by the PEARL diffractometer using the Paris-Edinburgh press in conjunction with DT sintered diamond anvils. Plot (a) shows the measured intensities for the sample inside its container $I^{\mathrm{E}}_{\mathrm{SC}}(Q)$ (black), a piece of vanadium at the same pressure $I^{\mathrm{E}}_{\mathrm{VC}}(Q)$ (red), and an empty uncompressed gasket $I^{\mathrm{E}}_{\mathrm{C}}(Q)$ (green). Plot (b) shows the container corrected intensity for the sample inside its container $I^{\mathrm{E*}}_{\mathrm{SC}}(Q)$ (black), calculated using equation 3.23 with a weighting coefficient $x_{\mathrm{S}} = 0.1$; and the container corrected intensity for the vanadium inside its container $I^{\mathrm{E*}}_{\mathrm{VC}}(Q)$, calculated using equation 3.24 with a weighting coefficient x_{V}= 0.11 (red). Plot (c) shows the total structure factor $F(Q)$ calculated using equation 3.25 using a weighting coefficient $W = 0.275$.

Applied Load [tns]	Sample Pressure [GPa]	$MgSiO_3$	Vanadium
2.0	Ambient	✓	✓
35.0	4.0(5)	✓	✓
75.0	8.7(5)	✓	✓
98.0	10.9(5)	✓	✓
120.0	14.4(5)	✓	✓
140.0	17.5(5)	✓	✓

Table 4.3: The applied load and corresponding sample pressures for the PEARL experiment on $MgSiO_3$ glass. The sample pressures were deduced from the calibration curve shown in Figure 3.8.

Sample	Pellet mass [g]	Ti-Zr gasket mass [g]
$MgSiO_3$	0.0914(1)	1.0938(1)
Vanadium	0.27027(1)	1.0951(1)

Table 4.4: The final pellet and Ti-Zr gasket masses used for the PEARL neutron diffraction experiment.

illustrates graphically the steps used to obtain the total structure factor $F(Q)$ for $MgSiO_3$ glass at 17.5 GPa.

4.3.4 Equation of State and Density Measurements

The mass density of the $MgSiO_3$ glass beads was measured using a helium pycnometer to be $\rho = 2.65(5)$ g cm^{-3}. This yielded an ambient atomic number density value of $n_0 = 0.07948(150)$ Å^{-3}. There is disagreement in the literature regarding the equation of state for glassy $MgSiO_3$. For the work presented here, a fourth order Birch-Murnaghan equation of state [36] was fitted to the pressure-volume data measured by Petitgirard *et al* [39] using X-ray absorption, shown in Figure 4.7. The fit parameters used were the same as quoted by Petitgirard *et al*: $B_0 = 16.9(3.2)$ GPa, $B_0' = 5.9(1.3)$, and $B_0'' = -0.004(770)$ GPa^{-1} [39]. The fit shows good agreement with the measured data. The atomic number densities obtained for each pressure point are presented in Table 4.5. The Birch-Murnaghan equation of state is described in further detail in Chapter 2.

After the D4c experiment, the density of the sample was remeasured using a helium pycnometer to be $\rho = 2.97(25)$ g cm^{-3}. This corresponds to an atomic number density of $n_0 = 0.089$ Å^{-3}, and represents an approximate 12% increase from the ambient value. The recovered sample from the PEARL experiment was not of sufficient mass to obtain a reliable measurement of its density.

Pressure [GPa]	Compression $\frac{V}{V_0}$	Atomic Number Density [Å^{-3}]
Ambient	1	0.07948(150)
1.7(5)	0.952(25)	0.08602(162)
3.0(5)	0.870(25)	0.08976(169)
3.9(5)	0.851(25)	0.09194(174)
4.0(5)	0.850(25)	0.09221(174)
5.4(5)	0.826(25)	0.09513(180)
7.1(5)	0.804(25)	0.09825(185)
8.2(5)	0.791(25)	0.10004(189)
8.7(5)	0.786(25)	0.10080(190)
10.9(5)	0.766(25)	0.10383(196)
14.4(5)	0.739(25)	0.10799(204)
17.5(5)	0.721(25)	0.11117(210)

Table 4.5: The compression and atomic number densities of the pressure points for the D4c and PEARL neutron diffraction experiments on $MgSiO_3$ glass.

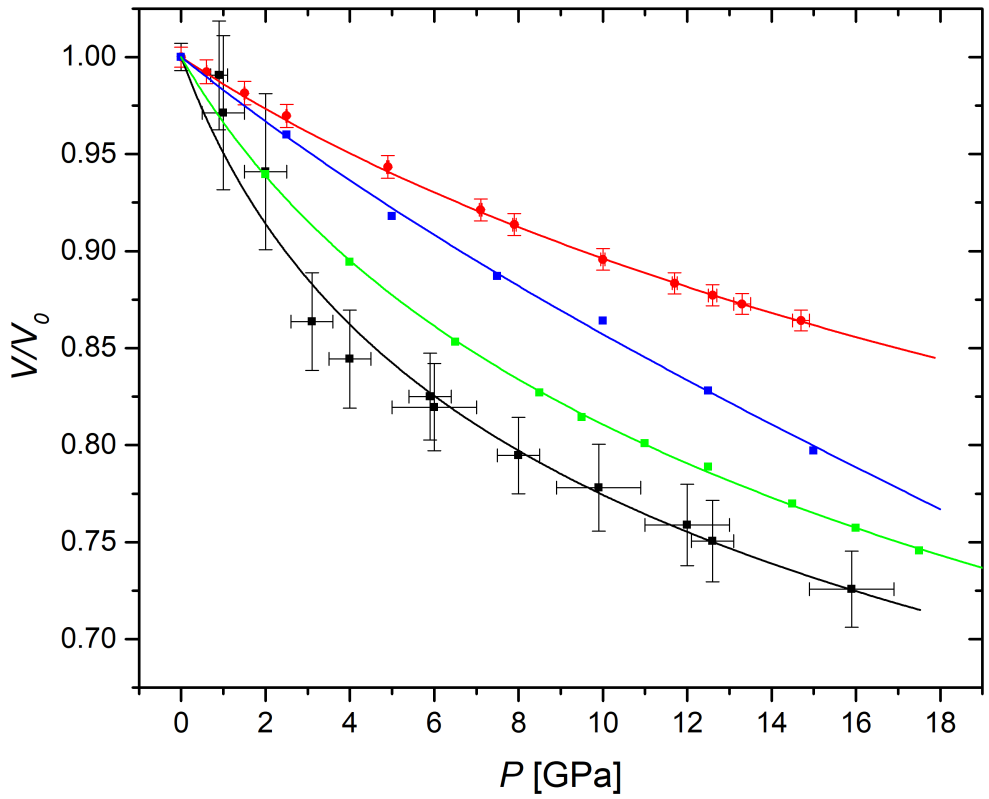

Figure 4.7: Pressure-volume equations of state for glassy $MgSiO_3$. The black squares with error bars show results from X-ray absorption measurements [39], and the red circles with error bars show results from Brillouin scattering measurements [74]. The green squares show results from the molecular dynamics simulations accompanying this work [75], and the blue squares show further molecular dynamics simulation results [76]. The solid curves show Birch-Murnaghan equations of state fitted to the data, where the red, blue and green curves are third order Birch-Murnaghan equations of state, and the black curve is a fourth order Birch-Murnaghan equation of state calculated using the parameters given in [39].

4.3.5 Molecular Dynamics Simulations

The molecular dynamics simulations accompanying this work were developed by Yoshiki Ishii and Mathieu Salanne [75], using an aspherical ion model (AIM) [77, 78]. The calculations were performed on systems containing 300 oxygen atoms, 100 silicon atoms and 100 magnesium or calcium atoms in the NPT ensemble using a timestep of 1.0 fs, where N is the number of particles, P is the pressure, and T is the temperature. The starting configuration was generated using an initially random distribution of atoms using a polarizable ion model. The AIM was then used to equilibrate the liquid state at 3000 K and ambient pressure. The pressure was then increased in steps of 0.5 GPa to 17.5 GPa, over a timescale of 7.0 ns. The liquid was quenched at the following pressures: 0.0 (Ambient), 2.0, 4.0, 6.5, 8.5, 9.5, 11.0, 12.5, 14.5, 16.0 and 17.5 GPa. At each pressure point, the liquid was quenched by decreasing the temperature from 3000 K to 300 K in steps of 100-500 K over a total timescale of 3.5 ns. At 8.5 and 17.5 GPa, the pressure was returned in steps of 0.5 GPa to ambient conditions over a timescale of 7.0 or 3.5 ns, respectively.

The procedure was repeated for eight different configurations of the liquid that was equilibrated at 3000 K and ambient pressure, hence eight independent glass configurations were studied. This allowed for a statistical analysis of structural parameters such as coordination numbers and the connectivity of network formers. The bridging state of the oxygen atoms, as defined by the O-Si coordination number, was also investigated. An oxygen atom bonded to zero, one, two or three silicon atoms is referred to as a free-oxygen, non-bridging oxygen (NBO), bridging oxygen (BO) or triple-bridging oxygen (TBO), respectively. The coordination numbers $\bar{n}_\alpha^\beta$ were calculated by integrating the over the first peak of the corresponding partial pair-distribution function $g_{\alpha\beta}(r)$.

The partial structure factors $S_{\alpha\beta}(Q)$ were obtained from the calculated $g_{\alpha\beta}(r)$ functions for $Q \geq 4$ Å^{-1} using the Fourier transform relation

$$S_{\alpha\beta}(Q) = 1 + \frac{4\pi\rho}{Q}\int_0^\infty r\sin(Qr)[g_{\alpha\beta}(r) - 1]dr, \tag{4.14}$$

where ρ is the average atomic number density. In order to avoid the introduction of Fourier transform artefacts, for $Q < 4$ Å^{-1}, $S_{\alpha\beta}(Q)$ was calculated using

$$S_{\alpha\beta}(Q) = 1 + \frac{[S_{\alpha\beta}^{\mathrm{AL}}(Q) - \delta_{\alpha\beta}]}{\sqrt{c_\alpha c_\beta}}, \tag{4.15}$$

where $\delta_{\alpha\beta}$ is the Kronecker delta. The Ashcroft-Langreth [79] partial structure factor $S^{\mathrm{AL}}_{\alpha\beta}(Q)$ is calculated using

$$S^{\mathrm{AL}}_{\alpha\beta}(Q) = \frac{1}{\sqrt{N_\alpha N_\beta}}\Big\langle \sum_i \sum_j \exp(i\mathbf{Q}\cdot\mathbf{r}_{i,j})\Big\rangle - \sqrt{N_\alpha N_\beta}\delta_{\mathbf{Q},0}, \tag{4.16}$$

where N_α denotes the number of ions of chemical species α, $\delta_{\mathbf{Q},0}$ is the Kronecker delta and the triangular brackets denote a thermal average.

4.4 Results

4.4.1 Total Structure Factors

Figure 4.8 shows the pressure dependence of the total structure factors $S(Q)$ obtained for $MgSiO_3$ glass. The plot compares the neutron diffraction results to the molecular dynamics simulations used in the present work at similar pressures, and the X-ray diffraction results of $MgSiO_3$ at ambient conditions. The ambient X-ray diffraction measurement is an average of all the measured $S(Q)$ functions for the individual beads, shown in Figure 4.4. The ambient X-ray and neutron total structure factors are in good agreement with previous work [67]. At ambient pressure there is good overall agreement between the experimental and simulation results. There is a clearly defined first-sharp diffraction peak (FSDP) at $\sim$1.9 Å^{-1}, followed by a principal peak at $\sim$2.8 Å^{-1}. There is a small disagreement in the FSDP position between the experimental and simulation results. There are occasional sharp peaks in the simulation results at low values of Q which are statistical in nature.

As pressure is increased, the FSDP position shifts to higher Q values until it becomes a low Q shoulder of the principal peak in the D4c data by 7.1(5) GPa. This behaviour is accompanied by a sharpening and increasing amplitude of the principal peak. At the highest pressures, the principal peak becomes even more dominant and continues to shift to higher values of Q. The FSDP does appear to increase in amplitude across the range of pressures studied with PEARL.

Figure 4.9 compares the total structure factors $S(Q)$ measured for $MgSiO_3$ under ambient conditions in a vanadium can, immediately after recovery from 8.2(5) GPa, and approximately one week after recovery from 8.2(5) GPa. The recovered X-ray total structure factor, measured approximately one month after the PEARL experiment is also plotted and compared to the ambient X-ray diffraction measurement. The neutron and X-ray total structure factors are also compared to those obtained from the molecular dynamics simulations [75], recovered from 8.5 GPa and 17.5 GPa, respectively. The recovered D4c datasets were analysed using an atomic number density of $\rho_0 = 0.089$ Å^{-3}, which corresponds to the measured mass density of the recovered sample. The X-ray diffraction dataset recovered from PEARL was analysed using the ambient atomic number density of $\rho_0 = 0.079483$ Å^{-3}. An analysis was made of the dataset using the atomic number density measured for the D4c recovered samples of $\rho_0 = 0.089$ Å^{-3},

which yielded a Si-O coordination number of $\bar{n}_{\mathrm{Si}}^{\mathrm{O}}$ of ∼4.3, which is higher than the any of the values measured under load. The recovered sample from PEARL was finely ground using an agate mortar and pestle prior to the X-ray diffraction experiment, whilst the D4c recovered sample was left in its original pellet form, inside its gasket. This suggests that the powdering process of the sample which was recovered from PEARL contributed towards structural relaxation.

The recovered datasets show a clear shift in the FSDP position to approximately 2.05 $\mathrm{Å}^{-1}$, which is intermediate between the ambient measured position of ∼1.91 $\mathrm{Å}^{-1}$ and the position measured at 8.2(5) GPa of ∼2.21 $\mathrm{Å}^{-1}$. Apart from the region of the FSDP, the ambient and recovered datasets are in good agreement. The FSDP and principal peak positions are plotted in Figure 4.10. The results show a dramatic shift in the FSDP position to higher Q values, which is mostly complete by 8.2(5) GPa. The higher pressure results from PEARL show a further increase in FSDP position, however it is more gradual than before. The principal peak position shows a continued but gradual increase between ambient conditions and the maximum pressure. The simulation FSDP and principal peak positions show generally good agreement with the experimental results. There is a disagreement of ∼0.2 $\mathrm{Å}^{-1}$ between the ambient and ∼4 GPa principal peak positions obtained from the D4c and PEARL experiments. This disagreement may originate from the method of sample preparation: in order to make a double toroid pellet the $MgSiO_3$ powder was compressed under a pressure of approximately 1 GPa. Hence, the $MgSiO_3$ pellet used in the PEARL experiment may have already been partially densified.

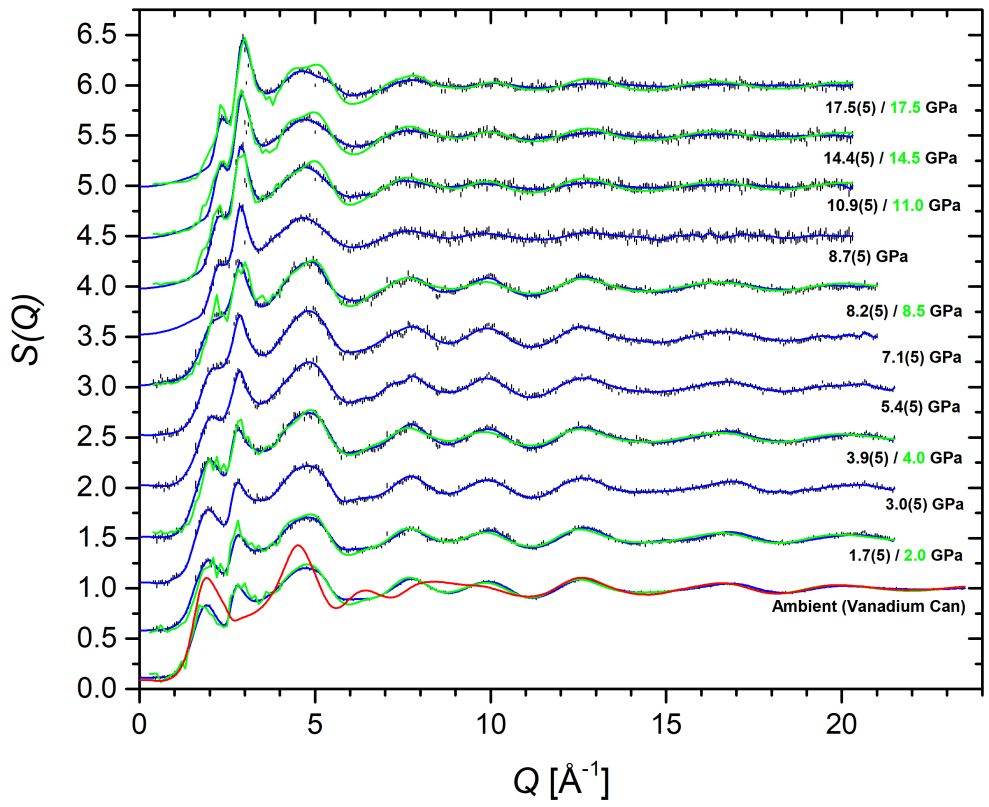

Figure 4.8: The pressure dependence of the total structure factors $S(Q)$ for $MgSiO_3$ glass, as measured using the D4c (ambient to 8.2(5) GPa) or PEARL (8.7(5) to 17.5(5) GPa) diffractometers. The vertical bars give the statistical errors on the measured datasets, and the blue curves show the back Fourier transforms of spline fits to the experimental data. The results are compared to those obtained from the molecular dynamics simulations at similar pressures (green curves) [75]. The solid red curve shows the X-ray total structure factor, averaged for all the $MgSiO_3$ glass beads, after synthesis. For the datasets originating from PEARL, the region $Q \leq 1.55$ Å^{-1} is inaccessible and the curves in this region correspond to fitted Lorentzian functions. The high pressure datasets have been offset vertically, and the PEARL dataset at 4.0 GPa is omitted, for clarity of presentation.

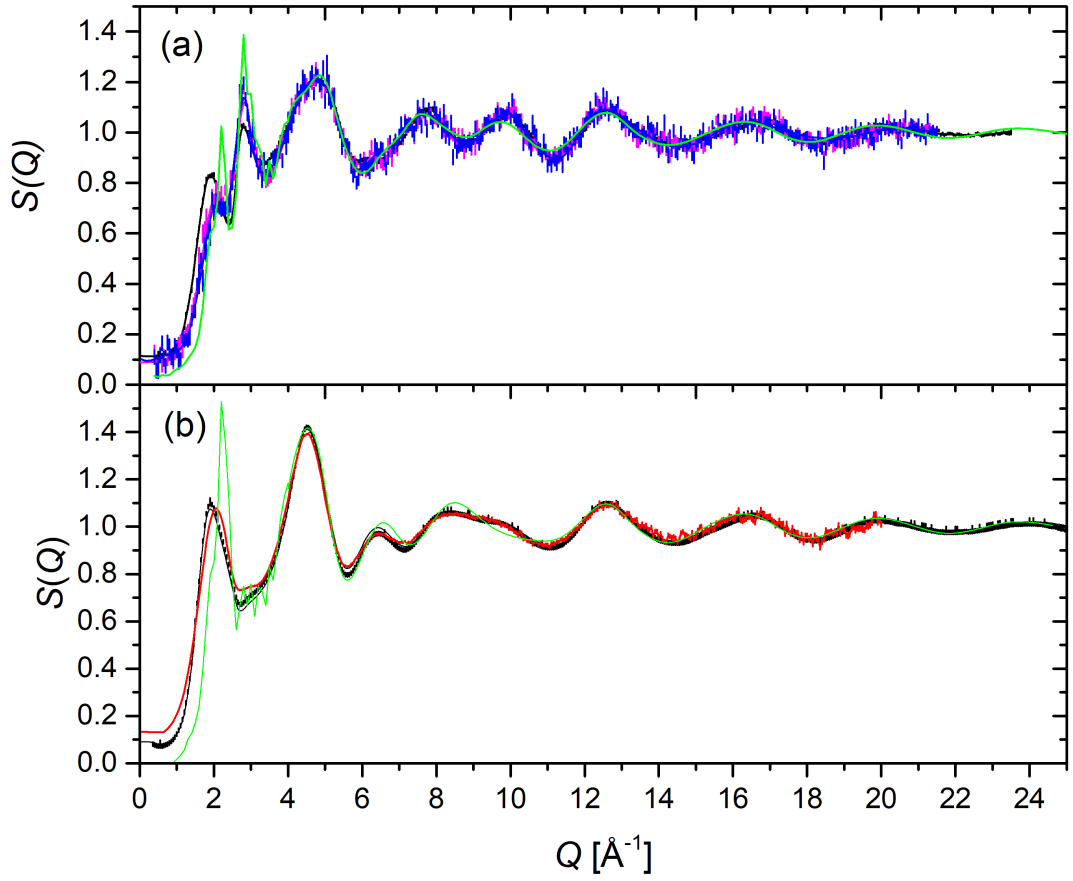

Figure 4.9: The total structure factors $S(Q)$ for glassy $MgSiO_3$ recovered from compression, as measured with neutron or X-ray diffraction. Plot (a) shows the total structure factors measured with the D4c diffractometer for the as-prepared sample using a vanadium can (solid black curve), immediately after recovery to ambient from 8.2(5) GPa (solid magenta curve), and approximately one week after recovery to ambient from 8.2(5) GPa (solid blue curve). Plot (b) shows the total structure factors measured for the as-prepared sample using the 6-ID-D diffractometer at the APS (solid black curve) [72], and for $MgSiO_3$ approximately one month after recovery from 17.5(5) GPa using a conventional Ag source laboratory X-ray diffractometer (solid red curve). The solid green curves in (a) or (b) show the total structure factors obtained from the molecular dynamics simulations immediately after recovery from 8.5 GPa or 17.5 GPa, respectively [75]. The vertical error bars give the statistical errors on the measured data points, and the solid curves are back Fourier transforms of spline fits to the data.

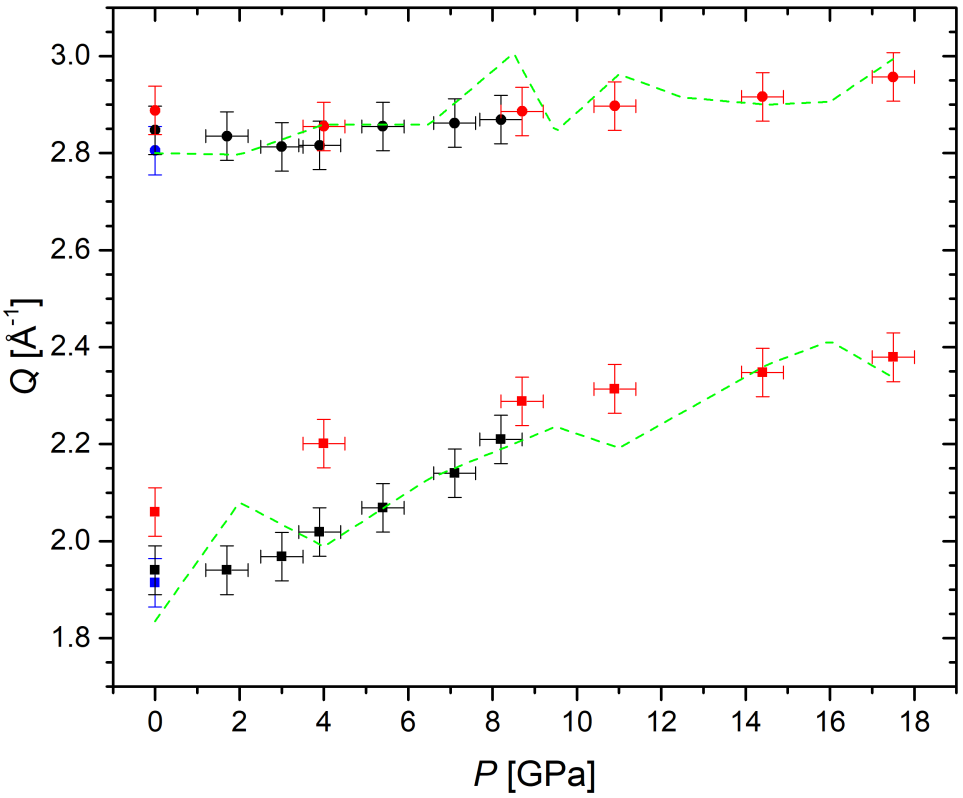

Figure 4.10: The pressure dependence of the FSDP position (squares) and the principal peak position (circles) for glassy $MgSiO_3$. The black and red datapoints show results from the D4c and PEARL experiments, respectively. The single blue datapoint is obtained from the vanadium can measurement on D4c. The green dashed lines show the results from the molecular dynamics simulations [75].

4.4.2 Pair-Distribution Functions

Figure 4.11 shows the pressure dependence of the total pair-distribution functions $G'(r)$ measured for $MgSiO_3$ glass. The reciprocal space datasets were Fourier transformed using a step modification function as shown in Equation 4.1. The ambient vanadium can measurement was Fourier transformed using $Q_{\max} = 23.5$ Å^{-1}. The PE press D4c measurements were Fourier transformed using $Q_{\max} = 21.5$ Å^{-1} in the range Ambient $\leq P \leq 5.4(5)$ GPa, and $Q_{\max} = 21.0$ Å^{-1} in the range 5.4(5) GPa $\leq P \leq 8.2(5)$ GPa. The PEARL datasets were Fourier transformed using $Q_{\max} = 20.3$ Å^{-1}. The ambient X-ray dataset was Fourier transformed using $Q_{\max} = 32.0$ Å^{-1}. At ambient, the peaks in the X-ray $G'(r)$ function differ from the neutron results due to the different weighting factors for the partial pair-distribution functions, with X-rays being more sensitive to silicon and less sensitive to oxygen. The experimental datasets are compared to the molecular dynamics simulation results at similar pressures.

At ambient conditions, the first peak is well defined at $r_{\mathrm{SiO}} = 1.609(20)$ Å, and is associated with Si-O correlations [20]. It is symmetric, indicating that the bond length distribution is centered around the peak maximum. The second real space peak is associated with Mg-O correlations [20], and is located at $r_{\mathrm{MgO}} = 1.988(20)$ Å. However, in contrast to the first peak, it is asymmetric in nature and exhibits a shoulder which extents in real space to ∼2.4 Å. This indicates that the distribution of Mg-O bond distances is not symmetric, but rather that there is a primary cluster of bond distances at ∼2 Å with a minority of longer bond distances also present. The third real space peak is comprised of an overlap of partial pair-distribution functions, and hence cannot easily be resolved for a single set of pair correlations.

As pressure is increased, the Si-O peak decreases in amplitude and becomes broader in nature. The shoulder feature of the Mg-O peak decreases in prominence and eventually becomes indistinguishable from the primary Mg-O peak. This transition is mostly complete by 7.1(5) GPa. Therefore, the distribution of Mg-O bond distances becomes more symmetric as pressure is increased. The datasets originating from PEARL contain noticibly broader peaks, which is due to the inferior real space resolution of the instrument. A detailed discussion of the disparity between the $G'(r)$ functions originating from D4c and PEARL is provided in Chapter 3.

Figure 4.12 compares the total pair-distribution functions $G'(r)$ measured for the as-prepared $MgSiO_3$ under ambient conditions in a vanadium can, immediately after

recovery from 8.2(5) GPa, approximately one week after recovery from 8.2(5) GPa and approximately one month after recovery from 17.(5) GPa after being finely ground in an agate mortar and pestle. The D4c and PEARL results are compared to the $G'(r)$ functions obtained from the accompanying molecular dynamics simulations, recovered from 8.5 GPa or 17.5GPa, respectively. The datasets were obtained by Fourier transforming the respective datasets in Figure 4.9. The D4c recovered datasets have been Fourier transformed using a cutoff $Q_{\max} = 21.5$ Å^{-1}, and the X-ray recovered dataset was Fourier transformed using a cutoff $Q_{\max} = 20.0$ Å^{-1}. For purposes of comparison, the ambient neutron and X-ray measurements shown in the plot were Fourier transformed using the same cutoff $Q_{\max}$ values as their respective recovered datasets. In order to obtain values of the Si-O and Mg-O coordination numbers, the $G'(r)$ functions were converted to $D(r)$ functions, and Gaussians convoluted with a sinc functions were fitted to each peak. For the X-ray diffraction results, the $Q = 0$ values of the Si-O and Mg-O weighting factors were used, since these weighting factors show a minimal deviation over the measured range of momentum transfer, as shown in Figure 4.2. The recovered datasets contain broader real space peaks, and the second peak which corresponds to Mg-O correlations does not exhibit a high r shoulder as observed at ambient, which shows that the sample has not reverted to its as-prepared atomic structure. The Mg-O coordination number was determined to be $\bar{n}^{\mathrm{O}}_{\mathrm{Mg}} = 4.85(5)$ for all recovered datasets. The fits used to obtain this result are plotted in Figures 4.22, 4.23 and 4.25.

Figures 4.13 and 4.14 show the pressure dependence of the mean Si-O coordination number and bond distance, and the mean Mg-O coordination number and bond distance, respectively. The bond distances have been determined both by measurement of the maximum peak position, and by calculating the weighted peak position by using Equation 4.4. The D4c coordination numbers have been obtained by using the RDFGenie program to fit a Gaussian function convoluted with a sinc function to the relevant peak in $D(r)$. The results are compared to the MD simulation results shown by the green dashed lines. The fits are displayed for all pressure points in Figures 4.15 to 4.25. The PEARL Si-O and Mg-O coordination numbers were calculated using Equations 4.5 and 4.6, respectively. The ambient values of the Si-O and Mg-O bond distances and coordination numbers are in agreement with those previously reported [67].

Both the mean Si-O bond distances and coordination numbers remain at their ambient pressure values of $r_{\mathrm{SiO}} = 1.609(20)$ Å and $\bar{n}^{\mathrm{O}}_{\mathrm{Si}} = 3.96(5)$ within the experimental

uncertainty, respectively. The calculated weighted peak position shows that the Si-O peak remains essentially symmetric throughout the measured pressure range. The Si-O bond distance obtained from simulation is consistently longer ($\sim$ 1.64 Å) than that obtained from experiment, and remains approximately constant throughout the measured pressure range. However, the mean Si-O coordination number obtained from simulation gradually increases beginning at $\sim$6 GPa, to a maximum value of $\bar{n}^{\mathrm{O}}_{\mathrm{Si}} = 4.35$ at 17.5 GPa. The results for $(\mathrm{MgO})_{0.62}(\mathrm{SiO_2})_{0.38}$ [80] appear to show that a glass with a richer Mg composition leads to a delay in the increase of the Mg-O coordination number.

The mean Mg-O coordination number increases from an ambient value of $\bar{n}^{\mathrm{O}}_{\mathrm{Mg}} = 4.50(5)$ to $\bar{n}^{\mathrm{O}}_{\mathrm{Mg}} = 6.1(1)$ at 17.5(5) GPa. The Mg-O bond distance obtained from D4c slowly increases from an ambient value of $r_{\mathrm{MgO}} = 1.99(1)$ Å to $r_{\mathrm{MgO}} = 2.01(1)$ Å at 8.2(5) GPa. This increase is not observed in the PEARL results, which is likely due to the significantly reduced real space resolution available on PEARL. The Mg-O bond distance obtained from PEARL is constant over the pressure range 4.0(5) GPa $\leq P \leq$ 14.4(5) GPa. At the highest pressure, the mean bond distance appears to decrease to a value of $r_{\mathrm{MgO}} = 1.97(2)$ Å. The weighted peak positions calculated using equation 4.4 show a gradual decrease in the mean bond distance from a value of $r_{\mathrm{MgO}} =$ 2.06(1) Å at ambient conditions, to $r_{\mathrm{MgO}} = 1.98(2)$ Å at 17.5(5) GPa. Hence, the distribution of Mg-O bond distances becomes more symmetric as pressure is increased.

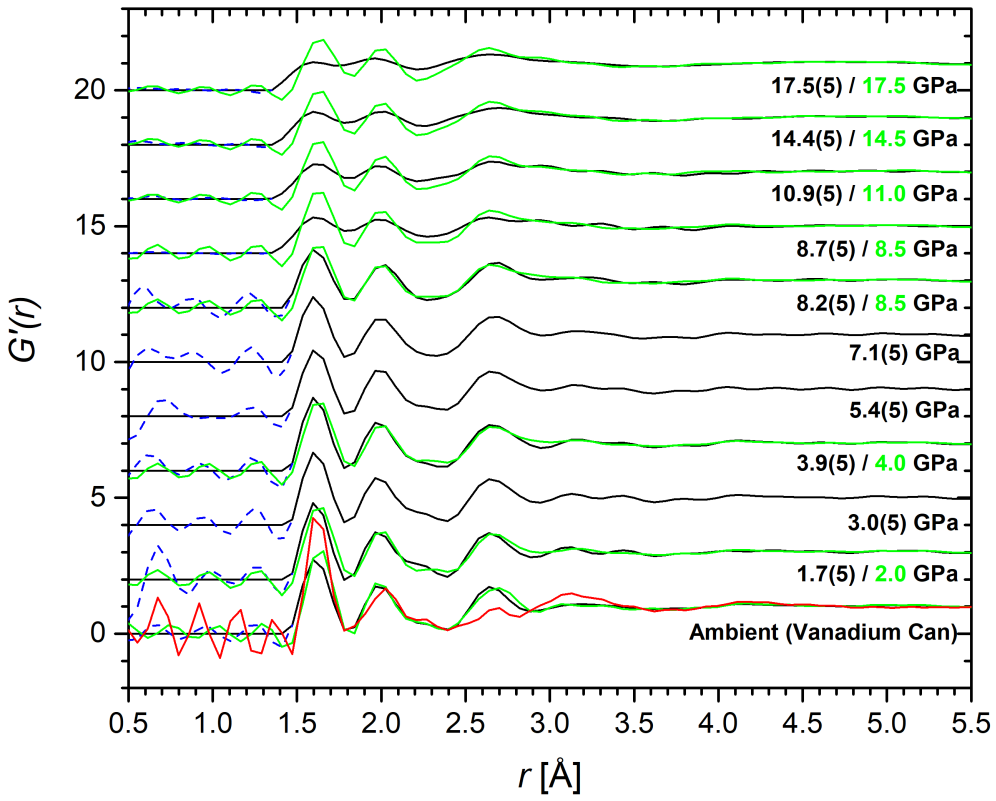

Figure 4.11: The total pair-distribution functions $G'(r)$ for $MgSiO_3$ glass (solid black curves), obtained by Fourier transforming the $S(Q)$ functions shown in Figure 4.8. The dashed blue curves show the unphysical Fourier transform artefacts at distances smaller than the closest approach between two atoms. The results are compared to those obtained from molecular dynamics simulations at similar pressures (green curves) [75]. The solid red curve shows the X-ray total pair-distribution function for the same $MgSiO_3$ glass used in the neutron diffraction work, measured before compression. The high pressure datasets have been offset vertically, and the PEARL measurement at 4.0 GPa omitted, for clarity of presentation.

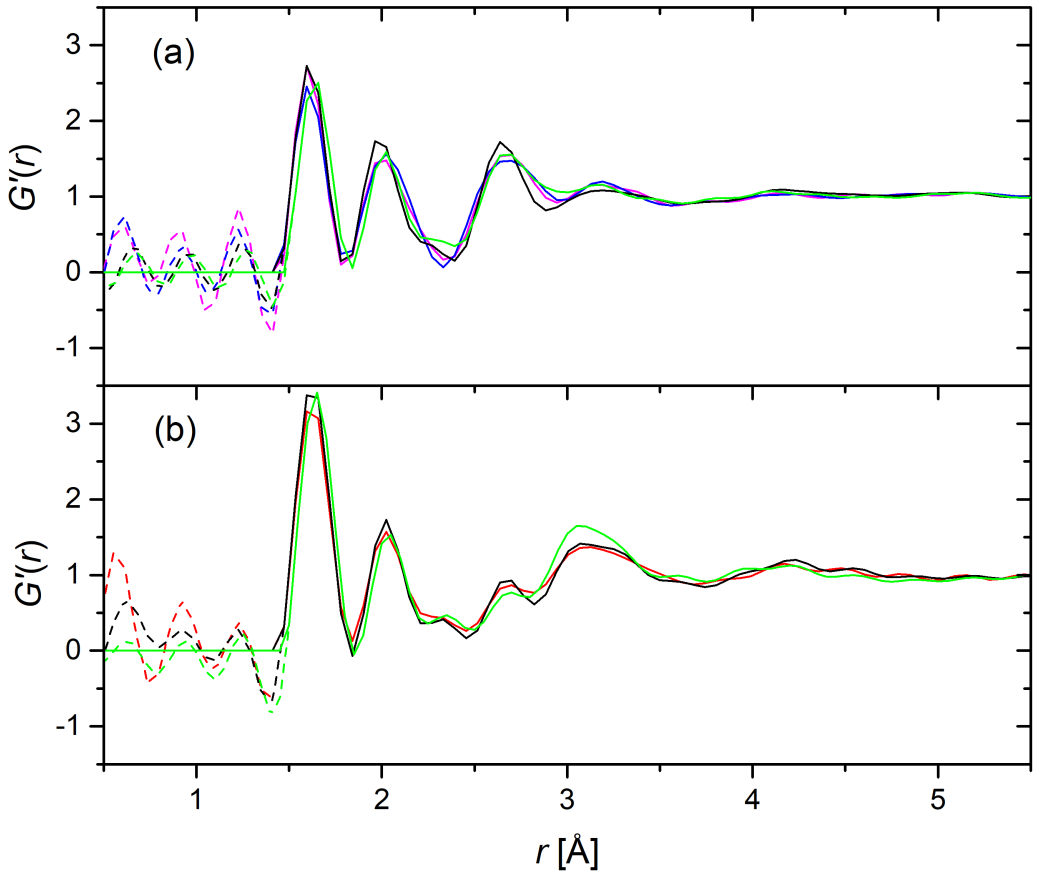

Figure 4.12: The total pair-distribution functions $G'(r)$ for glassy $MgSiO_3$ recovered from compression as measured with neutron or X-ray diffraction. Plot (a) shows the total pair-distribution functions measured with the D4c diffractometer for the as-prepared sample using a vanadium can (solid black curve), immediately after recovery to ambient from 8.2(5) GPa (solid magenta curve) and approximately one week after recovery to ambient from 8.2(5) GPa (solid blue curve). Plot (b) shows the total pair-distribution functions measured for the as-prepared sample using the 6-ID-D diffractometer at the APS (solid black curve) [72], and for $MgSiO_3$ approximately one month after recovery from 17.5(5) GPa using a conventional Ag source laboratory X-ray diffractometer (solid red curve). The solid green curves in (a) and (b) show the pair-distribution functions obtained from the molecular dynamics simulations immediately after recovery from 8.5 GPa or 17.5 GPa, respectively [75]. The solid curves are Fourier transforms of spline fits to the corresponding $S(Q)$ functions shown in Figure 4.9, and the dashed curves show the unphysical Fourier transform artefacts at distances smaller than the closest approach between two atoms.

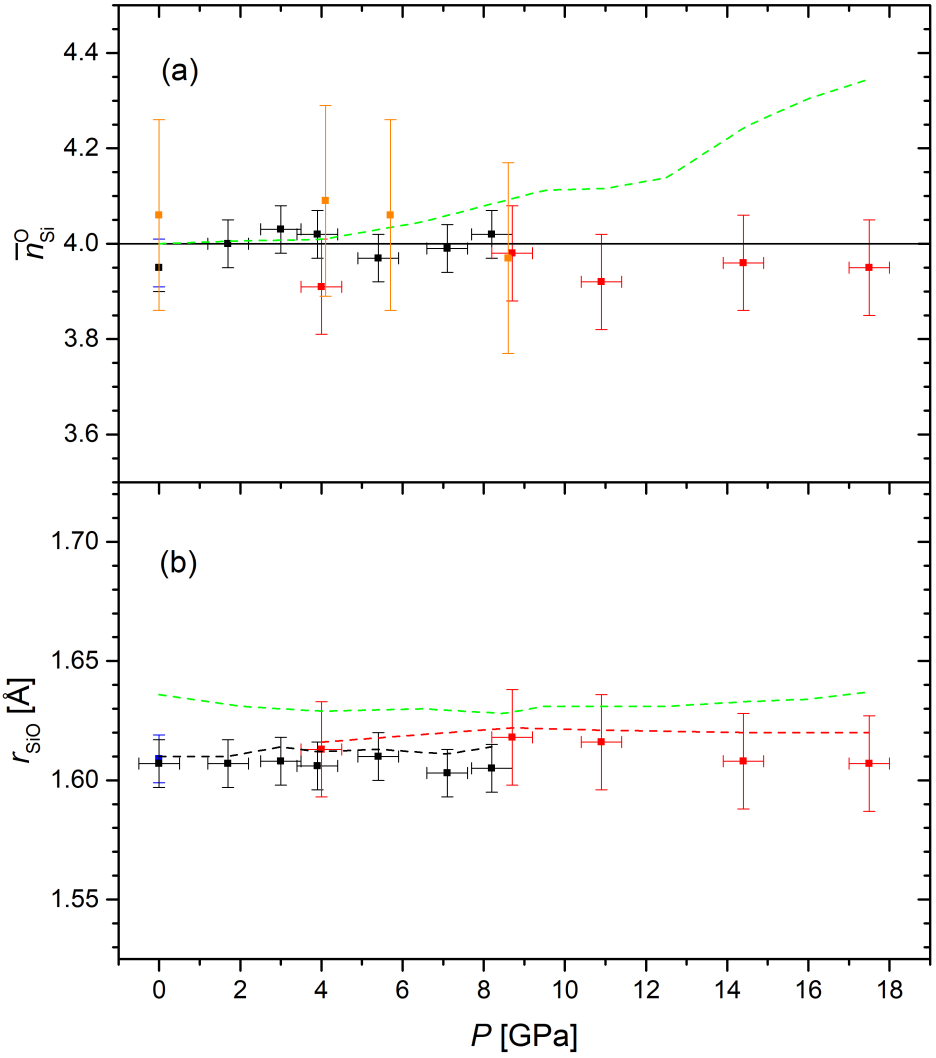

Figure 4.13: The pressure dependence of the (a) mean Si-O coordination number $\bar{n}^{O}_{Si}$, and (b) mean Si-O bond distance r_{SiO}, obtained for $MgSiO_3$ glass using neutron diffraction. The black markers show results from the D4c experiment, the red markers show results from the PEARL experiment, and the blue markers show results from the ambient vanadium can measurement on D4c. The results from the recovered samples of $MgSiO_3$ overlap with their respective ambient values, and have been omitted for clarity of presentation. The green dashed lines show results from the molecular dynamics simulations [75]. The black and red dashed lines show the weighted peak positions calculated using Equation 4.4 for the D4c and PEARL datasets, respectively. The orange markers show neutron diffraction results for glassy $(MgO)_{0.62}(SiO_2)_{0.38}$ [80].

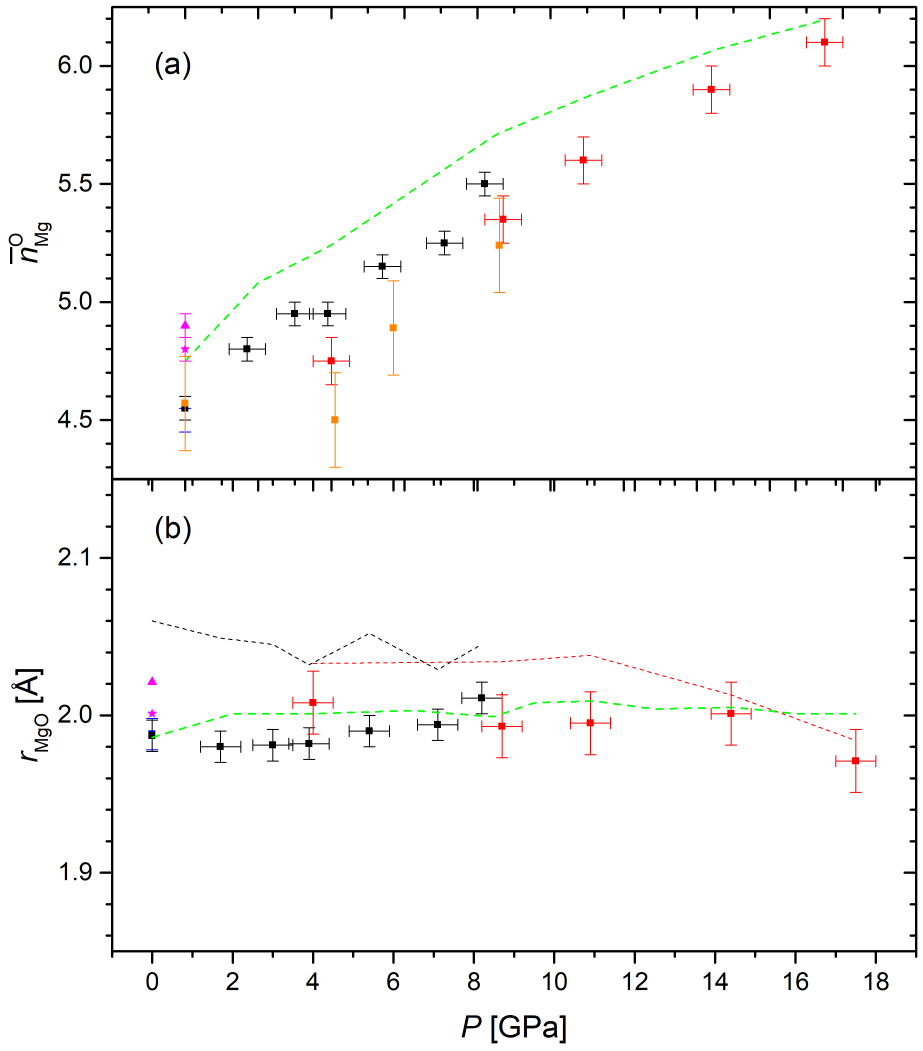

Figure 4.14: The pressure dependence of the (a) mean Mg-O coordination number $\bar{n}^{\mathrm{O}}_{\mathrm{Mg}}$, and (b) mean Mg-O bond distance r_{MgO}, obtained for $MgSiO_3$ glass using neutron diffraction. The black markers show results from the D4c experiment, the red markers show results from the PEARL experiment, and the blue markers show results from the ambient vanadium can measurement on D4c. The magenta star and triangle show the results for the recovered datasets measured immediately after decompression, and approximately one month after decompression, respectively. The green dashed lines show results from the molecular dynamics simulations [75]. The black and red dashed lines show the weighted peak positions calculated using Equation 4.4 for the D4c and PEARL datasets, respectively. The orange markers show neutron diffraction results for glassy $(MgO)_{0.62}(SiO_2)_{0.38}$ [80].

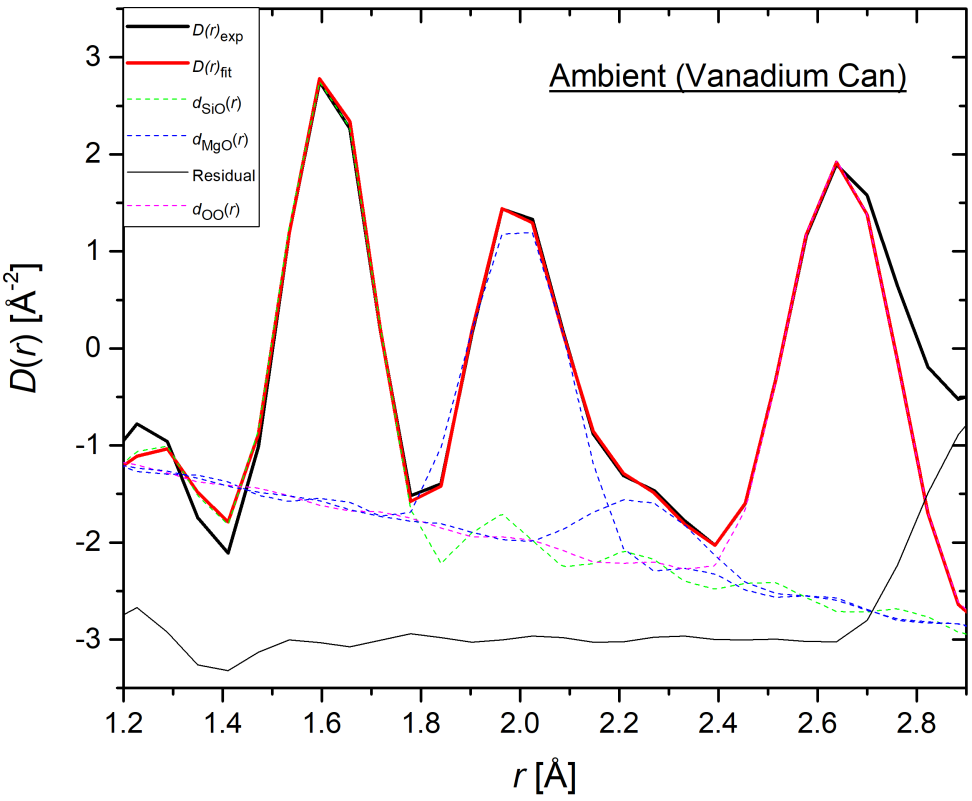

Figure 4.15: The density correlation function and fits obtained for $MgSiO_3$ glass at ambient conditions, measured in a vanadium can on the D4c diffractometer. The solid black line is the measured $D(r)_{\mathrm{exp}}$ function, which is fitted with four Gaussians convoluted with a sinc function using RDFGenie which combine to give the fit $D(r)_{\mathrm{fit}}$ (solid red curve). The dashed green and blue lines correspond to Si-O and Mg-O correlations, respectively. The dashed brown line is a constraint on the fit, and is used to estimate the mean O-O coordination number. The fit gives $R_\chi = 0.079$ for the range 1.14 - 2.50 Å.

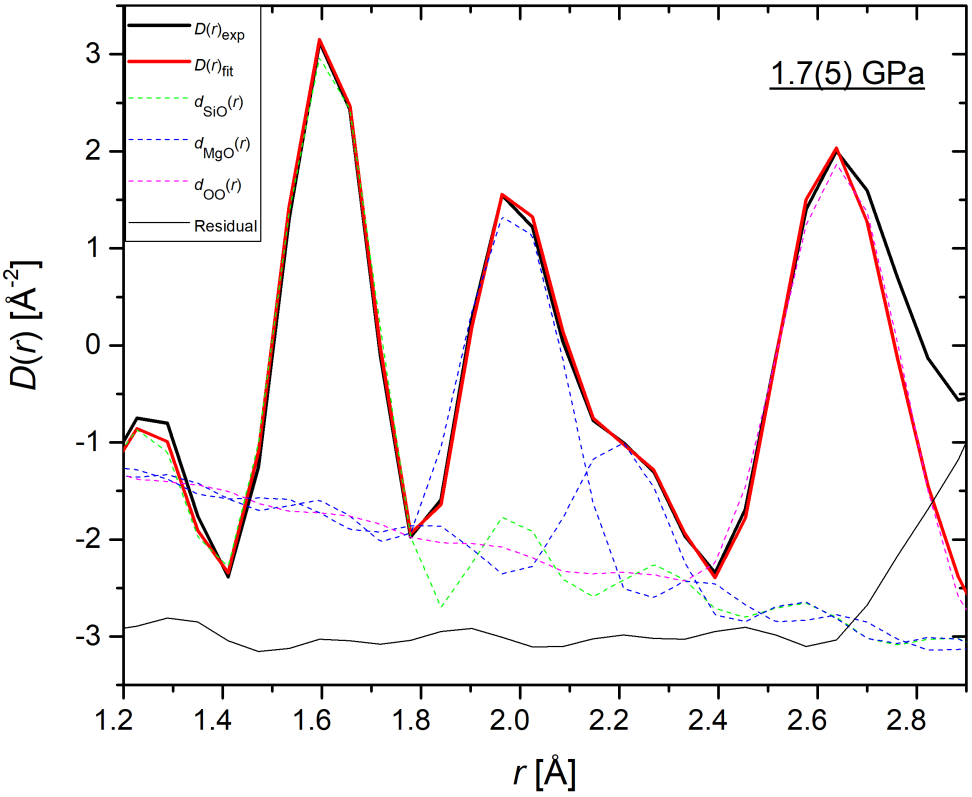

Figure 4.16: The density correlation function and fits obtained for $MgSiO_3$ glass at 1.7(5) GPa, measured on the D4c diffractometer. The solid black line is the measured $D(r)_{\text{exp}}$ function, which is fitted with four Gaussians convoluted with a sinc function using RDFGenie which combine to give the fit $D(r)_{\text{fit}}$ (solid red curve). The dashed green and blue lines correspond to Si-O and Mg-O correlations, respectively. The dashed brown line is a constraint on the fit, and is used to estimate the mean O-O coordination number. The fit gives $R_\chi = 0.058$ for the range 1.14 - 2.50 Å.

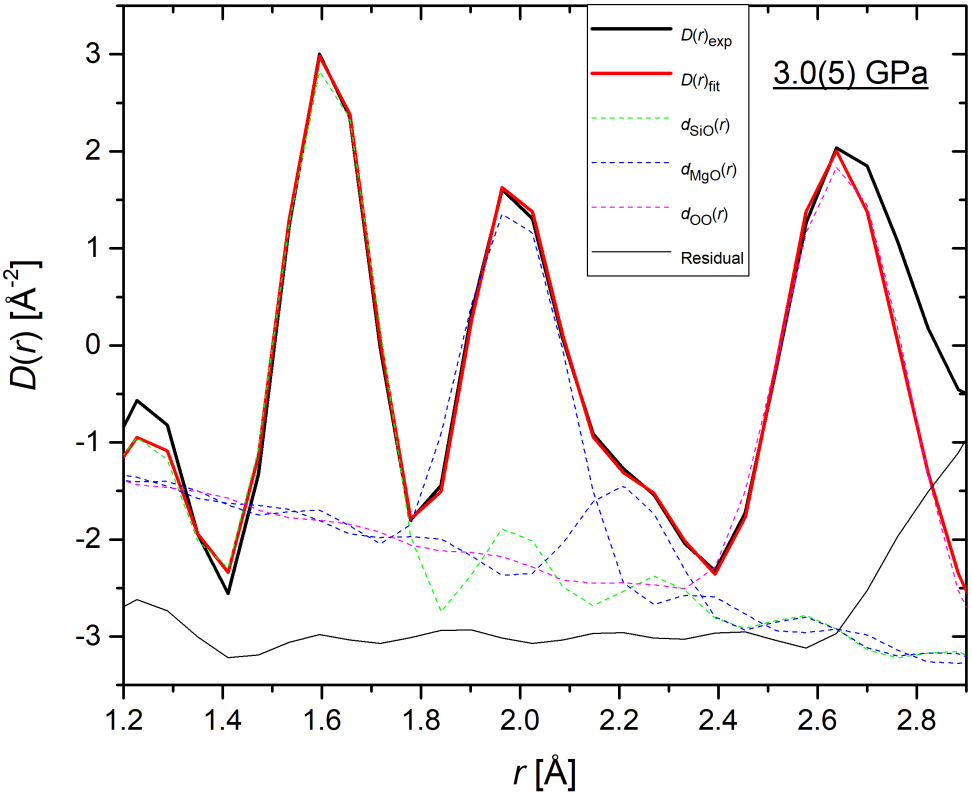

Figure 4.17: The density correlation function and fits obtained for $MgSiO_3$ glass at 3.0(5) GPa, measured on the D4c diffractometer. The solid black line is the measured $D(r)_{\text{exp}}$ function, which is fitted with four Gaussians convoluted with a sinc function using RDFGenie which combine to give the fit $D(r)_{\text{fit}}$ (solid red curve). The dashed green and blue lines correspond to Si-O and Mg-O correlations, respectively. The dashed brown line is a constraint on the fit, and is used to estimate the mean O-O coordination number. The fit gives $R_\chi = 0.079$ for the range 1.14 - 2.50 Å.

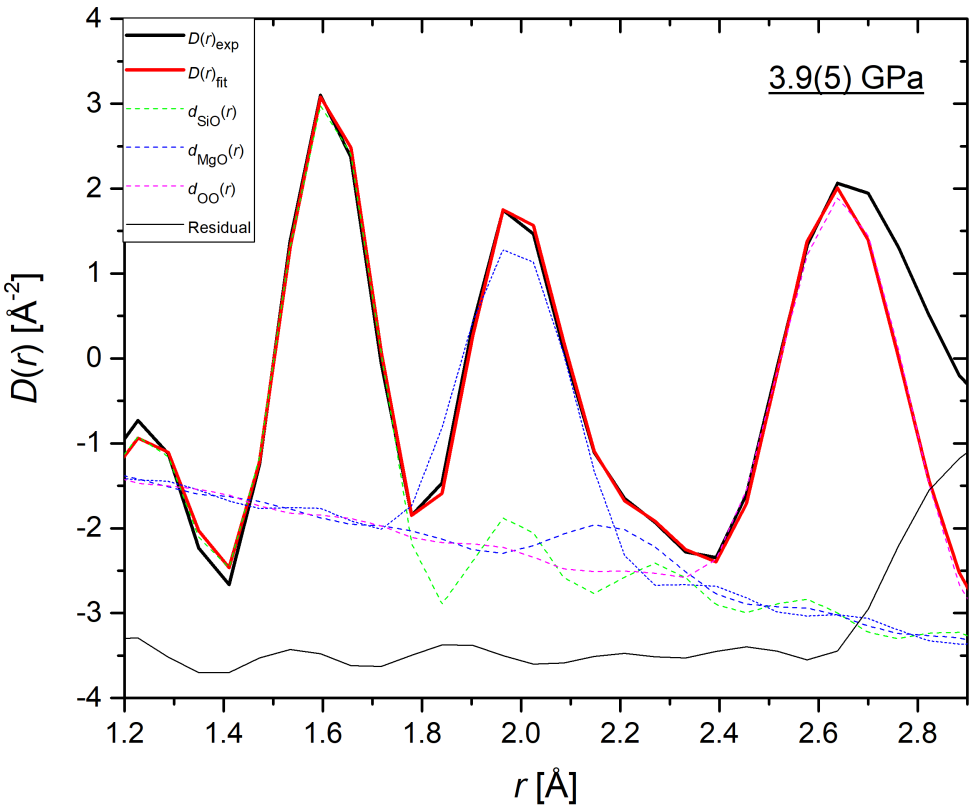

Figure 4.18: The density correlation function and fits obtained for $MgSiO_3$ glass at 3.9(5) GPa, measured on the D4c diffractometer. The solid black line is the measured $D(r)_{\text{exp}}$ function, which is fitted with four Gaussians convoluted with a sinc function using RDFGenie which combine to give the fit $D(r)_{\text{fit}}$ (solid red curve). The dashed green and blue lines correspond to Si-O and Mg-O correlations, respectively. The dashed brown line is a constraint on the fit, and is used to estimate the mean O-O coordination number. The fit gives $R_\chi = 0.062$ for the range 1.14 - 2.50 Å.

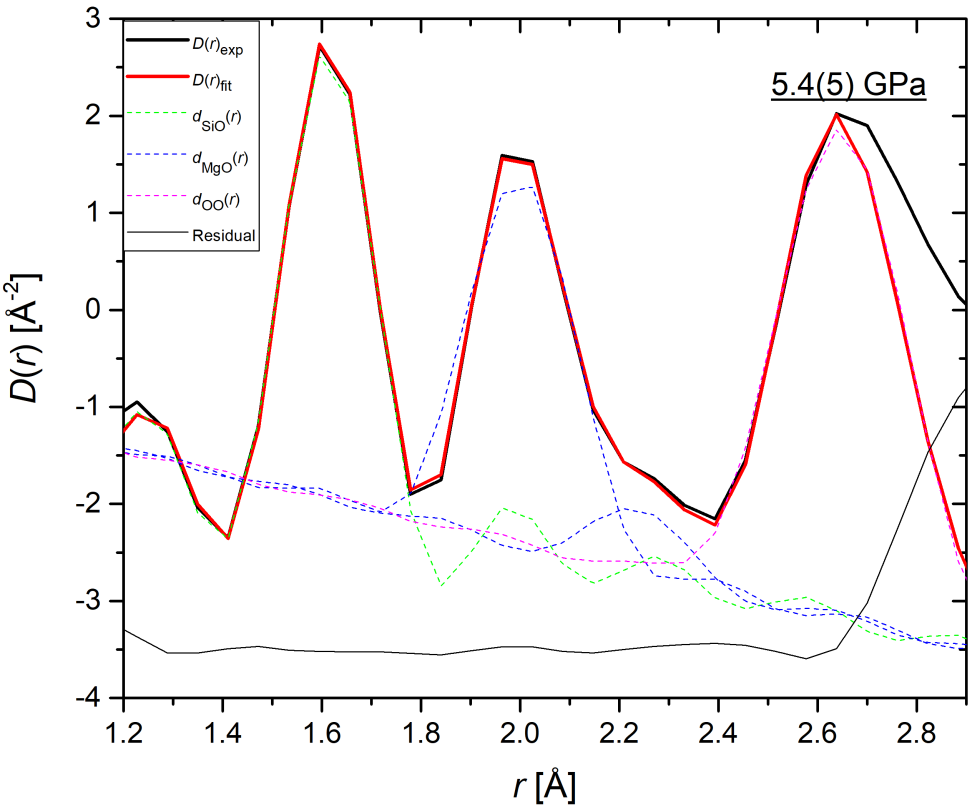

Figure 4.19: The density correlation function and fits obtained for $MgSiO_3$ glass at 5.4(5) GPa, measured on the D4c diffractometer. The solid black line is the measured $D(r)_{\text{exp}}$ function, which is fitted with four Gaussians convoluted with a sinc function using RDFGenie which combine to give the fit $D(r)_{\text{fit}}$ (solid red curve). The dashed green and blue lines correspond to Si-O and Mg-O correlations, respectively. The dashed brown line is a constraint on the fit, and is used to estimate the mean O-O coordination number. The fit gives $R_\chi = 0.058$ for the range 1.14 - 2.50 Å.

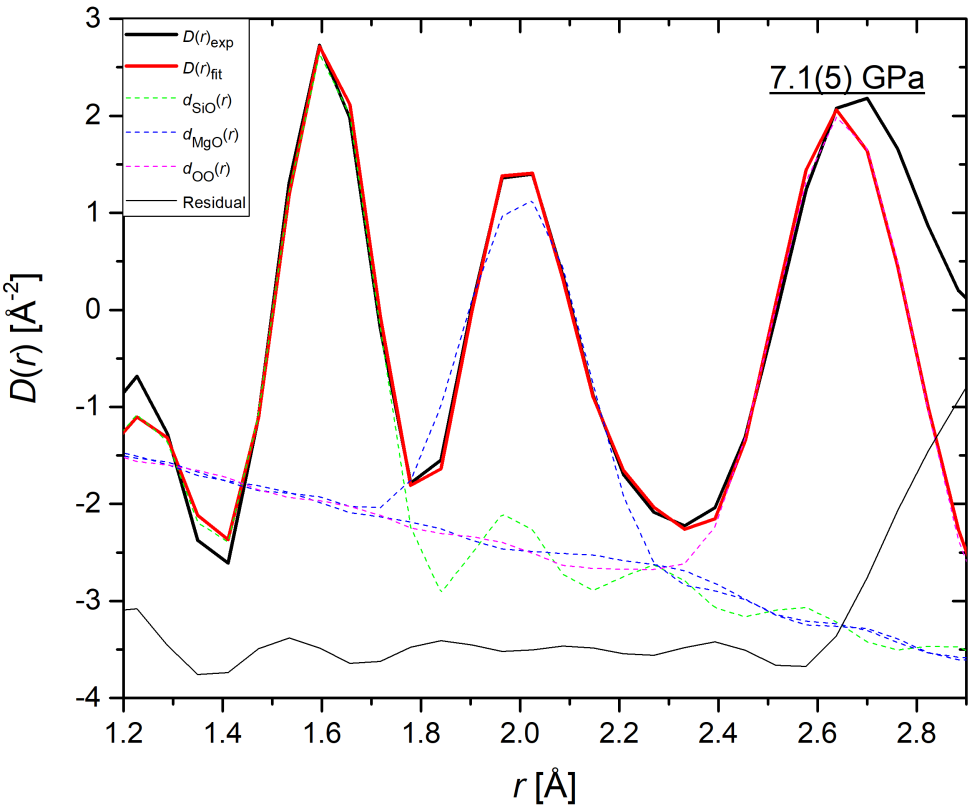

Figure 4.20: The density correlation function and fits obtained for $MgSiO_3$ glass at 7.1(5) GPa, measured on the D4c diffractometer. The solid black line is the measured $D(r)_{\text{exp}}$ function, which is fitted with four Gaussians convoluted with a sinc function using RDFGenie which combine to give the fit $D(r)_{\text{fit}}$ (solid red curve). The dashed green and blue lines correspond to Si-O and Mg-O correlations, respectively. The dashed brown line is a constraint on the fit, and is used to estimate the mean O-O coordination number. The fit gives $R_\chi = 0.094$ for the range 1.14 - 2.50 Å.

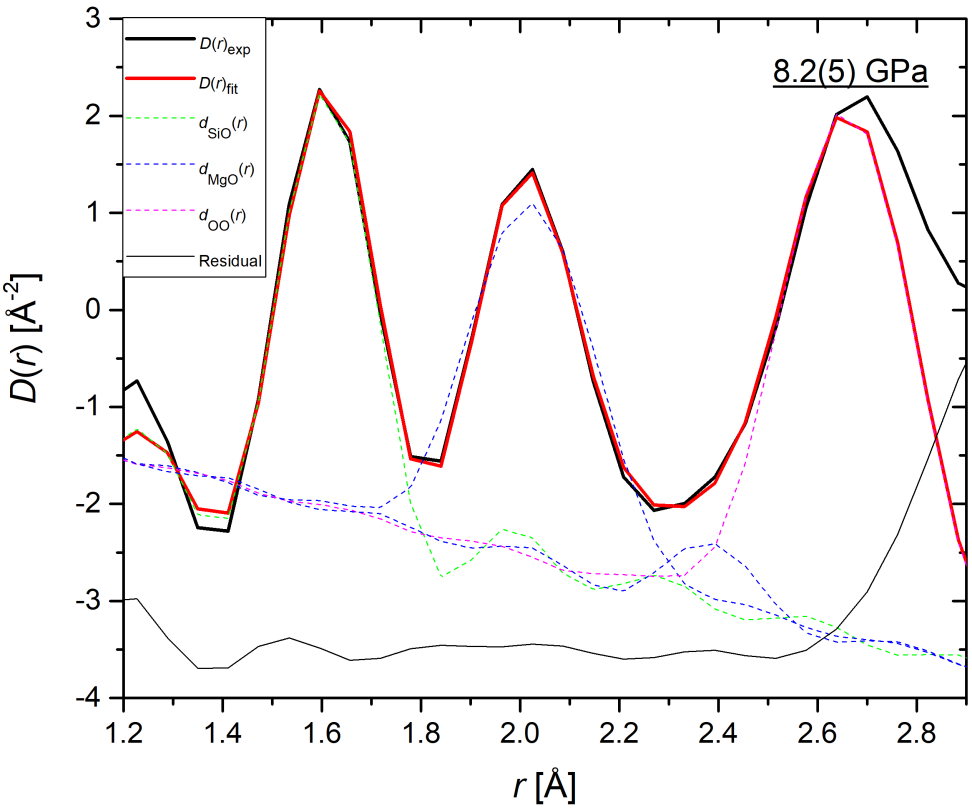

Figure 4.21: The density correlation function and fits obtained for $MgSiO_3$ glass at 8.2(5) GPa, measured on the D4c diffractometer. The solid black line is the measured $D(r)_{\text{exp}}$ function, which is fitted with four Gaussians convoluted with a sinc function using RDFGenie which combine to give the fit $D(r)_{\text{fit}}$ (solid red curve). The dashed green and blue lines correspond to Si-O and Mg-O correlations, respectively. The dashed brown line is a constraint on the fit, and is used to estimate the mean O-O coordination number. The fit gives $R_\chi = 0.116$ for the range 1.14 - 2.42 Å.

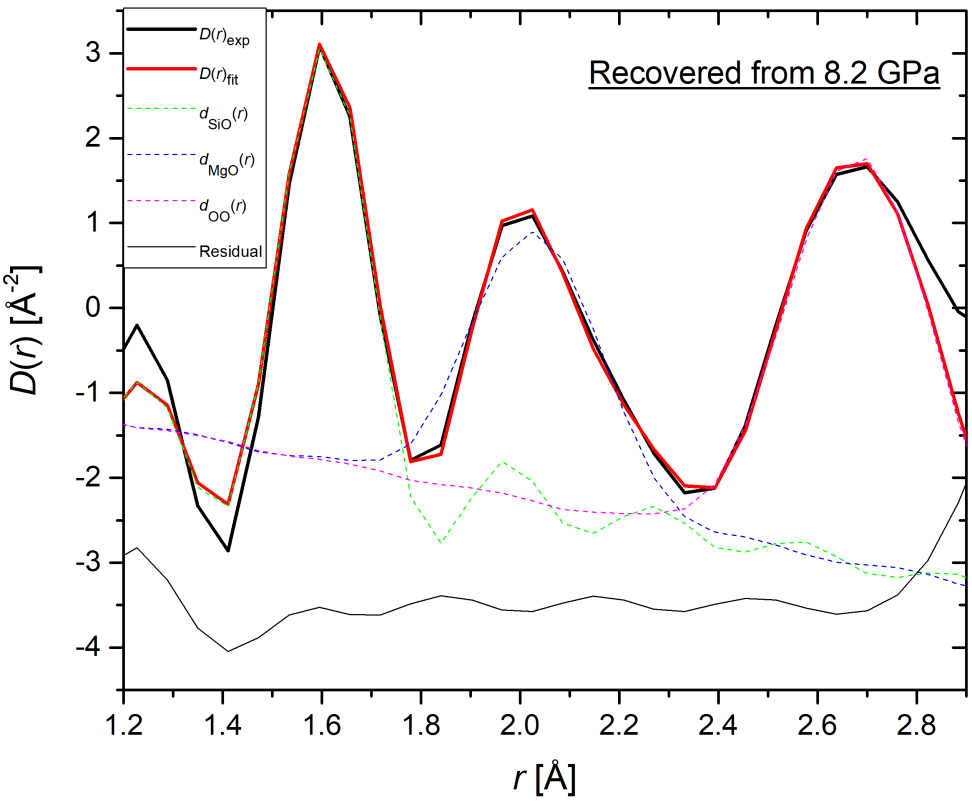

Figure 4.22: The density correlation function and fits obtained for $MgSiO_3$ glass recovered from 8.2(5) GPa, measured on the D4c diffractometer immediately after decompression. The solid black line is the measured $D(r)_{\rm exp}$ function, which is fitted with four Gaussians convoluted with a sinc function using RDFGenie which combine to give the fit $D(r)_{\rm fit}$ (solid red curve). The dashed green and blue lines correspond to Si-O and Mg-O correlations, respectively. The dashed brown line is a constraint on the fit, and is used to estimate the mean O-O coordination number. The fit gives $R_\chi = 0.163$ for the range 1.14 - 2.42 Å.

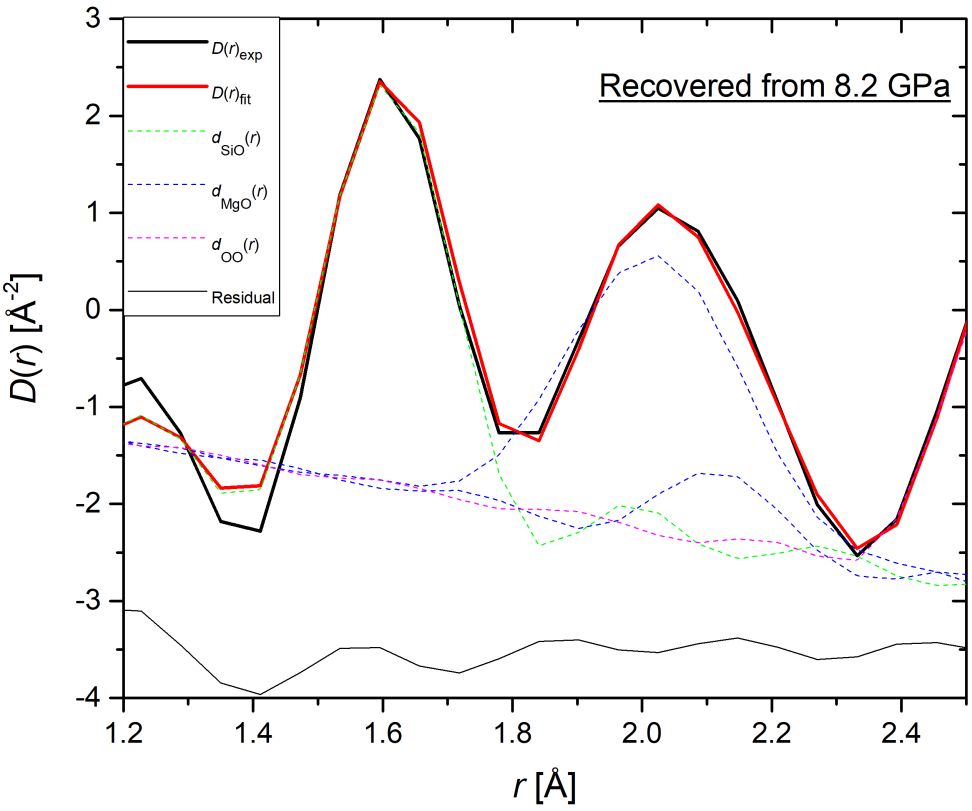

Figure 4.23: The density correlation function and fits obtained for $MgSiO_3$ glass recovered from 8.2(5) GPa, measured on the D4c diffractometer approximately one week after decompression. The solid black line is the measured $D(r)_{\mathrm{exp}}$ function, which is fitted with four Gaussians convoluted with a sinc function using RDFGenie which combine to give the fit $D(r)_{\mathrm{fit}}$ (solid red curve). The dashed green and blue lines correspond to Si-O and Mg-O correlations, respectively. The dashed brown line is a constraint on the fit, and is used to estimate the mean O-O coordination number. The fit gives $R_\chi = 0.140$ for the range 1.14 - 2.42 Å.

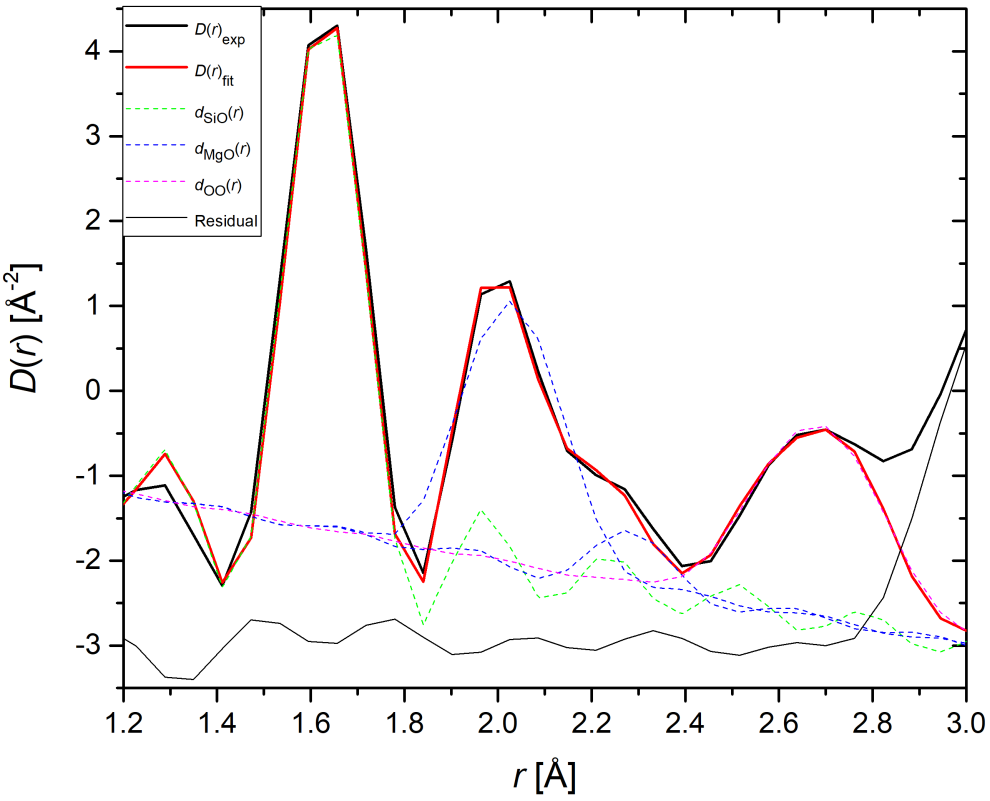

Figure 4.24: The density correlation function and fits obtained for $MgSiO_3$ glass at ambient conditions before compression, measured using X-ray diffraction on the 6-ID-D beamline at the Advanced Photon Source, USA. The solid black line is the measured $D(r)_{\text{exp}}$ function, which is fitted with four Gaussians convoluted with a sinc function using RDFGenie which combine to give the fit $D(r)_{\text{fit}}$ (solid red curve). The dashed green and blue lines correspond to Si-O and Mg-O correlations, respectively. The dashed brown line is a constraint on the fit, and is used to estimate the mean O-O coordination number. The fit gives $R_\chi = 0.0982$ for the range 1.15 - 2.55 Å.

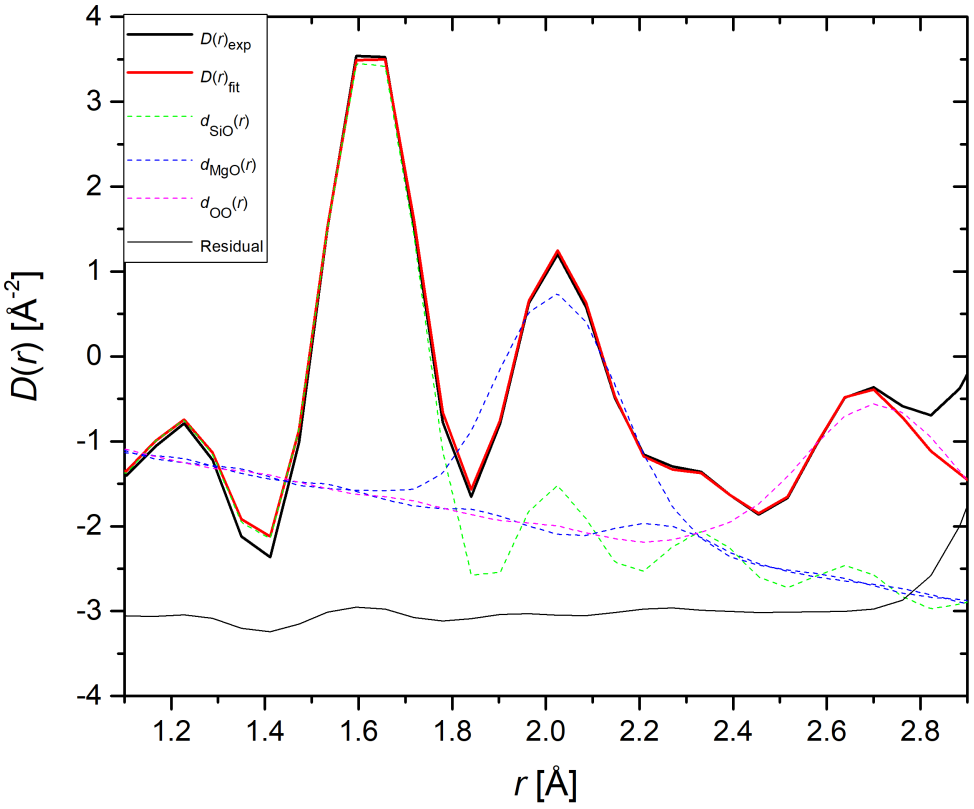

Figure 4.25: The density correlation function and fits obtained for $MgSiO_3$ glass recovered from 17.5(5) GPa, measured on a laboratory Ag source X-ray diffractometer approximately one month after decompression. The solid black line is the measured $D(r)_{\text{exp}}$ function, which is fitted with four Gaussians convoluted with a sinc function using RDFGenie which combine to give the fit $D(r)_{\text{fit}}$ (solid red curve). The dashed green and blue lines correspond to Si-O and Mg-O correlations, respectively. The dashed brown line is a constraint on the fit, and is used to estimate the mean O-O coordination number. The fit gives $R_\chi = 0.0520$ for the range 1.15 - 2.55 Å.

4.4.3 Estimation of the mean O-O Coordination Number and Distance

Figure 4.26 shows the six partial pair-distribution functions $g_{\alpha\beta}(r)$ of $MgSiO_3$ glass obtained from molecular dynamics simulations, at ambient conditions and at 17.5 GPa. The results confirm that the first and second real space peaks correspond exclusively to Si-O and Mg-O correlations, respectively. The third real space peak corresponds primarily to O-O correlations, with other contributions which become more significant at higher pressures. The mean O-O coordination number $\bar{n}_{\mathrm{O}}^{\mathrm{O}}$ and O-O separation r_{OO} estimated from the D4c neutron diffraction datasets are shown in Figure 4.27. The mean O-O separation was estimated by measurement of the third peak position of $G'(r)$, and the mean O-O coordination number was estimated by using the RDFGenie program to fit a Gaussian function convoluted with a sinc function to the third peak. The plots are shown in Figures 4.15 to 4.25.

The estimated O-O coordination number increases from an ambient value of $\bar{n}_{\mathrm{O}}^{\mathrm{O}} = 4.6(2)$, to a value of $\bar{n}_{\mathrm{O}}^{\mathrm{O}} = 6.8(2)$ at 8.2(5) GPa. This is accompanied by an increase in the mean O-O separation from $r_{\mathrm{OO}} = 2.65(2)$ Å at ambient, to $r_{\mathrm{OO}} = 2.68(2)$ Å at 17.5 GPa. It is important to emphasize that at higher pressures especially, the estimation of the O-O coordination number and separation becomes less accurate, as the contribution from other pair-correlations to the third peak becomes more significant.

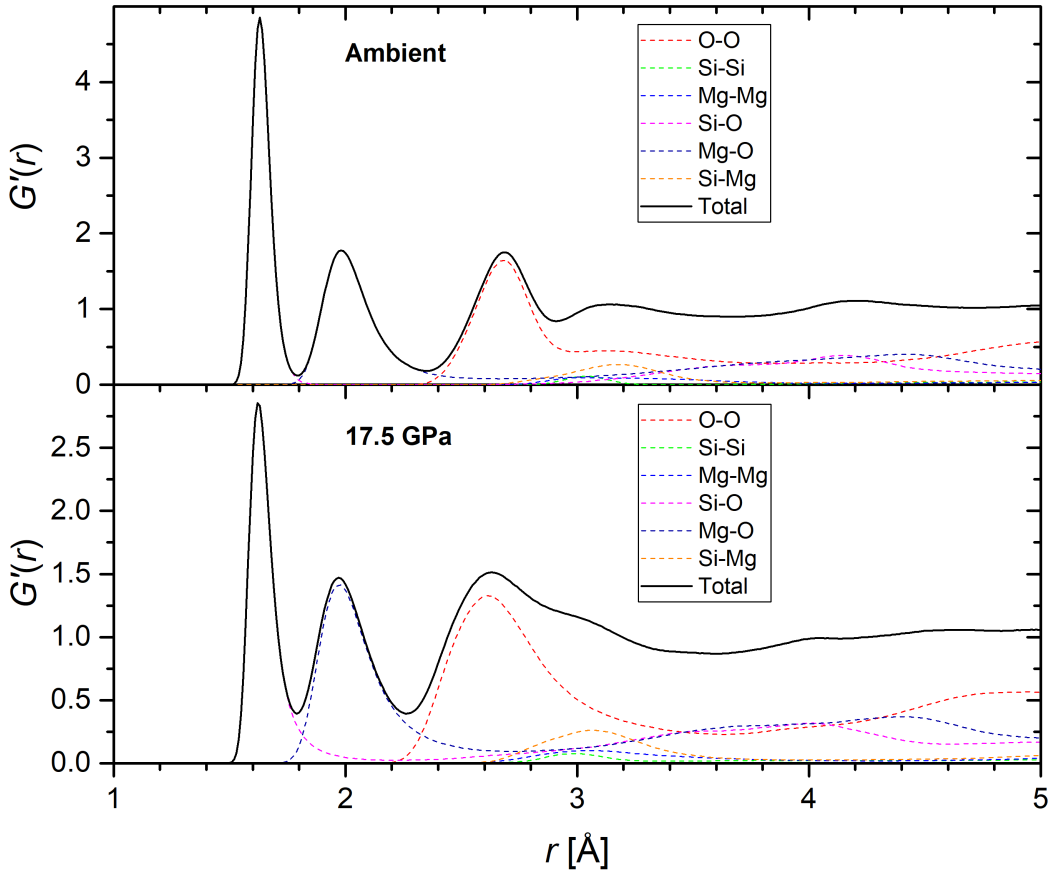

Figure 4.26: The six partial pair-distribution functions $g_{\alpha\beta}(r)$ of $MgSiO_3$ glass obtained from the molecular dynamics simulations accompanying this study [75], weighted for neutron diffraction. Also shown is the total pair-distribution function $G'(r)$, which is the sum of all the weighted partial $g_{\alpha\beta}(r)$ functions. The results are shown for ambient conditions and 17.5 GPa, which corresponds to the maximum pressure used in the neutron diffraction experiments.

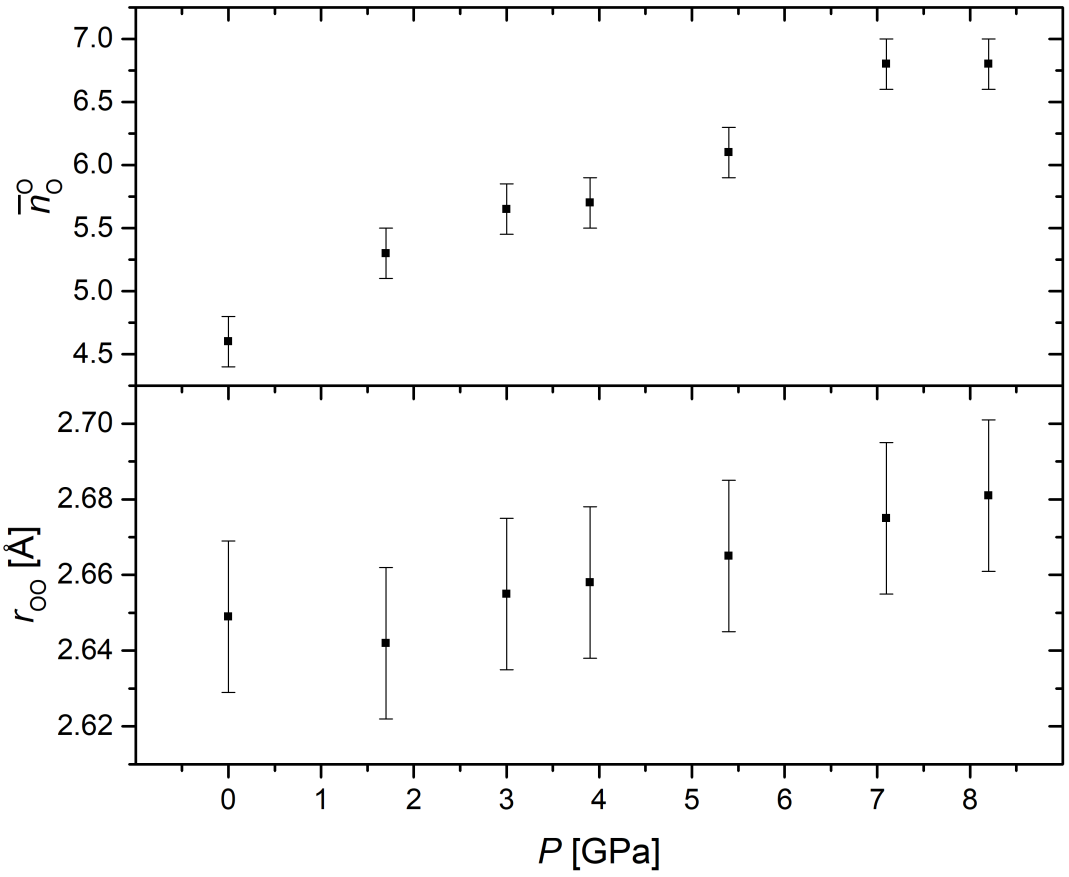

Figure 4.27: The pressure dependence of the estimated (a) mean O-O coordination number $\bar{n}_{\mathrm{O}}^{\mathrm{O}}$, and (b) mean O-O distance r_{OO}, obtained for $MgSiO_3$ glass using neutron diffraction. The results originate from the D4c high pressure experiment, and have been estimated by assuming that the third peak of $G'(r)$ originates exclusively from O-O correlations.

4.5 Discussion

The total structure factors obtained from both neutron diffraction and simulation exhibit a reduction in prominence of the FSDP and simultaneous enhancement of the principal peak with increasing pressure. This phenomenon is consistent with the results obtained from previous work on SiO_2 [81] and GeO_2 [49] glasses. The FSDP is associated with ordering on an intermediate length scale, and the principal peak is associated with extended range ordering up to a nanometre length scale [82]. The changes indicate a competition between intermediate and extended range ordering in the glass, where the latter dominates at higher pressures.

The neutron diffraction results show that the mean Si-O coordination number remains constant within the experimental error at $\bar{n}^{\mathrm{O}}_{\mathrm{Si}}$ ∼4 across the measured pressure range. This contrasts with previous work on SiO_2 glass, in which the Si-O coordination number increases to $\bar{n}^{\mathrm{O}}_{\mathrm{Si}} = 4.2(1)$ at 17.5(5) GPa and is accompanied by a decrease in the Si-O bond distance from 1.60(2) Å to 1.57(2) Å [81]. This result suggests that the inclusion of Mg as a modifying cation has an effect on the densification mechanism, as the SiO_4 tetrahedra in pure SiO_2 glass begin to deform at a lower pressure. The mean Si-O bond distance also remains constant across the measured pressure range at ∼1.61 Å. The results from the MD simulations contrast with these findings, and show that the Si-O coordination number begins to increase gradually at ∼7 GPa to reach a maximum value of $\bar{n}^{\mathrm{O}}_{\mathrm{Si}} = 4.35$ at 17.5 GPa. Furthermore, the Si-O bond distance is consistently longer at r_{SiO} ∼1.63 Å. These discrepancies likely result from the interatomic interaction model that was used in the simulations. Furthermore, the structure acquired from simulation was obtained using a hot compression procedure, in which the glass was heated to 3000 K and then compressed, before being quenched to 300 K. In contrast, the neutron diffraction samples were compressed at room temperature.

The second real space peak, which corresponds to Mg-O correlations, initially exhibits a shoulder feature which extends to higher r. This feature gradually becomes a tail as pressure is increased and disappears by 14.4(5) GPa, which can be demonstrated by the fact that the calculated weighted peak position falls within the experimental uncertainty of the peak maximum. This provides evidence that the distribution of Mg-O bond lengths is highly asymmetric at ambient conditions, with a cluster of preferred distances at r_{MgO} ∼2 Å and longer bond lengths also present. As pressure is increased, these longer bond distances gradually become shorter, and the distribution becomes

much more symmetric. Cormier *et al* [67] report a similar result for ambient $MgSiO_3$ glass, and distinguish two Mg-O contributions at ∼2 Å and ∼2.21 Å.

The neutron diffraction and MD simulation results show that the mean Mg-O coordination number gradually increases from $\bar{n}^{O}_{Mg} = 4.50(5)$ at ambient conditions, to $\bar{n}^{O}_{Mg} = 6.1(1)$ at 17.5(5) GPa. This reflects a transition from Mg being primarily 4-fold coordinated to becoming fully 6-fold coordinated, which is mostly complete by ∼15 GPa. Therefore, the application of pressure to the system enables Mg to convert to a fully network modifying role, which is reflected by the coordination number increase. The ambient Mg-O coordination number is in agreement with previously reported experimental results [67, 83]. Wilding *et al* [80] report a similar change in Mg-O coordination in $(MgO)_{0.62}(SiO_2)_{0.38}$ glass at pressures up to 8.3 GPa.

The mean O-O coordination number and separation has been estimated from the D4c neutron diffraction results by assuming that the third peak of $G'(r)$ is comprised exclusively of O-O contributions. The results show that the O-O coordination number increases from $\bar{n}^{O}_{O} = 4.6(2)$ at ambient conditions, to $\bar{n}^{O}_{O} = 6.8(2)$ at 8.2(5) GPa. This change is accompanied by a small increase in the mean O-O separation distance from $r_{OO} = 2.65(2)$ Å at ambient, to $r_{OO} = 2.68(2)$ Å at 17.5 GPa. The edge length of a perfect tetrahedron or octahedron may be calculated using equations 4.17 and 4.18, respectively.

$$r = \sqrt{\frac{8}{3}} r_{AO}, \tag{4.17}$$

$$r = \sqrt{2} r_{AO}, \tag{4.18}$$

where r_{AO} is the distance from the tetrahedron or octahedron centre, to a vertex. The expected O-O separation is ∼2.63 Å for a perfect SiO_4 tetrahedron and ∼3.27 Å for a perfect MgO_4 tetrahedron, whilst the expected O-O separation for a perfect MgO_6 octahedron is ∼2.83 Å. Therefore, only O-O correlations associated with SiO_4 sites and MgO_6 sites are able to contribute the third peak of $G'(r)$. Since the composition of $(MgO)_{0.5}(SiO_2)_{0.5}$ reflects an equal chance of a given O atom being bonded to a Si atom or Mg atom, the ambient O-O coordination number of 4.6 is consistent with a scenario in which Mg occupies primarily MgO_4 sites at ambient conditions. This is because a given oxygen atom bound to an SiO_4 tetrahedron will have three nearest oxygen neighbours, and has an equal chance of being connected to either another SiO_4

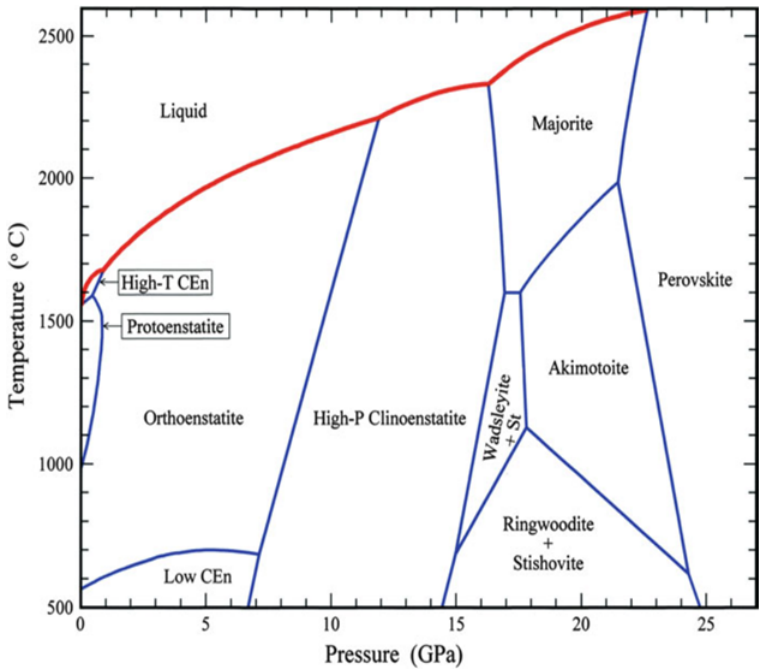

Figure 4.28: The P-T phase diagram of $MgSiO_3$, adapted from [84].

tetrahedron, or an MgO_4 tetrahedron. By 8.2(5) GPa, the higher O-O coordination number of 6.8 suggests that the local environment of Mg has transitioned to a majority of MgO_6 sites. However, it should be emphasized that this result is likely to be an overestimation, since other partial pair-correlation functions contribute a larger share of the third peak of $G'(r)$ at higher pressures.

The neutron diffraction results show that $MgSiO_3$ glass retains a limited extent of permanent structural change after recovery to ambient conditions. This is reflected by the fact that the mean Mg-O coordination number remains higher that its ambient value at $\bar{n}^{O}_{Mg} = 4.85(5)$, which indicates that Mg modifies the network structure to a greater extent than the uncompressed sample, leading to an increased mass density that is ∼12 % higher than its ambient value. Furthermore, the FSDP obtained from both the neutron and X-ray diffraction recovered datasets is at ∼2.05 $Å^{-1}$ which is between the ambient and 8.2(5) GPa values of 1.91(5) $Å^{-1}$ and 2.21(5) $Å^{-1}$, respectively. This provides evidence of change in the intermediate range ordering of the glass, suggesting permanent structural modification.

The crystalline structures of $MgSiO_3$ differ from the glass structure in that Mg is usually six-fold coordinated, although 4-fold coordinated Mg does exist in the akerman-

ite phase [85], but with an altered composition ($Ca_2MgSi_2O_7$) and a significantly shorter bond length (1.918 Å) than observed in the present work. Five-fold coordinated Mg exists in grandiderite [86], again with an altered composition ($(Mg_{0.9}Fe_{0.1})Al_3SiBO_9$). The P-T phase diagram of $MgSiO_3$ is shown in Figure 4.28. The structures of all the pyroxene polymorphs of $MgSiO_3$ consist of alternating chains of corner sharing SiO_4 tetrahedra, which cross link chains of octahedrally coordinated Mg atoms [87]. The structural configurations of the various polymorphs of $MgSiO_3$ differ in the configurations of these SiO_4 chains and their relative positions to the octahedral layers [87].

Periotto *et al.* [88] investigated the structure of $MgSiO_3$ orthoenstatite using single crystal X-ray diffraction from ambient conditions to 9.3 GPa. They concluded that Mg exists in two distinct crystallographic sites: a regular octahedral site with six Mg-O bond distances of approximately 2 Å length, and a highly distorted octahedral site with four bond distances of approximately 2 Å length and two much longer bond distances of approximately 2.3 Å and 2.45 Å. Hence, the asymmetric distribution of Mg-O bond distances observed for the glass also occurs in the crystalline structures. The longer bond distances correspond to bridging oxygen (BO) atoms between SiO_4 tetrahedra [88]. Therefore, the total number of Mg-BO bonds in orthoenstatite is $\frac{1}{6}$. In comparison, the MD results accompanying this study [75] predict that ∼10 % of Mg-O bonds correspond to BO atoms. In orthoenstatite, the Mg-BO bonds undergo the most significant contraction as pressure is increased, whilst the Mg-NBO bonds undergo a relatively small change. Hence in orthoenstatite the densification mechanism is dominated by the changing positions of the BO atoms relative to Mg [88].

Figure 4.29 shows the D4c total pair-distribution functions compared alongside the Si-O and Mg-O bond distances obtained by Periotto *et al.* [88] normalised to the number of crystallographic sites, measured at similar pressures. As pressure is increased the longer Mg-BO bond distances gradually shorten and hence become more symmetrically distributed around r ∼2 Å, a result which is analogous to the high pressure glass structure results. The highest pressure datasets for the glass show that the longest Mg-BO bond distance has significantly shortened and that the high r shoulder observed for the glass at ambient has dissapeared. In contrast, the shorter Mg-O bond distances have undergone a relatively small contraction.

Cormier and Cuello [67] determined the distribution of Q^n species in $MgSiO_3$ glass (where n corresponds to the number of BO atoms per SiO_4 tetrahedon), using ^{29}Si

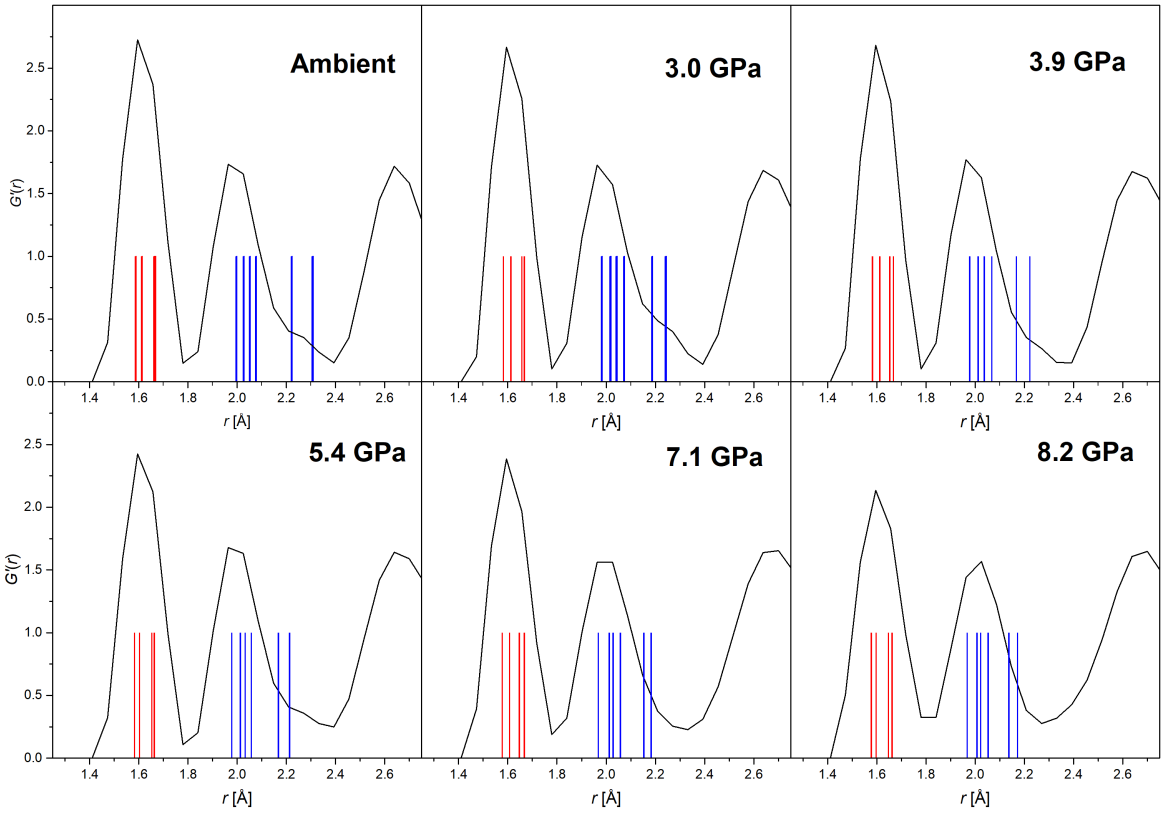

Figure 4.29: A selection of the total pair distribution functions $G'(r)$ for $MgSiO_3$ glass measured by the D4c diffractometer, compared with the distribution of bond lengths found by Periotto *et al* [88] for the enstatite structure at similar pressures. The bond lengths have been normalised to account for the presence of multiple Si and Mg crystalline sites, where each red or blue vertical bar represents the mean length for a Si-O or Mg-O bond, respectively.

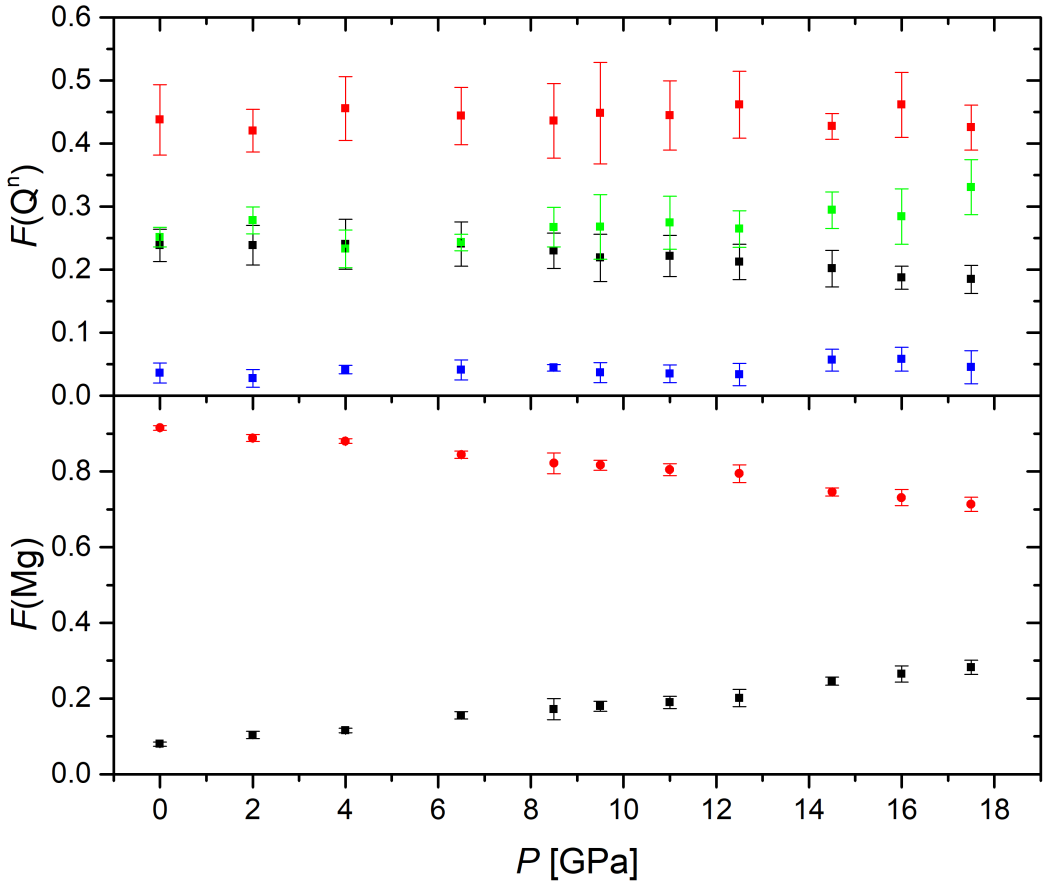

Figure 4.30: The pressure dependence of the (a) Q^n distribution Si^{IV} in $MgSiO_3$ glass, and (b) fractions of Mg-O bonds which correspond to bridging oxygen (BO) or non-bridging oxygen (NBO) atoms, obtained from the molecular dynamics simulations accompanying this study [75]. In (a) the markers give the fraction of Q^1 sites (black), Q^2 sites (red), Q^3 sites (green), and Q^4 sites (blue). In (b) the black and red markers give the fraction of Mg-BO and Mg-NBO bonds, respectively.

nuclear magnetic resonance (NMR). This study revealed that the silicate network is comprised primarily of Q^2 units (42 %), with Q^1 and Q^3 units comprising a further 25 % and 25.7 %, respectively. The average number of Si-BO bonds was determined to be 2.25, which is higher than the value of 2 predicted by the stoichiometry and observed in the orthoenstatite structure [88]. The pressure dependence of the Q^n distribution and fraction of Mg-BO or Mg-NBO bonds obtained from the molecular dynamics simulations accompanying this study [75], are plotted in Figure 4.30. At ambient conditions, the results are in close agreement with the ^{29}Si NMR results, predicting a Q^n speciation of Q^2 $\sim$44%, Q^1 $\sim$24% and Q^3 $\sim$25%. At higher pressures Q^3 sites begin to dominate over Q^1, reaching values of Q^3 $\sim$34% and Q^1 $\sim$19% at 17.5 GPa. This change is accompanied by an increase of $\sim$10% in the fraction of Mg-BO bonds at ambient conditions, to approximately 30 % at 17.5 GPa. Hence, the change in the Mg-O coordination environment appears to be driven by an increase in the fraction of Mg-BO bonds, whilst the fraction of BO atoms for each SiO_4 tetrahedra also increases. In contrast, in the orthoenstatite crystalline structure, the fraction of Mg-BO bonds and Si-BO bonds remain constant with pressure at $\frac{1}{6}$ and $\frac{1}{2}$ respectively, although the Mg-O bond lengths corresponding to these BO atoms undergo the most significant shortening.

4.6 Conclusions

The atomic structure of $MgSiO_3$ glass has been measured using *in situ* neutron diffraction with the D4c and PEARL diffractometers coupled with a Paris-Edinburgh press, at pressures up to 17.5(5) GPa. Molecular dynamics simulations have been performed alongside this study [75] which show an overall good agreement with the total structure factors $S(Q)$ and their Fourier transforms $G'(r)$ obtained from experiment.

Across the measured pressure range, the Mg-O coordination number increases from $\bar{n}^{\mathrm{O}}_{\mathrm{Mg}} = 4.50(5)$ at ambient conditions, to $\bar{n}^{\mathrm{O}}_{\mathrm{Mg}} = 6.1(1)$ at 17.5(5) GPa. In contrast, the SiO_4 tetrahedra remain undeformed across the measured pressure range, as reflected by the mean Si-O bond distance, and coordination number remaining at $r_{\mathrm{SiO}} = 1.61$ Å and $\bar{n}^{\mathrm{O}}_{\mathrm{Si}} = 4.0$, respectively. This result is in clear contrast with previous work on pure SiO_2 glass [81], and shows that the inclusion of Mg delays the pressure-induced increase of the Si-O coordination number from $\bar{n}^{\mathrm{O}}_{\mathrm{Si}} = 4$.

The distribution of Mg-O bond distances is highly asymmetric at ambient conditions, which is manifested in the form of a shoulder extending to the higher r region ($\sim$ 2.25 Å) of the second real space peak. As pressure is increased, this shoulder becomes less prominent and eventually disappears completely. A similar effect has been observed by Periotto *et al* [88] in a high pressure study of the orthoenstatite crystal structure in which the longer Mg-O distances, which correspond to BO atoms, decrease the most in length across the studied pressure range. Hence, the densification process is dominated by the shortening of these bonds. However, unlike the glass structure, Mg is six-fold coordinated at ambient conditions, and remains so across the measured pressure range. It has been proposed that the Mg coordination change observed in the glass structure is driven by an increase in the relative fraction of the total number of BO atoms in the network, which has been quantified via both an increase in the relative proportion of Q^3 sites associated with SiO_4 tetrahedra from $\sim$25 % to $\sim$34 %, and an increase in the total number of Mg-BO bonds from $\sim$10 % to $\sim$30 %.

5 Pressure Driven Structural Transformations In Calcium Silicate Glass

5.1 Introduction

Calcium silicates $(CaO)_x(SiO_2)_{1-x}$ have been extensively studied on account of their scientific and technological importance. For example, they form an integral part of cement and are commonly used as a safe alternative to asbestos in high-temperature insulation materials [89]. They are often used as components in bioactive materials, which have a wide range of medical applications [90]. Like magnesium silicates, they form an integral component of the Earth's mantle [91], and therefore an understanding of the high pressure structure of $CaSiO_3$ may have geological implications.

The ambient atomic structure of calcium silicate glass $CaSiO_3$ forms a network of SiO_4 tetrahedra linked by Ca^{2+} cations [21]. In this sense the atomic structure resembles that of magnesium silicate glass but with Ca^{2+} replacing Mg^{2+} as the modifying cation. Therefore, a high pressure investigation of the atomic structure of $CaSiO_3$ offers an opportunity to compare the effect of different network modifying cations on the densification mechanism of SiO_2 glass. For example, by measurement of the mean Si-O bond distance and coordination number as a function of pressure, it can be investigated if the replacement of Mg^{2+} with Ca^{2+} delays or hastens the pressure-driven change of the Si-O coordination number and bond distance.

The work presented in this chapter comprises two separate neutron diffraction experiments on glassy $CaSiO_3$. The experiments were performed using a Paris-Edinburgh press in conjunction with either the D4c diffractometer at pressures up to 8.2(5) GPa, or the PEARL diffractometer at pressures up to 17.5(5) GPa. The change in the silicon coordination environment is examined, and the results compared with molecular dynamics simulations and the high pressure neutron diffraction results of $MgSiO_3$ glass presented in Chapter 4.

This chapter is organised as follows. The essential theory is discussed in section 5.2, and the experimental procedures used are discussed in section 5.3. The results from the diffraction experiments and accompanying molecular dynamics simulations are provided in section 5.4, and a discussion and comparison with previous work on $MgSiO_3$ and SiO_2 glass is given in section 5.5. Finally, conclusions are drawn in section

5.6.

5.2 Theory

In neutron diffraction experiments, a modified version of Equation 2.13 is used which gives the Fourier transform relation relating the measured total structure factor $F(Q)$ to the total pair-distribution function $G(r)$,

$$G(r) = \frac{1}{2\pi^2 r\rho}\int_0^\infty QF(Q)\sin(Qr)M(Q)dr \tag{5.1}$$

where $M(Q)$ is a modification function, which is introduced for experimental work because a diffractometer can only measure over a finite Q range. $M(Q)$ is defined as

$$M(Q) = \begin{cases} 1 & Q \leq \mathrm{Q_{max}} \\ 0 & Q > \mathrm{Q_{max}} \end{cases} \tag{5.2}$$

where Q_{max} is the maximum value of Q that is used to truncate the dataset, and is usually chosen according the measurement range of the diffractometer. For a ternary glass such as $CaSiO_3$, the total pair-distribution function comprises six partial pair-distribution functions

$$\begin{aligned} G(r) = {} & \mathrm{c_{Ca}^2 b_{Ca}^2}[g_{\mathrm{CaCa}}(r) - 1] + \mathrm{c_{Si}^2 b_{Si}^2}[g_{\mathrm{SiSi}}(r) - 1] + \mathrm{c_O^2 b_O^2}[g_{\mathrm{OO}}(r) - 1] \\ & + 2\mathrm{c_{Ca}c_{Si}b_{Ca}b_{Si}}[g_{\mathrm{CaSi}}(r) - 1] + 2\mathrm{c_{Ca}c_O b_{Ca}b_O}[g_{\mathrm{CaO}}(r) - 1] + 2\mathrm{c_{Si}c_O b_{Si}b_O}[g_{\mathrm{SiO}}(r) - 1]. \end{aligned} \tag{5.3}$$

In the case that a peak is asymmetric, it is helpful to calculate a weighted peak position using

$$\bar{r}_{\alpha\beta} = \frac{\int_{r_1}^{r_2} r g_{\alpha\beta}(r)\mathrm{d}r}{\int_{r_1}^{r_2} g_{\alpha\beta}(r)\mathrm{d}r}. \tag{5.4}$$

If a given range in r is considered where all of the partial pair-distribution functions are equal to zero apart from the Si-O partial pair-distribution function $g_{\mathrm{SiO}}(r)$, it is possible to calculate the Si-O mean atomic coordination number as

$$\bar{n}_{\mathrm{Si}}^{\mathrm{O}} = \frac{2\pi\rho}{c_{\mathrm{Si}}b_{\mathrm{Si}}b_{\mathrm{O}}}\int_{r_1}^{r_2}[G(r) - G(r\to 0)]r^2\mathrm{d}r. \tag{5.5}$$

The limit $G(r \to 0)$ is given by

$$G(r\to 0) = -\sum_\alpha\sum_\beta c_\alpha c_\beta b_\alpha b_\beta = - < b >^2 = -0.297582(72)\ \text{barn} \tag{5.6}$$

As discussed in Chapter 2, it is sometimes necessary to convert the total pair-distribution function $G(r)$ to the density correlation function $D(r)$, using the relationship

$$D(r) = 4\pi\rho r \frac{G(r)}{< b >^2} = 4\pi\rho r \sum_{\alpha=1} \sum_{\beta=1} \frac{c_\alpha c_\beta b_\alpha b_\beta}{< b >^2} [g_{\alpha\beta}(r) - 1]. \tag{5.7}$$

The density correlation function $D(r)$ is comprised of a set of partial density correlation functions $d_{\alpha\beta}(r)$ where

$$d_{\alpha\beta}(r) = 4\pi\rho r[g_{\alpha\beta}(r) - 1]. \tag{5.8}$$

It is then possible to fit a Gaussian function convoluted with a sinc function to a peak associated with α-β correlations to obtain the mean coordination number $\bar{n}_\alpha^\beta$. This technique has the advantage of accounting for the truncation of each $F(Q)$ function at a finite $Q_{\max}$ value, and any overlap between the partial pair-distribution functions $g_{\alpha\beta}(r)$. The corresponding weighting factors for each Gaussian fit are given in Equations 5.9 and 5.10, which are used to calculate the values given in Table 5.1.

$$w_{\alpha\beta} = \frac{c_\alpha^2 b_\alpha^2}{< b >^2} \quad \text{for} \quad \alpha = \beta, \tag{5.9}$$

$$w_{\alpha\beta} = \frac{2c_\alpha c_\beta b_\alpha b_\beta}{< b >^2} \quad \text{for} \quad \alpha \neq \beta. \tag{5.10}$$

The total structure factors and pair-distribution functions may be rewritten to account for the neutron scattering length as

$$S(Q) = \frac{F(Q)}{< b >^2} + 1, \tag{5.11}$$

$$G'(r) = \frac{G(r)}{< b >^2} + 1. \tag{5.12}$$

Pair-correlation $\alpha - \beta$	$w_{\alpha\beta}$
Ca-Ca	0.03204
Si-Si	0.02497
O-O	0.43956
Ca-Si	0.05657
Ca-O	0.23734
Si-O	0.20952

Table 5.1: The six weighting factors of $CaSiO_3$ for neutron diffraction, calculated using Equations 5.9 and 5.10.

5.3 Experimental Method

5.3.1 Sample Preperation

The $CaSiO_3$ samples used in both diffraction experiments were prepared by K. Pizzey, University of Bath and provided is a summary of the sample preparation method originally discussed in [27].

To synthesize the glass, powdered SiO_2 and $CaCO_3$ were first dried separately at 800°C and 200°C respectively, for 16 hours. The powders were then mixed in an equimolar ratio inside a Pt-Rh crucible, and then heated to 800°C and held at this temperature for 12 hours. The purpose of this was to enable the calcium carbonate to decompose to calcium oxide according to the reaction:

$$CaSiO_3 \rightarrow CaO + CO_2 \uparrow . \tag{5.13}$$

After this, the crucible was heated to 1650°C which is above the melting temperatures of both SiO_2 and CaO, and held at this temperature for 3 hours. This ensured thorough melting and mixing of the liquid SiO_2 and CaO. Finally, the liquid was quenched to form glassy $CaSiO_3$ by placing the crucible on a copper block which was pre-cooled using liquid nitrogen. The crucible was then doused with further liquid nitrogen in order to cool the mixture as quickly as possible. Once the glass was formed a heatgun was used to increase the temperature to ambient conditions as quickly as possible in order to prevent moisture from forming on the glass. Finally, the glass was annealed at a temperature of 700°C in order to remove any tension in the structure.

The composition of the sample was verified to be almost perfectly stoichiometric, using Electron Probe Micro-Analysis (EPMA) measurements at Corning Inc, USA [73]. The exact atomic composition was determined to be $(CaO)_{0.49967}(SiO_2)_{0.50037}$ which represents a deviance of less than 0.1% from the ideal $(CaO)_{0.5}(SiO_2)_{0.5}$ composition.

5.3.2 D4c Experiment

The D4c neutron diffraction experiment studied calcium silicate glass at ambient temperature ($T \approx 300$ K) and pressures up to 8.2(5) GPa. An incident neutron wavelength of 0.49841(1) Å was used to optimise the incident flux of neutrons. Single toroid (ST) cubic BN anvils were used to compress the sample. Compression was controlled manually via the use of a hand pump throughout the entire experiment. No automated system to control the oil pressure was available, so the oil pressure typically relaxed by a small amount over the course of a pressure point measurement (20 - 30 bar). When changing oil pressure, periodic pauses were taken in order to allow the system to equilibrate. The pressure points measured for $CaSiO_3$ are shown in Table 5.2. During the course of a pressure point measurement, the ratio was taken of the measured intensities over different points in time. The purpose of this was to check that the ratio did not deviate from unity, i.e. if the measured intensities were consistent. No such deviation was observed over the course of the experiment. Vanadium measurements were made at ambient pressure for (a) an ST pellet of the usual dimensions inside a Ti-Zr gasket, (b) three deformed pellets with the same cap sizes but differing cylinder geometries and (c) two spherical caps machined to match the ST anvil profiles, in order to perform the data correction procedure described in section 3.4. An additional measurement was made of the $CaSiO_3$ sample inside a vanadium can. The D4c setup used in conjunction with a vanadium can offers a higher accessible Q range ($0.5\ \text{Å}^{-1} \leq Q \leq 23.5\ \text{Å}^{-1}$) and an improved signal to noise ratio.

The ideal mass for a single toroid pellet of $CaSiO_3$ was calculated to be 0.26751(1) g. In order to produce a ST pellet, a single piece of $CaSiO_3$ glass was finely ground using an agate mortar and pestle, and the resulting powder was then transferred into a die specially designed to produce the shape of a ST pellet. The powder was compressed in stages, allowing a relaxation time of approximately 5 minutes between each stage. The resultant pellet was then immediately transferred into a Ti-Zr gasket placed onto the piston anvil, and then placed immediately into the Paris-Edinburgh press. The mass

of the $CaSiO_3$ pellet was measured to be 0.26050(1) g and the mass of the Ti-Zr gasket was measured to be 1.1995(1) g. Immediately after decompression, a measurement was taken of the $CaSiO_3$ pellet in order to investigate the extent of permanent densification of the glass.

Oil Pressure [bar]	Applied Load [tns]	Sample Pressure [GPa]
100	6.8	Ambient
450	30.5	3.0(5)
600	40.7	3.9(5)
900	61.0	5.7(5)
1200	81.3	7.1(5)
1400	94.9	8.2(5)

Table 5.2: The oil pressures and corresponding sample pressures for the D4c experiment on $CaSiO_3$ glass. The sample pressures were deduced from the calibration curve shown in Figure 3.7.

The data correction procedure followed the methodology described in section 3.4.1. Figure 5.1 shows an example of the correction procedure used for the experiment, and illustrates graphically the steps used to obtain the background and container corrected sample intensity $I_{\mathrm{SC}}^{\mathrm{E}*}(\theta)$ for $CaSiO_3$ glass at 3 GPa.

5.3.3 PEARL Experiment

The PEARL experiment was performed by K. Pizzey, University of Bath and provided is a summary of the method originally discussed in [27].

The PEARL neutron diffraction experiment studied calcium silicate glass at ambient temperature ($T \approx 300$ K) and pressures up to 17.5(5) GPa. Sintered diamond double toroid (DT) anvils were used to compress the sample. Compression was controlled by an automated machine up to an oil pressure of $P_{\mathrm{oil}} = 980$ bar. After this, the oil pressure was increased manually via the use of a hand pump. The automated system ensured that the oil pressure was kept at a constant value, but use of the manual system meant that a small relaxation of the oil pressure was allowed to occur. The pressure points at which diffraction patterns were measured for $CaSiO_3$ are shown in Table 5.3. Equivalent measurements were made for a vanadium pellet of equal dimensions to the

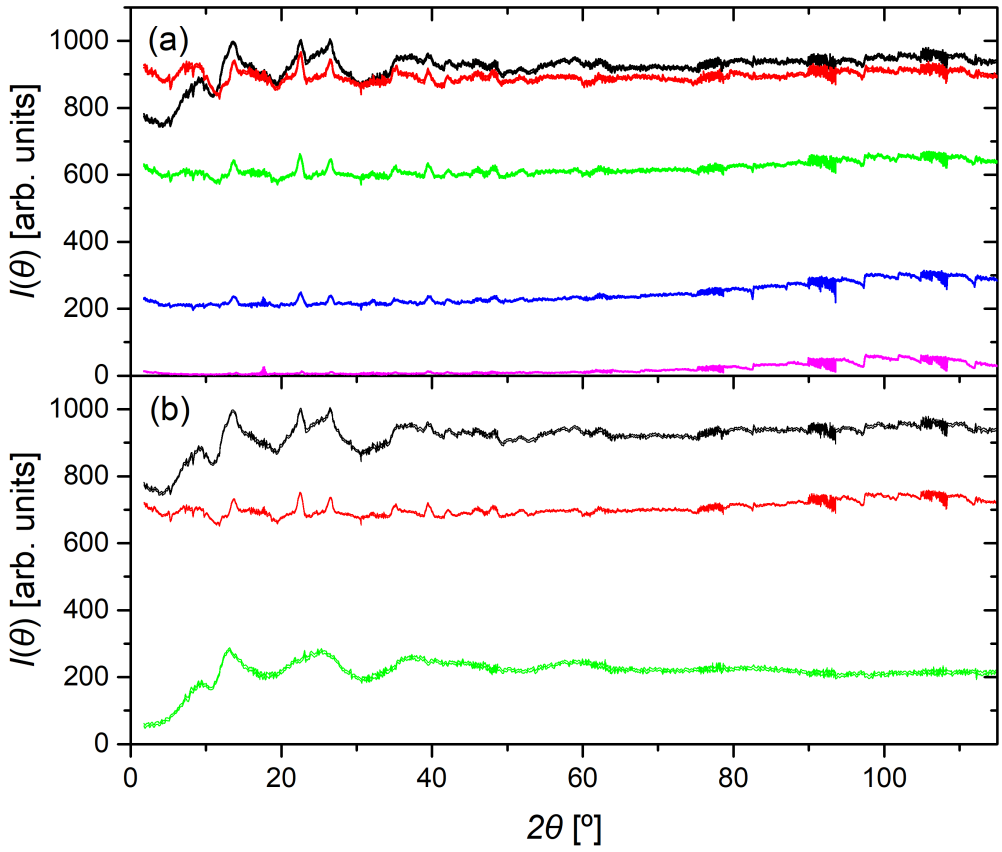

Figure 5.1: The data correction procedure used for the $CaSiO_3$ sample, measured at 3 GPa by the D4c diffractometer using the Paris-Edinburgh press in conjunction with ST BN anvils. Plot (a) shows the measured intensities for the sample inside its container $I^{\mathrm{E}}_{\mathrm{SC}}(\theta)$ (black), an empty uncompressed gasket $I^{\mathrm{E}}_{\mathrm{C1}}(\theta)$ (red), an empty uncompressed gasket that was previously compressed to 4.7 GPa $I^{\mathrm{E}}_{\mathrm{C2}}(\theta)$ (green), an empty gasket measured at 4.4 GPa that was previously compressed to 8.2 GPa $I^{\mathrm{E}}_{\mathrm{C3}}(\theta)$ (blue), and the empty anvils with no gasket or sample present $I^{\mathrm{E}}_{\mathrm{a}}(\theta)$ (magenta). Plot (b) shows the measured intensity for the sample inside its container $I^{\mathrm{E}}_{\mathrm{SC}}(\theta)$ (black); the background intensity $I^{\mathrm{E}}_{\mathrm{B}}(\theta)$ calculated using equation 3.15 with coefficients $x_{\mathrm{a}} = 0.2$, $x_{\mathrm{C1}} = 0.3$ and $x_{\mathrm{C2}} = 0.7$; and the background and container corrected sample intensity $I^{\mathrm{E*}}_{\mathrm{SC}}(\theta)$ calculated using equation 3.14.

sample, and of an empty $Ti_{0.676}Zi_{0.324}$ gasket at ambient conditions, in order to perform the data correction procedures described in section 3.4. As for the D4c experiment, the ratio of scattered intensities taken from different times was taken over the course of a measurement to check for measurement consistency.

The ideal mass of a double toroid (DT) pellet of $CaSiO_3$ was calculated to be 0.09816(1) g. In order to produce a DT pellet, a single piece of $CaSiO_3$ glass was ground to the appropriate shape using a Dremel multitool in conjunction with an aluminium oxide grinding stone. The ideal mass of a vanadium double toroid pellet is 0.20232(1) g. To make a vanadium pellet, the appropriate mass of vanadium foil was carefully folded and placed into the die designed to produce the shape of a DT pellet, and then compressed in stages. The final pellet and gasket masses are shown in Table 5.4.

Approximately four days after the experiment a measurement was made of the $CaSiO_3$ glass recovered from 17.5(5) GPa, inside a vanadium can using the PE press. Due to the absence of the press assembly, the five additional detector banks were used: three of which are high angle ($100^\circ \leq 2\theta \leq 160^\circ$), and two of which are low angle ($20^\circ \leq 2\theta \leq 50^\circ$). The additional detector banks increase the available measurement range of Q to 1.1 $\text{Å}^{-1} \leq Q \leq 27.5$ Å^{-1}, using this setup. In order to correct the data additional measurements were made of the same vanadium can empty, and the the belljar with no vanadium can or sample.

Applied Load [tns]	Sample Pressure [GPa]	$CaSiO_3$	Vanadium
2.0	Ambient	✓	✓
75.0	8.7(5)	✓	✓
98.0	10.9(5)	✓	✓
120.0	14.4(5)	✓	✓
140.0	17.5(5)	✓	✓

Table 5.3: The applied load and corresponding sample pressures for the PEARL experiment on $CaSiO_3$ glass. The sample pressures were deduced from the calibration curve shown in Figure 3.8.

Sample	Pellet mass [g]	Ti-Zr gasket mass [g]
$CaSiO_3$	0.1004(1)	1.0791(1)
Vanadium	0.2060(1)	1.0824(1)

Table 5.4: The final pellet and Ti-Zr gasket masses used for the PEARL neutron diffraction experiment.

5.3.4 Equation of State and Density Measurements

The mass density of the $CaSiO_3$ glass was measured using a helium pycnometer to be $\rho = 2.9111(28)$ g cm^{-3}. This yielded an ambient atomic number density value of $n_0 = 0.0755(1)$ Å^{-3}. The pressure-volume equation of state of $CaSiO_3$ glass has been calculated by molecular dynamics simulations performed by Shimoda *et al.* [76]. A third order Birch-Murnaghan equation of state was fitted to the data by K. Pizzey, University of Bath which yielded fit parameters of $B_0 = 51.96(2.18)$ GPa and $B_0' = 2.68(36)$ [27]. The equation of state and fit to the data is plotted in Figure 5.2, and the atomic number densities obtained for each pressure point are presented in Table 5.5. The Birch-Murnaghan equation of state is described in further detail in Chapter 2.

After the D4c experiment, the density of the sample was remeasured using a helium pycnometer to be $\rho = 3.04(10)$ g cm^{-3}. This corresponded to an atomic number density of $n_0 = 0.0788$ Å^{-3}, and represents an approximate 5% increase from the ambient value.

5.3.5 Molecular Dynamics Simulations

The molecular dynamics simulations accompanying this work were developed by Yoshiki Ishii and Mathieu Salanne [75], using an aspherical ion model (AIM) [77, 78]. The calculations were performed on systems containing 300 oxygen atoms, 100 silicon atoms and 100 magnesium or calcium atoms in the NPT ensemble using a timestep of 1.0 fs, where N is the number of particles, P is the pressure, and T is the temperature. The starting configuration was generated using an initially random distribution of atoms using a polarizable ion model. The AIM was then used to equilibrate the liquid state at 3000 K and ambient pressure. The pressure was then increased in steps of 0.5 GPa to 17.5 GPa, over a timescale of 7.0 ns. The liquid was quenched at the following pressures: 0.0 (Ambient), 2.0, 4.0, 6.5, 8.5, 9.5, 11.0, 12.5, 14.5, 16.0 and 17.5 GPa.

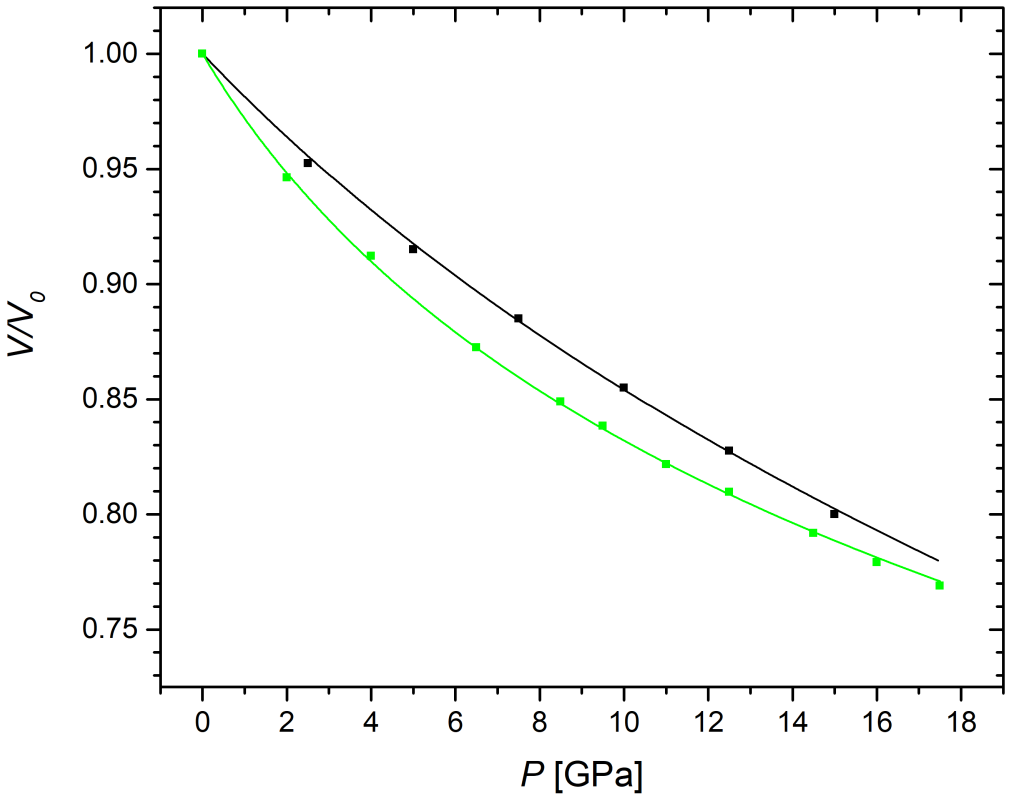

Figure 5.2: Pressure-volume equations of state for glassy $CaSiO_3$. The black squares show results from molecular dynamics simulations by Shimoda *et al.* [76], and the green squares show results from the and the molecular dynamics simulations accompanying this work [75]. The solid curves are third order Birch-Murnaghan fits to the data.

Pressure [GPa]	Compression $\frac{V}{V_0}$	Atomic Number Density [Å^{-3}]
Ambient	1.00	0.07550(10)
3.0(5)	0.948(1)	0.07964(11)
3.9(5)	0.934(1)	0.08084(12)
5.4(5)	0.912(1)	0.08279(12)
7.1(5)	0.889(1)	0.08493(12)
8.2(5)	0.875(1)	0.08629(12)
8.7(5)	0.869(1)	0.08688(13)
10.9(5)	0.844(1)	0.08945(13)
14.4(5)	0.808(1)	0.09344(14)
17.5(5)	0.780(1)	0.09679(14)

Table 5.5: The compression and atomic number densities of the pressure points for the D4c and PEARL neutron diffraction experiments on $CaSiO_3$ glass.

At each pressure point, the liquid was quenched by decreasing the temperature from 3000 K to 300 K in steps of 100-500 K over a total timescale of 3.5 ns. At 8.5 and 17.5 GPa, the pressure was returned in steps of 0.5 GPa to ambient conditions over a timescale of 7.0 or 3.5 ns, respectively.

The procedure was repeated for eight different configurations of the liquid that was equilibrated at 3000 K and ambient pressure, hence eight independent glass configurations were studied. This allowed for a statistical analysis of structural parameters such as coordination numbers and the connectivity of network formers. The bridging state of the oxygen atoms as defined by the O-Si coordination number, was also investigated. An oxygen atom bonded to zero, one, two or three silicon atoms is referred to as a free-oxygen, non-bridging oxygen (NBO), bridging oxygen (BO) or triple-bridging oxygen (TBO), respectively. The coordination numbers $\bar{n}_\alpha^\beta$ were calculated by integrating the over the first peak of the corresponding partial pair-distribution function $g_{\alpha\beta}(r)$, respectively.

The partial structure factors $S_{\alpha\beta}(Q)$ were calculated from the calculated $g_{\alpha\beta}(r)$ functions for $Q \geq 4$ Å^{-1} using the Fourier transform relation

$$S_{\alpha\beta}(Q) = 1 + \frac{4\pi\rho}{Q}\int_0^\infty r\sin(Qr)[g_{\alpha\beta}(r) - 1]dr, \tag{5.14}$$

where ρ is the average atomic number density. In order to avoid the introduction of

Fourier transform artefacts, for $Q < 4$ Å^{-1} $S_{\alpha\beta}(Q)$ was calculated using

$$S_{\alpha\beta}(Q) = 1 + \frac{[S^{\mathrm{AL}}_{\alpha\beta}(Q) - \delta_{\alpha\beta}]}{\sqrt{c_\alpha c_\beta}}, \tag{5.15}$$

where $\delta_{\alpha\beta}$ is the Kronecker delta. The Ashcroft-Langreth [79] partial structure factor $S^{\mathrm{AL}}_{\alpha\beta}(Q)$ is calculated using

$$S^{\mathrm{AL}}_{\alpha\beta}(Q) = \frac{1}{\sqrt{N_\alpha N_\beta}} \Big\langle \sum_i \sum_j \exp(i\mathbf{Q}\cdot\mathbf{r}_{i,j}) \Big\rangle - \sqrt{N_\alpha N_\beta}\delta_{\mathbf{Q},0}, \tag{5.16}$$

where N_α denotes the number of ions of chemical species α, $\delta_{\mathbf{Q},0}$ is the Kronecker delta and the triangular brackets denote a thermal average.

5.4 Results

Results for $CaSiO_3$ glass originating from the PEARL experiment were originally presented in [27]. For the present work, all the raw datasets were re-analysed, and altered conclusions were drawn. The Si-O coordination number was previously found to be $\bar{n}^{O}_{Si}$ $\sim$ 4.3 at 17.5 GPa. In the present work, the Si-O coordination number was determined to be $\bar{n}^{O}_{Si} = 4.12(10)$ at 17.5 GPa.

5.4.1 Total Structure Factors

Figure 5.3 shows the pressure dependence of the total structure factors $S(Q)$ obtained for $CaSiO_3$ glass. The plot compares the neutron diffraction results to the molecular dynamics simulations used in the present work at similar pressures [75]. At ambient pressure there is good overall agreement between the experiment and simulation results. There is a clearly defined first-sharp diffraction peak (FSDP) at $\sim$2.0 Å^{-1}, followed by a principal peak at $\sim$2.85 Å^{-1}. There is a small disagreement in the FSDP position between the experimental and simulation results. There are occasional sharp peaks in the simulation results at low values of Q which are statistical in nature.

As pressure is increased, the FSDP position shifts to higher Q values until it becomes a low Q shoulder of the principal peak in the D4c data at 5.4(5) GPa. This behaviour is accompanied by a sharpening and increasing amplitude of the principal peak. The experimental and simulation results remain mostly in agreement, however the FSDP positions begin to diverge at high pressures. At the highest pressures, the principal peak becomes even more dominant and continues to shift to higher values of Q.

Figure 5.4 compares the total structure factors $S(Q)$ measured using D4c for $CaSiO_3$ glass under ambient conditions in a vanadium can, immediately after recovery from 8.2(5) GPa, and using PEARL with a vanadium can $\sim$4 days after recovery from 17.5(5) GPa. The plot compares the measured total structure factors with those obtained from the molecular dynamics simulations [75] for $CaSiO_3$ glass recovered from either 8.5 GPa or 17.5 GPa. The recovered D4c dataset was analysed using an atomic number density of $\rho_0 = 0.083$ Å^{-3}, which corresponds to the measured mass density of the recovered sample. The recovered PEARL dataset was analysed using an atomic number density of $\rho_0 = 0.0805$ Å^{-3}, which was estimated from the position of the FSDP of the recovered dataset. The D4c and PEARL recovered datasets both show a clear

shift in the FSDP position to approximately 2.3 Å^{-1} or 2.1 Å^{-1}, respectively. Both these values are intermediate between the ambient value of ∼2.03 Å^{-1}, and the value of ∼2.43 Å^{-1} measured at 8.2(5) GPa. Apart from the region of the FSDP, the ambient and recovered datasets are in good agreement. The total structure factors obtained from the molecular dynamics simulations show good agreement with the experimental results.

The FSDP and principal peak positions are plotted in Figure 5.5, and show a large shift with pressure in the FSDP position to higher Q values, which is mostly complete by 8.2(5) GPa. The higher pressure results from PEARL show that the FSDP position appears to remain constant at higher pressures. The principal peak position shows a continued but gradual increase between ambient conditions and the maximum pressure. The MD simulations, and principal peak positions show a generally good agreement with the experimental results, however at higher pressures the FSDP positions from experiment and simulation diverge.

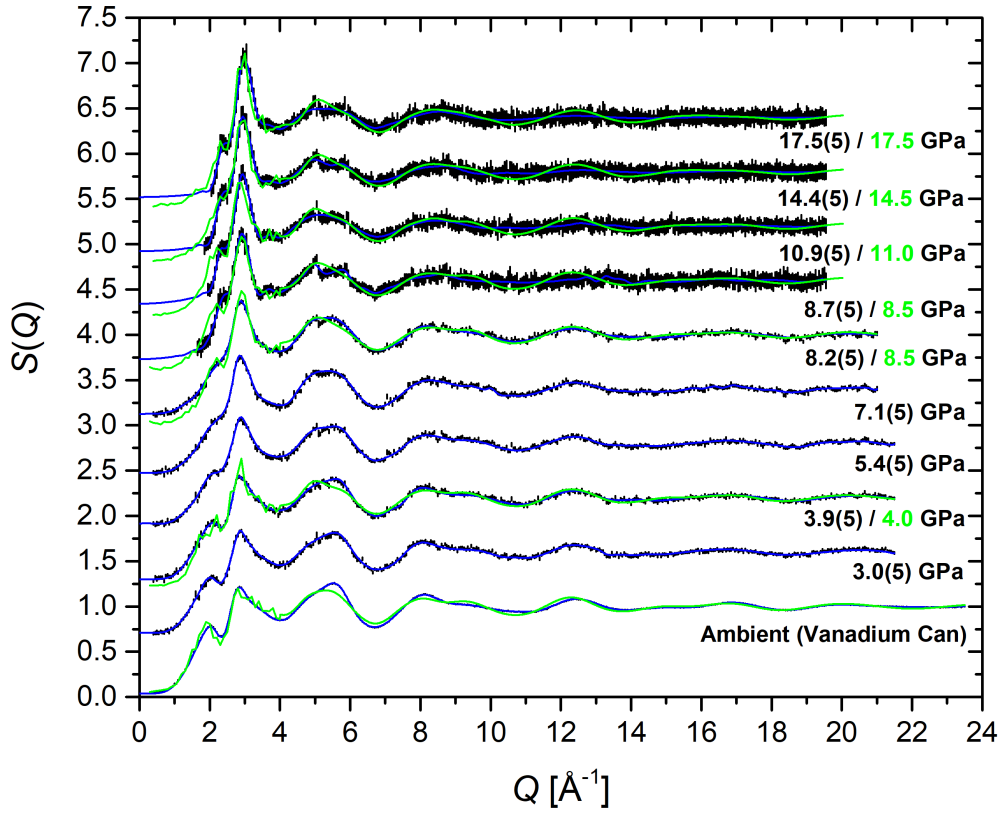

Figure 5.3: The pressure dependence of the neutron total structure factors $S(Q)$ for $CaSiO_3$ glass, as measured using the D4c (ambient to 8.2(5) GPa) or PEARL (8.7(5) to 17.5(5) GPa) diffractometers. The vertical bars give the statistical errors on the measured datasets, and the blue curves show the back Fourier transforms of spline fits to the experimental data. The results are compared to those obtained from molecular dynamics simulations at similar pressures (green curves) [75]. For the datasets originating from PEARL, the region Q $\leq$1.55 $Å^{-1}$ is inaccessible and the curves in this region correspond to fitted Lorentzian functions. The high pressure datasets have been offset vertically for clarity of presentation.

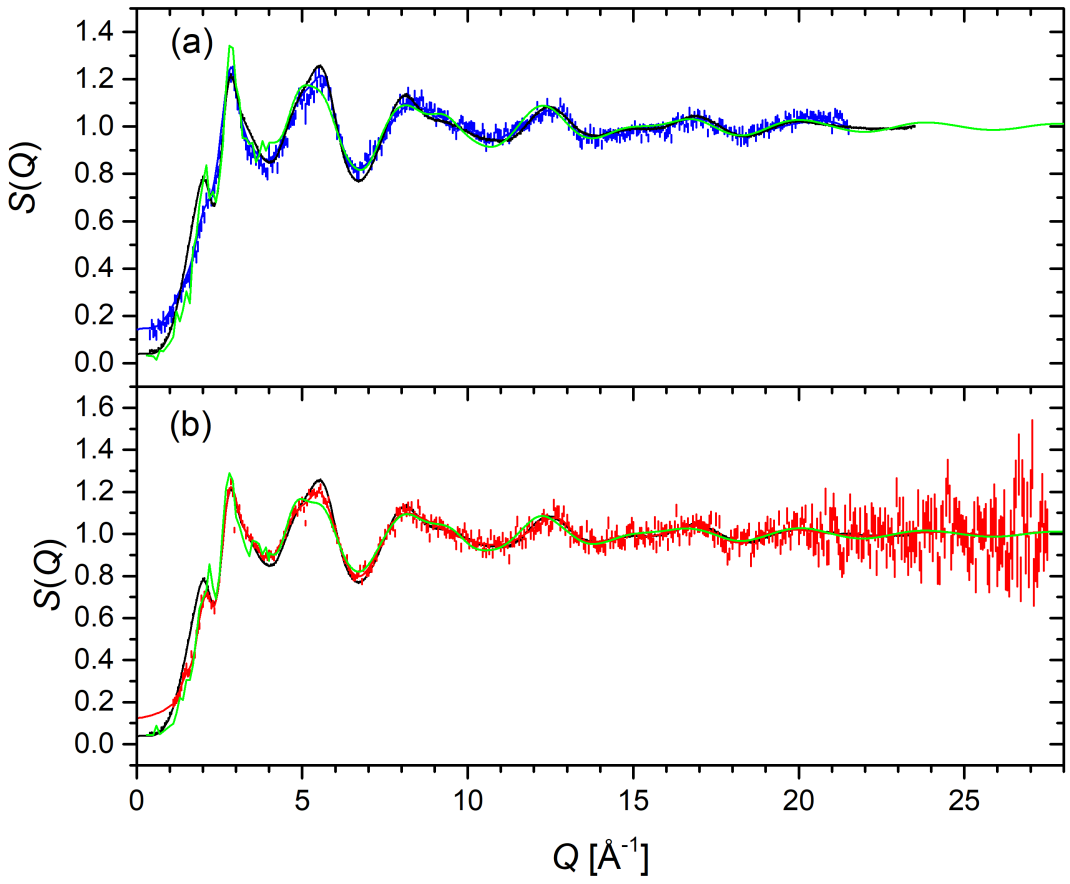

Figure 5.4: The total structure factors $S(Q)$ for glassy $CaSiO_3$ recovered from compression, as measured with neutron diffraction or molecular dynamics simulations [75]. Plot (a) shows the total structure factors measured with the D4c diffractometer for the as-prepared sample using a vanadium can (solid black curve), immediately after recovery to ambient from 8.2(5) GPa (solid blue curve), and from the molecular dynamics simulations immediately after recovery from 8.5 GPa (solid green curve). Plot (b) shows the total structure factors measured with the D4c diffractometer for the as-prepared sample using a vanadium can (solid black curve), approximately 4 days after recovery to ambient conditions from 17.5(5) GPa measured using the PEARL diffractometer with a vanadium can (solid red line), and from the molecular dynamics simulations immediately after recovery from 17.5 GPa (solid green curve).

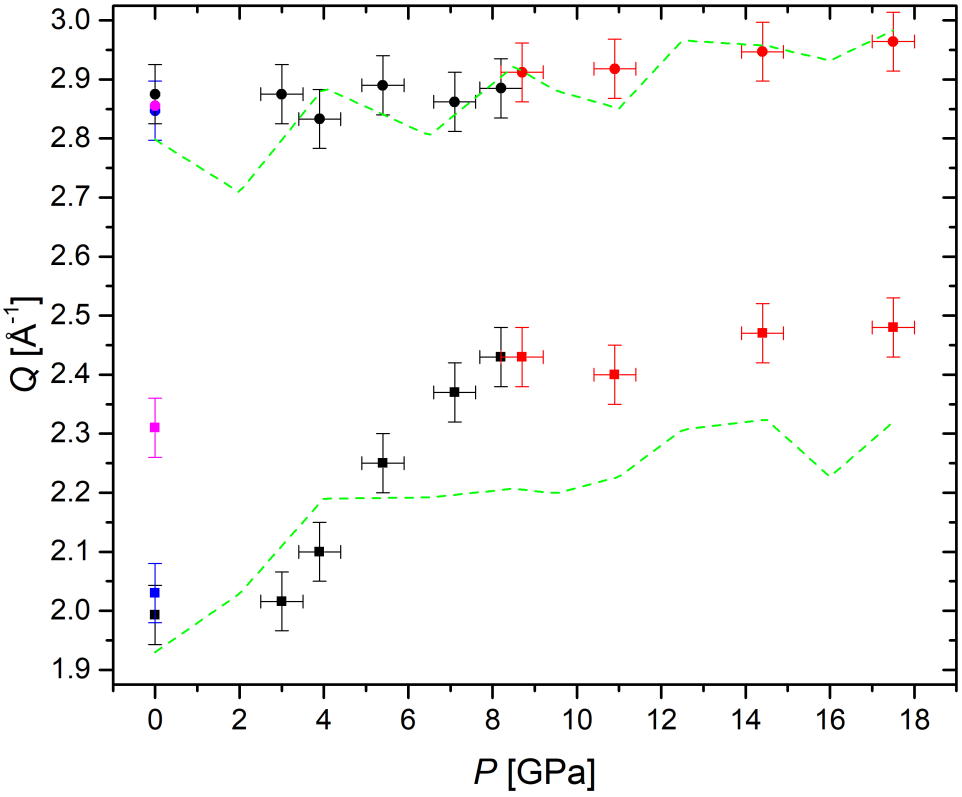

Figure 5.5: The pressure dependence of the first-sharp diffraction peak position (squares) and the principal peak position (circles) for glassy $CaSiO_3$. The black and red datapoints show results from the D4c and PEARL experiments, respectively. The blue datapoints at ambient pressure were obtained from the vanadium can measurement on D4c, and the magenta datapoints show the result for $CaSiO_3$ immediately after recovery from 8.2(5) GPa, as measured on the D4c diffractometer. The green dashed lines show the results from the molecular dynamics simulations [75].

5.4.2 Pair-Distribution Functions

Figure 5.6 shows the pressure dependence of the total pair-distribution functions $G'(r)$ measured for $CaSiO_3$ glass. The reciprocal space datasets were Fourier transformed using a step modification function as shown in Equation 5.2. The ambient vanadium can measurement was Fourier transformed using $Q_{max} = 23.5$ Å^{-1}. The PE press D4c measurements were Fourier transformed using $Q_{max} = 21.5$ Å^{-1} in the range ambient $\leq P \leq 5.4(5)$ GPa, and $Q_{max} = 21.0$ Å^{-1} in the range $5.4(5)$ GPa $\leq P \leq 8.2(5)$ GPa. The PEARL datasets were Fourier transformed using $Q_{max} = 19.55$ Å^{-1}. The experimental datasets are compared to the molecular dynamics simulation results at similar pressures.

At ambient conditions, the first peak is associated with Si-O correlations [21] and is well defined at $r_{SiO} = 1.615(20)$ Å. It is symmetric, indicating that the bond length distribution is centered around the peak maximum. The second real space peak is associated with Ca-O correlations [21], and is located at $r_{CaO} = 2.324(20)$ Å. The third real space peak is primarily associated with O-O correlations, and is located at $r_{OO} = 2.627(20)$ Å. The second and third peaks of $G'(r)$ overlap, and cannot be separately distinguished in the datasets originating from PEARL due to the reduced real space resolution of the instrument. A detailed discussion of the disparity between the $G'(r)$ functions originating from D4c and PEARL is provided in Chapter 3. Due to this overlap of the partial pair-distribution functions, it is not possible to accurately obtain the Ca-O and O-O coordination numbers from the experimental results, however the Si-O coordination number can be accurately obtained.

In the results from D4c, as pressure is increased the Si-O peak decreases in amplitude and becomes broader in nature. The Ca-O peak decreases in prominence and gradually becomes less distinguishable from the O-O peak. The small peak observed in the D4c results at approximately ∼2 Å is a Fourier transform artefact which originates from the fact that the reciprocal space data has been Fourier transformed using the modification function given in Equation 5.2.

Figure 5.7 compares the total pair-distribution functions $G'(r)$ measured using D4c for $CaSiO_3$ glass under ambient conditions in a vanadium can, immediately after recovery from 8.2(5) GPa, and using PEARL with a vanadium can ∼4 days after recovery from 17.5(5) GPa. The plot also compares the measured $G'(r)$ functions with those obtained from the molecular dynamics simulations [75] for $CaSiO_3$ glass recovered from either 8.5 GPa or 17.5 GPa. The datasets were obtained by Fourier transforming the

respective datasets in Figure 5.4. In (a) the datasets were Fourier transformed using a cutoff $Q_{\max} = 21.5$ Å^{-1}, and in (b) the datasets were Fourier transformed using a cutoff $Q_{\max} = 23.5$ Å^{-1}, this was in order to remove any discrepancies that could result from using different cutoff $Q_{\max}$ values. The mean Si-O bond distance and coordination number obtained from the recovered datasets remain within the experimental uncertainty of their respective ambient values. However, in both the recovered datasets the position of the Ca-O peak has slightly decreased from its ambient value of $r_{\mathrm{CaO}} = 2.324(20)$ Å to a value of $r_{\mathrm{CaO}} \sim 2.25$ Å.

Figure 5.8 shows the pressure dependence of the mean Si-O coordination number and bond distance. The bond distances have been determined both by measurement of the maximum peak position, and by calculating the weighted peak position by using Equation 5.4. The D4c coordination numbers have been obtained by using the RDF-Genie program to fit a Gaussian function convoluted with a sinc function to the first and second peaks, the latter of which serves to constrain the first peak. The results are compared to the MD simulation results shown by the green dashed lines. The fits are displayed for all pressure points in Figures 5.11 to 5.17. The PEARL Si-O coordination numbers were calculated using Equation 5.5.

The mean Si-O bond distance remains at its ambient value of $r_{\mathrm{SiO}} = 1.615(20)$ Å within the experimental uncertainty, across the measured pressure range. The calculated weighted peak position shows that the Si-O peak remains essentially symmetric throughout the measured pressure range from the D4c datasets, however the weighted peak positions calculated from the PEARL datasets show the peak to be more asymmetric, with the higher r side dominating. The mean Si-O coordination number remains constant at its ambient pressure value of $\bar{n}^{\mathrm{O}}_{\mathrm{Si}} = 4.00(5)$ at pressures up to 14.4(5) GPa. At the maximum pressure of 17.5(5) GPa, the mean Si-O coordination number is $\bar{n}^{\mathrm{O}}_{\mathrm{Si}} = 4.12(10)$, which indicates a small increase from the ambient value. The Si-O bond distance obtained from simulation is consistently longer ($\sim$1.64 Å) than that obtained from experiment, and remains approximately constant throughout the measured pressure range. However, the mean Si-O coordination number obtained from simulation gradually starts to increase at $\sim$6 GPa, and reaches a maximum value of $\bar{n}^{\mathrm{O}}_{\mathrm{Si}} = 4.3$ at 17.5 GPa.

Figure 5.9 shows the pressure dependence of the mean Ca-O coordination number obtained from molecular dynamics simulations [75], and the mean Ca-O bond distance

obtained from both the D4c neutron diffraction experiment and simulation. All bond distances were obtained by measurement of the maximum peak position of the second peak of $G'(r)$. Due to the reduced real space resolution available from the PEARL diffractometer, this second peak is not distinguishable from the third peak of $G'(r)$, it is therefore not possible to obtain an value of the Ca-O bond distance for the higher pressure datasets originating from PEARL.

The Ca-O bond distance measured using D4c increases slightly from an ambient value of $r_{\mathrm{CaO}} = 2.260(20)$ Å, to a value of $r_{\mathrm{CaO}} = 2.335(20)$ Å at 8.2(5) GPa. In contrast, the Ca-O bond distance obtained from simulation remains approximately constant across the studied pressure range at $r_{\mathrm{CaO}} \sim 2.27$ Å. There is a small disagreement between the Ca-O bond distance measured for $CaSiO_3$ inside a vanadium can before compression, and $CaSiO_3$ in the Paris-Edinburgh press at ambient conditions. This discrepancy may originate from the method of sample preparation: in order to make a single toroid pellet the $CaSiO_3$ powder was compressed under a pressure of approximately 1 GPa. Hence, the $CaSiO_3$ pellet used in the D4c experiment may have already been partially densified. The mean Ca-O coordination number obtained from simulation increases across the measured pressure range from an ambient value of $\bar{n}^{\mathrm{O}}_{\mathrm{Ca}} = 6.03$ to a value of $\bar{n}^{\mathrm{O}}_{\mathrm{Ca}} = 7.37$ at 17.5 GPa.

Figure 5.10 shows the six partial pair-correlations of $CaSiO_3$ glass obtained from molecular dynamics simulations, at ambient conditions and at 17.5 GPa. The results show that the first peak corresponds exclusively to Si-O correlations, whilst the second peak consists on an overlap of Ca-O and O-O correlations. The MD simulations predict that the Ca-O partial-correlation peak is highly asymmetric with a high r shoulder, which suggests that Ca-O bond distances are present that are significantly longer than the Ca-O peak position of approximately 2.3 Å.

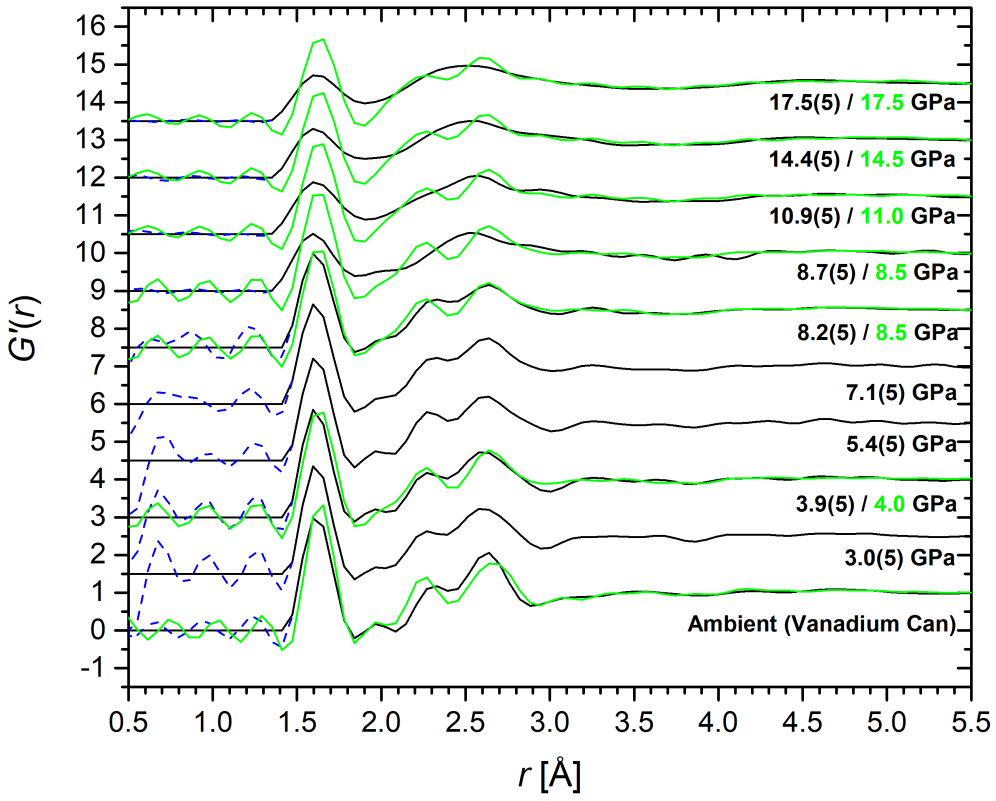

Figure 5.6: The total pair-distribution functions $G'(r)$ for $CaSiO_3$ glass (solid black curves), obtained by Fourier transforming the $S(Q)$ functions shown in Figure 5.3. The dashed blue curves show the unphysical Fourier transform artefacts at distances smaller than the closest approach between two atoms. The results are compared to those obtained from the molecular dynamics simulations at similar pressures (green curves) [75]. The high pressure datasets have been offset vertically for clarity of presentation.

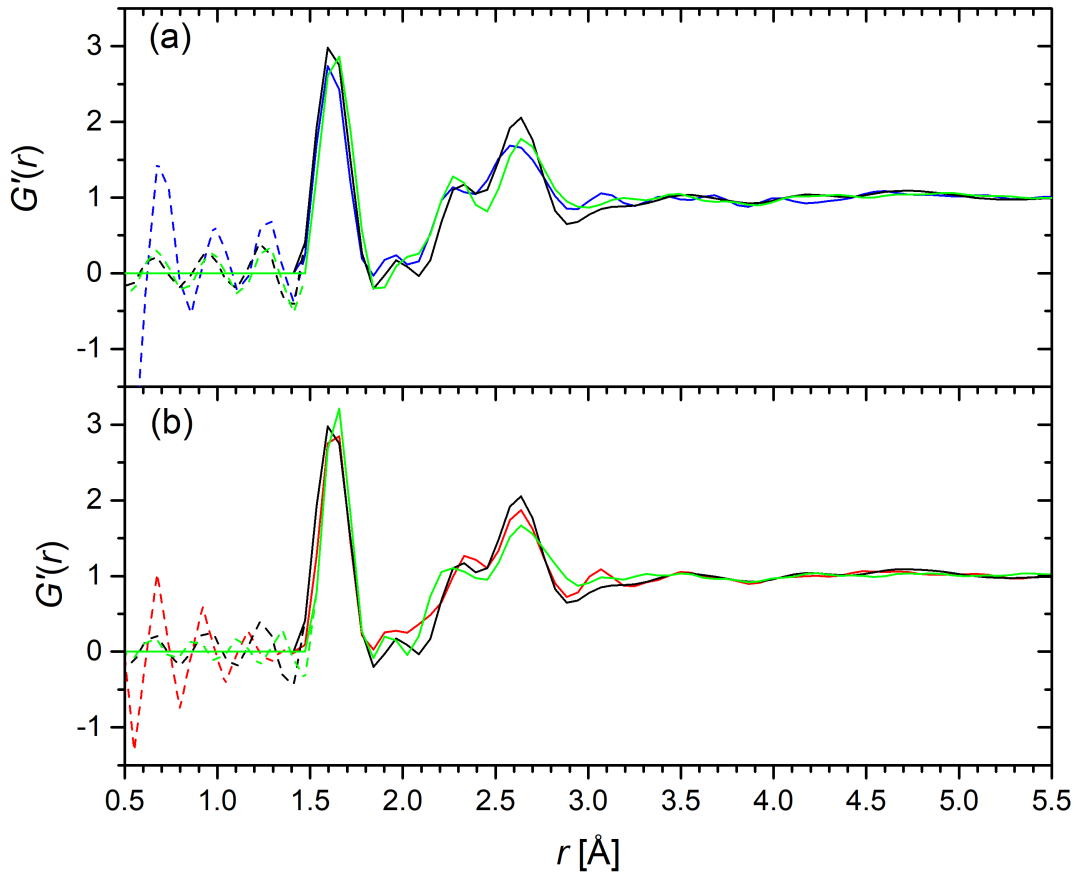

Figure 5.7: The total pair-distribution functions $G'(r)$ for glassy $CaSiO_3$ recovered from compression, as measured with neutron diffraction or molecular dynamics simulations [75]. Plot (a) shows the $G'(r)$ functions measured with the D4c diffractometer for the as-prepared sample using a vanadium can (solid black curve), immediately after recovery to ambient from 8.2(5) GPa (solid blue curve), and from the molecular dynamics simulations immediately after recovery from 8.5 GPa (solid green curve). Plot (b) shows the $G'(r)$ functions measured with the D4c diffractometer for the as-prepared sample using a vanadium can (solid black curve), measured immediately after recovery to ambient conditions from 17.5(5) GPa using the PEARL diffractometer with a vanadium can (solid red line), and from the molecular dynamics simulations immediately after recovery from 17.5 GPa (solid green curve). The dashed lines show unphysical Fourier transform artefacts at distances smaller than the closest approach between two atoms.

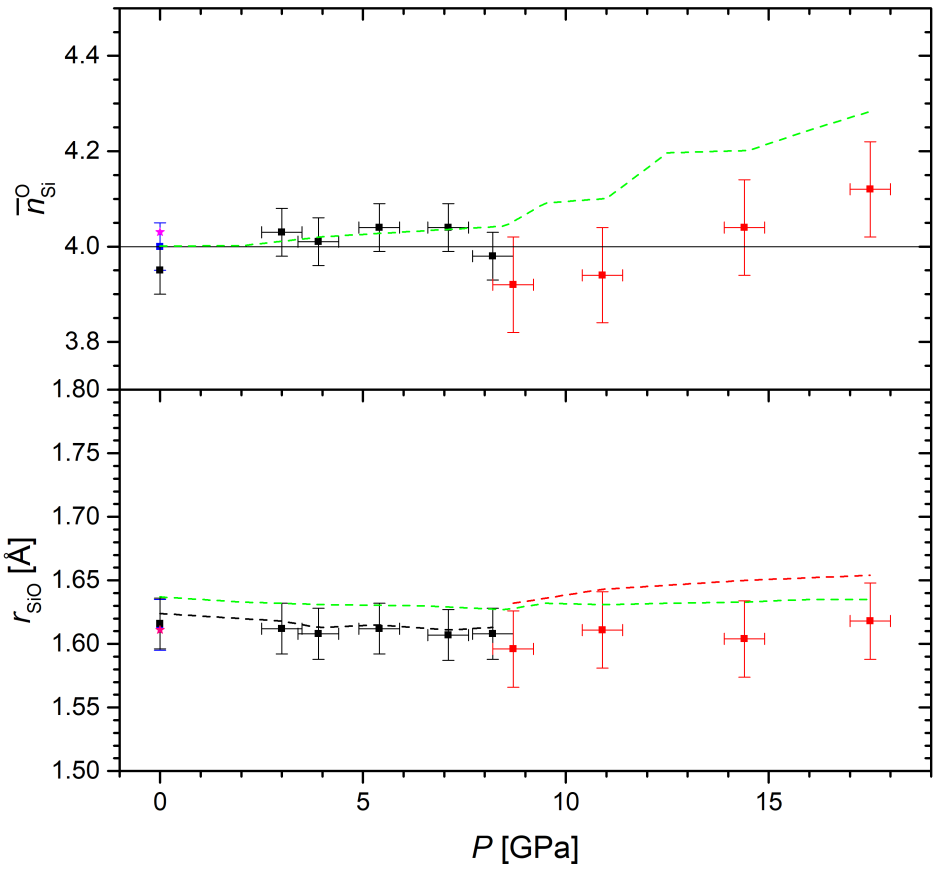

Figure 5.8: The pressure dependence of the (a) mean Si-O coordination number $\bar{n}^{\mathrm{O}}_{\mathrm{Si}}$, and (b) mean Si-O bond distance r_{SiO}, obtained for $CaSiO_3$ glass using neutron diffraction. The black markers show results from the D4c experiment, the red markers show results from the PEARL experiment, and the blue markers show results from the ambient vanadium can measurement on D4c. The magenta star shows the result for the sample measured immediately after recovery from 8.2(5) GPa on D4c. The green dashed lines show results from the molecular dynamics simulations [75]. The black and red dashed lines show the weighted peak positions calculated using Equation 5.4 for the D4c and PEARL datasets, respectively.

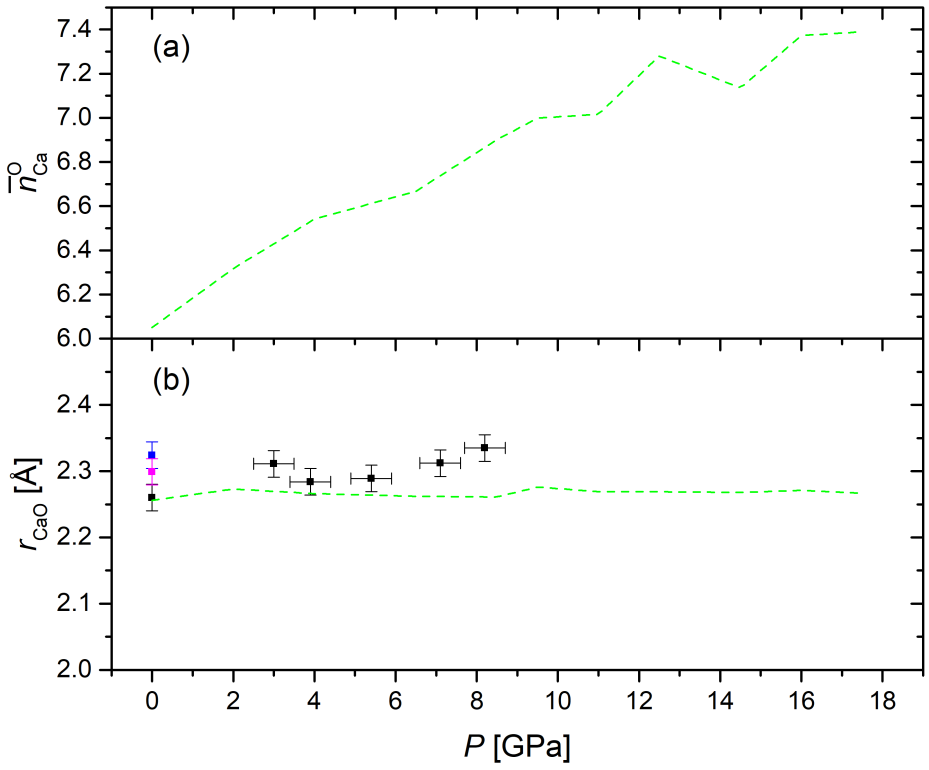

Figure 5.9: The pressure dependence of the (a) mean Ca-O coordination number $\bar{n}^{O}_{Ca}$, and (b) mean Ca-O bond distance r_{CaO}, obtained for $CaSiO_3$ glass using neutron diffraction. The black markers show results from the D4c experiment, and the blue marker shows the result from the ambient vanadium can measurement on D4c. The magenta star shows the result for the sample measured immediately after recovery from 8.2(5) GPa on D4c. The green dashed lines show results from the molecular dynamics simulations [75].

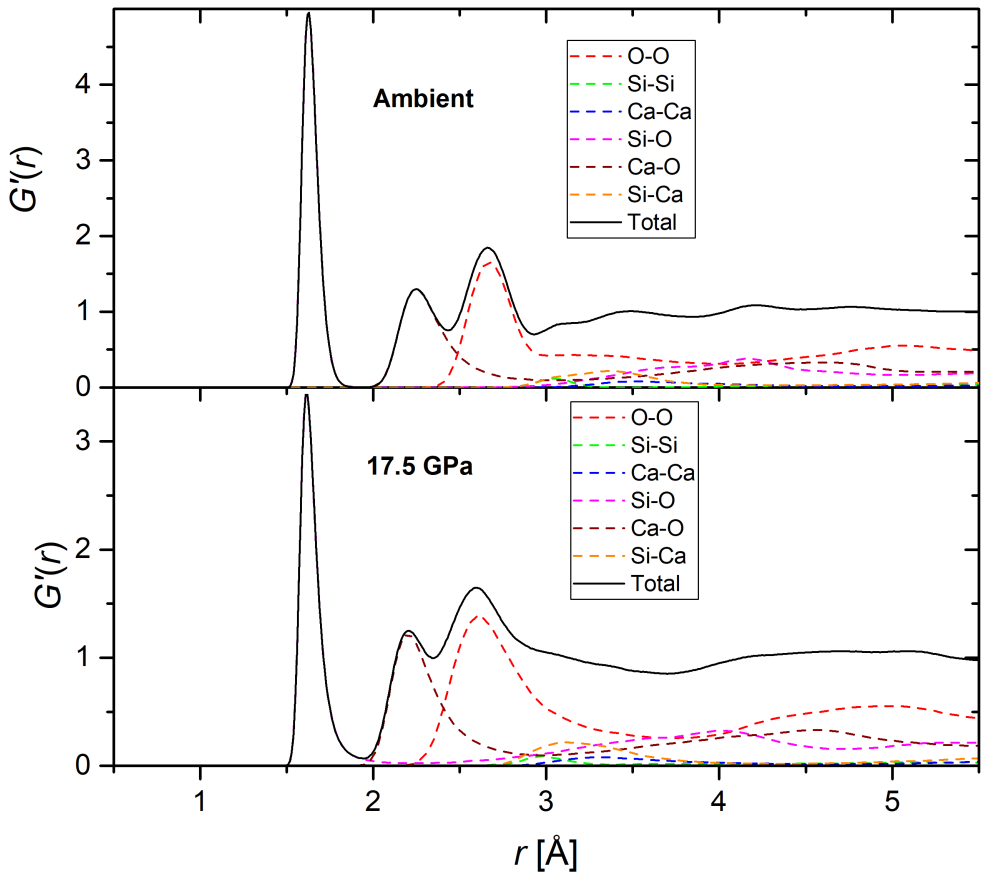

Figure 5.10: The six partial pair-correlations functions comprising $CaSiO_3$ glass obtained from the molecular dynamics simulations accompanying this study [75], weighted for neutron diffraction. Also shown is the total pair-distribution function $G'(r)$, which is the sum of all partial $g_{\alpha\beta}(r)$ functions. The results are shown for ambient conditions and 17.5 GPa, which corresponds to the maximum pressure used in the neutron diffraction experiments.

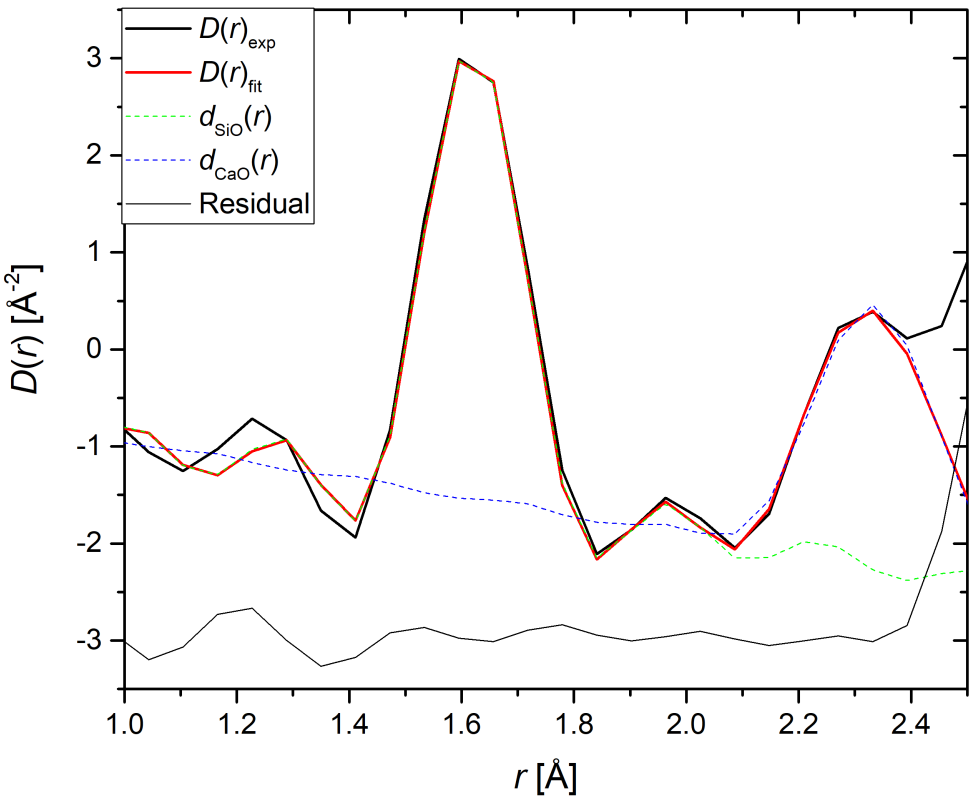

Figure 5.11: The density correlation function and fits obtained for $CaSiO_3$ glass at ambient conditions, measured in a vanadium can on the D4c diffractometer. The solid black line is the measured $D(r)_{\mathrm{exp}}$ function, which is fitted with two Gaussians convoluted with a sinc function using RDFGenie which combine to give the fit $D(r)_{\mathrm{fit}}$ (solid red curve). The dashed green and blue lines correspond to Si-O and Ca-O correlations, respectively. The fit gives $R_\chi = 0.087$ for the range 1.20 - 2.10 Å.

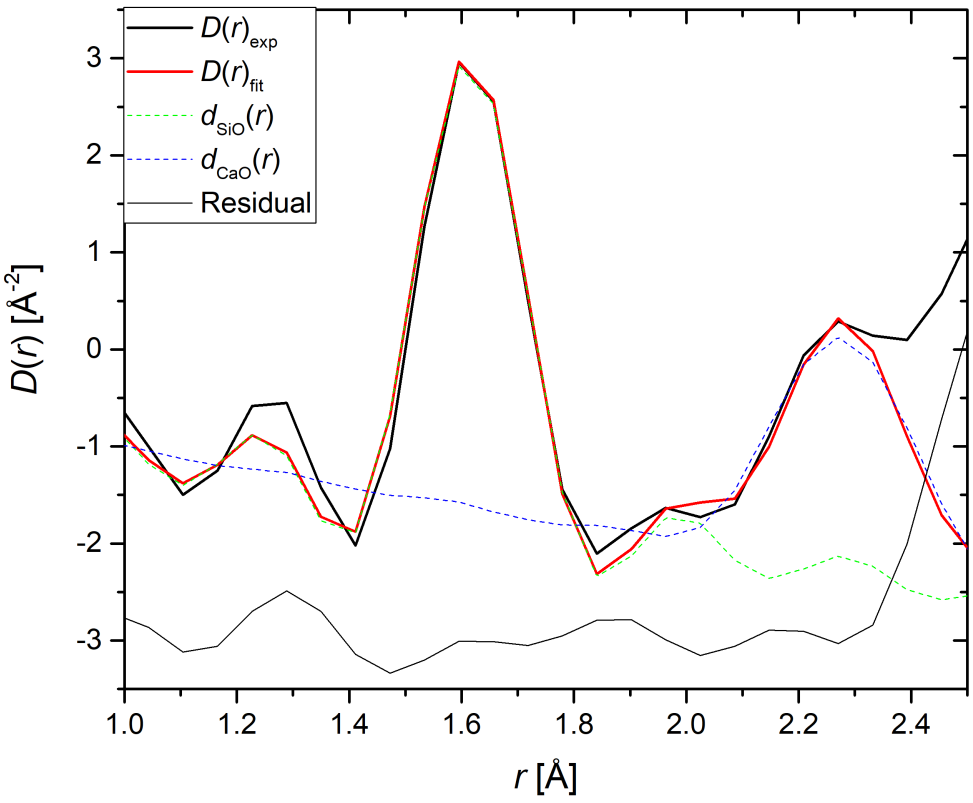

Figure 5.12: The density correlation function and fits obtained for $CaSiO_3$ glass at 3.0(5) GPa, measured on the D4c diffractometer. The solid black line is the measured $D(r)_{\mathrm{exp}}$ function, which is fitted with two Gaussians convoluted with a sinc function using RDFGenie which combine to give the fit $D(r)_{\mathrm{fit}}$ (solid red curve). The dashed green and blue lines correspond to Si-O and Ca-O correlations, respectively. The fit gives $R_\chi = 0.129$ for the range 1.20 - 2.10 Å.

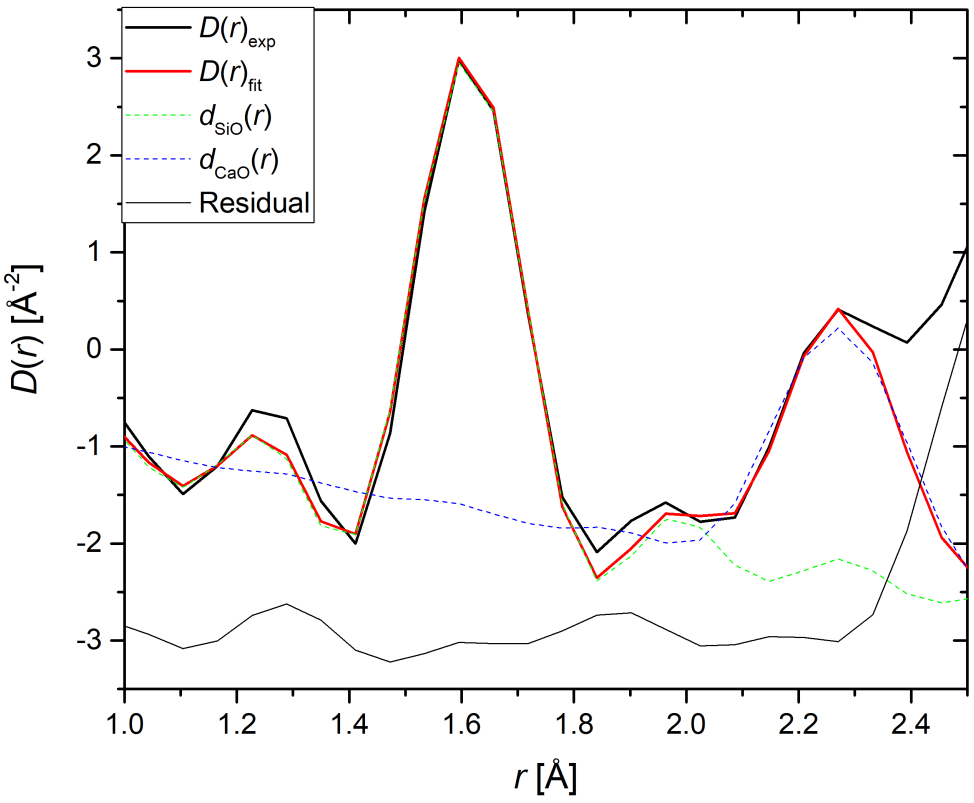

Figure 5.13: The density correlation function and fits obtained for $CaSiO_3$ glass at 3.9(5) GPa, measured on the D4c diffractometer. The solid black line is the measured $D(r)_{\mathrm{exp}}$ function, which is fitted with two Gaussians convoluted with a sinc function using RDFGenie which combine to give the fit $D(r)_{\mathrm{fit}}$ (solid red curve). The dashed green and blue lines correspond to Si-O and Ca-O correlations, respectively. The fit gives $R_\chi = 0.107$ for the range 1.20 - 2.10 Å.

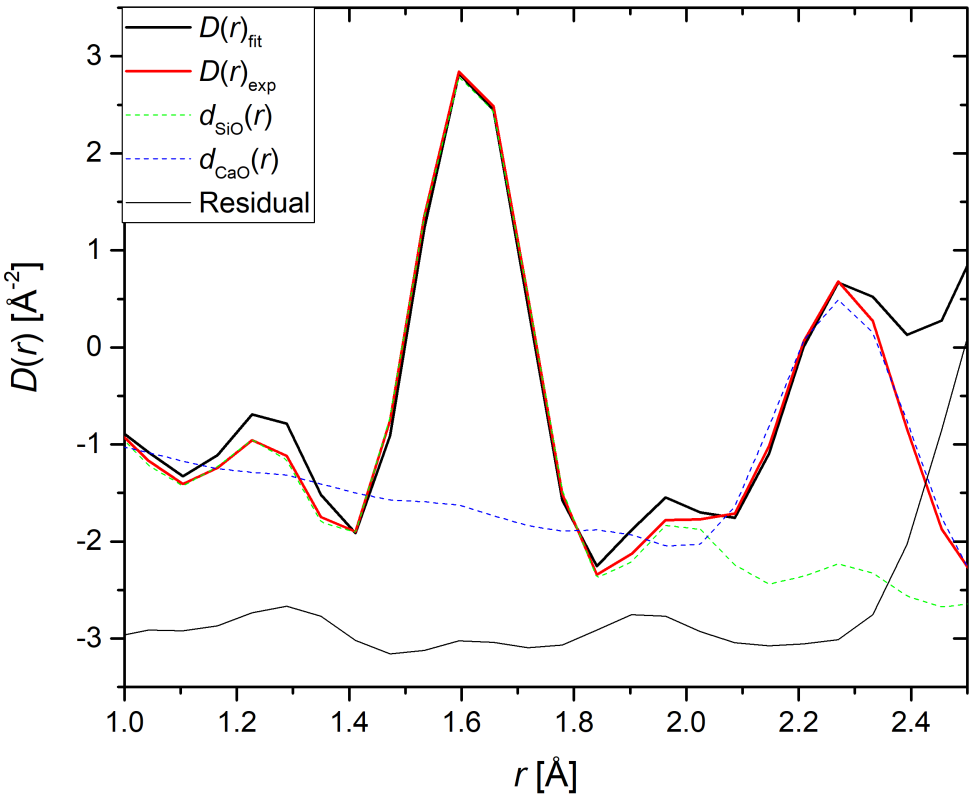

Figure 5.14: The density correlation function and fits obtained for $CaSiO_3$ glass at 5.4(5) GPa, measured on the D4c diffractometer. The solid black line is the measured $D(r)_{\text{exp}}$ function, which is fitted with two Gaussians convoluted with a sinc function using RDFGenie which combine to give the fit $D(r)_{\text{fit}}$ (solid red curve). The dashed green and blue lines correspond to Si-O and Ca-O correlations, respectively. The fit gives $R_\chi = 0.099$ for the range 1.20 - 2.10 Å.

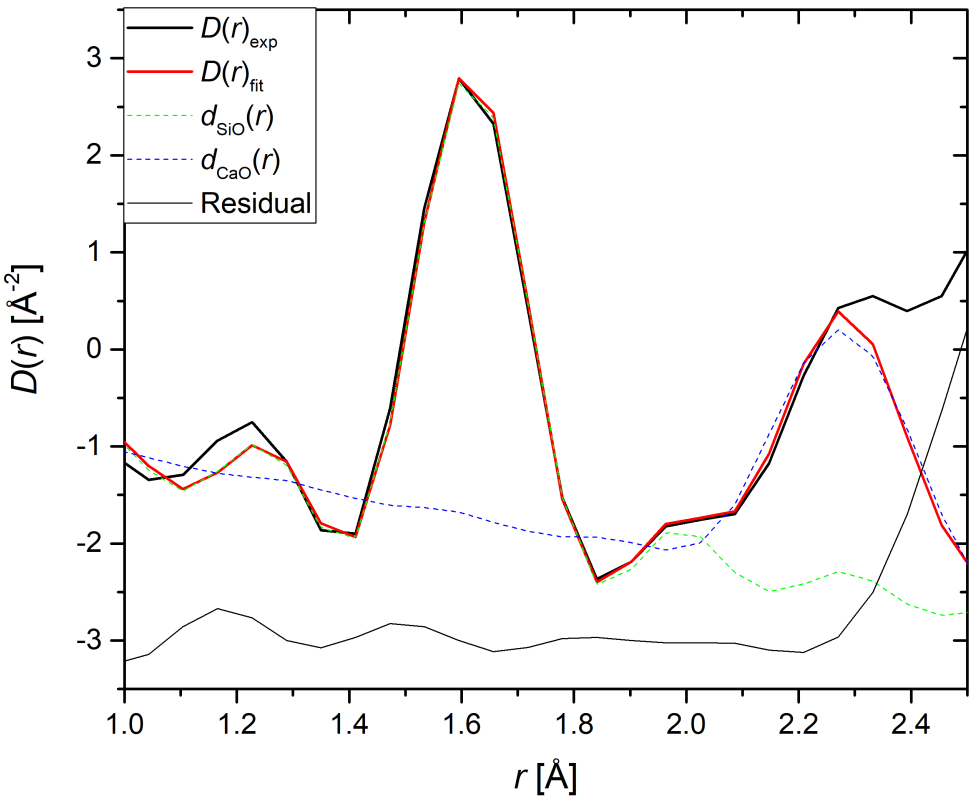

Figure 5.15: The density correlation function and fits obtained for $CaSiO_3$ glass at 7.1(5) GPa, measured on the D4c diffractometer. The solid black line is the measured $D(r)_{\mathrm{exp}}$ function, which is fitted with two Gaussians convoluted with a sinc function using RDFGenie which combine to give the fit $D(r)_{\mathrm{fit}}$ (solid red curve). The dashed green and blue lines correspond to Si-O and Ca-O correlations, respectively. The fit gives $R_\chi = 0.071$ for the range 1.20 - 2.10 Å.

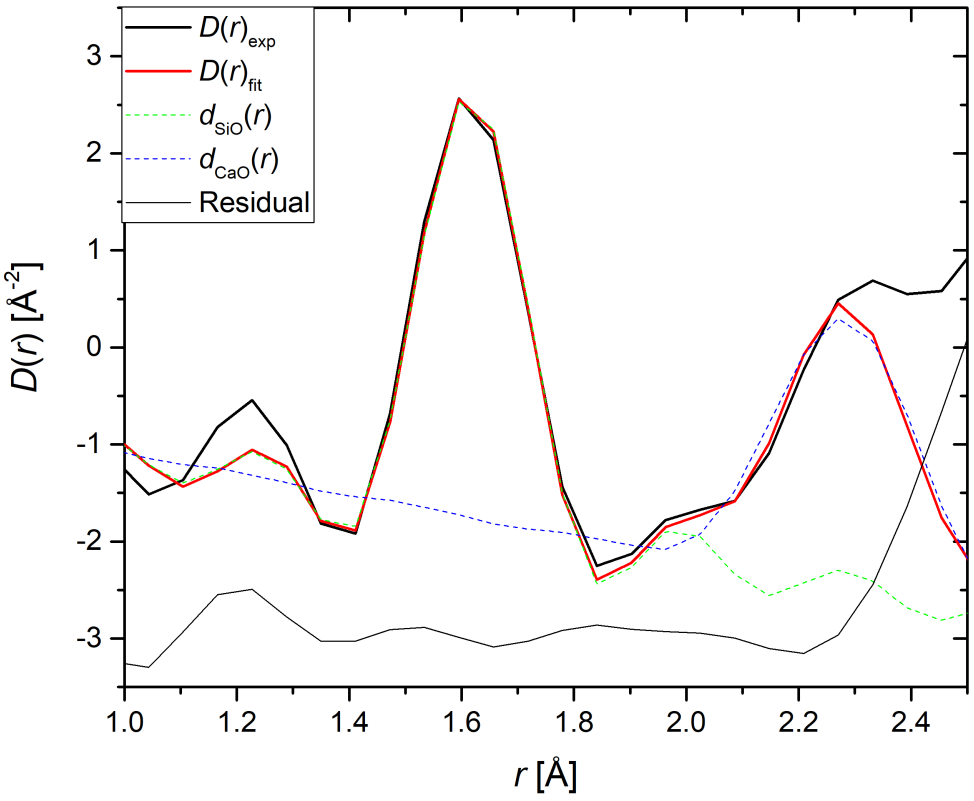

Figure 5.16: The density correlation function and fits obtained for $CaSiO_3$ glass at 8.2(5) GPa, measured on the D4c diffractometer. The solid black line is the measured $D(r)_{\text{exp}}$ function, which is fitted with two Gaussians convoluted with a sinc function using RDFGenie which combine to give the fit $D(r)_{\text{fit}}$ (solid red curve). The dashed green and blue lines correspond to Si-O and Ca-O correlations, respectively. The fit gives $R_\chi = 0.118$ for the range 1.20 - 2.10 Å.

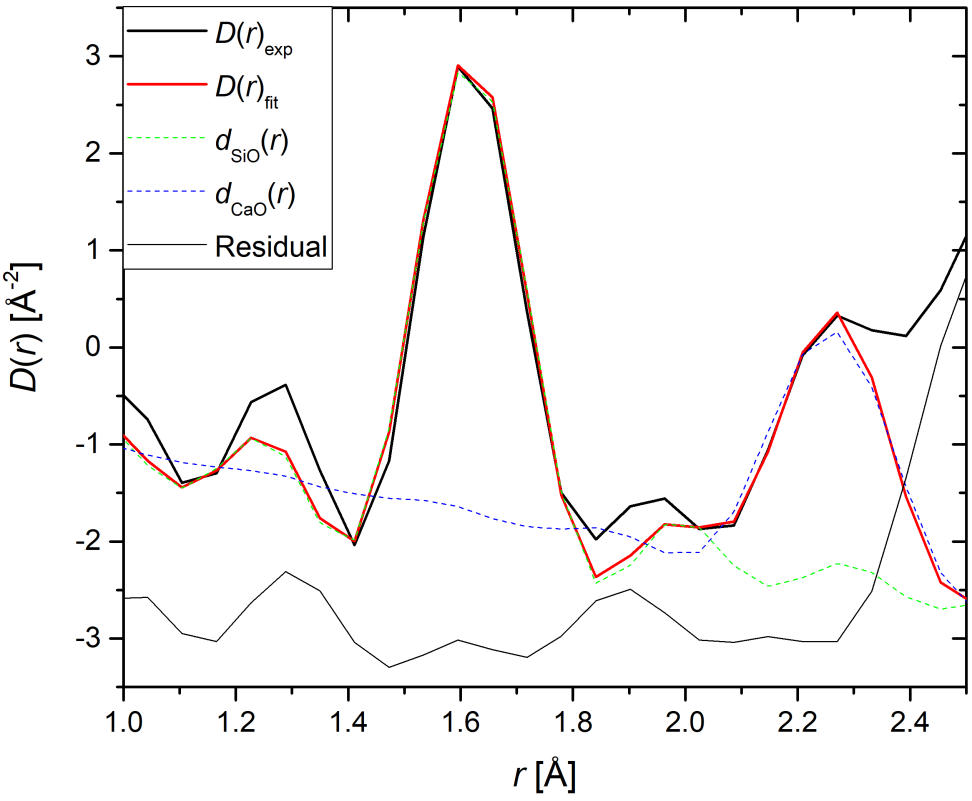

Figure 5.17: The density correlation function and fits obtained for $CaSiO_3$ glass immediately recovered from 8.2(5) GPa, measured on the D4c diffractometer. The solid black line is the measured $D(r)_{\mathrm{exp}}$ function, which is fitted with two Gaussians convoluted with a sinc function using RDFGenie which combine to give the fit $D(r)_{\mathrm{fit}}$ (solid red curve). The dashed green and blue lines correspond to Si-O and Ca-O correlations, respectively. The fit gives $R_\chi = 0.186$ for the range 1.20 - 2.10 Å.

5.5 Discussion

The total structure factors obtained from both neutron diffraction and simulation exhibit a reduction in prominence of the FSDP and simultaneous enhancement of the principal peak with increasing pressure, a result which is consistent with the findings of $MgSiO_3$ glass in the last chapter, and previous work on SiO_2 [81] and GeO_2 [49] glasses. The FSDP is associated with ordering on an intermediate length scale, and the principal peak is associated with extended range ordering up to a nanometre length scale [82]. The changes indicate a competition between intermediate and extended range ordering in the glass, where the latter dominates at higher pressures.

The neutron diffraction results show that the mean Si-O coordination number remains constant within the experimental error at $\bar{n}^{O}_{Si} = 4$ from ambient conditions to a maximum pressure of 14.4(5) GPa. At the highest pressure point studied of 17.5(5) GPa, the Si-O coordination number increases slightly to a value of $\bar{n}^{O}_{Si} = 4.12(10)$. In the case of SiO_2 glass, the Si-O coordination number reaches a value of $\bar{n}^{O}_{Si} = 4.2(1)$ at 17.5(5) GPa, and is accompanyied by a decrease in the Si-O bond distance from 1.60(2) Å to 1.57(2) Å [81]. In $MgSiO_3$ at the same pressure, no change in the mean Si-O coordination number or bond distance is observed. This indicates that the pressure-driven change of the SiO_4 tetrahedra in $CaSiO_3$ glass begins to occur at an intermediate pressure between that of $MgSiO_3$ glass, and pure SiO_2 glass. This result suggests that the replacement of Mg^{2+} with Ca^{2+} as the network modifying cation acts to hasten the pressure-driven change of the SiO_4 tetrahedra, although the inclusion of Ca^{2+} still delays the structural change that occurs in unmodified SiO_2 glass. The results from the MD simulations contrast with these findings, and show that the Si-O coordination number begins to increase gradually at ∼6 GPa to reach a maximum value of $\bar{n}^{O}_{Si} = 4.30$ at 17.5 GPa. Furthermore, the Si-O bond distance is consistently longer at r_{SiO} ∼1.635 Å. These discrepancies likely result from the interatomic interaction model that was used not sufficiently reproducing the atomic structure. Furthermore, the structure acquired from simulation was obtained using a hot compression procedure, in which the glass was heated to 3000 K and then compressed, before being quenched to 300 K. In contrast, the neutron diffraction samples were compressed at room temperature.

The crystalline structure of $CaSiO_3$ (wollastonite) consists of repeated chains of SiO_4 tetrahedra, linked to columns of Ca centered polyhedra [92]. Ca occupies three distinct crystalline sites, the first two are regular octahedral sites in which Ca is six-fold coordi-

nated, whilst in the third site Ca is seven-fold coordinated. Therefore, the mean Ca-O coordination number is $\bar{n}^{O}_{Ca} = 6.33$ [92]. Figure 5.18 shows the distribution of Si-O and Ca-O bond lengths found in wollastonite [93]. The distribution of Si-O bond distances appears to be symmetric, whilst the distribution of Ca-O bond distances appears to be relatively asymmetric, a result in common with diffraction studies of $MgSiO_3$ enstatite [88]. In particular, the longest Ca-O bond distance which only occurs in the crystalline site where Ca is seven-fold coordinated is significantly longer (r_{CaO}=2.636 Å), than the average Ca-O distance of (r_{CaO} ∼2.4 Å). In each crystalline site, Ca is bound to one bridging oxygen (BO) atom, and the remaining Ca-O bonds are to non-bridging oxygen (NBO) atoms. Approximately 15% of the total Ca-O bonds correspond to BO atoms. However unlike $MgSiO_3$ enstatite, the BO distances are not necessarily the longest bond distances, and only in the case of the seven-fold site is the Ca-BO bond the longest distance. There does not appear to be experimental information available for the high pressure structure of crystalline $CaSiO_3$, therefore it is currently unknown how the local environments of Ca and Si in $CaSiO_3$ change as a function of pressure.

Due to the close overlap of the Ca-O and O-O partial pair-distribution functions $g_{CaO}(r)$ and $g_{OO}(r)$ and the unknown distribution of Ca-O bond lengths in the glass, it is not possible to accurately determine the mean Ca-O coordination number from the neutron diffraction results. A previous neutron diffraction with isotopic substition experiment (NDIS) [94] has determined the ambient Ca-O coordination number to be $\bar{n}^{O}_{Ca} = 6.15(17)$. The molecular dynamics simulations accompanying this study [75] calculated a mean Ca-O coordination number of $\bar{n}^{O}_{Ca}$ ∼6 at ambient, which increases to a value of $\bar{n}^{O}_{Ca}$ ∼7.4 at 17.5 GPa, as shown in Figure 5.9.

Figure 5.19 shows the pressure dependence of the fraction of Ca-BO or Ca-NBO bonds and the Q^n distribution of $CaSiO_3$ glass, obtained from the molecular dynamics simulations accompanying this study [75]. Approximately 15% of Ca-O bonds correspond to BO atoms at ambient, a fraction that increases to approximately 30% at 17.5 GPa. This is accompanied by a change in the distribution of Q^n species (where n corresponds to the number of BO atoms per SiO_4 tetrahedra) from approximately 50% Q^2 sites at ambient to approximatly 45% Q^2 sites at 17.5 GPa, driven by an increase in the number of Q^3 and Q^4 sites. Reverse Monte-Carlo studies of $CaSiO_3$ glass [21] have calculated the ambient Ca-O coordination number to be $\bar{n}^{O}_{Ca} = 5.83$, with approximately 15% of Ca-O bonds corresponding to BO atoms, in close agreement with the

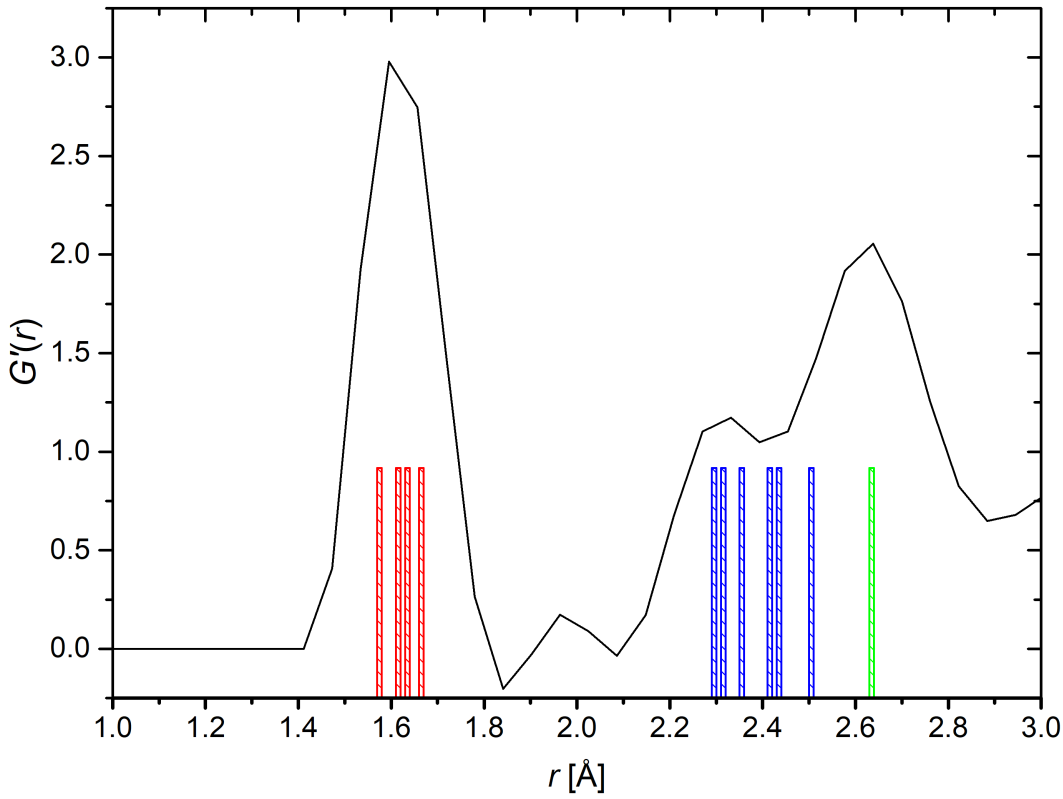

Figure 5.18: The total pair distribution function $G'(r)$ of $CaSiO_3$ glass measured by the D4c diffractometer at ambient pressure using a vanadium can, compared with the distribution of bond lengths found for the wollastonite crystal structure [93]. The bond lengths have been normalised to account for the presence of multiple Si and Ca crystalline sites. The red bars correspond to Si-O bonds, and the blue bars correspond to Ca-O bonds. The single green bar shows the longest Ca-O bond distance that occurs in the seven-fold coordinated Ca site.

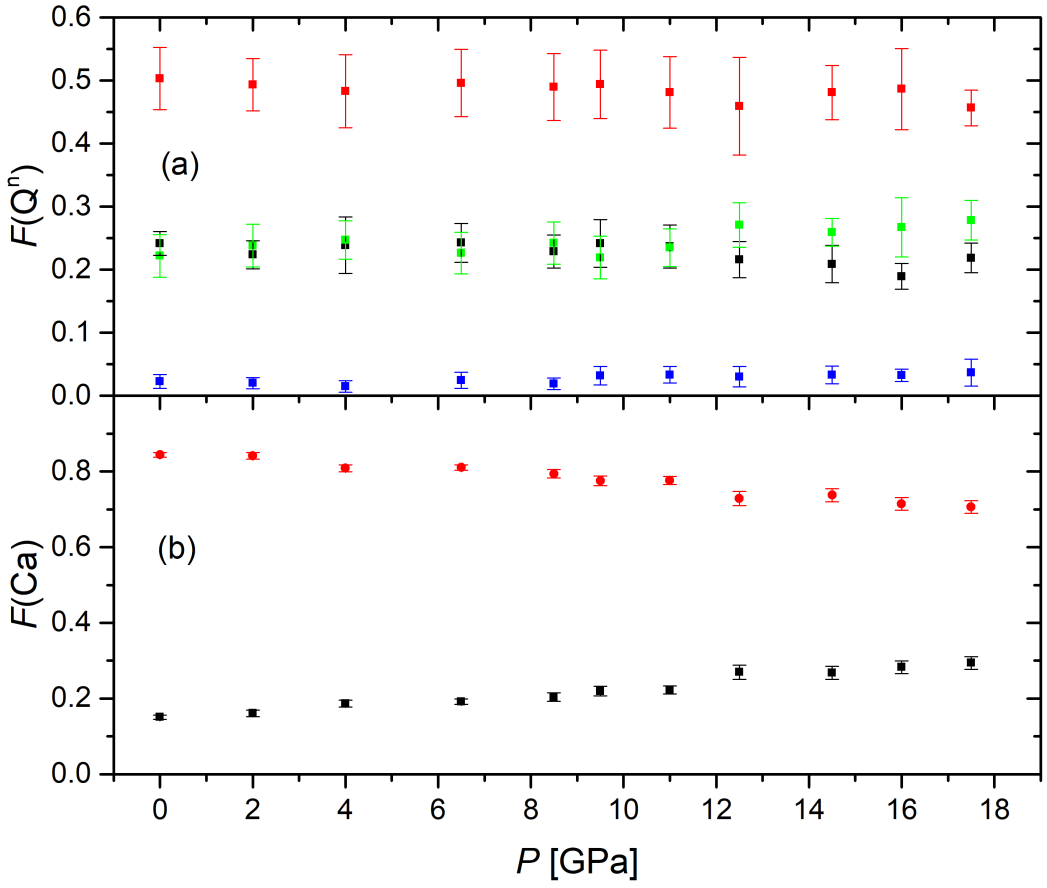

Figure 5.19: The pressure dependence of the (a) Q^n distribution of 4-fold coordinated Si in $CaSiO_3$ glass, and (b) fractions of Ca-O bonds which correspond to bridging oxygen (BO) or non-bridging oxygen (NBO) atoms, obtained from the molecular dynamics simulations accompanying this study [75]. In (a) the markers give the fraction of Q^1 sites (black), Q^2 sites (red), Q^3 sites (green), and Q^4 sites (blue). In (b) the black and red markers give the fraction of Ca-BO and Ca-NBO bonds, respectively.

present work. Another molecular dynamics study [95] of $CaSiO_3$ at 10 GPa finds a similar change in the Ca-O coordination number and fraction of Ca-BO bonds as seen in the present work.

It therefore appears that unlike $MgSiO_3$, the local environment of Ca^{2+} in the glass structure resembles much more closely its crystalline counterpart at ambient conditions. Molecular dynamics simulations from the present study and others suggest that the Ca-O coordination change in the glass is driven by an increase in the fraction of Ca-BO bonds, a result which is analogous to the $MgSiO_3$ glass structure findings discussed in the previous chapter. However in order to confirm this, it is necessary to perform a high pressure neutron diffraction with isotopic substitution (NDIS) experiment to isolate the Ca-O pair-correlation function $g_{\mathrm{CaO}}(r)$. This will allow the Ca-O coordination number and the distribution of Ca-O bonds in the glass to be determined directly, as a function of pressure.

5.6 Conclusions

The atomic structure of $CaSiO_3$ glass has been measured using *in situ* neutron diffraction with the D4c and PEARL diffractometers coupled with a Paris-Edinburgh press, at pressures up to 17.5(5) GPa. The measured total structure factors $S(Q)$, and their Fourier transforms $G'(r)$ show an overall good agreement with MD simulations performed alongside this study.

At pressures up to 14.4(5) GPa, the mean Si-O coordination number remains at its ambient value of $\bar{n}^{\mathrm{O}}_{\mathrm{Si}} = 4$. At the highest pressure of 17.5(5) GPa, the Si-O coordination number increases slightly to a value of $\bar{n}^{\mathrm{O}}_{\mathrm{Si}} = 4.12(10)$, a result which contrasts to the neutron diffraction study of $MgSiO_3$ glass presented in Chapter 4 where no change is observed, and previous work on SiO_2 glass [81] where the Si-O coordination number increases to $\bar{n}^{\mathrm{O}}_{\mathrm{Si}} = 4.2(1)$ at 17.5(5) GPa. This suggests that the replacement of Mg^{2+} with Ca^{2+} as the network modifying cation enables the Si local environment to begin to change at a lower pressure. With the absence of a modifying cation, pure SiO_2 appears to undergo the largest structural change by 17.5 GPa. These results suggest that the inclusion of a modifying cation delays the pressure-driven distortion of SiO_4 tetrahedra, with Mg^{2+} providing a larger resistance to pressure than Ca^{2+}.

Although it is not possible to reliably determine the mean Ca-O coordination number from the neutron diffraction data, the molecular dynamics simulations accompanying this study predict that the Ca-O coordination number increases significantly across the measured pressure range from $\bar{n}^{\mathrm{O}}_{\mathrm{Ca}} \sim 6$ at ambient to $\bar{n}^{\mathrm{O}}_{\mathrm{Ca}} \sim 7.4$ at 17.5 GPa. It is predicted that, like in the case of $MgSiO_3$ glass, the change in Ca-O coordination number is driven by an increase in the relative fraction of network modifier to bridging oxygen bonds from approximately 15% at ambient conditions, to approximately 30% at 17.5 GPa. This change is accompanied by a small increase in the fraction of Q^3 and Q^4 sites. In order to confirm the pressure-driven change of the local environment of Ca^{2+} in the glass structure, it is necessary to perform a high pressure neutron diffraction with isotopic substitution experiment (NDIS) in order to isolate the partial pair-distribution function $g_{\mathrm{CaO}}(r)$ at high pressure.

6 Pressure Driven Structural Transformations In Arsenic Selenide Glass

6.1 Introduction

Arsenic selenide As_xSe_{1-x} glasses possess important technological applications. For example, they are commonly used as infra-red transmitting materials, as the host matrix for infra-red lasers [3, 96], and as components in prisms, windows and wave guides [97]. Furthermore, they exhibit properties such as photoluminesence and photoconduction, leading to opto-electronic applications [4].

The structural motifs found in As_xSe_{1-x} glasses differ significantly to those found in the silicate glasses $MgSiO_3$ and $CaSiO_3$, discussed in chapters 4 and 5, respectively. At ambient conditions, the main structural motif found in As_2Se_3 glass is the pyramidal $AsSe_3$ unit, whilst in AsSe glass cage-like As_4Se_4 motifs can form in which both As-As and Se-Se bonds are present. [22–24]. Therefore, it is expected that the densification mechanism of AsSe glass will differ substantially from other network forming glasses. A previous study using Raman spectroscopy [98], found that the ambient structure of AsSe glass is dominated by $AsSe_3$ pyramidal units, along with As_4Se_4 and As_4Se_3 'caged' molecules.

The work presented in this chapter comprises two separate neutron diffraction experiments on glassy AsSe. The experiments were performed using a Paris-Edinburgh press in conjunction with either the D4c diffractometer at pressures up to 8.2(5) GPa, or the PEARL diffractometer at pressures up to 14.4(5) GPa. Using this technique, the pressure-dependence of the effective nearest neighbour coordination number and the most likely inter-atomic distances were investigated. This information can provide a valuable insight into the densification mechanisms of the glass.

This chapter is organised as follows. The essential theory is discussed in section 6.2, and the experimental procedures used are discussed in section 6.3. The results from the diffraction experiments are provided in section 6.4, and a discussion and comparison with the crystalline AsSe structure is given in section 6.5. Finally, conclusions are drawn in section 6.6.

6.2 Theory

In neutron diffraction experiments, the following equation is used which gives the Fourier transform relating the measured total structure factor $F(Q)$ to the total pair-distribution function $G(r)$,

$$G(r) = \frac{1}{2\pi^2 r\rho}\int_0^\infty QF(Q)\sin(Qr)M(Q)dr \tag{6.1}$$

where $M(Q)$ is a modification function, which is introduced for experimental work because a diffractometer can only measure over a finite Q range. $M(Q)$ is defined as

$$M(Q) = \begin{cases} 1 & Q \leq \mathrm{Q_{max}} \\ 0 & Q > \mathrm{Q_{max}} \end{cases} \tag{6.2}$$

where Q_{max} is the maximum value of Q that is used to truncate the dataset, and is usually chosen according to the measurement range of the diffractometer. For a binary glass such as AsSe, the total pair distribution function comprises three partial pair distribution functions

$$G(r) = c_{\mathrm{As}}^2 b_{\mathrm{As}}^2[g_{\mathrm{AsAs}}(r)-1] + c_{\mathrm{Se}}^2 b_{\mathrm{Se}}^2[g_{\mathrm{SeSe}}(r)-1] + 2c_{\mathrm{As}}c_{\mathrm{Se}}b_{\mathrm{As}}b_{\mathrm{Se}}[g_{\mathrm{AsSe}}(r)-1], \tag{6.3}$$

where c_α and b_α are the atomic concentration and mean coherent scattering length of chemical species α, respectively. The mean coherent scattering lengths of As and Se are $b_{\mathrm{As}} = 6.58(1)$ fm and $b_{\mathrm{Se}} = 7.970(1)$ fm, respectively [30]. The limit $G(r \to 0)$ is given by

$$G(r\to 0) = -\sum_\alpha\sum_\beta c_\alpha c_\beta b_\alpha b_\beta = -<b>^2 = -0.52926(196)\ \text{barn}. \tag{6.4}$$

In the case that a peak in $G(r)$ is associated with multiple partial pair-correlations, it is possible to calculate the effective coordination number which can be used to investigate the relative change of the coordination environment at high pressure. The effective coordination number is defined as

$$\bar{n}' = \frac{4\pi\rho}{<b>^2}\int_{r_1}^{r_2} r^2[G(r) - G(r\to 0)]dr. \tag{6.5}$$

The effective coordination number can be expressed alternatively as

$$\begin{aligned}\bar{n}' &= \frac{4\pi\rho}{< b >^2}\int_{r_1}^{r_2} r^2\Big[c_{\mathrm{As}}^2 b_{\mathrm{As}}^2 g_{\mathrm{AsAs}}(r) + c_{\mathrm{Se}}^2 b_{\mathrm{Se}}^2 g_{\mathrm{SeSe}}(r) + 2c_{\mathrm{As}}c_{\mathrm{Se}}b_{\mathrm{As}}b_{\mathrm{Se}}g_{\mathrm{AsSe}}(r)\Big] \\ &= \frac{4\pi\rho c_{\mathrm{As}}^2 b_{\mathrm{As}}^2}{< b >^2}\int_{r_1}^{r_2} r^2 g_{\mathrm{AsAs}}(r)dr + \frac{4\pi\rho c_{\mathrm{Se}}^2 b_{\mathrm{Se}}^2}{< b >^2}\int_{r_1}^{r_2} r^2 g_{\mathrm{SeSe}}(r)dr \\ &+ \frac{8\pi\rho c_{\mathrm{As}}c_{\mathrm{Se}}b_{\mathrm{As}}b_{\mathrm{Se}}}{< b >^2}\int_{r_1}^{r_2} r^2 g_{\mathrm{AsSe}}(r)dr \\ &= \frac{c_{\mathrm{As}}b_{\mathrm{As}}^2}{< b >^2}\bar{n}_{\mathrm{As}}^{\mathrm{As}} + \frac{c_{\mathrm{Se}}b_{\mathrm{Se}}^2}{< b >^2}\bar{n}_{\mathrm{Se}}^{\mathrm{Se}} + \frac{2c_{\mathrm{As}}b_{\mathrm{As}}b_{\mathrm{Se}}}{< b >^2}\bar{n}_{\mathrm{As}}^{\mathrm{Se}}.\end{aligned} \tag{6.6}$$

As discussed in Chapter 2, it is sometimes necessary to convert the total pair-distribution function $G(r)$ to the density correlation function $D(r)$, using the relationship

$$D(r) = 4\pi\rho r\frac{G(r)}{< b >^2} = 4\pi\rho r\sum_{\alpha=1}\sum_{\beta=1}\frac{c_\alpha c_\beta b_\alpha b_\beta}{< b >^2}[g_{\alpha\beta}(r) - 1]. \tag{6.7}$$

The density correlation function $D(r)$ is comprised of a set of partial density correlation functions $d_{\alpha\beta}(r)$ where

$$d_{\alpha\beta}(r) = 4\pi\rho r[g_{\alpha\beta}(r) - 1]. \tag{6.8}$$

It is then possible to fit a Gaussian function convoluted with a sinc function to a peak associated with α-β correlations to obtain the mean coordination number $\bar{n}_\alpha^\beta$, using equation 2.27. This technique has the advantage of accounting for the truncation of each $F(Q)$ function at a finite $Q_{\max}$ value, and any overlap between the partial pair-distribution functions $g_{\alpha\beta}(r)$. This technique can be used to calculate the effective coordination number associated with a peak by attributing a weighting factor $w_{\alpha\beta} = 1$, to the Gaussian fit.

6.2.1 Network Models

The effective coordination numbers determined from neutron diffraction may be compared to those calculated using either the random covalent network (RCN), or the chemically ordered network (CON) models [99]. Both models assume that the '8-N' rule holds, which states that the coordination number for a given atom is equal to 8 minus the number of valence electrons of that element [99]. Therefore, the rule states that As and Se should always be 3-fold and 2-fold coordinated, respectively. In the RCN model, it is assumed that there no effects that lead to preferential ordering i.e the

distribution of bonds is statistical. In this case, the total number of bonds is

$$z = \frac{c_{\mathrm{As}} z_{\mathrm{As}} + c_{\mathrm{Se}} z_{\mathrm{Se}}}{2}, \tag{6.9}$$

where z_α denotes the number of bonds for a given atom. The individual coordination numbers for AsSe may be calculated using the following equations [**?**],

$$\bar{n}^{\mathrm{As}}_{\mathrm{As}} = c_{\mathrm{As}} \frac{z^2_{\mathrm{As}}}{2z} \tag{6.10}$$

$$\bar{n}^{\mathrm{Se}}_{\mathrm{Se}} = c_{\mathrm{Se}} \frac{z^2_{\mathrm{Se}}}{2z} \tag{6.11}$$

$$\bar{n}^{\mathrm{Se}}_{\mathrm{As}} = c_{\mathrm{Se}} \frac{z_{\mathrm{As}} z_{\mathrm{Se}}}{2z}, \tag{6.12}$$

which gives coordination numbers of $\bar{n}^{\mathrm{As}}_{\mathrm{As}} = 1.8$, $\bar{n}^{\mathrm{Se}}_{\mathrm{Se}} = 0.8$ and $\bar{n}^{\mathrm{Se}}_{\mathrm{As}} = 1.2$. Using Equation 6.6, the average coordination number predicted by the RCN model is $\bar{n} = 2.41$.

The CON model assumes that heteropolar bonds are favoured, such that only As-Se and As-As bonds occur for arsenic rich compositions of AsSe ($c_{\mathrm{As}} < 0.4$). Since selenium must be 2-fold coordinated according to the '8-N' rule, the coordination numbers for AsSe are predicted to be $\bar{n}^{\mathrm{Se}}_{\mathrm{As}} = 2$, $\bar{n}^{\mathrm{As}}_{\mathrm{As}} = 1$ and $\bar{n}^{\mathrm{Se}}_{\mathrm{Se}} = 0$. Using Equation 6.6, the average coordination number predicted by the CON model is $\bar{n} = 2.39$.

6.3 Experimental Method

6.3.1 Sample Preperation

The amorphous AsSe samples were prepared by K. Pizzey, University of Bath. To synthesize the glass, powdered arsenic and selenium were mixed in an equimolar ratio, and placed into an ampoule which was evacuated, left overnight and then sealed. The ampoule was then heated inside a rocking furnace, past the melting points of selenium and arsenic and then the boiling point of selenium, allowing time to dwell at each step. The purpose of this procedure was to ensure homogenization of the melt. The exact heating procedure is described below:

- Heat to melting point of selenium (221°C), at a rate of 1 °C per minute
- Hold at melting point of selenium (221°C), for 4 hours
- Heat to sublimation point of arsenic (615°C), at a rate of 1 °C per minute

- Hold at sublimation point of arsenic (615°C), for 4 hours
- Heat to boiling point of selenium (685°C), at a rate of 1°C per minute
- Hold at boiling point of selenium (685°C), for 48 hours
- Cool to 400 °C, at a rate of 1 °C per minute
- Immediately quench in water

After quenching, the ampoule was annealed at a temperature of 130°C for 45 minutes in order to remove any residual stress within the glass.

6.3.2 D4c Experiment

The D4c neutron diffraction experiment studied arsenic selenide glass at ambient temperature ($T \approx 300$ K) and pressures up to 8.2(5) GPa. An incident neutron wavelength of 0.49841(1) Å was used to optimise the incident flux of neutrons. Single toroid (ST) cubic BN anvils were used to compress the sample. Compression was controlled manually via the use of a hand pump throughout the entire experiment. No automated system to control the oil pressure was available, so the oil pressure typically relaxed by a small amount over the course of a pressure point measurement (20 - 30 bar). When changing oil pressure, periodic pauses were taken in order to allow the system to equilibrate. The pressure points measured for AsSe are shown in Table 6.1. During the course of a pressure point measurement, the ratio was taken of the measured intensities over different points in time. The purpose of this was to check that the ratio did not deviate from unity, i.e. if the measured intensities were consistent. No such deviation was observed over the course of the experiment. Vanadium measurements were made at ambient pressure for (a) a ST pellet of the usual dimensions inside a Ti-Zr gasket, (b) three deformed pellets with the same cap sizes but differing cylinder geometries and (c) two spherical caps machined to match the ST anvil profiles, in order to perform the data correction procedure described in section 3.4.

In order to make a pellet, a Dremel multitool was used to grind a piece of AsSe into the appropriate mass and dimensions expected for a single toroid pellet, inside an Ar filled glovebag. The ideal mass for a single toroid pellet of AsSe was calculated to be 0.4080(1) g. The mass of the AsSe pellet was measured to be 0.41041(1) g.

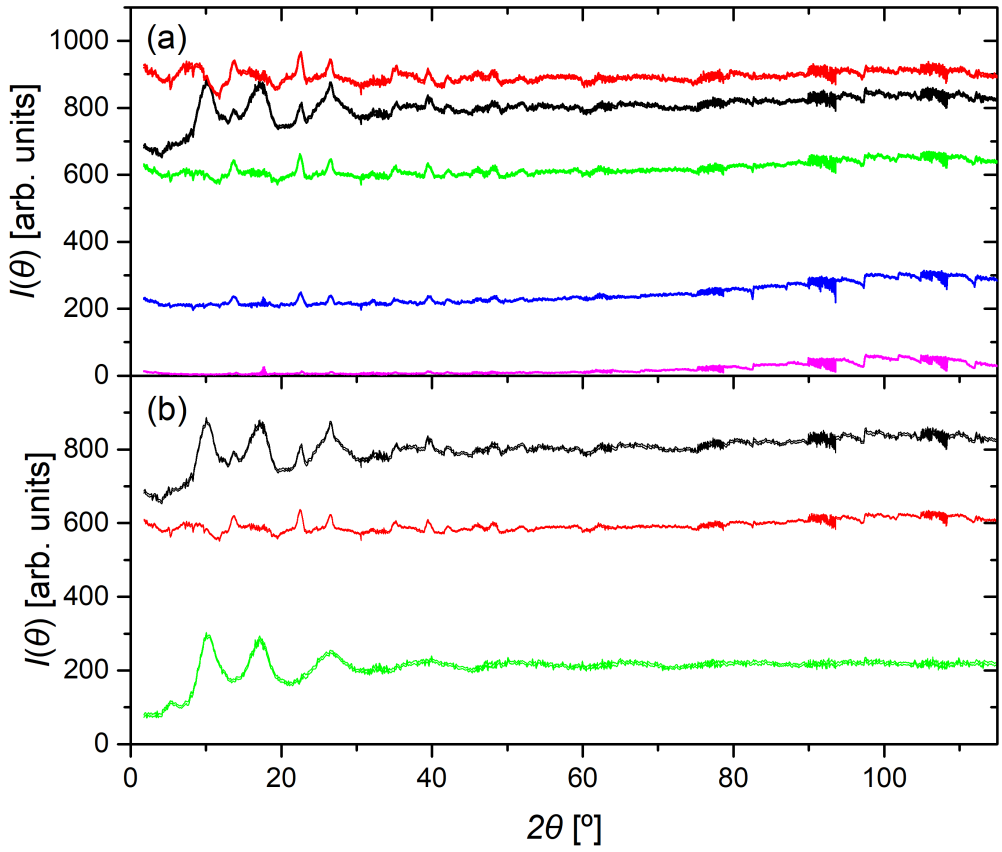

Figure 6.1: The data correction procedure used for the AsSe sample, measured at 3 GPa by the D4c diffractometer using the Paris-Edinburgh press in conjunction with ST BN anvils. Plot (a) shows the measured intensities for the sample inside its container $I^{\mathrm{E}}_{\mathrm{SC}}(\theta)$ (black), an empty uncompressed gasket $I^{\mathrm{E}}_{\mathrm{C1}}(\theta)$ (red), an empty uncompressed gasket that was previously compressed to 4.7 GPa $I^{\mathrm{E}}_{\mathrm{C2}}(\theta)$ (green), an empty gasket measured at 4.4 GPa that was previously compressed to 8.2 GPa $I^{\mathrm{E}}_{\mathrm{C3}}(\theta)$ (blue), and the empty anvils with no gasket or sample present $I^{\mathrm{E}}_{\mathrm{a}}(\theta)$ (magneta). Plot (b) shows the measured intensity for the sample inside its container $I^{\mathrm{E}}_{\mathrm{SC}}(\theta)$ (black); the background intensity $I^{\mathrm{E}}_{\mathrm{B}}(\theta)$ calculated using equation 3.15 with coefficients $x_{\mathrm{C1}} = 0.25$ and $x_{\mathrm{C2}} = 0.6$; and the background and container corrected sample intensity $I^{\mathrm{E*}}_{\mathrm{SC}}(\theta)$ calculated using equation 3.14.

Oil Pressure [bar]	Applied Load [tns]	Sample Pressure [GPa]
100	6.8	Ambient
450	30.5	3.0(5)
900	61.0	5.7(5)
1200	81.3	7.1(5)
1400	94.9	8.2(5)

Table 6.1: The oil pressures and corresponding sample pressures for the D4c experiment on AsSe glass. The sample pressures were deduced from the calibration curve shown in Figure 3.7.

The data correction procedure followed the methodology described in section 3.4.1. Figure 6.1 shows an example of the correction procedure used for the experiment, and illustrates graphically the steps used to obtain the background and container corrected sample intensity $I_{\mathrm{SC}}^{\mathrm{E}*}(\theta)$ for AsSe glass at 3 GPa.

6.3.3 PEARL Experiment

The PEARL experiment was performed by K. Pizzey, University of Bath. The PEARL neutron diffraction experiment studied arsenic selenide glass at ambient temperature ($T \approx 300$ K) and pressures up to 14.4(5) GPa. Sintered diamond double toroid (DT) anvils were used to compress the sample. Compression was controlled by an automated machine up to an oil pressure of $P_{\mathrm{oil}} = 980$ bar. After this, the oil pressure was increased manually via the use of a hand pump. The automated system ensured that the oil pressure was kept at a constant value, but use of the manual system meant that a small relaxation of the oil pressure was allowed to occur. The pressure points at which diffraction patterns were measured for AsSe are shown in Table 6.2. Equivalent measurements were made for a vanadium pellet of equal dimensions to the sample, and for an empty $\mathrm{Ti}_{0.676}\mathrm{Zi}_{0.324}$ gasket at ambient conditions, in order to perform the data correction procedures described in section 3.4. As for the D4c experiment, the ratio of scattered intensities recorded during different times was taken over the course of a measurement to check for measurement consistency.

The ideal mass of a double toroid (DT) pellet of AsSe glass was calculated to be 0.14971(1) g. In order to produce a DT pellet, a single piece of AsSe glass was ground

to the appropriate shape using a Dremel multitool, inside an Ar filled glovebag. The mass of the AsSe pellet was measured to be 0.15373(1) g. The ideal mass of a vanadium double toroid pellet is 0.20232(1) g. To make a vanadium pellet, the appropriate mass of vanadium foil was carefully folded and placed into a die designed to produce the shape of a DT pellet, and then compressed in stages. The final mass of the vanadium pellet was measured to be 0.20600(1) g.

Applied Load [tns]	Sample Pressure [GPa]	AsSe	Vanadium
2.0	Ambient	✓	✓
75.0	8.7(5)	✓	✓
98.0	10.9(5)	✓	✓
120.0	14.4(5)	✓	✓

Table 6.2: The applied load and corresponding sample pressures for the PEARL experiment on AsSe glass. The sample pressures were deduced from the calibration curve shown in Figure 3.8.

6.3.4 Equation of State and Density Measurements

The mass density of the AsSe samples was measured using a helium pyconometer to be 4.44(1) g cm^{-3}, which corresponds to an atomic number density of 0.0348(23) $Å^{-3}$. At present the equation of state for AsSe glass has not been measured. However, the pressure-volume equation of state of As_2Se_3 glass has been obtained from optical microscopy measurements [100], shown in Figure 6.2. The measurement technique used is described in detail in [101]. A cubic polynomial was fitted to the data by K. Pizzey, which was found to give better agreement to the data than a Birch-Murnaghan equation of state [27]. For the present work, the equation of state was scaled such that the ambient atomic number density matches the measured ambient atomic number density of AsSe glass, this is plotted in Figure 6.3.

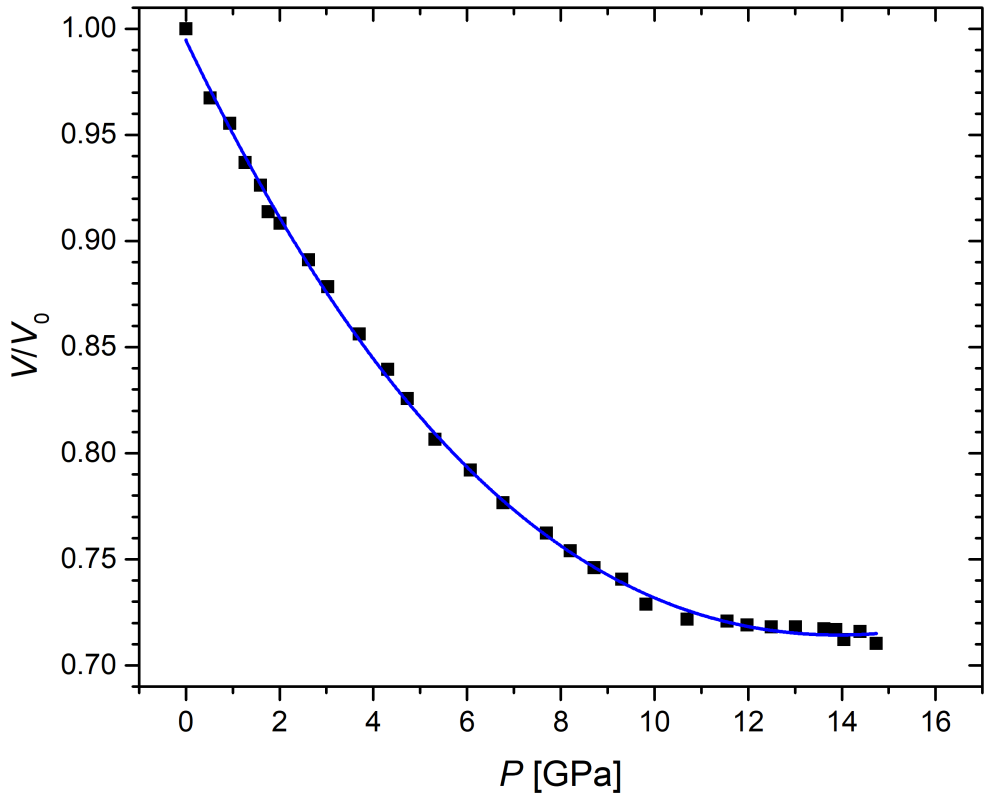

Figure 6.2: The pressure-volume equation of state for glassy As_2Se_3. The black squares show results of molecular dynamics simulations obtained from [100]. The blue line is a cubic polynomial fit to the data [27].

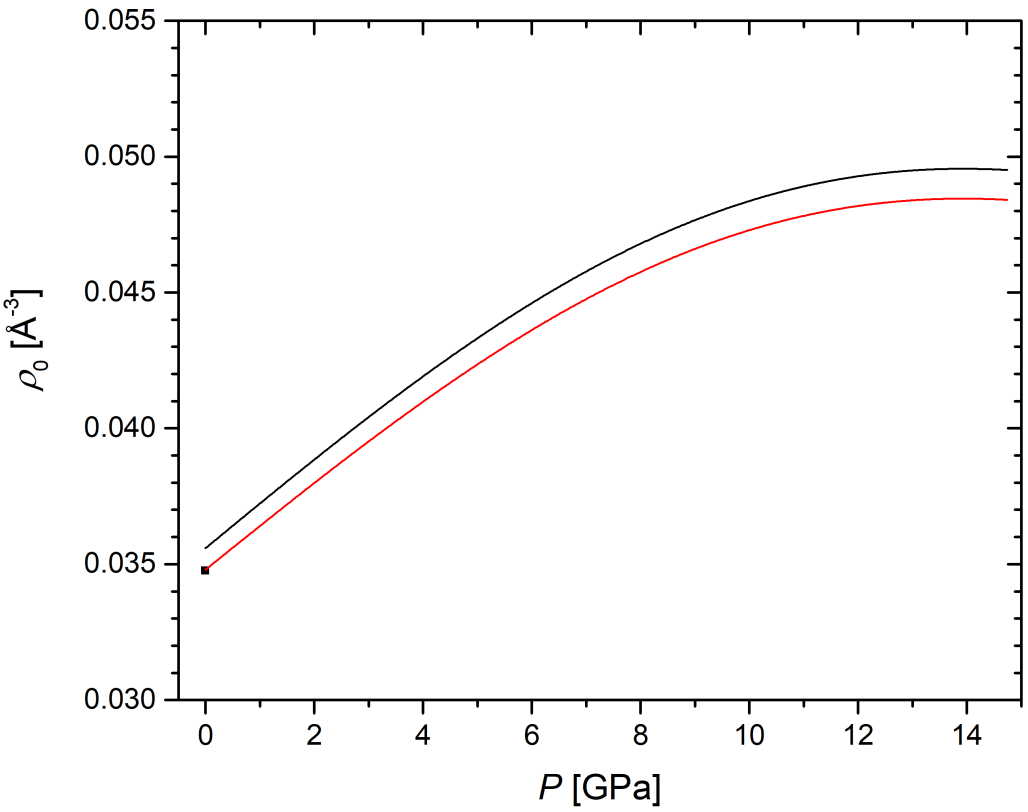

Figure 6.3: The equation of state for glassy As_2Se_3 [100], scaled to correspond to the measured AsSe atomic number density at ambient. The black curve corresponds to the cubic polynomial fit shown in Figure 6.2, which has been converted into the form of atomic number density as a function of pressure. The red curve is the black curve scaled to match the ambient measured atomic number density of AsSe, shown by the single black marker.

6.4 Results

6.4.1 Total Structure Factors

Figure 6.4 shows the pressure dependence of the total structure factors $F(Q)$ obtained for AsSe glass. At ambient, there is a clearly defined first sharp diffraction peak (FSDP) at $\sim$1.15 Å^{-1}, followed by a principal peak at $\sim$2.15 Å^{-1}. As pressure is increased, the FSDP quickly reduces in intensity and becomes absent from the datasets after 3.0(5) GPa. This behaviour is accompanied by a sharpening and increasing amplitude of the principal peak.

The FSDP and principal peak positions are plotted for both AsSe and a previous high pressure study of As_2Se_3 [27], in Figure 6.5. The results show that the FSDP of As_2Se_3 glass at ambient conditions is at a higher value of Q $\sim$1.3 Å^{-1}, than the corresponding value for AsSe glass at Q $\sim$1.15 Å^{-1}. The FSDP of As_2Se_3 glass disappears by the first measured pressure point of 3.0(5) GPa, whilst in AsSe glass the FSDP is still discernible at this pressure, and has increased from its ambient value to Q $\sim$1.2 Å^{-1}. At ambient conditions, the principal peak of As_2Se_3 glass is at a slightly higher value of Q $\sim$2.25 Å^{-1}, than the value for AsSe glass at Q $\sim$2.15 Å^{-1}. The principal peak position shifts to higher Q as pressure is increased for both glasses, and in the case of AsSe shifts by a greater amount so that the peak positions overlap by $\sim$5 GPa. At the maximum pressure of 14.4(5) GPa, the principal peak position is at Q $\sim$2.5 Å^{-1} for both glasses.

6.4.2 Pair-Distribution Functions

Figure 6.6 shows the pressure dependence of the total pair-distribution functions $G(r)$ measured for AsSe glass. The reciprocal space datasets were Fourier transformed using a step modification function as shown in Equation 6.2. The D4c measurements were Fourier transformed using $Q_{\max}$ = 21.5 Å^{-1} and the PEARL datasets were Fourier transformed using $Q_{\max}$ = 19.55 Å^{-1}. At ambient conditions, the first peak is well defined at r = 2.412(20) Å and corresponds to the nearest neighbour atomic separation found in AsSe. There are further overlapping peaks at longer distances of approximately 3.1 Å, 3.4 Å and 3.7 Å.

As pressure is increased the first peak of $G(r)$ becomes noticeably broader, and the contributions at longer distances overlap to a greater extent. Furthermore, the peak

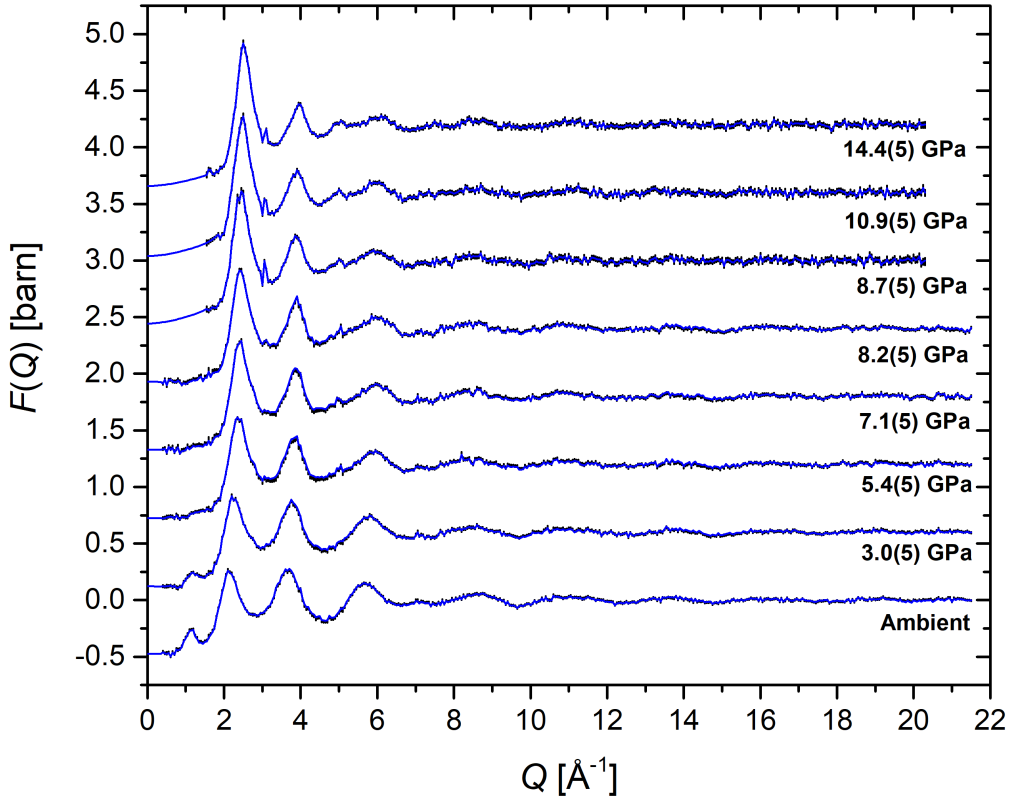

Figure 6.4: The pressure dependence of the neutron total structure factors $F(Q)$ for AsSe glass, as measured using the D4c (ambient to 8.2(5) GPa) or PEARL (8.2(5) to 14.4(5) GPa) diffractometers. The vertical bars give the statistical errors on the measured datasets, and the blue curves show the back Fourier transforms of spline fits to the experimental data. For the datasets originating from PEARL, the region Q $\leq$1.55 Å^{-1} is inaccessible and the curves in this region correspond to fitted Lorentzian functions. The high pressure datasets have been offset vertically for clarity of presentation.

with the highest intensity after the first peak shifts from an ambient value of r ∼3.7 Å, to a value of r ∼3.2 Å at 8.2(5) GPa. In the datasets originating from PEARL, the first real space peak is much broader than observed for D4c, and the contributions at longer distances overlap to a greater extent. In the highest pressure dataset (14.4(5) GPa), it appears that individual peaks after the first peak becomes visible again, however this effect is likely due to the increased measurement time that was used for this dataset leading to improved counting statistics. A detailed discussion of the disparity between the $G(r)$ functions originating from D4c and PEARL is provided in Chapter 3.

Figure 6.7 shows the pressure dependence of the effective coordination number $\bar{n}'$ and nearest neighbour bond distance $\bar{r}$, corresponding to the first peak of the $G(r)$ functions obtained for AsSe glass. The effective coordination numbers originating from the D4c datasets were obtained by using the RDFGenie program to fit a Gaussian convoluted with a sinc function, using a weighting factor $w_{\alpha\beta} = 1$, these fits are plotted in Figures 6.8 to 6.12. The effective coordination numbers originating from the PEARL datasets were calculated by integration of the first real space peak, using Equation 6.5. The bond distances were obtained by measurement of the first peak position in $G(r)$. As pressure is increased, the effective coordination number decreases slightly from $\bar{n}'$ = 2.35(10) at ambient, to $\bar{n}'$ = 2.1(2) at 14.4(5) GPa. The mean nearest neighbour bond distance appears to remain constant at its ambient value of $\bar{r}$ = 2.412(20) Å. The results are compared to the equivalent values obtained for As_2Se_3 glass at high pressure [27]. The values are broadly in agreement with those previously obtained for As_2Se_3 [27], although the ambient effective coordination number is lower in the case of As_2Se_3 ($\bar{n}$ ∼2.2). As pressure is increased, the AsSe and As_2Se_3 values reach closer agreement. The effective coordination numbers of AsSe calculated using Equation 6.6 for a random covalent network model ($\bar{n}$ = 2.41), and a chemically ordered continuous random network model ($\bar{n}$ = 2.39), are also plotted.

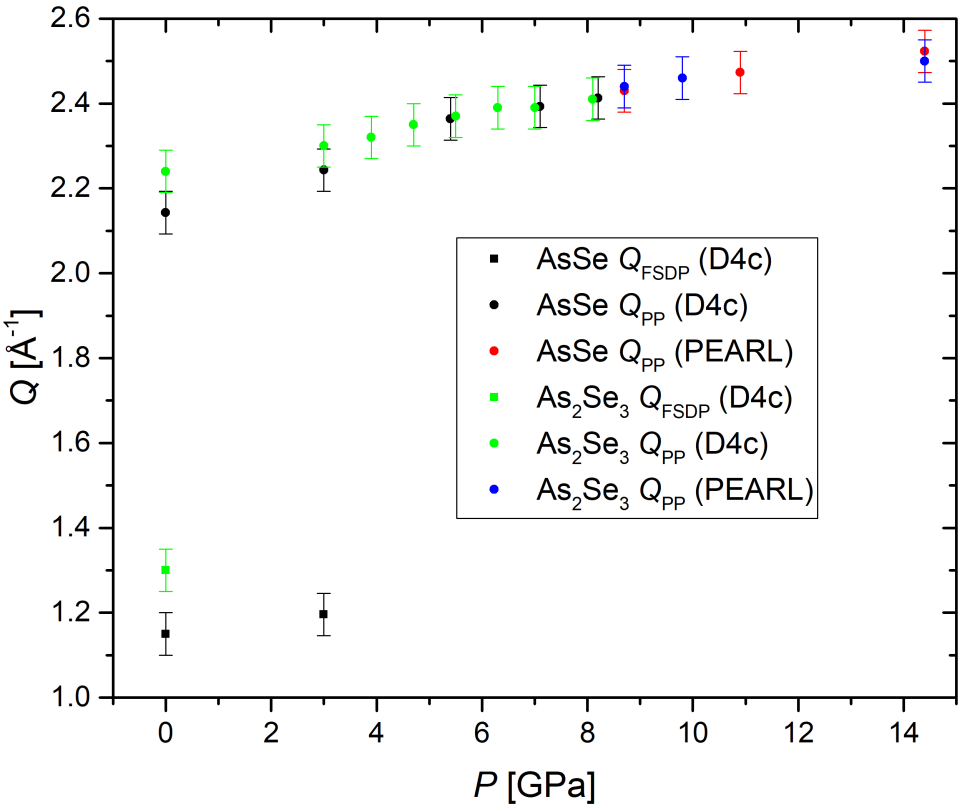

Figure 6.5: The pressure dependence of the first sharp diffraction peak position (squares) and the principal peak position (circles) for glassy AsSe from the present work, and As_2Se_3 [27]. The black and red datapoints show results from the AsSe D4c and PEARL experiments, respectively. The green and blue datapoints show results from the As_2Se_3 D4c and PEARL experiments, respectively [27].

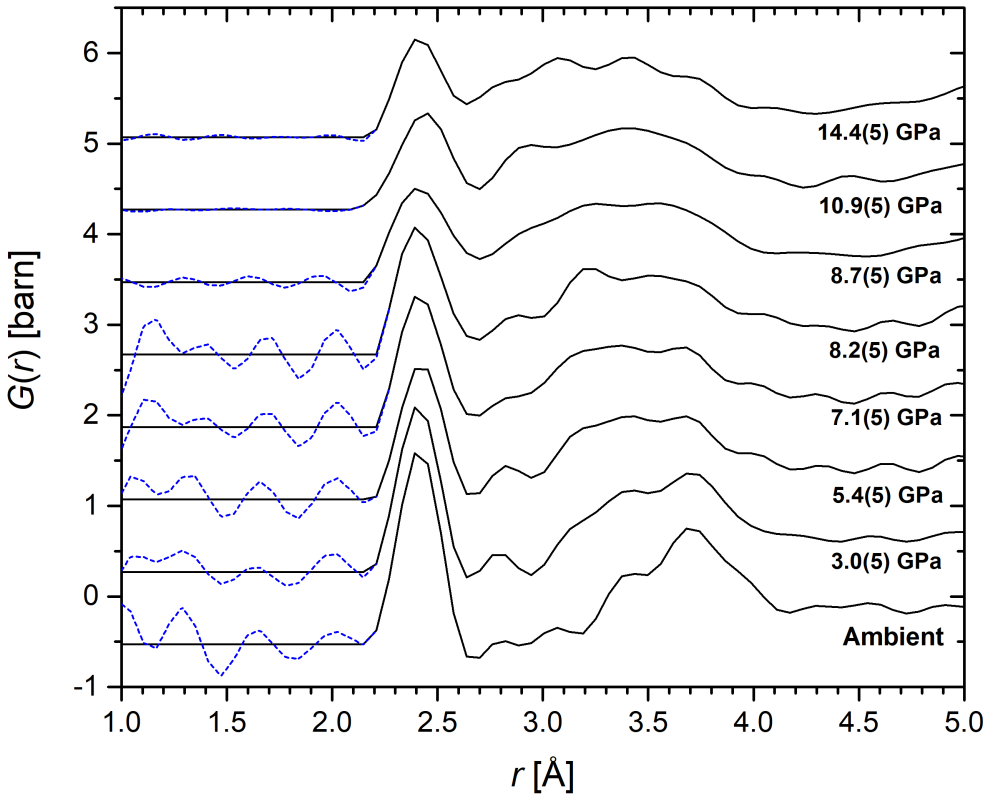

Figure 6.6: The total pair-distribution functions $G(r)$ for AsSe glass (solid black curves), obtained by Fourier transforming the $F(Q)$ functions shown in Figure 6.4. The dashed blue curves show the unphysical Fourier transform artefacts at distances smaller than the closest approach between two atoms. The high pressure datasets have been offset vertically for clarity of presentation.

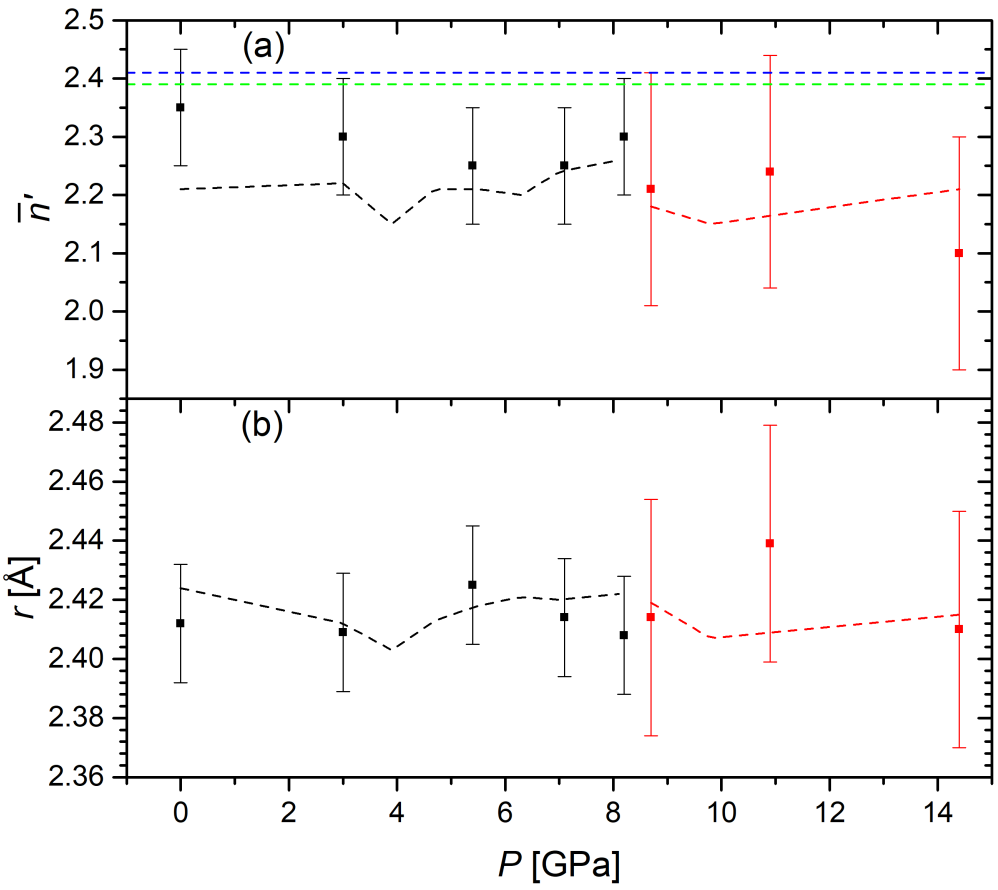

Figure 6.7: The pressure dependence of the (a) effective coordination number of AsSe $\bar{n}'$ calculated using equation 6.5, and (b) the position of the first peak of the total pair-distribution function $G(r)$. The black markers show results from the D4c experiment, and the red markers show results from the PEARL experiment. The black and red dashed lines show results obtained from previous D4c and PEARL high pressure experiments on As_2Se_3 glass, respectively. The blue and green dashed lines show the effective coordination numbers of AsSe calculated using Equation 6.6, for a random covalent network model and a chemically ordered continuous random network model, respectively.

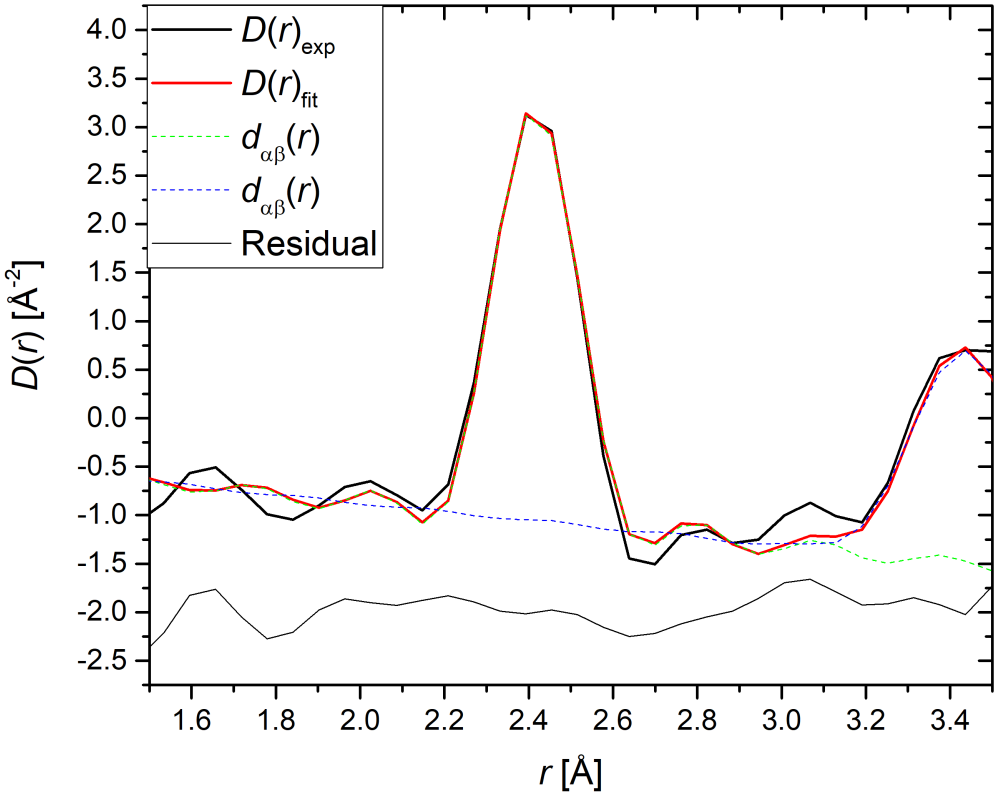

Figure 6.8: The density correlation function and the fits obtained for AsSe glass at ambient conditions in the Paris-Edinburgh press, measured on the D4c diffractometer. The solid black line is the measured $D(r)_{\mathrm{exp}}$ function, which is fitted with two Gaussians convoluted with a sinc function using RDFGenie, which combine to give $D(r)_{\mathrm{fit}}$ (solid red curve). The dashed green line is used to calculate the effective coordination numbers plotted in Figure 6.7a, the dashed blue line is used to constrain the fit. The fit gives $R_{\chi} = 0.0862$ for the range 1.90 - 2.90 Å.

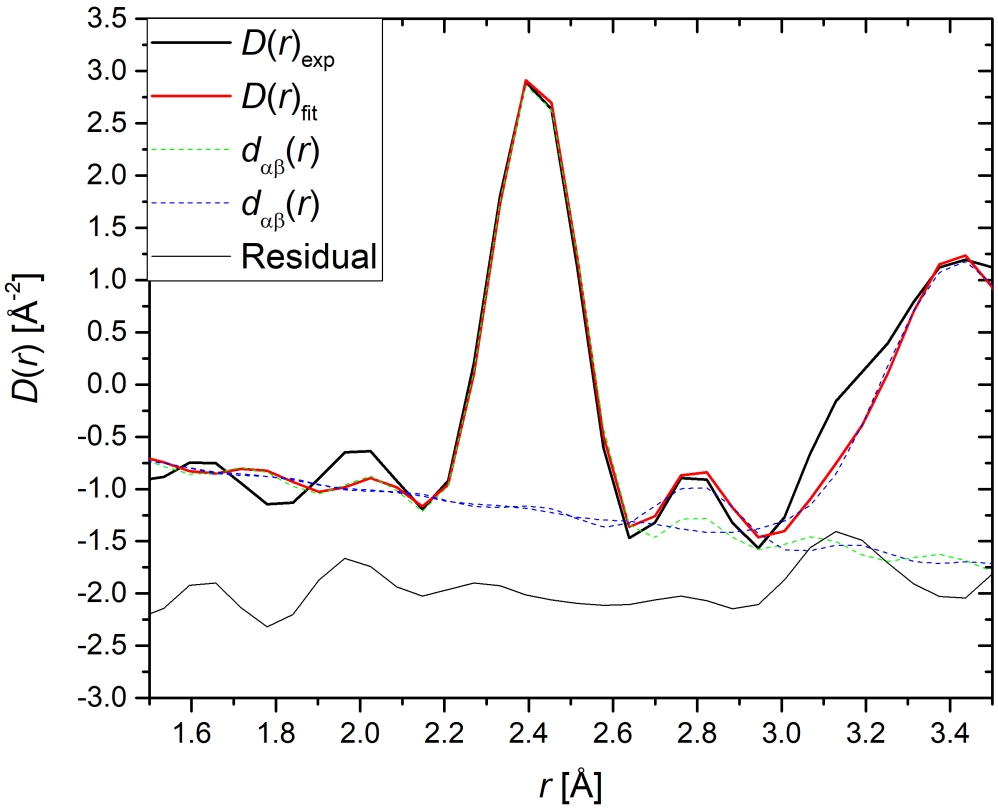

Figure 6.9: The density correlation function and the fits obtained for AsSe glass at 3.0(5) GPa, measured on the D4c diffractometer. The solid black line is the measured $D(r)_{\text{exp}}$ function, which is fitted with three Gaussians convoluted with a sinc function using RDFGenie which combine to give $D(r)_{\text{fit}}$ (solid red curve). The dashed green line is used to calculate the effective coordination numbers plotted in Figure 6.7a, the dashed blue line is used to constrain the fit. The fit gives $R_{\chi} = 0.0987$ for the range 1.90 - 2.90 Å.

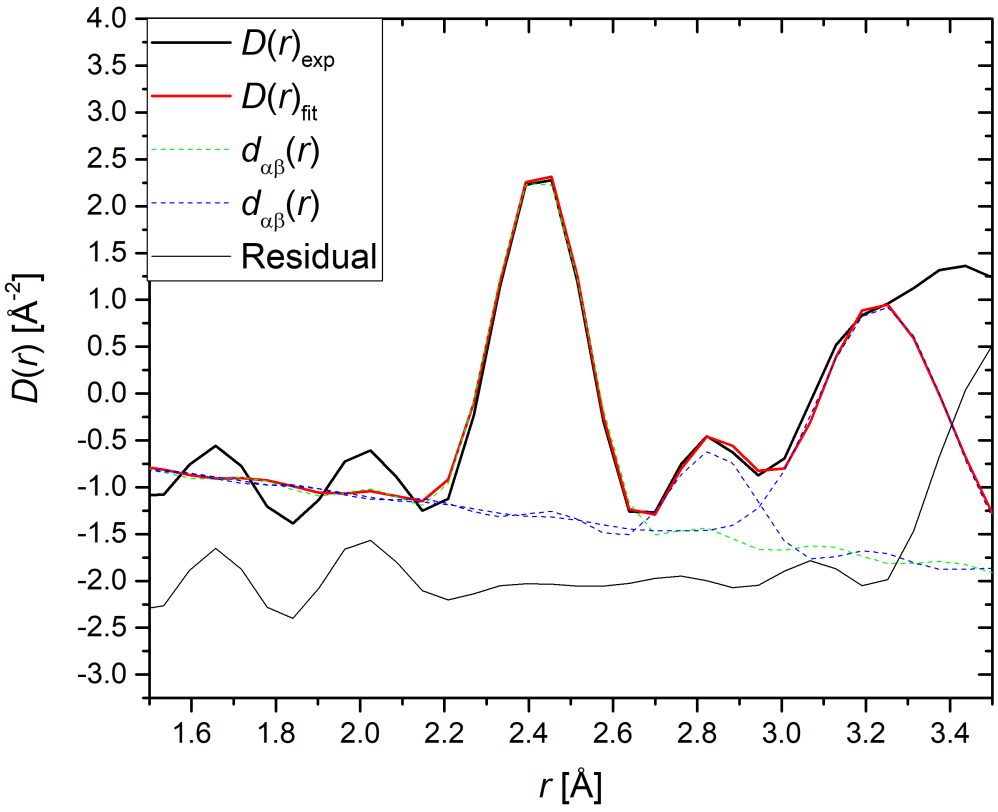

Figure 6.10: The density correlation function and the fits obtained for AsSe glass at 5.4(5) GPa, measured on the D4c diffractometer. The solid black line is the measured $D(r)_{\text{exp}}$ function, which is fitted with three Gaussians convoluted with a sinc function using RDFGenie which combine to give $D(r)_{\text{fit}}$ (solid red curve). The dashed green line is used to calculate the effective coordination numbers plotted in Figure 6.7a, the dashed blue line is used to constrain the fit. The fit gives $R_\chi = 0.157$ for the range 1.90 - 2.725 Å.

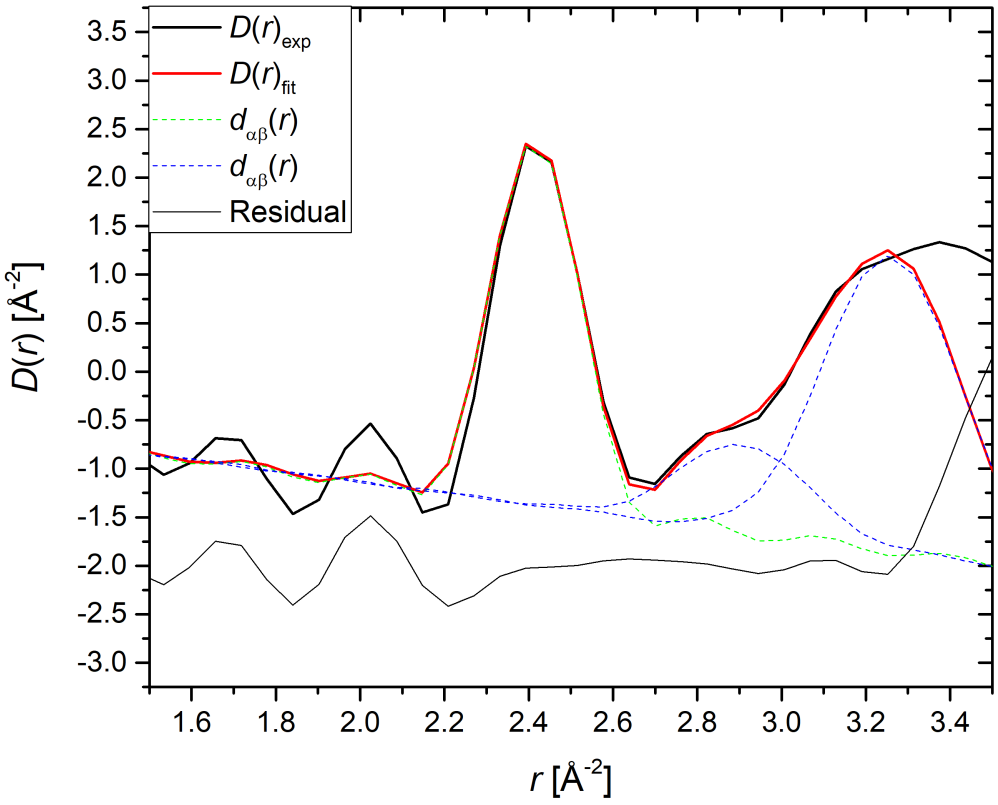

Figure 6.11: The density correlation function and the fits obtained for AsSe glass at 7.1(5) GPa, measured on the D4c diffractometer. The solid black line is the measured $D(r)_{\text{exp}}$ function, which is fitted with three Gaussians convoluted with a sinc function using RDFGenie which combine to give $D(r)_{\text{fit}}$ (solid red curve). The dashed green line is used to calculate the effective coordination numbers plotted in Figure 6.7a, the dashed blue line is used to constrain the fit. The fit gives $R_\chi = 0.195$ for the range 1.90 - 2.725 Å.

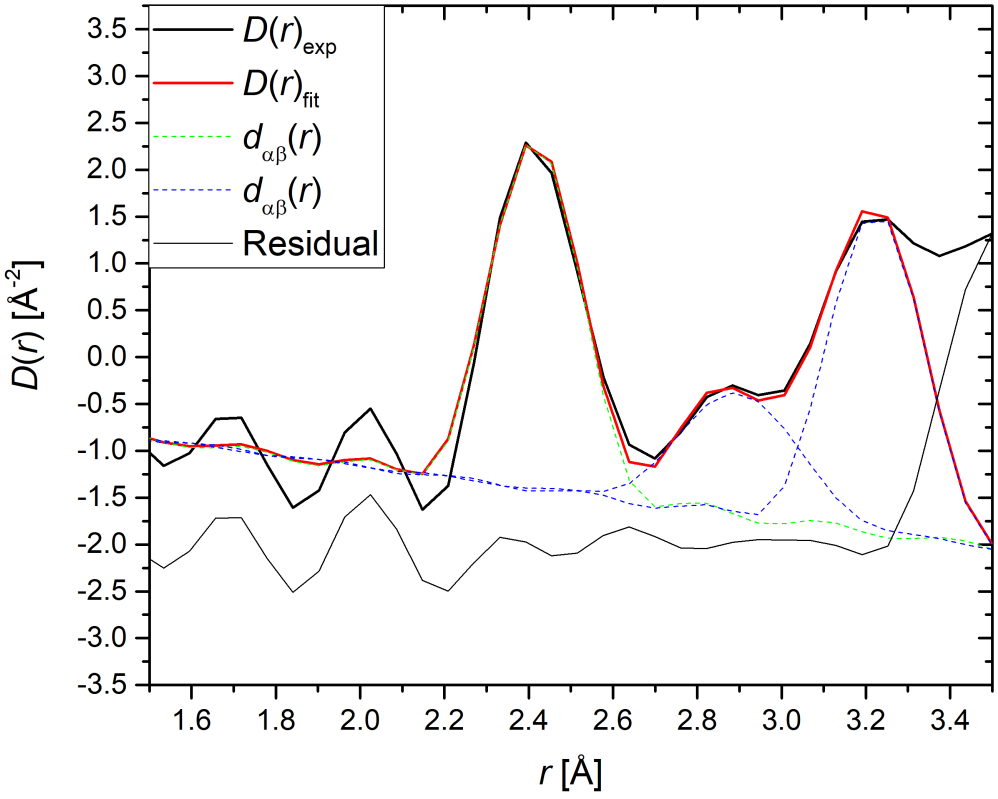

Figure 6.12: The density correlation function and the fits obtained for AsSe glass at 8.2(5) GPa, measured on the D4c diffractometer. The solid black line is the measured $D(r)_{\text{exp}}$ function, which is fitted with three Gaussians convoluted with a sinc function using RDFGenie which combine to give $D(r)_{\text{fit}}$ (solid red curve). The dashed green line is used to calculate the effective coordination numbers plotted in Figure 6.7a, the dashed blue line is used to constrain the fit. The fit gives $R_\chi = 0.222$ for the range 1.90 - 2.725 Å.

6.5 Discussion

The total structure factors obtained from neutron diffraction exhibit a reduction in the height of the FSDP and simultaneous increase in the height of the principal peak, with increasing pressure. This phenomenon is consistent with the results obtained from previous work on SiO_2 [81], GeO_2 [49] and $GeSe_2$ glasses [102]. The FSDP is associated with ordering on an intermediate length scale, and the principal peak is associated with extended range ordering up to a nanometre length scale [82]. The changes indicate a competition between intermediate and extended range ordering in the glass, where the latter dominates at higher pressures.

The neutron diffraction results show that the effective coordination number decreases slightly from $\bar{n}' = 2.35(10)$ at ambient to $\bar{n}' = 2.1(2)$ at 14.4(5) GPa, whilst the mean nearest neighbour bond distance remain constant within the experimental error across the measured pressure range. The effective coordination numbers obtained are consistently lower than the values predicted by the random covalent network (RCN) and chemically ordered network (CON) models of 2.41 and 2.39 respectively. This suggests that neither of these models provide an accurate description of the network, or that the '8-N' rule is not applicable. The effective coordination numbers and mean nearest neighbour bond distances are compared to the results obtained for As_2Se_3 glass across a similar pressure range [27]. The results show that the ambient effective coordination number of As_2Se_3 remains lower ($\bar{n}'$=2.2) than that of AsSe ($\bar{n}'$=2.35), whilst the mean nearest neighbour bond distances are in agreement. Previous diffraction studies at ambient on the glasses of lower As concentration $As_{0.35}Se_{0.65}$ and $As_{0.3}Se_{0.7}$ [41], have also revealed an effective coordination number $\bar{n}'$=2.2. This suggests that the higher ambient effective coordination number of AsSe originates from a greater concentration of As in the glass. Furthermore, as a change in the effective coordination number is observed for AsSe but not As_2Se_3, this suggests that As is more susceptible to a pressure-driven coordination change, than Se. As pressure is increased, there is no significant variation in the effective coordination numbers and bond distances between the two compositions.

Figure 6.13 shows the ambient pair-distribution function $G'(r)$ of AsSe glass measured using the D4c diffractometer, compared with the inter-atomic bond distances and separations obtained for the AsSe crystalline structure by Goldstein *et. al.* [103]. In this crystalline structure, the As and Se atoms form As_4Se_4 'cage-like' molecules. All bond distances correspond to the first real space peak centered at ∼2.4 Å. Each As

atom is three-fold coordinated which comprises one As-As bond and two As-Se bonds, whilst each Se atom is two-fold coordinated to As (there are no Se-Se bonds present). Therefore, the '8-N' rule holds and the crystalline structure conforms to the chemically ordered network (CON) model. Figure 6.13 also shows the averaged inter-atomic separations which correspond to intra-molecular distances, which are clustered in the range 3.5 Å $\leq r \leq$ 4.0 Å. In the glass structure, this corresponds to the wide peak centered at r ∼3.7 Å. The large width of this peak observed for the glass structure shows that there is also a large distribution of intra-molecular separations beyond the first coordination shell.

Figure 6.14 shows the pressure dependence of the difference functions $\Delta G_{\mathrm{P}}(r)$ obtained from D4c, which are defined as

$$\Delta G_P(r) = G_P(r) - G_0(r), \tag{6.13}$$

where $G_{\mathrm{P}}(r)$ and $G_0(r)$ are the total pair-distribution functions at a given pressure P, and ambient pressure, respectively. The plot shows that as pressure is increased, the peak centered at r ∼3.7 Å decreases in intensity, whilst simultaneously the peak centered at r ∼3.2 Å become more significant. This suggests that the densification mechanism of AsSe glass is dominated by a rearrangement of the intra-molecular distances, whilst the nearest neighbour coordination shell remains mostly unchanged.

The structure of AsSe glass has recently been investigated using X-ray diffraction and Raman spectroscopy, with accompanying *ab-initio* molecular dynamics simulations, across a similar pressure range to the current study [104]. It was reported that as AsSe is compressed, the structure transforms from a quasi-layered structure dominated by pyramidal $AsSe_3$ units, to a more tightly packed amorphous 3D network in which the pyramidal units are distorted. Raman spectra revealed that this transition is mostly complete by ∼7.6 GPa, and is finally completed at ∼14 GPa. The effective coordination number calculated from integrating the first peak of the total pair-distribution function obtained from the accompanying molecular dynamics simulations, was observed to initially reduce from ∼2.2 at ambient, to ∼2.0 at ∼7 GPa. At higher pressures, the effective coordination number gradually increased to a maximum value of ∼3.3 at 22 GPa. The values at ambient and 7 GPa are lower than those obtained in the present work, however they were obtained from the accompanying *ab-initio* simulations, rather than diffraction data.

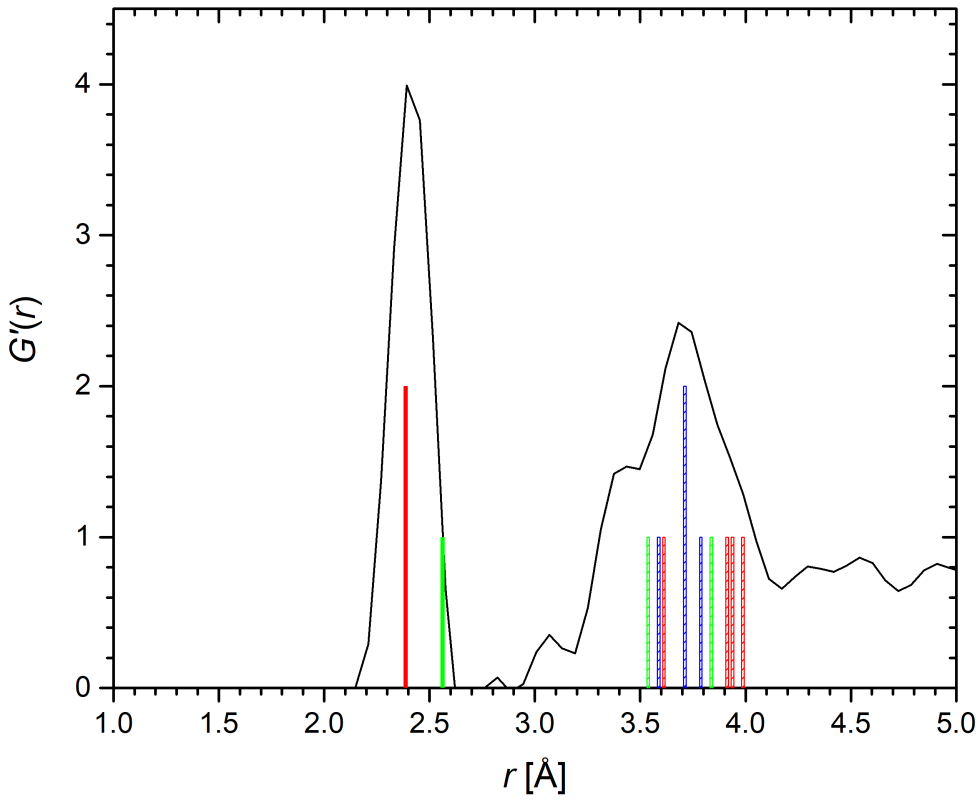

Figure 6.13: The total pair-distribution function $G'(r)$ for AsSe glass measured by the D4c diffractometer using the Paris-Edinburgh press at ambient conditions, compared with the bond lengths and intra-molecular separations found by Goldstein *et al* [103] for the As_4Se_4 crystalline structure. The bond lengths or separations have been normalised to account for the presence of multiple As and Se crystalline sites, where each red, green or blue vertical bar represents an As-Se, As-As or Se-Se bond or separation, respectively. Bonds are shown as solid bars, whilst separations are shown as dashed bars. The shorter bars correspond to a single bond, whilst the higher bars correspond to two bonds.

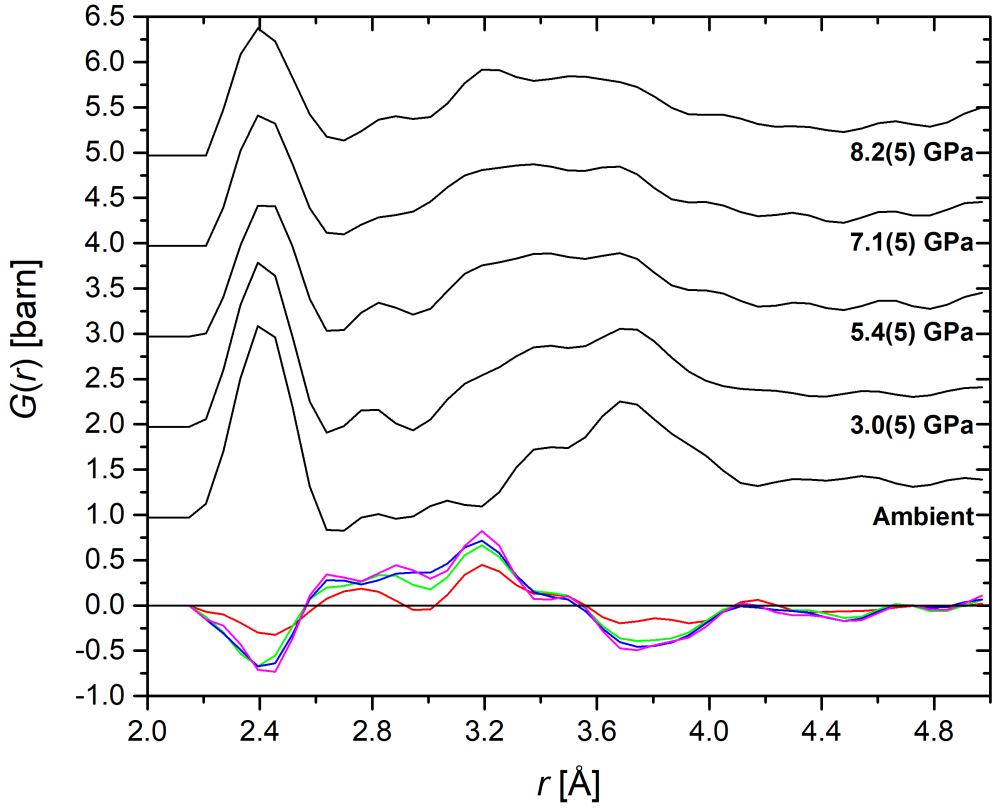

Figure 6.14: The total D4c pair-distribution functions $G(r)$ for AsSe glass (solid black curves), obtained by Fourier transforming the $F(Q)$ functions shown in Figure 6.4. The datasets have been offset vertically for clarity of presentation. The coloured lines correspond to the difference functions calculated using Equation 6.13: $\Delta G_{3.0\mathrm{GPa}}(r)$ (red), $\Delta G_{5.4\mathrm{GPa}}(r)$ (green), $\Delta G_{7.1\mathrm{GPa}}(r)$ (blue) and $\Delta G_{8.2\mathrm{GPa}}(r)$ (magneta).

6.6 Conclusions

The structure of AsSe glass was investigated using *in-situ* neutron diffraction at pressures up to 14.4(5) GPa using the Paris-Edinburgh press in conjunction with either the D4c or PEARL diffractometers. The effective coordination number decreases slightly from $\bar{n}' = 2.35(10)$ at ambient, to $\bar{n}' = 2.1(2)$ at 14.4(5) GPa. This contrasts with previous work on As_2Se_3 glass [27], where no change in the effective coordination number was observed. It is therefore proposed that the higher ambient effective coordination number of AsSe originates from an increased concentration of As, and furthermore that As is more susceptible to a pressure-driven coordination change than Se. As pressure is increased, the large peaks at $r \sim 3.4$ Å and $r \sim 3.7$ Å shift to lower values of r, and these changes are prominent across the range of measured pressure points. In contrast, no change is observed in the nearest neighbour bond distance with pressure ($r \sim 2.41$ Å). These results imply that the densification mechanism of AsSe glass is dominated by a reorganisation of larger structural units, which is reflected by a shortening of intra-molecular distances, whilst the nearest neighbour coordination shell appears to remain mostly unchanged although a small decrease in effective coordination is observed. These results appear to be in agreement with high pressure Raman spectroscopy studies [104], which indicate a breakdown of the dominant $AsSe_3$ structural unit which forms a quasi-layered structure, to a more random 3D network in which no structural unit is dominant.

In order to obtain a more detailed understanding of the densification process of AsSe glass, it is necessary to perform a high pressure neutron diffraction with isotopic substitution (NDIS) experiment [105]. This technique can be used to isolate the first-order difference pair-distribution functions with either the As-As, As-Se or Se-Se correlations removed. This information can provide insight into the behaviour of individual pair-correlations as a function of pressure, and what drives the densification process.

7 Temperature Calibrations of a High-Pressure High-Temperature Setup for Neutron Diffraction with the Paris-Edinburgh Press

7.1 Introduction

The work presented in this thesis has used neutron diffraction with cold compression, in which the sample is compressed at ambient temperature. However, it is desirable to have detailed structural information at both high pressure *and* high temperature (HPHT) conditions. Sample cells for HPHT X-ray diffraction are relatively abundant, and are available for use at several X-ray synchotron facilities worldwide [106, 107]. However, development of the corresponding technology for use with neutron diffraction is comparatively less advanced. As neutron diffraction offers complementary information to X-ray diffraction, increasing the maximum temperature accessible for *in situ* neutron diffraction experiments will create new experimental possibilities. The ability to replicate upper mantle like conditions of temperature and pressure in experiment is also of significant geological interest.

The sample cells so far developed for HPHT neutron diffraction use a cylindrical resistive heater, typically graphite, which contains a sample enclosed inside an electrically insulating material. The heater is typically enclosed within a material of very low thermal conductivity, which serves to minimise heat loss to the surrounding environment. However, accurately determining the sample temperature of HPHT setups is challenging. When beamline access is available, the temperature may be determined using neutron absorption resonance. For example, if a piece of Ta foil is embedded with the sample, the width of the Ta absorption lines has a direct relationship to temperature via the Doppler effect [108]. However, this requires complicating the sample cell preparation in a time-critical beamline environment, and reduces the available sample space. Thermocouples may be used to directly measure the sample temperature, however such experiments are prone to failure due to the vulnerability of the thermocouple wire to shear strain, hence this technique cannot be relied on in a time-critical beamline environment.

The setup used in this chapter was originally developed by Le Godec *et. al.* [25], and further adapted by Klotz *et. al.* [26]. This chapter presents the results of temper-

ature calibrations of the latter setup using thermocouples, with the aim of facilitating automated use i.e so the sample temperature may be inferred directly from the power input. The setup and ancillary equipment, and the method of the calibration experiments are described in detail in section 7.2. The results are presented and interpreted in section 7.3, and finally conclusions are drawn in section 7.4.

7.2 Experimental Method

7.2.1 Setup

The temperature calibrations presented in this chapter were performed using the setup developed by Klotz *et. al* [26]. For these experiments, a VX4 Paris-Edinburgh press was used in conjunction with single toroid tungsten carbide (WC) anvils. Figure 7.1 gives an overview of the experimental setup. A hand pump (Enerpac SCR256H) is connected to an oil inlet on the underside of the VX4 PE press, which is used to provide pressure. The oil pressure is monitored both at the position of the hand pump, and at the oil inlet of the PE press using two transducers. A refrigerator and circulator (Julabo FP50-HL) was used to channel cooling fluid to regulate the temperature of the PE press. A power supply (TkD-Lambda GEN10-330), was used to heat the setup.

The HPHT cell is shown in Figure 7.2, and has been adapted to match the profile of the WC anvils, the drawings of which are shown in Figure 7.3. The dimensions for each component in the assembly are provided in Table 7.1. The sample sits inside a cylindrical magnesia (MgO) container, with two discs at either end to form a closed container. Magnesia is used as a sample container because of its excellent refractory properties: it is physically and chemically stable at high temperatures, and it is electrically insulating. The MgO container is encased in a graphite cylinder, with two graphite discs at either end to form a closed furnace. As graphite is an excellent conductor of electricity, a piece of sufficiently thin cross section can be used to obtain high temperatures via Joule heating. The amount of heat generated by the furnace is proportional to the size of current and electrical resistance, according to the relation

$$P \propto I^2 R. \tag{7.1}$$

The resistance of the conductor is temperature dependent, and is defined by the fol-

Figure 7.1: An overview of the experimental setup (top), and the TkD-Lambda GEN10-330 power supply (bottom). The numbers correspond to: (1) the VX4 Paris-Edinburgh press, (2) copper plating attached to the press which cooling fluid was channeled through (additional plating is located on the underside of the press), (3) Julabo FP50-HL Refrigerator and Circulator, (4) Enerpac SCR256H Hand Pump.

Component	Diameter [mm]	Height [mm]
Stainless Steel / Molybdenum Rings	ID=3.00(+0.01), OD=3.50(-0.01)	0.80
Magnesia Discs (outer)	3.00(-0.01)	0.65
Magnesia Discs (inner)	3.00(-0.01)	0.50
Magnesia Cylinder	ID=2.00(-0.01), OD=3.00(-0.01)	1.60
Graphite Disc	3.50(-0.01)	0.55
Graphite Cylinder	ID=3.00(+0.01), OD=3.50(-0.01)	2.60

Table 7.1: The dimensions of the constituent parts of the furnace assembly, inner diameters (ID) and outer diameters (OD) are specified when appropriate.

lowing relationship

$$R = \frac{\rho l}{A}, \tag{7.2}$$

where l, A and ρ denote the length, cross-sectional area, and electrical resistivity of the conductor, respectively. Electrical resistivity varies with temperature, and is therefore an important consideration for selecting the appropriate furnace material. Figure 7.4 shows the electrical resistivity of graphite, compared against metals typically used for resistive heating furnaces. Graphite possesses a key advantage over metal foil resistive heaters, since its electrical resistivity initially decreases with temperature, before increasing again. In contrast, the electrical resistivity of metals typically increases linearly with temperature. In practice, this effect makes metal foil furnaces harder to control at higher temperatures [109].

In order to pass current from the anvils to the graphite furnace, stainless steel rings are typically used to provide electrical contact. In the calibration experiments presented in this chapter, Molybdenum (Mo) rings were used. Molybdenum possesses a significantly higher ambient pressure melting point of 2896 K, compared to stainless steel (1600 K to 1800 K depending on the specific grade), hence reducing the likelihood of the contact material melting and rendering the setup unstable. Inside the Mo rings, MgO discs were placed in order to provide extra thermal insulation between the furnace and anvils. The Mo rings protrude from the MgO discs by 0.15 mm, in order to optimise electrical contact.

Encasing the graphite furnace is a pyrophyllite bicone, followed by a further pyrophyllite gasket. The drawings for these components are shown in Figure 7.5. Pyro-

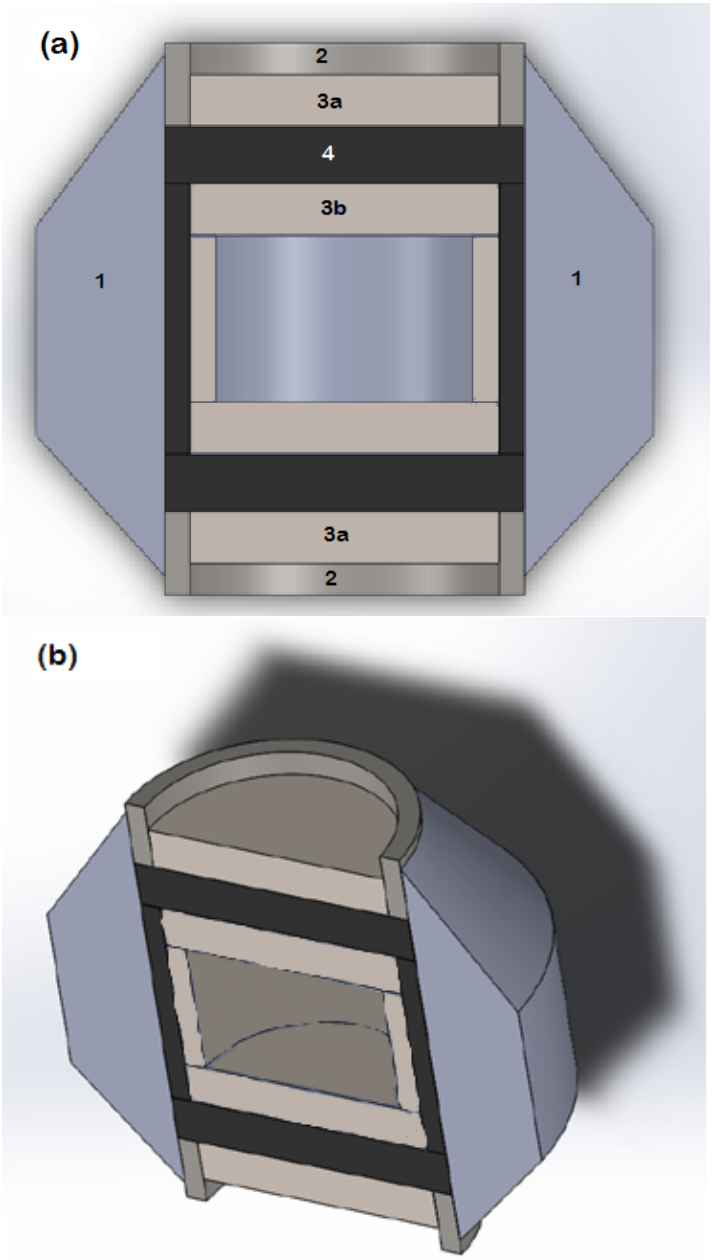

Figure 7.2: The furnace assembly design for the HPHT cell. In (a) the cross section of the setup is shown with the components labelled: 1) pyrophyllite bicone, 2) stainless steel / Mo ring and discs, 3a) MgO discs, 3b) MgO sample holder and 4) graphite furnace. Shown in (b) is the assembly viewed from an elevated angle to highlight the geometry of the setup. The dimensions of the pyrophyllite bicone are provided in Figure 7.5, and the dimensions of the rest of the constituent parts are provided in Table 7.1. Drawings courtesy of Michela Buscemi, University of Bath.

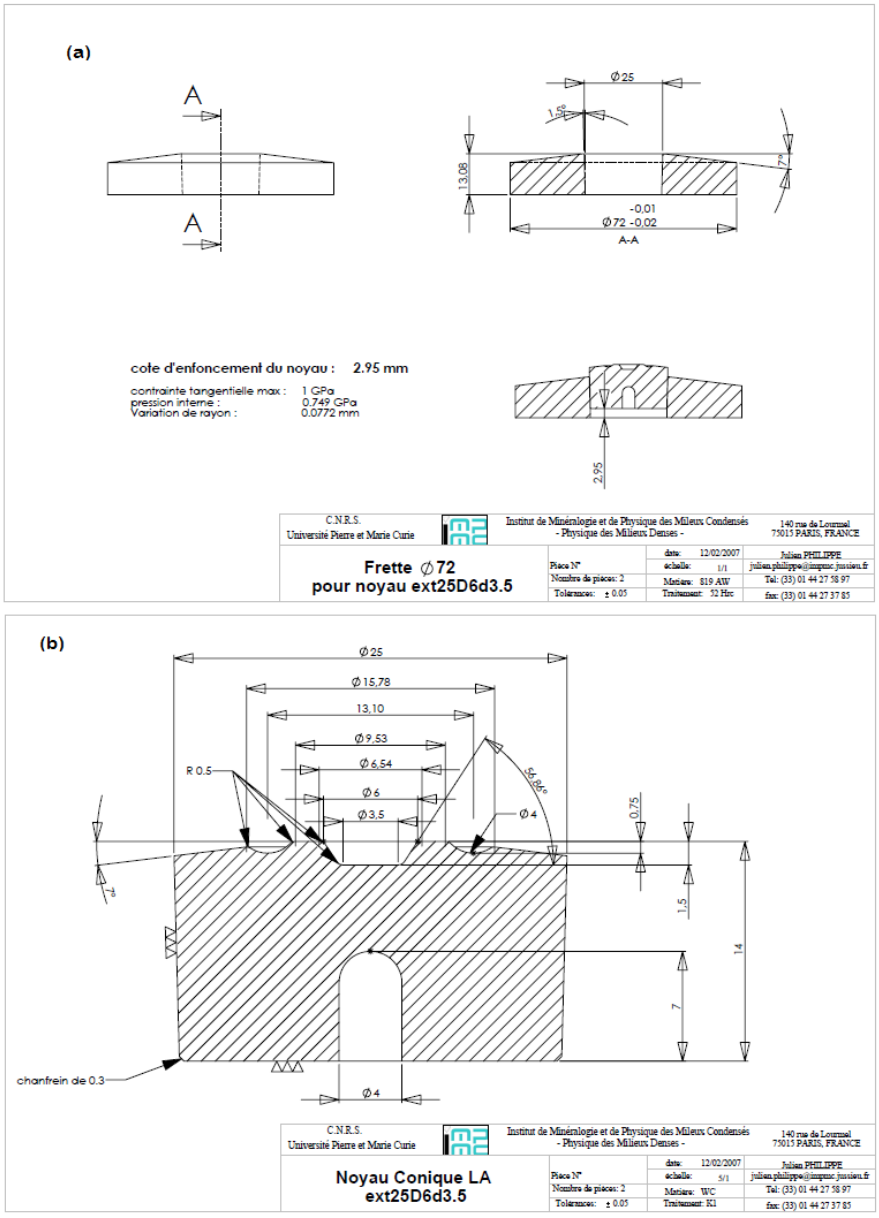

Figure 7.3: Drawings of the anvils in which the furnace assembly was mounted: (a) the anvils as a whole, and (b) the WC die [111].

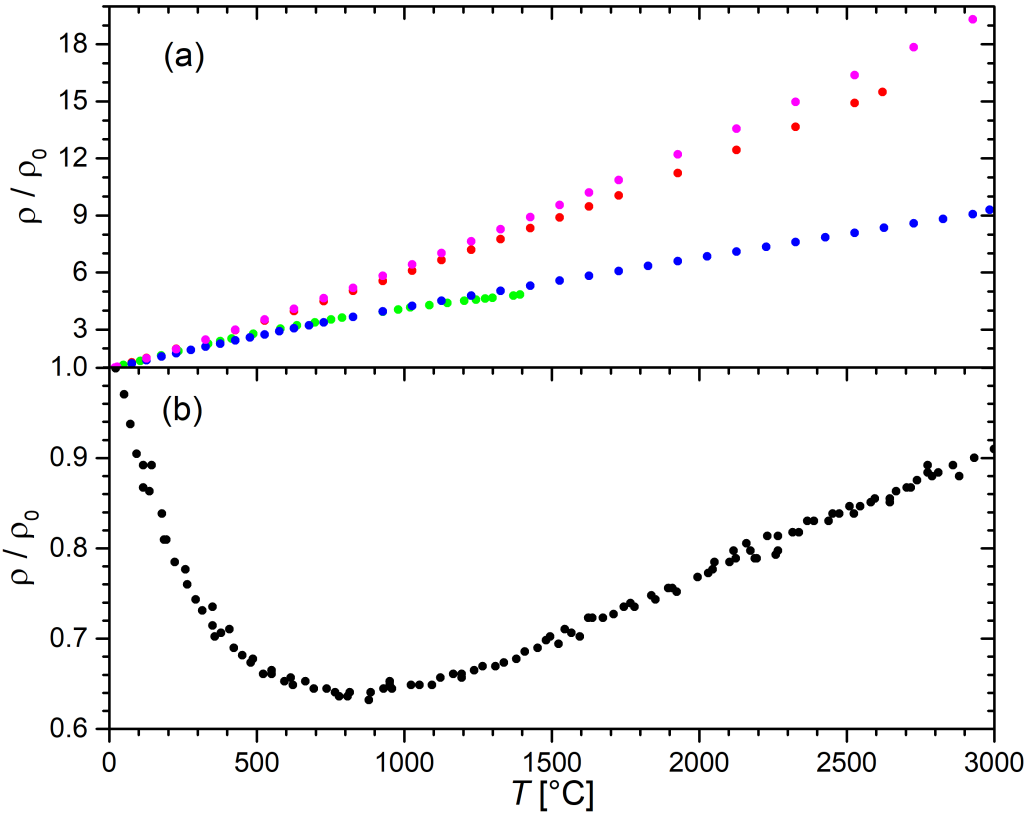

Figure 7.4: The temperature dependence of the relative electrical resistivity of (a) the metals W (magneta), Mo (red), Ta (blue) and Re (green), and (b) typical values for graphite. The relative electrical resistivity is calculated based on the room temperature value ρ_0. The values for W, Mo and Ta are taken from [112], the values for Re are taken from [113], and the values for graphite are taken from [114]. The graphite dataset was originally published in [115].

phyllite is a silicate mineral of chemical formula $Al_2Si_4O_{10}(OH)_2$. Pyrophyllite in its natural state is very easy to machine, but it can be heat treated to gain excellent refractory properties. When natural pyrophyllite is heat treated, water is removed from the material, its physical strength is improved and its melting temperature is increased. There are two commercial heat treated grades of pyrophyllite that were used in this work, so-called Ceramit 10 and Ceramit 14 [110]. The Ceramit 14 grade is heat treated to 1400°C, and possesses the lowest thermal conductivity and compressibility, whilst Ceramit 10 is heat treated to 800°C - 1000°C, and possesses intermediate properties between Ceramit 14 and the natural state. The annealing process for each pyrophyllite grade is given in Table 7.2, and the properties of each grade are listed in Table 7.3. Overall, heat treated pyrophyllite serves as an excellent thermal and electrical insulator, and its high mechanical strength makes it able to withstand the extreme pressures encountered in HPHT setups.

Ceramit 10	Ceramit 14
Heat at rate of 50°C per hour to 400°C	Heat at rate of 50°C per hour to 400°C
Heat at rate of 100°C per hour from 400°C to 900°C	Heat at rate of 100°C per hour from 400°C to 1300°C
Hold at 900°C for one hour	Hold at 1300°C for one hour
Allow to cool naturally inside the furnace	Allow to cool naturally inside the furnace

Table 7.2: The pyrophyllite heat treatment processes for Ceramit 10 and Ceramit 14 grades [110].

Property	Natural Pyrophyllite	Ceramit 10	Ceramit 14
Hardness [Mohs]	2.5	5	7
Softening Temperature [°C]		1600	1600
Coefficient of linear thermal expansion [x10^{-6}]		2.9 - 3.5	6 - 8
Thermal Conductivity [W mK^{-1}]		1.5	1.9
Compressive Strength [kN cm^{-2}]		10.3	15.16
Cross-bending Strength [kN cm^{-2}]			
Tensile Strength [kN cm^{-2}]			
Volume Resistivity [500 MΩ cm^{-3}]	10^6	10^6	

Table 7.3: The known physical properties of natural pyrophyllite and the two heat treated states [110].

Encasing the pyrophyllite gasket is a copper berryllium gasket (CuBe), which is

split into two equal halves on its lateral axis. The drawing for a single half is shown in Figure 7.6. The specific alloy used is Berylco 25, which is primarily composed of copper, and contains 2.0% beryllium, and trace amounts of cobalt, nickel and iron [47]. It is used because of its excellent mechanical properties, and it is easy to anneal the alloy in any laboratory to achieve the specific properties required. The CuBe split gaskets were machined from a rod of Berylco 25 (unannealed), and initially preformed in a laboratory press by placing the gasket between a WC anvil, and a metal block with a flat surface, to a load of 20 tonnes. The purpose of this was to enable the gasket to take the shape of the toroidal profile of the anvil's surface. After this, the gasket was annealed at a temperature of ∼300 °C for 30 minutes. During this process, beryllium precipitates out of the alloy which results in a hardening of the material [47]. Finally, the flat surface of the gasket was polished using sandpaper of 600 grit size, and the inner edges filed to ensure the pyrophyllite gasket fit inside (the CuBe gasket typically expands outwards as it is preformed). For each experiment, the two split CuBe gaskets were glued together using Resbond 919, an electrically insulating adhesive [116] primarily composed of MgO, and binding agents. The purpose of this procedure is to provide electrical insulation between the two split CuBe gaskets, in order to avoid electrical shorting. Resbond 919 has a maximum continuous operating temperature of ∼1500°C, making it suitable for high temperature applications.

Despite the insulating properties of pyrophyllite and MgO, due to the very high temperatures the graphite furnace is capable of reaching it is necessary to cool the setup externally in order to: (a) Prevent the oil in the press piston from heating significantly, and (b) Avoid heating the main body of the Paris-Edinburgh press significantly. If oil temperature heats significantly, it becomes difficult to maintain a constant pressure during operation, which in turn makes the collection of reliable data difficult. Furthermore, the temperature of the Paris-Edinburgh press should not exceed 80°C, as this can weaken the mechanical properties of the steel [109]. A refrigerator circulator (Julabo FP50-HL) was connected to specially designed copper rings which enclosed the anvils, which enabled the circulation of fluid maintained at a constant temperature (typically 10°C) in order to regulate the temperature of the Paris-Edinburgh press. In order to provide power to the system, a high power supply (TDK-Lambda, GEN10-330) was connected in series to the setup, via copper bars attached to the cooling rings surrounding each anvil.

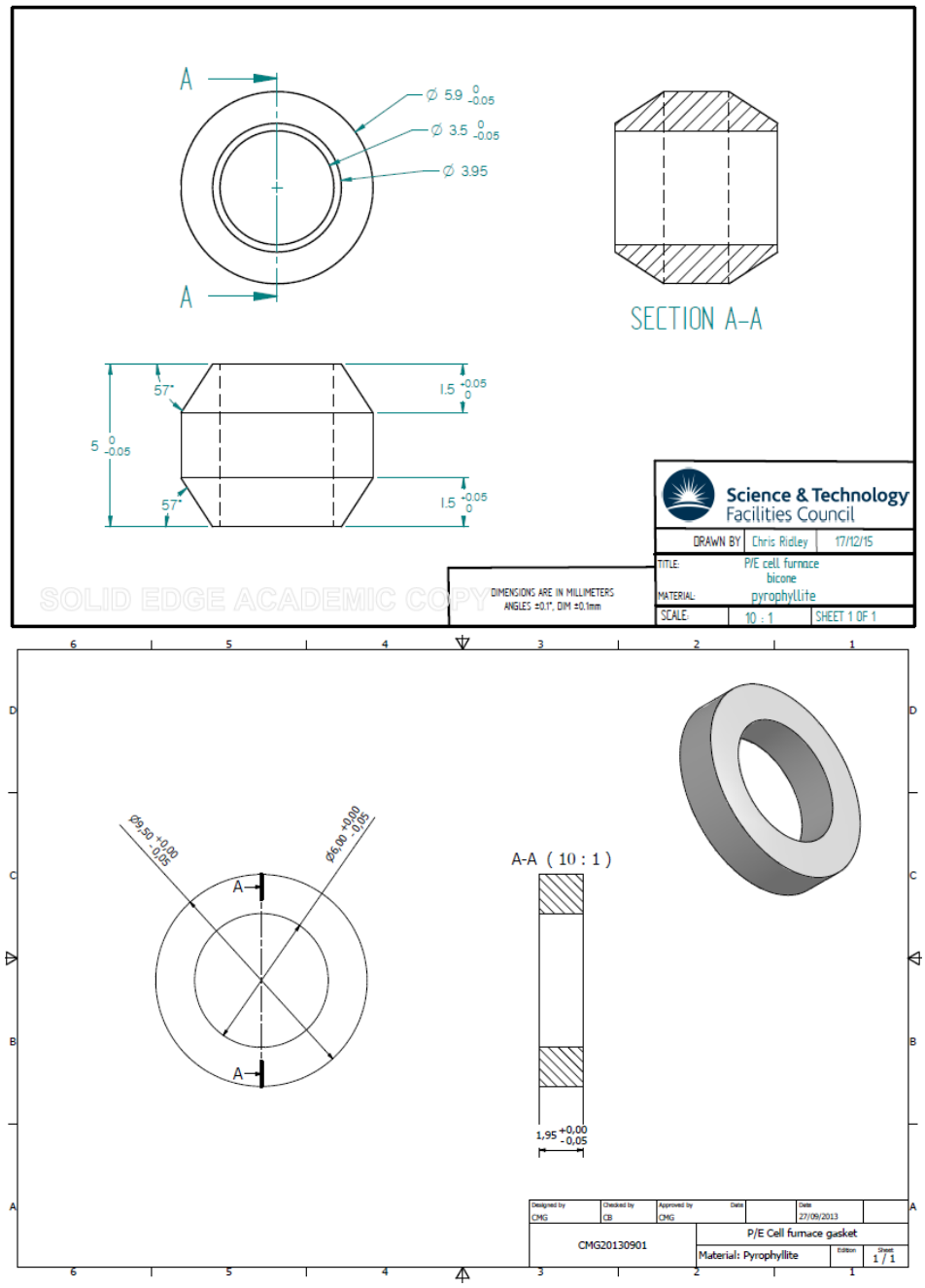

Figure 7.5: Drawings of the pyrophyllite bicone (top) and pyrophyllite gasket (bottom) [109].

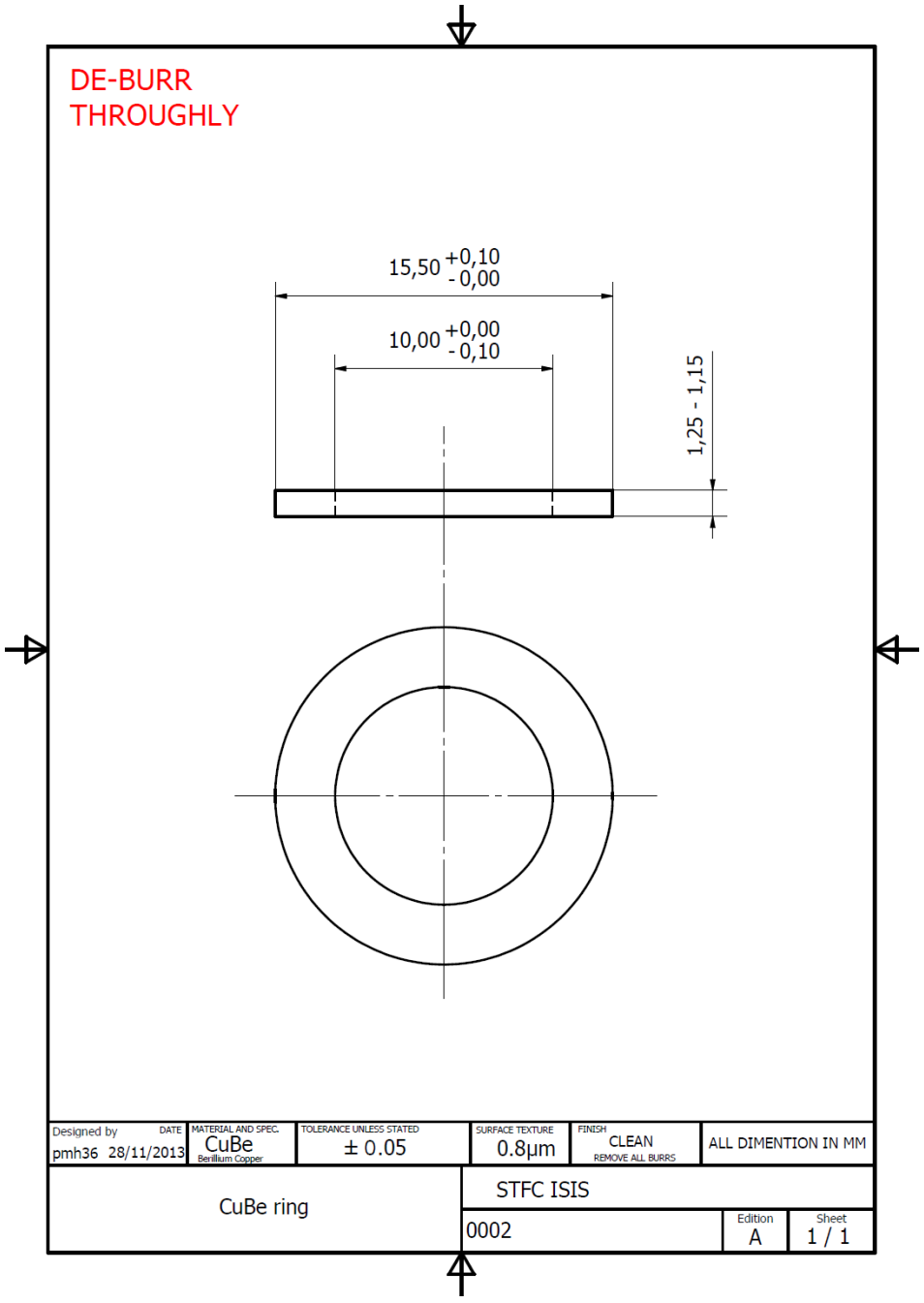

Figure 7.6: Drawing of the split CuBe gasket [109]. For each experiment, two gaskets were used and glued together with electrically insulating Resbond 911 paste.

7.2.2 Temperature Calibration Method

This chapter presents the results of five thermocouple temperature calibration experiments performed for the described setup, using a VX4 Paris-Edinburgh press at the University of Bath. The calibration setup used for each experiment was identical to the setup presented in Figure 7.2, except that the MgO sample holder was replaced with two solid MgO tubes each with a diameter of 3.0 mm and a height of 1.0 mm. When assembling the setup, the first MgO tube was placed inside the graphite furnace, and then a layer of finely ground MgO powder was placed, with the second MgO tube on top. The purpose of was to fill as much space as possible in the assembly, since in early calibration attempts the setup would collapse on compression and destroy the thermocouple junction.

A thermocouple consists of two dissimilar electrical conductors joined at one end: when this end is heated a voltage is generated as a consequence of the thermoelectric effect, which can then be measured and converted to a temperature. For all experiments, K-type (Chromel-Alumnel) thermocouples were used to measure the temperature inside the graphite furnace. K-type thermocouples were chosen for these experiments as they are accurate, easy to use and have a large temperature operating range (-270°C to 1260°C [117]). Each leg of the thermocouple wire was inserted into the assembly via small holes (0.5 mm) which were drilled into the assembly perpendicular to the axis of compression, at opposite ends. The two conductors were joined by arc welding, and placed in the approximate centre of the graphite furnace, however in practice the exact position of each thermocouple junction varied with each experiment. Furthermore, upon compression of the setup the thermocouple junction is likely to shift position. For experiments 1-4 two thermocouples were used (hence 4 holes drilled), whilst for experiment 5 only one thermocouple was used (2 holes drilled). In experiments where two thermocouples were used, it was ensured when assembling the setup that the two junctions were not in contact and separated by MgO powder. However, in experiments 1-4 the second thermocouple was lost during compression to 150 bar, so only one thermocouple was functional during these calibrations.

For experiments 4 and 5, the thermocouple wires were protected within alumina (Al_2O_3) sheaths, the aim of this was to provide extra mechanical protection to the thermocouple wire during compression, since the wires were often sheared during compression of the setup. It also served to thermally insulate the thermocouple wire; the

insulation of the wire perfluoroalkoxy alkane (PFA), melts at 315°C. Therefore, there is a risk that an unprotected thermocouple wire may come into electrical contact with the graphite furnace, which could interfere with measurements. Experiments 1-4 used pyrophyllite heat treated to Ceramit 14 grade (Tables 7.2 and 7.3), and experiment 5 used pyrophyllite heat treated to Ceramit 10 grade. The purpose of performing a calibration with Ceramit 10 grade was to investigate the effect of increasing the compressibility of the pyrophyllite bicone and gasket. In experiments 4 and 5, the surface temperature of the CuBe gasket was also recorded, via a K-type thermocouple attached to the side of the gasket. The purpose of this was to determine if direct measurement of the gasket temperature during an experiment could be used to reliably infer the corresponding sample temperature inside the furnace.

All the calibration experiments followed the same basic procedure. The setup was assembled and compressed to the required pressure point in steps of 50 bar. In experiments 1-3, the thermocouple junction was destroyed during compression between 150-300 bar, whilst experiments 4 and 5 used a maximum oil pressure of 300 bar and 350 bar, respectively. During calibration, the output current of the power supply was gradually increased in steps of typically 5 A or 10 A, and the corresponding voltage was recorded (and hence the output power calculated). The current was held at each step until the measured sample temperature stabilized. In experiments 4 and 5 where the gasket temperature was also recorded, the current was held constant for three minutes in order to ensure the gasket temperature had stabilized, since the low thermal conductivity of pyrophyllite introduced a thermal lag between the graphite furnace and the CuBe gasket. A cooling fluid temperature of 10°C was used to regulate the temperature of the Paris-Edinburgh press. Table 7.4 provides the specific details of each calibration experiment.

Experiment	Successful Oil Pressure Points [bar]	Al_2O_3 sheaths used and gasket temperature measured?	Pyrophyllite Grade
1	150	No	Ceramit 14
2	150	No	Ceramit 14
3	150	No	Ceramit 14
4	150(4a), 150(4b), 300(4c)	Yes	Ceramit 14
5	50(5a), 150(5b), 250(5c), 350(5d)	Yes	Ceramit 10

Table 7.4: The details of each calibration experiment presented in this chapter. In each calibration measurement the setup was heated, and then cooled to room temperature. Runs 4a and 4b were performed under the same pressure, the latter approximately three days after the former, and the setup was not decompressed in the intermediate period.

7.3 Results & Discussion

Figure 7.7 presents the measured temperature in the approximate centre of the graphite furnace, for five calibration experiments at an oil pressure of 150 bar. Generally, a linear relationship is observed between the measured sample temperature, and applied power. To demonstrate this, linear fits have made to the datasets, the parameters for which are given in Table 7.5. In experiments 1-3 where the thermocouple wires are not protected, the highest sample temperature is observed for a given power. The results of experiments 1-3 are in mostly excellent agreement, however at higher temperatures (T $\sim$500°C) the results begin to diverge. It is likely that since the thermocouple wires were unprotected, the PFA insulation was melted during the calibration (T_{melt} $\sim$300°C). This may have resulted in the thermocouple wire being exposed to the live graphite furnace, which could affect the measured voltage and yielded unrealistically high sample temperatures.

Experiment 4 consists of two repeated measurements (4a and 4b), with the latter measurement taken approximately 72 hours after the former. Both measurements were taken at an oil pressure of 150 bar and the sample cell was not decompressed in the intermediate period. The thermocouple wires were protected inside an alumina sheath, with only the junction in the approximate centre of the furnace being exposed. This appears to have protected the thermocouple insulation to a higher temperature (approximately 1000°C), the results generally show a linear power-temperature relationship and are mostly in excellent agreement with each other. In experiment 4b, a limited curvature can be observed in the power-temperature relationship at lower tem-

peratures. In both runs, the maximum stable furnace temperature was approximately 1000°C, however in experiment 4b a sample temperature of approximately 1100°C was held for a short period. Experiment 5 was identical in all respects to experiment 4, except that Ceramit 10 grade pyrophyllite was used instead of Ceramit 14 grade. This has had the affect of lowering the recorded sample temperature for a given power, a result which can be explained because of the increased thermal conductivity of Ceramit 10 pyrophyllite compared to Ceramit 14.

Figure 7.8 presents the measured temperature in the approximate centre of the graphite furnace as a function of power, for experiments 4 and 5 showing the results for runs at different pressures. As for Figure 7.7, linear fits have made to the datasets, the parameters for which are given in Table 7.5. In all cases, the effect of increasing sample pressure results in lowering the sample temperature, for a given power. The maximum stable sample temperature achieved was approximately 1000°C at ∼450 W in run 4a, whilst in run 4b the maximum temperature was ∼900°C at ∼500 W. In experiment 5, the same effect of pressure on sample temperature is observed across the range of measured pressure points (50 bar,150 bar,250 bar,350 bar). In runs 5a, 5b and 5c the measurements were halted at a sample temperature of ∼800°C in order to ensure the survival of the thermocouple wires. In run 5d (at 350 bar), a maximum sustained sample temperature of ∼1200°C was recorded.

Experiment	a_0 [°C W^{-1}]	T_0 [°C]
1,2,3	2.826(11)	21.73(85)
4a,4b	2.413(19)	30.9(3.8)
4c	1.881(5)	14.00(1.15)
5a	2.753(15)	9.53(2.04)
5b	2.262(17)	12.40(3.00)
5c	2.071(15)	14.97(2.79)
5d	2.011(12)	9.13(3.84)

Table 7.5: The parameters a_0 and T_0 obtained for each of the linear fits of the form $T = a_0 P + T_0$, shown in Figures 7.7 and 7.8.

Figure 7.9 presents the measured temperature in the approximate centre of the graphite furnace as a function of the measured gasket temperature, for experiments 4

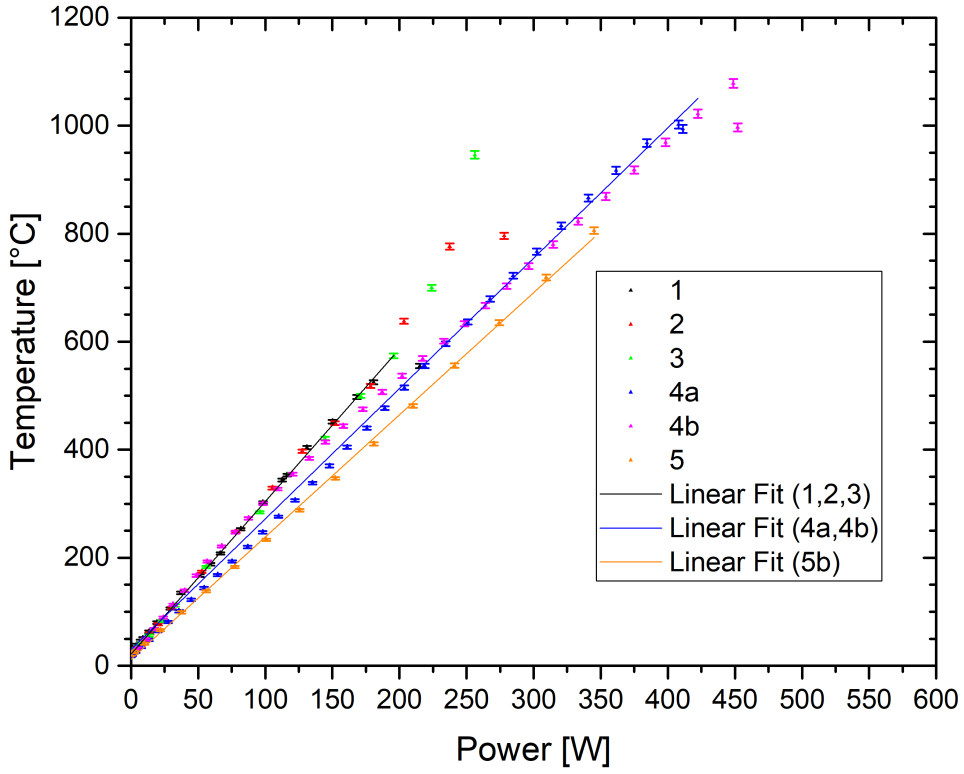

Figure 7.7: The measured temperature in the approximate centre of the graphite furnace as a function of power, for five calibration experiments. In the legend, the numbers refer to a given setup, whilst the letters denote an individual measurement run. All measurements were taken at an oil pressure of 150 bar. Errors in power are negligible.

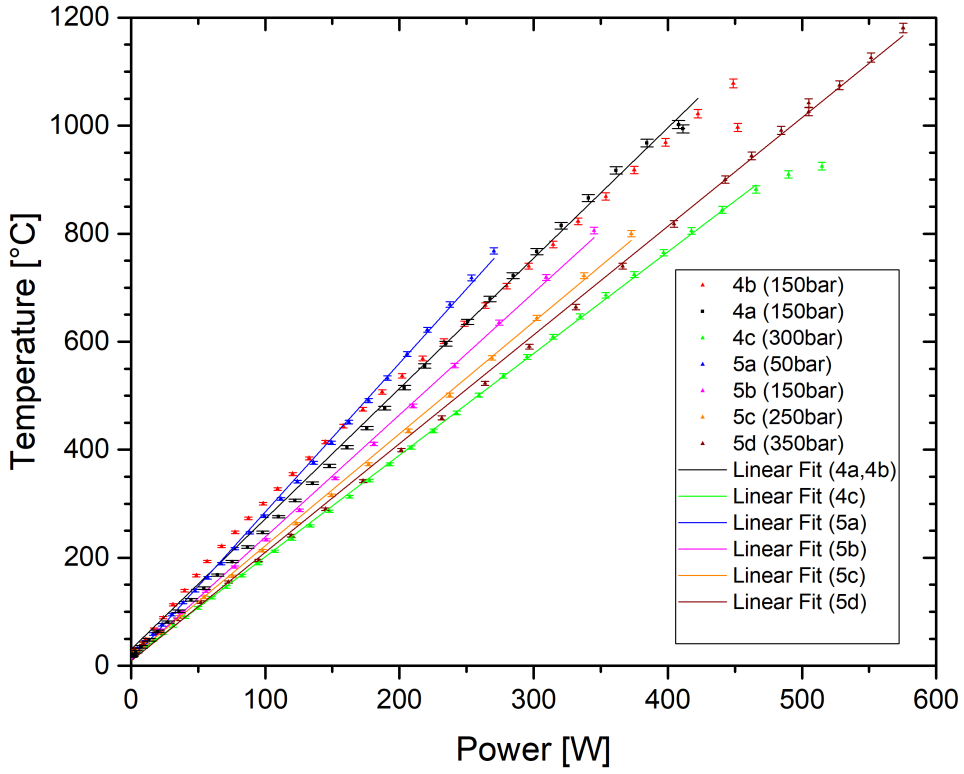

Figure 7.8: The measured temperature in the approximate centre of the graphite furnace as a function of power, for two calibration experiments at varying pressures. In the legend, the numbers refer to a given setup, whilst the letters denote an individual measurement run. Errors in power are negligible.

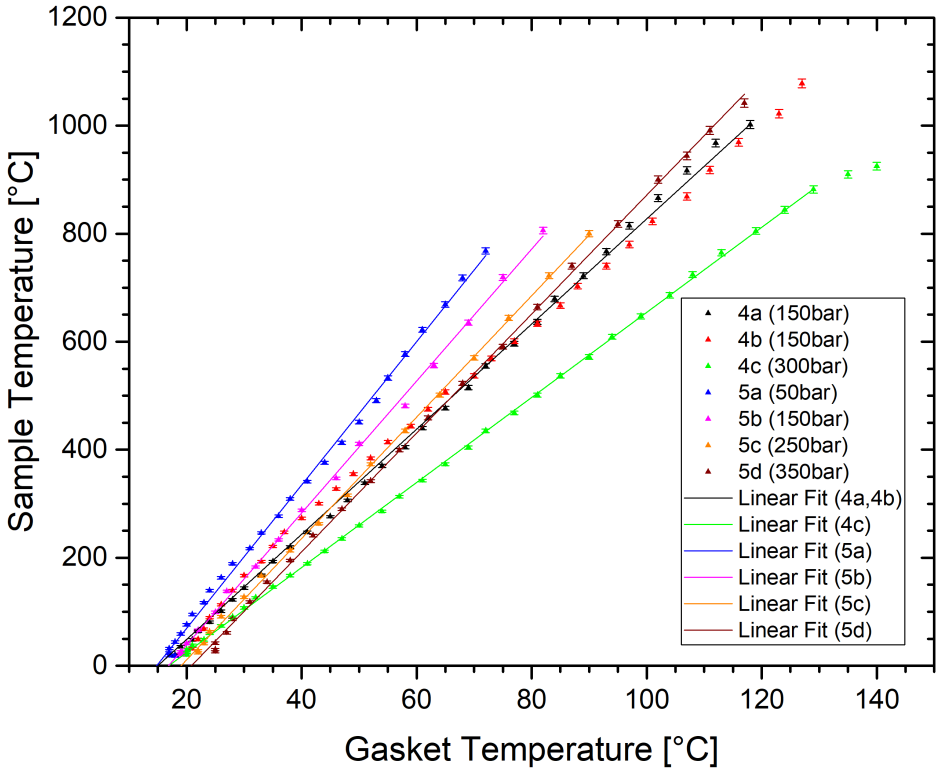

Figure 7.9: The measured temperature in the approximate centre of the graphite furnace as a function of the measured gasket temperature, for two calibration experiments at varying pressures. In the legend, the numbers refer to a given setup, whilst the letters denote an individual measurement run. Errors on the measured gasket temperature are omitted for clarity of presentation, and are +/- 2.2°C [117].

and 5. Generally, a linear relationship between sample temperature and gasket temperature is observed, and increasing the sample pressure lowers the measured sample temperature, for a given gasket temperature. Linear fits have been made to the datasets, the parameters of which are given in Table 7.6. At each step after increasing power, readings were taken after 3 minutes in order to allow the gasket temperature to equilibrate. The results indicate that for a given pyrophyllite grade the gasket temperature can be used to provide a reasonable estimation of the corresponding sample temperature. For example, the values from experiment runs 4a and 4b (both at 150 bar using Ceramit 14 pyrophyllite) show good agreement, and in these cases a measured gasket temperature of ∼120°C corresponds to a sample temperature of ∼1000°C. The same setup calibrated at 300 bar yields a lower sample temperature for the same gasket temperature, i.e a gasket temperature of ∼120°C corresponds to a sample temperature of ∼800°C, indicating more heat is lost to the surroundings as pressure is increased. In experiment 5 where Ceramit 14 grade pyrophyllite is replaced with Ceramit 10 grade pyrophyllite, a given gasket temperature corresponds to a higher sample temperature at the same pressure of 150 bar. For example at 150 bar, a gasket temperature of ∼60°C corresponds to a sample temperature of ∼450°C for the setup using Ceramit 14, and a sample temperature of ∼550°C for the setup using Ceramit 10. This result confirms that the Ceramit 10 pyrophyllite transfers a greater amount of heat to the surrounding anvils, than the Ceramit 14 pyrophyllite.

Experiment	a_0	T_0 [°C]
4a,4b	9.738(65)	-146.15(4.22)
4c	7.871(20)	-132.73(1.36)
5a	13.27(12)	-195.82(4.90)
5b	12.21(11)	-205.60(5.11)
5c	11.240(72)	-213.99(3.73)
5d	11.011(61)	-229.7(4.16)

Table 7.6: The parameters a_0 and T_0 obtained for each of the linear fits of the form $T = a_0 T_g + T_0$, shown in Figure 7.9.

7.4 Conclusions

The power-temperature relationship of the graphite furnace internal heating setup, originally developed by Le Godec *et. al* [25] and adapted by Klotz [26], has been investigated with calibration experiments using type-K thermocouples. Generally a linear relationship between power and sample temperature has been demonstrated in all experiments, and verified from linear fits. However, the exact temperature corresponding to a given power has been shown to be highly dependent on the sample pressure, with higher pressures yielding a lower sample temperature for the same power output. As Ceramit 14 grade pyrophyllite was replaced with Ceramit 10 grade, the corresponding sample temperature for a given power increased, albeit to a lesser extent. This can be explained via the increased thermal conductivity of Ceramit 10 pyrophyllite, compared to Ceramit 14. In two of the calibration experiments, the gasket temperature was also recorded. It was again demonstrated that increasing the sample pressure results in a lower sample temperature, for the same gasket temperature.

The calibration results indicate that it is possible to reliably determine the sample temperature for a given power output, or gasket temperature. However, it is necessary to perform further calibration experiments in the future under identical conditions, in order to provide a more reliable understanding of the power or gasket temperature versus sample temperature relationship. Furthermore, the experiments presented in this chapter have all used type-K thermocouples. It is also desirable to perform calibration experiments using type-C thermocouples, which can reliably measure temperatures up to $T{\sim}2300$°C [117]. In experiment 5d, a maximum sample temperature of ∼1300°C was recorded, which corresponds to the limit of the type-K thermocouple measurement capability. Hence, in order to investigate if higher sustained sample temperatures are possible with this type of sample cell, it is necessary to perform a successful calibration experiment with type-C thermocouples. At present, several calibration experiments have been attempted using type-C thermocouples, however none as of yet have survived compression of the setup.

Finally it is currently uncertain what sample pressure corresponds to a given oil pressure, for this type of setup. As discussed in Chapter 3, on a beamline the sample pressure corresponding to a given oil pressure may be determined by measuring a crystalline material with a known equation of state, for example NaCl [49]. However, such an experiment is not possible without access to a beamline, and it is therefore nec-

essary to use another method to obtain an accurate pressure calibration of the setup. For example, bismuth has four phase transitions (at 2.5 GPa, 2.7 GPa, 4.5 GPa and 6.5 GPa) in the range of ambient pressure to 8 GPa, at room temperature [118, 119]. Each of these phase transitions of bismuth is accompanied to a change in its electrical resistivity. It is therefore an ideal material to use as a pressure calibrant when conventional diffraction methods are unavailable. By placing a sample of bismuth in the centre of the sample cell, and then measuring its electrical resistance as a function of oil pressure, the corresponding sample pressure may be obtained.

8 Overall Conclusions

In this thesis, the structures of the modified silicate network glasses $MgSiO_3$ and $CaSiO_3$ were investigated using *in situ* neutron diffraction with a Paris-Edinburgh press at pressures up to 17.5(5) GPa. The structure of the chalcogenide glass AsSe was also investigated at pressures up to 14.4(5) GPa. Finally, the relationship between the applied power and sample temperature of a high pressure high temperature (HPHT) setup was investigated with a series of calibration experiments.

In chapter 4, the structure of magnesium silicate glass was investigated at pressures up to 17.5(5) GPa using *in situ* neutron diffraction. It was found that the mean Mg-O coordination number increases from an ambient value of $\bar{n}^{\mathrm{O}}_{\mathrm{Mg}} = 4.50(5)$, to $\bar{n}^{\mathrm{O}}_{\mathrm{Mg}} = 6.1(1)$ at 17.5(5) GPa. In contrast, the mean Si-O coordination number remains constant at its ambient value, $\bar{n}^{\mathrm{O}}_{\mathrm{Si}} = 4.0$. At ambient conditions, the distribution of Mg-O bonds was found to be highly asymmetric, as manifested by a high r shoulder observed in the second peak of the measured $G'(r)$ functions. This shoulder gradually disappears as pressure is increased, and shows that the distribution of Mg-O bonds becomes more symmetrical at higher pressures. In the crystalline enstatite structure, Mg is six-fold coordinated at ambient conditions, and the longer Mg-O bonds correspond to bridging-oxygen (BO) atoms, however the Mg-O coordination number remains constant with pressure i.e $\bar{n}^{\mathrm{O}}_{\mathrm{Mg}} = 6.0$ [88]. It is proposed that the Mg coordination change observed in the glass is driven by an increase in the relative fraction of magnesium to bridging oxygen (BO) atom bonds in the network. The accompanying molecular dynamics simulations have predicted an increase in the proportion of Q^3 sites associated with SiO_4 tetrahedra from ∼25% to ∼34%, and an increase in the fraction of Mg-BO bonds from ∼10% to ∼30% [75].

In chapter 5, the structure of calcium silicate glass was investigated at pressures up to 17.5(5) GPa using *in situ* neutron diffraction. It was found that the mean Si-O coordination number increases slightly from an ambient value of $\bar{n}^{\mathrm{O}}_{\mathrm{Si}} = 4.0$ to a value of $\bar{n}^{\mathrm{O}}_{\mathrm{Si}} = 4.12(10)$ at 17.5(5) GPa. The extent of coordination change is intermediate between that observed for $MgSiO_3$ ($\bar{n}^{\mathrm{O}}_{\mathrm{Si}} = 4.0(1)$) and SiO_2 [81] ($\bar{n}^{\mathrm{O}}_{\mathrm{Si}} = 4.2(1)$) glasses at 17.5(5) GPa. It is proposed that the inclusion of a network modifying cation delays the pressure-driven distortion of the SiO_4 tetrahedra in network glasses, and that Mg^{2+} provides a larger resistance to pressure than Ca^{2+}. Unfortunately, the Ca-O coordi-

nation number is not directly accessible with neutron diffraction due to overlap of the partial pair-distribution functions $g_{\mathrm{CaO}}(r)$ and $g_{\mathrm{OO}}(r)$. However, the accompanying molecular dynamics simulations [75] have predicted a large increase in the Ca-O coordination number from $\bar{n}^{\mathrm{O}}_{\mathrm{Ca}}$ ∼6 at ambient to $\bar{n}^{\mathrm{O}}_{\mathrm{Ca}}$ ∼7.4 at 17.5(5) GPa. Furthermore, a large increase in the fraction of Ca-BO bonds is also predicted from ∼15% at ambient to ∼30% at 17.5 GPa, accompanied by a small increase in the fraction of Q^3 and Q^4 sites. It is proposed therefore that the densification mechanism of $CaSiO_3$ glass is broadly similar to that which occurs in $MgSiO_3$ glass, however Ca^{2+} possesses a higher coordination number at ambient conditions, than Mg^{2+}.

In chapter 6, the structure of arsenic selenide glass was investigated at pressures up to 14.4(5) GPa using *in situ* neutron diffraction. It was found that effective coordination number decreased slightly from $\bar{n}' = 2.35(10)$ at ambient, to $\bar{n}' = 2.1(2)$ at 14.4(5) GPa. Previous high pressure diffraction work on As_2Se_3 glass [27] found no change across the same pressure range, although a lower ambient effective coordination number was found ($\bar{n}'$ ∼2.2). This suggests that the small decrease in effective coordination observed for AsSe originates from a higher concentration of As in the glass. As pressure is increased, the two peaks observed in the experimental $G'(r)$ functions of AsSe at r ∼3.4 Å and r ∼3.7 Å, shift to lower values of r. These distances are longer than the nearest neighbour distances, it is therefore proposed that the densification mechanism of AsSe glass is driven by a rearrangement of larger structural units whilst the nearest neighbour coordination environment remains mostly unchanged.

In chapter 7 the results of five temperature calibration experiments were presented for a high pressure high temperature setup for neutron diffraction, originally developed by Le Godec [25] and adapted by Klotz [26]. Generally, a linear relationship between power and sample temperature was found and verified from fits, and a lower sample temperature was found for a given power output, as pressure was increased. It was also found that replacing Ceramit 14 grade pyrophyllite with Ceramit 10 grade pyrophyllite, lowered the sample temperature recorded for a given power output. In two experiments, the relationship between the gasket temperature and sample temperature was also investigated. A linear relationship was determined, however the sample temperature was again found to be highly dependent on pressure, with a higher pressure resulting in a lower sample temperature for the same power. The results of these experiments show that it is possible to accurately measure the relationship between sample temperature

and gasket temperature and/or power for this setup, and potentially other HPHT setups. This therefore makes possible the automated use of the setup, where the need for a calibrant material is avoided.

Several future avenues of research have been proposed for the material presented in this thesis. The molecular dynamics simulations accompanying this thesis have predicted a large increase in the Ca-O coordination number as a function of pressure. However, it is not possible to extract the Ca-O coordination number from the experimental $G'(r)$ functions, due to significant overlap between the $g_{\mathrm{CaO}}(r)$ and $g_{\mathrm{OO}}(r)$ partial pair-distribution functions. It is therefore necessary to perform a high pressure neutron diffraction with isotopic substitution (NDIS) experiment on $CaSiO_3$ glass, which could be used to eliminate the partial pair-distribution functions not involving Ca. In this way, the first peak of the $g_{\mathrm{CaO}}(r)$ function could be isolated, and the coordination of Ca^{2+} in $CaSiO_3$ glass could be verified experimentally. The second proposed experiment to continue this work is a high pressure NDIS study on AsSe glass. It is only possible to obtain the effective coordination number from the experimental $G'(r)$ functions of AsSe glass. A high pressure NDIS experiment on AsSe glass could therefore be used to isolate the first-order difference $G'(r)$ functions with either the As-As, As-Se or Se-Se correlations removed. Therefore, a more detailed understanding of the densification mechanism of AsSe glass could be obtained.

Several future developments have been proposed to improve the HPHT calibration procedure. It is desirable to perform a series of temperature calibration experiments using type-C thermocouples. The limit of the type-K thermocouple is T ~1300°C, whilst type-C thermocouples can provide stable temperature measurements up to T ~2300°C. Therefore, a series of calibration experiments using type-C thermocouples will provide a greater understanding of the high temperature behaviour of the setup. Furthermore, the temperature calibration experiments presented in this thesis have been conducted based on the oil pressure of the Paris-Edinburgh press. However, for automated use of the setup it is necessary to construct a calibration curve for the sample pressure of the HPHT cell, as a function of oil pressure and/or temperature. It has been suggested that a series of pressure calibration experiments are performed, using Bismuth as a calibrant material. Bismuth has four phase transitions up to a pressure of 8 GPa at room temperature (2.5 GPa, 2.7 GPa, 4.5 GPa, 6.5 GPa) [118, 119]. These phase transitions are accompanied by a change in the electrical conductivity.

Hence, by measuring the electrical conductivity of a piece of Bismuth placed inside the setup, it is possible to generate a pressure calibration curve. These experiments will together provide a detailed understanding of the pressure and temperature behaviour of the setup, and enable fully automated use where the relationships between power and temperature, and oil and sample pressure, are fully understood.

Bibliography

[1] J. S. Sanghara, I. D. Aggarwal, L. B. Shaw, L. E. Busse, P. Thielen, V. Nguyen, P. Pureza, S. Bayya and F. Kung. Applications of chalcogenide glass fibres at NRL. *J. Optoelec. Adv. Mat.*, **3**:627, 2001

[2] A. Zakery and S. R. Elliot. Optical Properties and Applications of Chalcogenide Glasses: a Review. *J. Non-Cryst. Solids*, **330**:1, 2003

[3] B. J. Eggleton, B. Luther-Davies and K. Richardson. Chalcogenide Photonics. *Nature Phot.*, **5**:141, 2011

[4] M. Yamane and Y. Asahara. *Glasses for Photonics*. Cambridge University Press, Cambridge, U.K, 2000

[5] D. L. Anderson. *New Theory of the Earth*. Cambridge University Press, Cambridge, U.K, 2007

[6] J. P. Poirier. *Introduction to the physics of the Earth's interior*. Cambridge University Press, Cambridge, U.K, 1991

[7] F. Franks. *Water: A Matrix of Life*. Cambridge University Press, Cambridge, U.K, 2nd edition, 2000

[8] A. K. Varshneya. *Fundamentals of Inorganic Glasses*, 2nd edition. Society of Glass Technology, Sheffield, U.K, 2013

[9] R. L. Mozzi and B. E. Warren. The Structure of Vitreous Silica. *J. Appl. Crystallogr.*, **2**:164, 1969

[10] H. E. Fischer, A. C. Barnes and P. S. Salmon: Neutron and X ray diffraction studies of liquids and glasses. *Rep. Prog. Phys.*, **69**:233, 2006

[11] S. A. Amin, K. Leinenweber, C. J. Benmore, J. K. R. Weber and J. L. Yarger. Characterizing Pressure-Induced Coordination Changes in $CaAl_2O_4$ Glass using ^{27}Al NMR. *J. Phys. Chem. C*, **116**:2068, 2012

[12] S. K. Lee, Y. S. Yi, G. D. Cody, K. Mibe, Y. Fei and B. O. Mysen. Effect of Network Polymerization on the Pressure-Induced Structural Changes in Sodium Aluminosilicate Glasses and Melts: ^{27}Al and ^{17}O Solid-State NMR Study. *J. Phys. Chem. C*, **116**:2183, 2012

[13] P. F. McMillan. Polyamorphic Transformations in Liquids and Glasses. *J. Mater. Chem.*, **14**:1506, 2004

[14] V. V. Brazhkin and A. G. Lyapin. High pressure phase transformations in liquids and amorphous solids. *J. Phys. Condens. Matt.*, **15**:6059, 2003

[15] K. Arai, K. Kumata, K. Kadota, K. Yamamoto, H. Namikawa and S. Saito. Pressure effects of electrical conduction in Glasses. *J. Non-Cryst. Solids*, **34**:2143, 1973

[16] G. Pfister. Pressure dependent electronic transport in amorphous As_2Se_3. *Phys. Rev. Lett.*, **33**:1474, 1974

[17] R. Ota and O. L. Anderson. Variations in the mechanical properties of glass by induced high-pressure phase change. *J. Non-Cryst. Solids*, **24**:235, 1977

[18] J. C. Thompson and K. E. Bailey. A survey of the elastic properties of some semiconducting glasses under pressure. *J. Non-Cryst. Solids*, **27**:161, 1978

[19] B. B. Karki, J. Zhang and L. Stixrude. First-principles viscosity and derived models for MgO-SiO_2 melt system at high temperatures. *Geophys. Res. Lett.*, **40**:94, 2013

[20] C. D. Yin, M. Okuno, H. Morikawa, F. Marumo. Structure analysis of $MgSiO_3$ Glass. *J. Non-Cryst. Solids*, **55**:131, 1983

[21] L. Cormier and G. J. Cuello. Structural investigation of glasses along the $MgSiO_3$-$CaSiO_3$ join: Diffraction studies. *Geochimica et Cosmochimica Acta*, **122**:498, 2013

[22] A. L. Renninger and B. L. Averbach. Crystalline structures of As_2Se_3 and As_4Se_4. *Acta. Cryst. B*, **29**:1583, 1973

[23] C. J. Benmore and P. S. Salmon. Structure of fast ion conducting and semiconducting glassy chalcogenide alloys. *Phys. Rev. Lett.*, **73**:264, 1994

[24] S. Xin, J. Liu and P. S. Salmon. Structure of Cu-As-Se glasses investigated by neutron diffraction with copper isotope substitution. *Phys. Rev. B*, **78**:064207, 2008

[25] Y. Le Godec, M. Dove, S. Redfern, M. Tucker, W. Marshall, G. Syfosse and J. Besson. A new high P-T cell for neutron diffraction up to 7 GPa and 2000 K with measurement of temperature by neutron radiography. *High Pressure Research*, **21**:263, 2001

[26] S. Klotz, Y. Le Godec, T. Strassle, U. Stuhr. The $\alpha-\gamma-\eta$ triple point of Iron investigated by high pressure-high temperature neutron scattering. *App. Phys. Lett.*, **93**:091904, 2008

[27] K. J. Pizzey. *Glasses Under Extreme Conditions*. PhD Thesis, University of Bath, 2015

[28] J. W. E. Drewitt. *Structure of copper halide melts, rare earth chalcogenide glasses, and glassy germania at high pressure*. PhD Thesis, University of Bath, 2009

[29] G. E. Bacon. *Neutron Diffraction*. Oxford: Clarendon, 1975.

[30] V. F. Sears. Neutron Scattering Lengths and Cross Sections. *Neutron News*, **3**:26, 1992

[31] G. Placzek. The scattering of neutrons by systems of heavy nuclei. *Phys. Rev.*, **86(3)**:377, 1952

[32] T. E. Faber and J. M. Ziman. A Theory of the Electric Properties of Liquid Metals III: The Resistivity of Binary Alloys. *Philosophical Magazine*, **11(109)**:153, 1965

[33] G. Fournet. *Handbuch der Physik*. Berlin:Springer, **32**:317

[34] R. A. Martin, P. S. Salmon, H. E. Fischer and G. J. Cuello. Structure of dysprosium and holmium phosphate glasses by the method of isomorphic substitution in neutron diffraction. *J. Phys. Condens. Matter*, **15**:8235, 2003

[35] D. I. Grimley and A. C. Wright. Neutron scattering from vitreous silica IV, time of flight diffraction. *J. Non-Cryst. Solids*, **119**:49, 1990

[36] R. J. Angel. Equations of State. *Rev. Mineral. Geochem.*, **41**:35, 2000

[37] F. D. Murnaghan. The compressibility of media under extreme pressures. *Proc. Natl. Acad. Sci., USA*, **30**:244, 1944.

[38] F. Birch. Finite elastic strain of cubic crystals. *Phys. Rev.*, **71**:809, 1947

[39] S. Petitgirard, W. J. Malfait, R. Sinmyo, I. Kupenko, L. Hennet, D. Harries, T. Dane, M. Burghammer, D. C. Rubie. Fate of $MgSiO_3$ melts at core-mantle boundary conditions. *Proc. Natl. Acad. Sci. USA*, **112**:14186, 2015

[40] https://www.ill.eu/reactor-environment-safety/safety/faq-reactor-safety/what-are-the-technical-specifications-of-the-ills-reactor/ (accessed September 2016)

[41] A. Polidori. *Structure of disordered materials: From geological fluids to network glasses.* PhD Thesis, University of Bath, 2017

[42] H. E. Fischer, G. J. Cuello, P. Palleau, D. Feltin, A. C. Barnes, Y. S. Badyal and J. M. Simonson. D4c: A very high precision diffractometer for disordered materials. *Applied Physics A: Materials Science and Processing*, **74**:S160, 2002

[43] http://www.isis.stfc.ac.uk/about-isis/how-isis-works—in-depth4371.html (accessed August 2016)

[44] R. F. Rowlands. *The role of structural disorder in crystalline, glassy and liquid materials.* PhD Thesis, University of Bath, 2015

[45] C. L. Bull, N. P. Funnell, M. G. Tucker, S. Hull, D. J. Francis and W. G. Marshall. PEARL: the high pressure neutron powder diffractometer at ISIS. *High Pressure Research*, **36**:493, 2016

[46] D. A. J. Whittaker. *The Structure and Dynamics of Fundamental Glasses by Neutron and X-ray Scattering Techniques.* PhD Thesis, University of Bath, 2012

[47] S. Klotz. *Techniques in High Pressure Neutron Scattering.* CRC Press, Baton Rouge, U.S.A, 2012

[48] P. S. Salmon and A. Zeidler. Networks under pressure: The development of *in situ* high-pressure neutron diffraction for glassy and liquid materials. *J. Phys. Condens. Matt*, **27**:133201, 2015

[49] P. S. Salmon, J. W. E. Drewitt, D. A. J. Whittaker, A. Zeidler, K. Wezka, C. L. Bull, M. G. Tucker, M. C. Wilding, M. Guthrie and D. Marrocchelli. Density-driven structural transformations in network forming glasses: A high pressure neutron diffraction study of GeO_2 glass up to 17.5 GPa. *J. Phys. Condens. Matter*, **24**:415102, 2012

[50] R. J. Hemley, A. P. Jephcoat, H. K. Mao, C. S. Zha, L. W. Finger and D. E. Cox. Static compression of H_2O ice to 128 GPa (1.28 Mbar). *Nature*, **330**:737, 1987

[51] D. Martínez-García, Y. Le Godec, M. Mézouar, G. Syfosse, J. P. Itié and J. M. Besson. Equations of State of MgO at high pressure and temperature. *High Press. Res.*, **18**:339, 2000

[52] A. Le Bail, H. Duroy and J. L. Fourquet. Ab-initio structure determination of LiSbWO by x-ray powder diffraction. *Mater. Res. Bull.*, **23**:447, 1988

[53] C. L. Bull, M. Guthrie, S. Klotz, J. Phillipe, T. Strassle, R. J. Nelmes, J. S. Loveday and G. Hamel. Toroidal anvils for single-crystal neutron studies. *High Pressure Research*, **25(4)**:229, 2005

[54] H. H. Paalman and C. J. Pings. Numerical evaluation of x-ray absorption factors for cylindrical samples and annular sample cells. *J. Appl. Phys.*, **33(8)**:2635, 1962

[55] A. K. Soper and P. A. Egelstaff. Multiple scattering and attenuation of neutrons in concentric cylinders: 1. Isotropic first scattering. *Nucl. Instrum. Methods*, **178**:415, 1980

[56] J. E. Enderby, D. M. North and P. A. Egelstaff. The partial structure factors of liquid Cu-Sn. *Phil. Mag.*, **14**:961, 1966

[57] D. M. North, J. E. Enderby and P. A. Egelstaff. The structure factors for liquid metals I. The application of neutron diffraction techniques. *J. Phys. C.*, **1**:784, 1968

[58] S. E. McLain, D. T. Bowron, A. C. Hannon and A. K. Soper. *GUDRUN: A computer program developed for analysis of neutron diffraction data.* Technical Report, ISIS Facility, Rutherford Appleton Laboratory, 2009

[59] A. K. Soper and P. A. Egelstaff. Multiple scattering and attenuation of neutrons in concentric cylinders. *Nuc. Inst. Meth.*, **178(2-3)**:415, 1980

[60] M. A. Howe, R. L. McGreevy and W. S. Howells. The analysis of liquid structure data from time of flight neutron diffractometry. *J. Phys. Condens. Matter*, **1(22)**:3433, 1989

[61] P. S. Salmon and J. Liu. The relation between the melt topology and glass-forming ability for liquid Ge-Se alloys. *J. Phys. Condens. Matter*, **6**:1449, 1994

[62] A. P. Sokolov, A. Kishuk, M. Soltwisch and D. Quitmann. Medium-range order in glasses: Comparison of Raman and diffraction measurements. *Phys. Rev. Lett.*, **69**:1540, 1992

[63] P. S. Salmon. Decay of the pair-correlations and small-angle scattering for binary liquids and glasses. *J. Phys. Condens. Matter*, **18**:11443, 2006

[64] E. Lorch. Neutron diffraction by germania, silica and radiation-damaged silica glasses. *J. Phys. C*, **2**:229, 1969

[65] A. Pedone, G. Malavasi, M. Cristina Menziani, U. Segre and A. N. Cormack. Role of Magnesium in Soda-Lime Glasses: Insight into Structural, Transport and Mechanical properties through computer simulations. *J. Phys. Chem. C*, **112**:11034, 2009

[66] M. C. Wilding, C. J. Benmore and J. K. R. Weber. Changes in the local environment surrounding magnesium ions in fragile MgO-SiO_2 liquids. *Europhysics Letters*, **89**:26005, 2010

[67] L. Cormier and G. J. Cuello. Mg coordination in a $MgSiO_3$ glass using neutron diffraction coupled with isotope substitution. *Phys. Rev. B*, **83**:224204, 2011

[68] S. Kohara *et al.* Relationship between topological order and glass forming ability in densely packed enstatite and forsterite composition glasses. *Proc. Natl. Acad. Sci. USA*, **108**:14780, 2011

[69] https://www.uni-muenster.de/Chemie.pc/eckert/glass.html (webpage accessed September 2016)

[70] D. Waasmaier and A. Kirfel. New analytical scattering factor functions for free atoms and ions. *Acta. Cryst.*, **A51**:416, 1995

[71] http://www.bristol.ac.uk/physics/research/complex/research/glasses/ (webpage accessed August 2016)

[72] C. Benmore. Private Communication, 2015

[73] Corning Inc. Private Communication, 2017

[74] C. Sanchez-Valle and J. Bass. Elasticity and pressure-induced structural changes in vitreous $MgSiO_3$ - enstatite to lower mantle pressures. *Earth and Planetary Science Letters*, **295(3)**:523, 2010

[75] M. Salanne and Y. Ishii. Private Communication, 2018

[76] K. Shimoda and M. Okuno. Molecular dynamics study of $CaSiO_3$-$MgSiO_3$ glasses under high pressure. *J. Phys. Condens. Matt.*, **18**:6531, 2012

[77] P. A. Madden and M. Wilson. 'Covalent' Effects in 'ionic' systems. *Chem. Soc. Rev.*, **25**:339, 1996

[78] M. Salanne, B. Rotenberg, S. Jahn, R. Vuilleumier, C. Simon and P. A. Madden. Including many-body effects in models for ionic liquids. *Theor. Chem. Acc.*, **131**:1143, 2012

[79] N. W. Ashcroft and D. C. Langreth. Structure of Binary Liquid Mixtures I. *Phys. Rev.*, **156**:685, 1967

[80] M. C. Wilding, M. Guthrie, S. Kohara, C. L. Bull, J. Akola, M. G. Tucker. The structure of MgO-SiO_2 Glasses at Elevated Pressure. *J. Phys. Condens. Matter*, **24**:22, 2012

[81] A. Zeidler, K. Wezka, R. F. Rowlands, D. A. J. Whittaker, P. S. Salmon, A. Polidori, J. W. E. Drewitt, S. Klotz, H. E. Fischer, M. C. Wilding, C. L. Bull, M. G. Tucker, M. Wilson. High Pressure Transformation of SiO_2 glass from a Tetrahedral to an Octahedral Network: A Joint Approach Using Neutron Diffraction and Molecular Dynamics. *Phys. Rev. Lett.*, **113**:135501, 2014

[82] P. S. Salmon, A. Zeidler. Identifying and characterising the different structural length scales in liquids and glasses: An Experimental Approach. *Phys. Chem. Chem. Phys.*, **15**:15286, 2013

[83] M. C. Wilding, C. J. Benmore, J. A. Tangeman, S. Sampath. Coordination changes in magnesium silicate glasses. *Europhys. Lett.*, **67(2)**:212, 2004

[84] T. Gasparik. *Phase Diagrams for Geoscientists: An Atlas of the Earth's Interior*. Springer: Berlin, 2003

[85] I. P. Swainson, M. T. Dove, W. W. Schmahl, A. Putnis. Neutron powder diffraction study of the akermanite-gehlenite solid solution series. *Physics and Chemistry of Minerals*, **19(3)**:185, 1992

[86] D. A. Stephenson and P. B. Moore. The Crystal Structure of Grandiderite, (MgFe)Al_3SiBO_9. *Acta. Crystallogr. B*, **28**:267, 1968

[87] C. T. Prewitt, R. T. Downs. *Ultra High-Pressure Mineralogy: Physics and Chemistry of the Earth's Deep Interior. Rev. Miner.*, **37**:283, 1998

[88] B. Periotto, T. Balic-Zunic, F. Nestola, A. Katerinopoulou, R. J. Angel. Re-investigation of the crystal structure of enstatite under high-pressure conditions. *American Mineralogist*, **97**:1741, 2012

[89] F. M. Lea. *Lea's Chemistry of Cement and Concrete*, 4th edition. Elsevier:Amsterdam, 1998

[90] T. Kokubo, H.-M. Kim and M. Kawashita. Novel bioactive materials with different mechanical properties. *Biomaterials*, **24**:2161, 2003

[91] T. S. Duffy. Synchrotron Facilities and the study of the Earth's deep interior. *Rep. Prog. Phys.*, **68**:1811, 2005

[92] E. Mazzucato and A. F. Gualtieri. Wollastonite polytypes in the CaO-SiO_2 system. *Phys. Chem. Minerals*, **27**:565, 2000

[93] F. J. Trojer. The crystal structure of parawollastonite. *Z. Kristalloger.*, **127**:291, 1968

[94] M. C. Eckersley, P. H. Gaskell, A. C. Barnes and P. Chieux. Structural ordering in a calcium silicate glass. *Nature*, **335**:525, 1988

[95] R. N. Mead and G. Mountjoy. A molecular dynamics simulation study of densfication mechanisms in calcium silicate glasses $CaSi_2O_5$ and $CaSiO_3$ at pressures of 5 and 10 GPa. *J. Chem. Phys.*, **125**:154501, 2006

[96] A. R. Hilton. *Chalcogenide Glasses for Infrared Optics.* McGraw-Hill, New York, 2009

[97] D. Lezal, J. Pedlikova, and J. Zavadil. Chalcogenide glasses for optical and photonics applications. *Chal. Lett.*, **1**:11, 2004

[98] V. Kovanda, M. Vlcek and H. Jain. Structure of As-Se and As-P-Se glasses studied by Raman spectroscopy. *J. Non-Cryst. Solids*, **326**:88, 2003

[99] J. E. Shelby. *Introduction to Glass Science and Technology.* Royal Society of Chemistry, Cambridge, U.K, 2005

[100] E. Soignard. Private Communication, 2012

[101] S. A. Amin, E. N. Rissi, K. McKiernan and J. L. Yarger. Determining the equation of state of amorphous solids at high pressure using optical microscopy. *Rev. Sci. Instrum.*, **83**:033702, 2012

[102] K. Wezka, A. Bouzid, K. J. Pizzey, P. S. Salmon, A. Zeidler, S. Klotz, H. E. Fischer, C. L. Bull, M. G. Tucker, M. Boero, S. Le Roux, C. Tugene, C. Massobrio. Density-driven defect-mediated network collapse of $GeSe_2$ glass. *Phys. Rev. B*, **90**:054206, 2014

[103] P. Goldstein and A. Paton. The Crystal and Molecular Structure of Tetrameric Arsenic Selenide, As_4Se_4. *Acta Cryst. B*, **30**:915, 1974

[104] A. S. Ahmad, K. Glazyrin, H. P. Liermann, H. Franz, X. D. Wang, Q. P. Cao, D. X. Zhang, J. Z. Jiang. Breakdown of intermediate range order in AsSe chalcogenide glass. *J. Appl. Phys.*, **120**:145901, 2016

[105] J. E. Enderby. Neutron diffraction, isotopic substitution and the structure of aqueous solutions. *Phil. Trans. R. Soc. Lond. B*, **290**:553, 1980

[106] A. Yamada, Y. Wang, T. Inoue, W. Yang, C. Park, T. Yu and G. Shen. High pressure X-ray diffraction studies on the structure of liquid silicate using a Paris-Edinburgh type large volume press. *Rev. Sci. Instrum.*, **82**:015103, 2011

[107] A. D. Rosa, J. Pohlenz, C. de Grouchy, B. Cochain, Y. Kono, S. Pasternak, O. Mathon, T. Irifune and M. Wilke. In-situ characterisation of liquid network structures at high pressure and temperature using X-ray absorption spectroscopy coupled with the Paris-Edinburgh press. *High Pressure Research*, **36**:332, 2016

[108] H. J. Stone, M. G. Tucker, F. M. Meducin, M. T. Dove, S. A. T. Redfern, Y. Le Godec and W. G. Marshall. Temperature measurement in a Paris-Edinburgh cell by neutron resonance spectroscopy. *J. Appl. Phys.*, **98**:064905, 2005

[109] C. Bull. Private Communication, 2017

[110] Ceramic Substrates Ltd. Private Communication, 2017

[111] S. Klotz. Private Communication, 2016

[112] P. D. Desai, T. K. Chu, H. M. James and C. Y. Ho. Electrical Resistivity of Selected Elements. *J. Phys. Chem. Ref. Data*, **13**:1069, 1984

[113] R. W. Powell, R. P. Tye and M. J. Woodman. The thermal conductivity and electrical resistivity of rhenium. *Journal of the Less Common Metals*, **5**:49, 1963

[114] M. Okada, N. Ohta, O. Yoshimoto, M. Tatsumi and M. Inagaki. Review on the high-temperature resistance of graphite in inert atmospheres. *Carbon*, **116**:737, 2017

[115] A. I. Lutcov, V. I. Volga and B. K. Dymov. Thermal conductivity, electric resistivity and specific heat of dense graphites. *Carbon*, **8**:753, 1970

[116] http://www.cotronics.com/vo/cotr/pdf/919 (webpage accessed Dec 2018)

[117] www.thermocoupleinfo.com (Accessed Dec 2018)

[118] F. P. Bundy. Phase Diagram of Bismuth to 130 000 kg / cm^2, 500°C. *Phys. Rev.*, **110**:314, 1958

[119] C. Hai-Yan, X. Shi-Kai, Y. Xiao-Zhen, Z. Li-Rong, Z. Yi, L. Sheng-Gang, B. Yan. Phase transition of solid bismuth under high pressure. *Chinese Physics B*, **25**:108103, 2016